UNIVERSITAT POLITÈCNICA DE CATALUNYA
BARCELONATECH

Department of Signal Theory
and Communications

PhD Thesis Dissertation

# Contribution to advanced sensor development for passive imaging of the Earth

Author

**Israel Durán**

Department of Signal Theory and Communications

Universitat Politècnica de Catalunya (UPC)

C/ Jordi Girona 1-3, D3-116, 08034 Barcelona (Spain)

israel.duran@tsc.upc.edu

PhD Thesis Advisors

**Dr. Francesc Torres Torres**

**Dr. Núria Duffo Úbeda**

[xtorres, duffo]@tsc.upc.edu

Department of Signal Theory and Communications

Universitat Politècnica de Catalunya (UPC)

Barcelona, September 2017

# Abstract

This work has been formally undertaken within the frame of the scholarship number BES-2012-053917 of 1 December 2012, by the "Secretario de Estado de Investigación del Ministerio de Economía y Competitividad" related to the program "Formación de Personal Investigador (FPI)". The scholarship is related to the research project at the Universitat Politècnica de Catalunya (UPC) number TEC2011-25865. In a more general scope, this thesis is related to the Remote Sensing Laboratory (Signal Theory & Communication Department, UPC) on-going activities, within the SMOS (Soil Moisture and Ocean Salinity) mission by the European Space Agency (ESA). These activities have been organized to provide original advances in the following four main topics:

1) SMOS calibration and performance

Since the launch of the instrument in 2009, SMOS imaging has been performing exclusively in co-polar mode. However, SMOS measurements are fully polarimetric. This feature was not operationally exploited due to the large errors yielded by full-pol images. In this context my work was addressed to support better characterization of the antenna. Based on the idea that SMOS polarization mode was recently implemented using Full-pol measurements, the so-called relative phases have been recomputed by using co-polar and cross-polar measurements.

SMOS moderate Side Lobe Level (SLL) is caused by the limited coverage of the measured visibility samples in the frequency domain, so another objective of this work has been devoted to assess the impact of calibration errors into SMOS side lobes level (SLL). The main objective on this topic has been to reproduce by simulation SMOS measured side-lobe levels (SLL) by adding errors to a point source response, in order to identify the dominant source of error.

During commissioning phase it was detected that SMOS heater system were introducing small and random sporadic PMS offset steps (jumps) in several units. Another work during this thesis has been devoted to mitigate those PMS jumps by trimming calibration date from single LICEF averaged TA jumps over the ocean.

2) SMOS spatial bias assessment

SMOS measurements still have mathematical image reconstruction errors that must be properly assessed. The aim of this work is to focus on the so-called “floor error”, defined in an error free end-to-end image reconstruction simulation. In order to reduce this error, different inversion approaches have been implemented and tested, as the so-called Gibbs 2 approach

3) SMOS improved imaging

One of the problems of most concern within the SMOS mission is related to the so-called “land-sea contamination” (LSC), an artificial increase of ocean brightness temperature close to land masses. Therefore, a systematic assessment has been performed in this thesis in order to understand and mitigate this artifact. This subject is related to one of the main original outcomes of the thesis, since it has a relevant impact on the quality of SMOS imaging. The LSC mitigation technique developed during the work of the thesis has been presented and validated by different methods.

4) SMOS follow-on missions advanced configurations

This work is devoted to assess the impact of instrumental errors on the radiometric accuracy (pixel bias) of one of the selected array configurations of the so-called Super-MIRAS instrument. The aim of this work has been focused on the assessment of different array geometries and instrument architectures of future L-band synthetic aperture radiometers to improve spatial resolution while maintaining radiometric sensitivity.

## Resumen

Esta tesis se ha llevado a cabo en el marco de la beca FPI BES-2012-053917 del 1 de diciembre de 2012, por el "Secretario de Estado de Investigación del Ministerio de Economía y Competitividad", asociada al proyecto TEC2011-25865 (Universidad Politècnica de Catalunya). En un sentido más amplio, el trabajo se engloba dentro de las actividades del Grupo de Teledetección (RSLab) del Departamento de Teoría de la Señal y Comunicaciones, UPC, en el marco de la misión SMOS (Soil Moisture and Ocean Salinity) de la Agencia Espacial Europea del Espacio (ESA). El trabajo se divide en:

1) Calibración y prestaciones del sensor SMOS

Desde el lanzamiento del instrumento en 2009, la imagen de SMOS se ha obtenido utilizando medidas en modo co-polar. Sin embargo, las medidas en SMOS se realizan en full-pol. Esto no se había llevado a cabo debido a los grandes errores que se obtenían con imágenes en full-pol. En este contexto mi trabajo se ha enfocado en la realización de una mejor caracterización de la antena. Basado en la idea de que el modo full-pol ha sido recientemente implementado en SMOS, las fases relativas entre antenas han sido recalculadas utilizando medidas co-polares y cross-polares.

Los lóbulos secundarios de SMOS (SLL) son causados por la cobertura limitada de las visibilidades medidas en el dominio frecuencial, así que otro de los objetivos de este trabajo ha sido analizar el impacto de errores de calibración en los lóbulos secundarios de SMOS. Básicamente se han reproducido los lóbulos secundarios de SMOS mediantes simulaciones añadiendo errores a una fuente puntual, identificando las principales fuentes de error.

Durante la fase de comisionado se detectó que el sistema de calentamiento de SMOS introducía pequeños saltos aleatorios del offset del PMS en diferentes unidades. Para hacer un seguimiento y corregir estos saltos se realizaron calibraciones de offset semanales justo después de la fase de comisionado, así que otro de los trabajos realizados en esta tesis ha sido dirigido a mitigar estos saltos introduciendo calibraciones adicionales antes de los mismos a partir de medir la temperatura de antena media calculada en el océano.

2) Técnicas de reducción de los errores espaciales

SMOS tiene un error matemático de reconstrucción en la imagen que ha sido investigado en este trabajo. Así que este trabajo se ha focalizado en el “floor error” definido como el error de reconstrucción en un instrumento ideal libre de errores. Para reducir este error se han utilizado diferentes aproximaciones como Gibbs 2.

3) Mejoras en la inversión de imagen

Uno de los mayores problemas durante los primeros cinco años de misión SMOS ha sido la llamada “land-sea contamination” (contaminación tierra-mar). Así pues, se ha realizado un estudio sistemático para comprender y mitigar este artefacto. Este tema está relacionado con uno de los descubrimientos más importantes de esta tesis ya que este tiene un gran impacto en la calidad de la imagen de SMOS. La técnica encontrada para mitigar este error es presentada y validada mediante diferentes métodos.

4) Misiones futuras

Este trabajo está enfocado en la investigación del impacto de errores instrumentales en la precisión radiométrica de errores espaciales de una de las posibles nuevas configuraciones de array propuestas para construir un nuevo instrumento llamado Super-MIRAS. El propósito principal de este trabajo está orientado en el desarrollo de diferentes geometrías de arrays y arquitecturas de instrumentos para una futura misión en banda L, en la que se diseñaría un nuevo radiómetro de apertura sintética para mejorar la resolución espacial manteniendo la sensibilidad radiométrica.

# Contents

# 1 Introduction

## 1.1 Scope of this work

This work has been formally undertaken within the frame of the scholarship number BES-2012-053917 of 1 December 2012, by the "Secretaría de Estado de Investigación del Ministerio de Economía y Competitividad" related to the program "Formación de Personal Investigador (FPI)". This scholarship is related to the research project at the Universitat Politècnica de Catalunya (UPC) number TEC2011-25865, titled "SMOS: Activities of the operational phase and future missions".

In a more general scope, the activities performed within the working plan of this thesis are related to the general on-going activities of the Remote Sensing Laboratory (RSLab) at the Signal Theory and Communications Department (UPC) within the SMOS (Soil Moisture and Ocean Salinity) mission by the European Space Agency (ESA). The main projects directly related to my research activity are the following:

- "SMOS+ Innovation: polarimetry". (EOEP-STSE-EOPG-SW-11-0004) sponsored by the European Space Agency (ESA), as subcontractor of ACRI-ST Sophia-Antipolis (France). 10/2011 to 12/2012.
- "SMOS after Commissioning - L1 ESL (Expert Support Laboratory) support for the 2010-2014 period" sponsored by the European Space Agency (ESA) as subcontractor of DEIMOS Engenharia (Portugal). 10/2010 to 10/2014.
- SMOS ESL L1 "SMOS Expert Support Laboratory for Level 1 – Calibration and image reconstruction for the period 2014-2019" European Space Agency (ESA), Deimos Engenharia.
- "Study of a high spatial resolution MIRAS (Super-MIRAS)"
  European Space Agency (ESA), EADS Astrium. 2010-2012.
- "Digital Receiver for Radiometers" (DiReRa).
  European Space Agency (ESA), Mier Comunicaciones. 2013-2014.

Additionally, part of the work in this thesis is developed according to my participation as a researcher in three projects by the "Ministerio de Economía y Competividad. Plan Nacional de I+D+I", to accomplish several specific objectives:

- "*MIDAS-6. SMOS productos de salinidad del océano y humedad de la tierra*" Demostración y aplicaciones. Subproyecto parte UPC". AYA2010-22062-C05-05 (subprograma ESP). From 01/2010 to 12/2011.
  - SMOS Level 0 activities: Analysis of L0-L1 SMOS data and development of data visualization and processing tools.
    - Task R4. System performance assessment.
- "*MIDAS-7: Productos y aplicaciones avanzados de SMOS y futuras misiones*". Parte UPC. AYA2012-39356-C05-01. From 01/2013 to 12/2015.

    - WP 1: Improvement of SMOS products quality
        - 1.1 Analysis of errors in the Extended Alias-Free Field of View (EAF-FoV).
        - 1.2 SMOS full-pol up-grade.
- *"Optimización de las prestaciones de SMOS y futuras misiones".* Convocatoria Retos de investigación. Ministerio de Economía y Competitividad TEC2014-58582-R. Dirección General de Investigación Científica y Técnica. 2015-2017.

When I joined the RSLab research team in September 2009, SMOS was a mature project. RSLab initial activities on passive interferometry started around 1994, as reflected in the PhD thesis by Adriano Camps "Applications of interferometric Radiometry to Earth observation", (UPC, 1996). This work reviewed the theoretical measurement background and settled the basic principles on passive interferometry for Earth observation regarding image reconstruction, error analysis and calibration procedures. This work has been the reference for many projects and studies undertaken at the RSLab, mainly sponsored by the European Space Agency. These initial prospective activities eventually ended with the approval of the SMOS mission in 1999, as an ESA Explorer Opportunity mission, a technology demonstration satellite project in ESA's Living Planet Program, in cooperation with CNES (France) and CDTI (Centro para el Desarrollo Tecnológico e Industrial), Madrid, Spain. Casa Construcciones Aeronauticas (Spain) was the main contractor of SMOS single payload, the MIRAS (Microwave Imaging Radiometer by Aperture Synthesis) instrument. The RSLab was the main research group to provide scientific and technologic support to the industry. The RSLab team also has had relevant role in the SMOS/MIRAS payload ground characterization tests that took place in Maxwell anechoic chamber, at ESA premises (The Netherlands) on spring 2007 and the MDPP (MIRAS Demostrator Pilot Project) airbone demonstrator [Martin-Neira *et al.*, 2008b].

SMOS was successfully launched in November 2009 and since then it has been providing a continuous stream of high quality data to yielding a continuous flow of fully polarimetric brightness temperature images. After more than seven years of operation, SMOS has proven to be highly useful for a variety of scientific applications related to soil moisture over land, ocean salinity and winds over ocean, as well as specific studies over the ice covered surfaces. Just before launch, within SMOS pre-commissioning activities, the UPC team was recognized as a SMOS Expert Support Laboratory (ESL) by ESA to support flight calibration and system performance activities.

The miscellaneous research topics that I have been involved within this framework have been directly related to the RSLab projects dealing with SMOS pre-commissioning, commissioning and operational specific issues. The work undertaken both in my PFC (Proyecto final de carrera) and master thesis were related to SMOS amplitude calibration and in-flight characterization during pre-commissioning and commissioning phases. Once my FPI scholarship was granted in 2012, my activity was readdressed to work on the error budget and system performance of the so-called "Super MIRAS", a SMOS follow-on prospective project. However, since some of the major findings out of this initial work were very suitable to the MIRAS/SMOS sensor, my research activity was shifted to support SMOS full-pol performance improvements. This activity was undertaken in collaboration with Wu Lin PhD activities [Wu, 2014] and resulted in several publication co-authoring. In parallel, some residual activity on SMOS calibration and system performance issues was also undertaken to cope with specific SMOS operational troubleshooting. It must be pointed out that some of the activity described in this thesis has been undertaken in collaboration with other researchers that are properly credited when appropriate: Marc Vizcarro, Miriam Pablos and Verónica González.

All these activities have been documented in a long list of technical notes (see chapter 9) and resulted into a number of co-authored publications (chapter 9). For the sake of clarity, the different chapters of this thesis have not been arranged according to follow the historical timeline. Instead, the thesis outline follows a more conventional structure, from general to specific topics, trying to focus on the original contributions and particular tasks related to my research work. For consistency, the different topics are also grouped into general area (calibration, imaging or system performance) no matter when they have been addressed. SMOS literature is huge and cannot be summarized in this work. Only those specific topics required to follow the research activities presented in this thesis are briefly sketched and proper references are included for those readers interested to go deeper in any particular issue.

## 1.2 SMOS overview

The SMOS mission (Soil Moisture and Ocean Salinity) has been designed to observe soil moisture over the Earth’s landmasses and salinity over the oceans (http://www.esa.int/Our_Activities/Observing_the_Earth/SMOS). SMOS is the second Earth Explorer Opportunity mission developed as part of ESA’s Living Planet Programme in cooperation with Centre National d’Etudes Spatiales (CNES) in France and Centro para el Desarrollo Tecnológico Industrial (CDTI) in Spain. Several European institutions, including UPC have taken part in the instrument development and in the measurement campaigns.

The main contribution in the design and analysis of instrument operation was performed by the radiometric team of the Remote Sensing Laboratory (RSLab) of TSC (Theory of Signal and Communications Department) at UPC. Researches from several European Universities and other institutions, among them the SMOS Barcelona Expert Centre on Radiometric Calibration and Ocean Salinity (SMOS-BEC) are also involved in the data processing.

*Figure 1.1 SMOS in orbit*

The initial SMOS mission main objectives are to globally observe soil moisture over the Earth's landmasses and salinity over the oceans for a period of 3-5 years with an innovate technology on board a satellite, a Microwave Imaging Radiometer by Aperture Synthesis (MIRAS). This is possible because both the moisture and salinity affect the electrical properties of matter and the emissivity of any material based on these properties. The MIRAS instrument is based on the property that the moisture and salinity decrease the emissivity of soil and seawater, respectively. The SMOS satellite was launched the 2nd of November 2009 from the Plesetsk Cosmodrome in northern Russia, to a nearly sun-synchronous orbit of 763 km, forcing an orbital period of about 100 minutes. This means that the satellite goes around our planet 14.4 times per day and the revisit time in any point on the Earth is guaranteed below 3 days. Passive interferometry for Earth observation is of huge importance for the remote sensing community due to the possibility to provide radiometric images without the need for mechanical scanning of large real aperture antennas, especially at low frequencies (e.g. L band).

The SMOS mission is being developed under the management of ESA in two areas: the Satellite Operations Ground Segment (SOGS) and the Data Processing Ground Segment (DPGS). The Centre National d'Etudes Spatiales (CNES) located in Toulouse, France, is in charge of the spacecraft operations via an S-band station in Kiruna, Sweden. The European Space Astronomy Centre (ESAC) is ESA’s centre for space science. It is located in Villanueva de la Cañada, close to Madrid in Spain, and hosts the science operation centres for all ESA astronomy and planetary missions together with their scientific archives. It is in charge of the data processing, where the payload data are received via a X-band link. A consortium formed by different Spanish companies, like EADS-CASA Espacio, GMV Aerospace and Defence and INDRA Espacio, and a Portuguese company Deimos Space, performs data processing and validation. European Universities and other institutions, among them UPC and the SMOS Barcelona Expert Centre on Radiometric Calibration and Ocean Salinity (SMOS-BEC) are also involved in the data processing. Since 2013 I have been attending the frequent SMOS calibration meetings at ESAC, as part of this UPC SMOS Expert Support Laboratory.

SMOS single payload, MIRAS, operates at 1.4 GHz (L-band) and it includes 69 small antennas evenly distributed on the arms of a Y shape mechanical structure. Its operation is interferometric in 2D so that it gets brightness temperature maps by mathematical inversion of the so called visibility function [Corbella *et al.*, 2005]. The visibility corresponding to zero spacing is measured independently and redundantly by three dedicated Noise Injection Radiometers (NIR) located near the centre of the array [Colliander *et al.*, 2007]. The instrument provides a spatial resolution similar to that of a real aperture radiometer of similar overall dimensions and gets maps of brightness temperature at said resolution without the need of any mechanical scanning.

## 1.3 General objectives and thesis outline

### 1.3.1 General objectives

The research activities undertaken in the frame of this thesis are expected to conduct to original advances in several topics:

1) SMOS calibration and performance

Since launch, SMOS imaging has been performing exclusively in co-polar mode. However, SMOS measurements are fully polarimetric. This feature was not operationally exploited due to the large errors yielded by full-pol images. In this context my work is addressed to support better characterization of the antenna. Based on the idea that SMOS polarization mode was recently implemented using Full-pol measurements, the so-called relative phases are recomputed by using co-polar and cross-polar measurements.

Another objective of this work is undertaken in the frame of the project "CCN-1 Super MIRAS Study". This task is devoted to assess the impact of calibration errors into SMOS side lobes level (SLL). The main objective is to reproduce by simulation SMOS measured side-lobe levels (SLL) by adding errors to a point source, identify the dominant source of error and eventually improve performance.

2) SMOS spatial bias assessment

Some mathematical errors in the reconstruction of the image are assessed in that work. At this point improving visibility inversion requires understanding truncation, aliasing, redundancy, antenna pattern differences and other effects in an undetermined linear system of equations. The aim of this work is to investigate on these image reconstruction limitations in order to eventually design an improved methodology, able to further reduce the present artifacts on the SMOS images.

The instrument has a “floor error” defined as the residual error that appears in an error free end-to-end image reconstruction simulation. Moreover, part of this work is devoted to assess the capability of two inversion methods to mitigate the “floor error”. In order to reduce this mathematical error, different inversion approaches are implemented (the so-called basic, model and Gibbs 2 approach).

3) SMOS improved imaging

One of the problems of most concern within the SMOS mission is related with the so-called land-sea contamination (LSC). So, a systematic assessment is performed in order to understand and mitigate this artifact. This activity is crystallized in the periodic development of data processor versions at different levels. For example, the latest Level-1 operational processor (L1OP v620) become nominal in spring 2015 and has been used in the second mission reprocessing completed in September 2015. Among other calibration enhancements described in chapter 5 and chapter 6, this version includes a fully polarimetric image reconstruction scheme.

Further work will be done using new inversion approaches as Gibbs 2 in order to reduce the floor error.

4) SMOS follow-on missions advanced configurations

This work is devoted to assess the impact of instrumental errors on the radiometric accuracy (pixel bias) of one of the selected array configurations of the so-called Super-MIRAS instrument. Some of the relevant advances resulted in improvements to the SMOS mission and have been further developed in other chapters. For instance, the X-MIRAS study on the impact of antenna pattern differences conducted to the origin and model of the so-called “floor error” and proved the way to develop a specific image inversion procedure that mitigates its impact on SMOS retrievals to a large extend.

### 1.3.2 Thesis outline

This thesis is divided into nine chapters.

Chapter 1 describes the framework of this thesis and gives the motivation and historical background related to the original research activities performed throughout this thesis.

Chapter 2 briefly describes the fundamentals on radiometry, as presented by [Ulaby, 1981]. The basic concepts of radiometry are summarized in order to understand the principles of remote sensing and the MIRAS instrument. A deeper insight into aperture synthesis radiometry, including SMOS image reconstruction fundamentals, can be followed in [Camps, 1996], [Camps *et al.,* 1997], [Corbella, 2008] and [Corbella *et al.*, 2005a].

Chapter 3 focuses in the MIRAS payload and the most important subsystems of the instrument are described in depth. Further insight on MIRAS/SMOS architecture can be found in [Barre *et al.*, 2008] and [McMullan *et al.*, 2008]. Also, the calibration and measurement modes of the MIRAS sensor are outlined. Those topics required to follow specific research activity undertaken in the thesis are developed in more detail. However, if a deeper insight on SMOS calibration and measurement mode is required, it can be found [Torres *et al.*, 1996], [Brown *et al.*, 2008], [Corbella *et al.*, 2005], [Corbella *et al.*, 2008], [Corbella *et al.*, 2011], [Oliva *et al.*, 2013], [Martin-Neira *et al.*, 2002] and [Corbella, 2008].

Chapter 4 is devoted to describe the improvements in SMOS calibration and modeling achieved during the work of the thesis. The different parameters were accurately characterized on ground. However, these parameters change in orbit because of seasonal temperature variation and can cause very large errors if not properly tracked down. This chapter is devoted to describe several calibration up-grades that have been undertaken within this PhD work as improved inter element Full-pol phase calibration, SLL performance and PMS offset improved calibration.

Chapter 5 is devoted to a set of different activities aimed to improve SMOS modeling. In particular, this work addressed the impact on system performance of several antenna features such as antenna pattern differences or cross-polar components. The impact of truncation and the so called “floor error” are also assessed in detail. The outcomes of this activity contributed to develop SMOS current operational fully polarimetric image reconstruction technique [Wu, 2014] and [Wu *et al.*, 2013], included in the version v620 of SMOS L1 operational processor.

Chapter 6 is devoted to assess the capability of two different inversion methods to mitigate the “floor error” analyzed in chapter 5. In order to reduce this mathematical error, different inversion approaches are implemented (the so-called basic and model approach and Gibbs 2). The impact of these techniques on SMOS full-pol brightness temperatures, especially on Stokes 3rd and 4th parameters is assessed in detail. Assessment and validation on these techniques is undertaken by means of global error maps.

Chapter 7 is devoted to one residual error that persists in the last version of the L1 Operational Processor (V620, May 2015), called “land–sea contamination” (LSC). This subject is related one of the main original outcomes of the thesis, since it has relevant impact on the quality of SMOS imaging. This artifact consists fundamentally of a slight increase in brightness temperature of water in zones near large land areas. It makes difficult OS retrievals close to the coast. The LSC mitigation technique found during the work of the thesis is presented and validated by different methods.

Chapter 8 is devoted to a SMOS follow on mission, currently under discussion, with the so-called Super MIRAS project. Some simulations and analysis have been performed about this new concept of instrument, oriented to analyze different array geometries and instrument architectures with the goal of improving spatial resolution while maintaining radiometric sensitivity. The chapter mainly focuses in the error budget of this new sensor, my main contribution to this project.

Chapter 9 summarizes the main conclusions and contributions of this work. The main additional research activities required to further improve SMOS performance are also outlined.

# 2 Fundamentals on radiometry

Any body with a physical temperature higher than 0 K emit electromagnetic radiation. The radiometry is the field of the engineering that studies and measures this radiation. In this chapter, the basic concepts of radiometry are explained in order to understand the principles of remote sensing and the operation fundamentals of the MIRAS instrument.

## 2.1 Microwave thermal radiation

The power emitted by a body in a given direction $(\theta, \phi)$ at a solid angle per unit area $[W \cdot sr^{-1} \cdot m^{-2}]$ is called brightness $B(\theta, \phi)$. The definition of brightness for an extended source of incoherent radiation with a determined pattern is [Ulaby, *1981*]:

$$B(\theta, \phi) = \frac{F_t(\theta, \phi)}{A_t} \tag{2. 1}$$

where $F_t(\theta, \phi)$ is the directional distribution function $[W \cdot sr^{-1}]$ of the source and $A_t$ $[m^2]$ is the effective radiating area. Considering the case of two lossless antennas separated a distance $R$, oriented in the direction of maximum directivity with an effective area $A_t$ $[m^2]$ for the transmitting antenna and $A_r[m^2]$ for the receiving antenna, being $R$ large enough to be considered a constant power over a solid angle $\Omega$ $(sr)$, then the measured power by the receiving antenna is described by:

$$P_r = B \cdot A_t \cdot \Omega_r \tag{2. 2}$$

where $P_r$ is the power measured by the receiving antenna. The solid angle subtended by the receiving antenna $\Omega_r$ when observed by the transmitting antenna is:

$$\Omega_r = \frac{A_r}{R^2} \tag{2. 3}$$

Since the solid angle of the radiating body (transmitter) as seen from the receiving antenna can also be expressed as:

$$\Omega_t = \frac{A_t}{R^2} \tag{2. 4}$$

Then the power measured by the receiver antenna is usually expressed as:

$$P_r = BA_r\Omega_t \tag{2. 5}$$

Now, in general the brightness seen by the receiving antenna is written as $B(\theta, \phi)$ since it is not constant in the different direction $(\theta, \phi)$ defined in the receiving antenna frame. Moreover, if the brightness is not constant with frequency, it is defined as the spectral brightness density $B_f(\theta,\phi)$ [ $W \cdot sr^{-1} \cdot m^{-2} \cdot Hz^{-1}$ ]. Therefore, the total power measured by the receiving antenna can be obtained by integrating the expression in bandwidth and space as:

$$P = \frac{1}{2} A_r \int_{f}^{f+\Delta f} \iint_{4\pi} B_f(\theta,\phi) |F_n(\theta,\phi)|^2 d\Omega df \tag{2. 6}$$

$F_n(\theta,\phi)$ is the complex normalized field antenna pattern. The term $1/2$ takes into account that the antenna presents a determined polarization and only half of the thermal emitted power is measured if the source emission is randomly polarized. The bandwidth of the receiving system is given by $\Delta f$. In the case of a black body (opaque perfectly ideal body that absorbs all incident radiation of all frequencies, without reflecting anything) the radiated energy follows Planck's law. That is, it radiates uniformly in all directions with a spectral brightness [ $W\ m^{-2}\ sr^{-1}\ Hz^{-1}$ ], as given by the following expression:

$$B_f = \frac{2hf^3}{c^2} \cdot \frac{1}{e^{\frac{h \cdot f}{k_B \cdot T_{ph}}} - 1} \tag{2. 7}$$

In the previous expression $f$ corresponds to the frequency ( $Hz$ ), $k_B$ is the Boltzmann's constant, $T_{ph}$ is the absolute temperature in Kelvin, $c$ is the speed of light and $h$ is the Planck constant. In the case of low frequencies the function approaches the Rayleigh-Jeans law. As shown in equation (2.8), there is a linear relationship between spectral brightness density and physical temperature.

$$B_f = \frac{2 f^2 k_B T_{ph}}{c^2} = \frac{2 k_B T_{ph}}{\lambda^2} \tag{2. 8}$$

Figure 2.1 shows the Rayleigh-Jeans law.

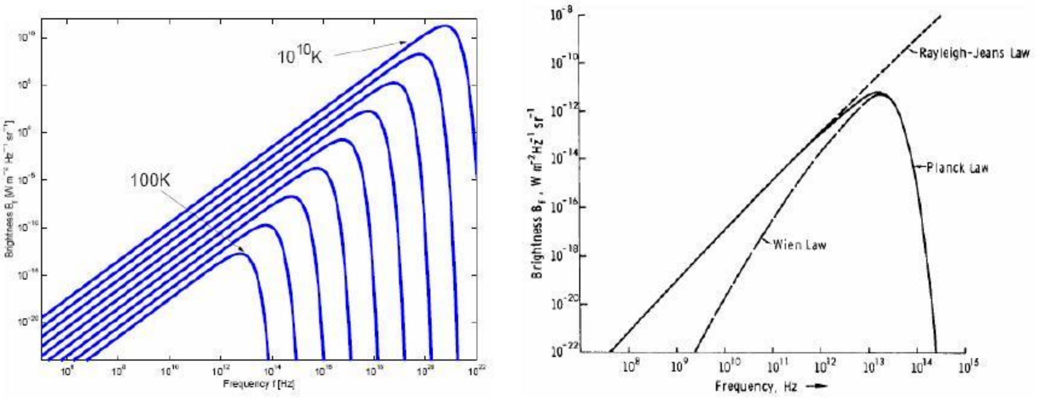

*Figure 2.1 Brightness spectral density vs frequency for different physical temperatures (left) and approaches the Planck's radiation law: the law of Rayleigh-Jeans(low frequency) and Wien's law(high Frequency) (right)*

A black body, in thermal equilibrium, radiates all the energy it has absorbed and therefore emits as much energy to a specific physical temperature (perfect absorber).On the other hand, real materials (also called gray bodies) emit less power than a black body because they do not absorb all the energy incident on them.

In the case of a gray body, the brightness emitted depends on the direction $B(\theta,\phi)$ and can be expressed as follows:

$$B(\theta,\phi) = 2 \cdot \frac{k_B}{\lambda^2} \cdot T_B(\theta,\phi) \cdot B \tag{2. 9}$$

where $T_B$ is the brightness temperature and $B$ is the bandwidth .

The relationship between brightness $B(\theta,\phi)$ of a material and the brightness of a black body that is on the same physical temperature is called emissivity:

$$e(\theta,\phi) = \frac{B(\theta,\phi)}{B_{bb}} = \frac{T_B(\theta,\phi)}{T_{ph}} \tag{2. 10}$$

where $0 \le e(\theta,\phi) \le 1$. The brightness temperature of a gray body expresses its emission properties (angular dependent) compared with that of a black body.

Since the brightness temperature of a gray body is less than of a black body, the brightness temperature of a material is always less or equal than its physical temperature. Therefore, the emissivity has value 0 for a fully reflective material and has value 1 for a perfect absorber (black body).

The incident radiation over an antenna consists of several items from various sources: the radiation emitted by the ground, $T_B$, the radiation emitted by the atmosphere and the radiation emitted by the atmosphere that falls on the ground and that is reflected.

The apparent radiometric temperature, $T_{AP}(\theta,\phi)$, is the distribution of the temperature of an equivalent black body, and its brightness distribution, $B_i(\theta,\phi)$, is the incident energy over the antenna:

$$B_i(\theta,\phi) = \frac{2k_B}{\lambda^2} \cdot T_{AP}(\theta,\phi) \cdot \Delta f \tag{2. 11}$$

The brightness temperature, $T_B(\theta,\phi)$, is related to the radiation received on a surface or volume, while the apparent temperature, $T_{AP}(\theta,\phi)$, is related to the incident energy received by the antenna. In the case that atmosphere losses were negligible, the apparent temperature would be equal to the brightness temperature.

As seen, the brightness's distribution of a gray body can be expressed in terms of the apparent temperature. Thus, taking into account the previous theory and the expression (2.6) the power received by the antenna can be expressed as follows:

$$P = \frac{1}{2} \cdot A_r \cdot \iint_{4\pi} \frac{2k_B}{\lambda^2} \cdot T_{AP}(\theta,\phi) \cdot \Delta f \cdot \left|F_n(\theta,\phi)\right|^2 \cdot d\Omega \tag{2. 12}$$

when computing the transfer function of the receiver, measuring the output voltage as a function of physical temperature of a load placed at the receiver input, it is possible to obtain the noise power, $P_N$ , which is proportional to physic temperature. If the correspondence is done with the power supplied by the antenna to the receiver, it is called radiometric antenna temperature, $T_A$, such as an equivalent resistance to deliver the same power:

$$P_N = P = k_B \cdot T_A \cdot \Delta f \tag{2. 13}$$

Therefore, the antenna temperature can be expressed in terms of the normalized power radiation diagram of the antenna, $\left|F_n(\theta,\phi)\right|^2$, and its effective area, $A_r$ as follows:

$$T_A = \frac{A_r}{\lambda^2} \cdot \iint_{4\pi} T_{AP}(\theta,\phi) \cdot \left|F_n(\theta,\phi)\right|^2 \cdot d\Omega \tag{2. 14}$$

A passive radiometer is an instrument that measures the spontaneous electromagnetic emission. This radiation is normally associated with thermal effect: the brightness temperature. Unlike other receivers, such as radar receivers that consider that the antenna radiometric temperature $T_A$ is a noise (undesired) contribution, the radiometers obtain from thus signal information on the emission characteristics of the scene being viewed.

## 2.2 Radiometers and interferometers

A radiometer is a device for measuring the spontaneous electromagnetic radiation of a distant body (brightness temperature). Generally, the term radiometer denotes an infrared radiation detector, yet it also includes detectors operating on any electromagnetic wavelength. A microwave radiometer is a radiometer that measures energy emitted at sub-millimeter-to centimeter wavelength (frequencies ranging from 1 GHz to 1000 GHz) known as microwaves.

### 2.2.1 Total power radiometer

A microwave radiometer is an important instrument for Earth observation in a large scale from space. In a real aperture radiometers (RAR) the pixel size is related to the projection on ground of the antenna half power beam width of the main beam. It uses a single antenna and its spatial resolution is defined by the antenna size.

Until SMOS mission, all microwave radiometers used for observation of the Earth have been real aperture radiometers. The more simplified version of this type of radiometers is the Total Power Radiometers (TPR).

A TPR consists of an antenna connected to a superheterodyne receiver with bandwidth $B$ and total gain $G$, followed by a power detector and a lowpass filter. The antenna receives the RF power emitted by the observed body and and an RF amplifier (low noise) increases the noise power of the adquired signal. A bandpass filter selects the desired frequency band which is converted in the mixer. The signal is amplified before passing through the power detector. Since the signal detected by the power detector is random, it is necessary to use a low pass filter to average the measured voltage. In a total power radiometer, the output voltage is proportional to the noise temperature of the system and can be written as:

$$v_{out} = k_B \cdot T_{sys} \cdot B \cdot G \tag{2. 15}$$

where $G$ is the system gain (zero offset system), $T_{sys} = T_A + T_R$ is the system noise temperature, $T_A$ is the equivalent noise temperature measured by the antenna, $T_R$ is the equivalent noise temperature of the receiver and $B$ is the bandwidth.

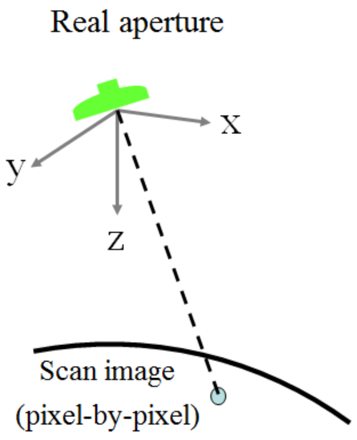

*Figure 2.2 Real aperture radiometer [Corbella, 2008]*

### 2.2.2 Interferometric Radiometer with aperture synthesis

The spatial resolution that can reach a radiometer is limited by the size of the antenna. The measurements of geophysical parameters such as soil moisture and ocean salinity at L-band require high spatial resolution, and therefore the large size of the antenna of a real aperture radiometer to allow such resolution is not technologically viable. At L-band, radiometric interferometry has been seen as the most promising approach to overcome this problem.

An interferometric radiometer consists of an array of antennas. The output voltages of different pairs of antennas are correlated and return the so-called visibility function. From the samples of this function, using image inversion algorithms, the image is reconstructed obtaining brightness temperature maps of the scene. This type of radiometers require a previous correction of the measured correlation samples since the interferometric radiometer by aperture synthesis does not measure the distribution of brightness temperature but the samples of its Fourier transform. Chapter 3 gives a summarized description of radiometric interferometry principles.

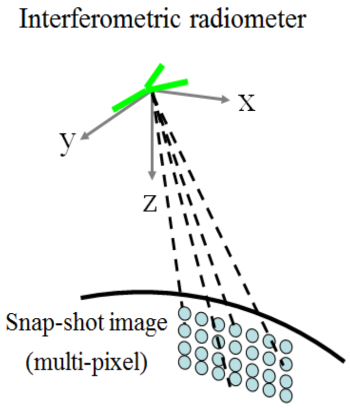

*Figure 2.3 Interferometric radiometer [Corbella, 2008]*

## 2.3 Basics on SMOS image reconstruction

The SMOS measured and calibrated visibility is transformed to brightness temperature by using an image reconstruction algorithm, a process that transforms the frequency domain measurements into a time domain image, therefore the brightness temperature can be seen as a time domain expression of the image and the visibility samples the image frequency components.

This section is devoted to explain the fundamentals of the image reconstruction procedure that is necessary for understanding the assessments of the next chapters. For instance, SMOS Field of View (FoV) or the different inversion approaches used to obtain brightness temperature.

### 2.3.1 Image reconstruction principle

SMOS measures the so-called visibility samples $V_{kj}$ (units of Kelvin) obtained from the complex correlation of the analytical signals $b_k$ and $b_j$ collected by each pair of antennas *"k"* and *"j"* in the array (Figure 2.4):

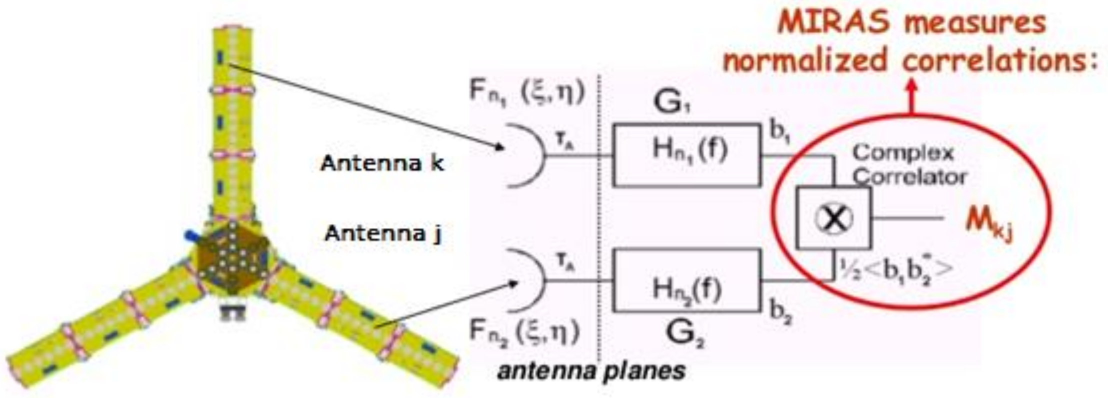

*Figure 2.4 Simplified block diagram of a single baseline*

The visibility equation is calculated for all baselines, out of the correlations, using the following equation:

$$V_{kj}(u,v) = \frac{1}{k_B\sqrt{B_k B_j}\sqrt{G_k G_j}}\frac{1}{2}\langle b_k b_j^* \rangle \tag{2. 16}$$

where $(u,v)$ corresponds to the set of spatial frequencies where the visibility function is sampled (antenna separation in wavelengths), $G_k, G_j$ are the power gains of each receiver chain, $B_k, B_j$ correspond to the equivalent noise bandwidths $k_B$ is the

Boltzmann constant and $b_k$ , $b_j$ are the analytical signals collected by each pair of receivers (baseline) to be correlated.

The visibility samples are related to the brightness temperature to be measured by the visibility integral given by:

$$V_{kj}(u,v)=\iint_{\xi^2+\eta^2\le 1}\frac{T_B(\xi,\eta)-T_r}{\sqrt{1-\xi^2-\eta^2}}\cdot\frac{F_{n_k}(\xi,\eta)\cdot F_{n_j}^*(\xi,\eta)}{\sqrt{\Omega_k\Omega_j}}\cdot\overset{=}{\tilde{r}}_{kj}\left(-\frac{u\xi+v\eta}{f_0}\right)\cdot e^{-j2\pi(u\xi+v\eta)}d\xi d\eta \qquad (2.\ 17)$$

where $T_r$ is the mean physical temperature of the receivers (assumed equal in both antennas), $\overset{=}{\tilde{r}}_{kj}$ corresponds to the Fringe Washing function normalized to unity and it is related to the spatial decorrelation errors, $T_B(\xi,\eta)$ is the brightness temperature, $F_{n_k}(\xi,\eta)$ , $F_{n_j}(\xi,\eta)$ are the normalized voltage antenna patterns, $\Omega_k$ , $\Omega_j$ correspond to the equivalent solid angle of the antennas and $(\xi,\eta)$ are the director cosines with respect to X and Y axes ( $\xi=\sin\theta\cos\phi$ , $\eta=\sin\theta\sin\phi$ ), respectively and $(u_{kj},v_{kj})$ is the antenna separation measured in wavelength for each pair “k, j”.

A function of the antenna patterns can be defined as:

$$AP_{kj}(\xi,\eta)=\frac{F_{n_k}(\xi,\eta)\cdot F_{n_j}^*(\xi,\eta)}{\sqrt{1-\xi^2-\eta^2}\sqrt{\Omega_k\Omega_j}} \qquad (2.\ 18)$$

In an ideal case (equal antenna patterns for all receivers and neglecting the Fringe Washing Function), the brightness temperature can be retrieved out of the inverse Fourier transform of the calibrated visibility samples:

$$T^{'}(\xi,\eta)=\Im^{-1}[V(u,v)] \qquad (2.\ 19)$$

where $T'(\xi,\eta)$ is the modified brightness temperature defined as:

$$T^{'}(\xi,\eta)=\frac{(T_B(\xi,\eta)-T_r)}{\sqrt{1-\xi^2-\eta^2}}\frac{\left|F_n(\xi,\eta)\right|^2}{\Omega} \qquad (2.\ 20)$$

Finally, in this ideal case, the brightness temperature of the scene is retrieved as:

$$T_B(\xi,\eta) = T'(\xi,\eta)\frac{\Omega\cdot\sqrt{1-\xi^2-\eta^2}}{|F_n(\xi,\eta)|^2} + T_r \qquad (2.\ 21)$$

In a real case as SMOS, antenna patterns present non-negligible differences that must be accurately measured on ground. To correct for these differences the Fourier transformation cannot be applied and the so-called G-matrix technique is required and once the *Tr* term is removed, it turns into the following matrix relationship:

$$V = G\cdot T_B \qquad (2.\ 22)$$

where *V* are the visibility samples measured by SMOS, *G* is the G-matrix and $T_B$ is the brightness temperature of the scene. If *G* is known, then the brightness temperature can be estimated using the following equation:

$$T_B = G^+\cdot V \qquad (2.\ 23)$$

where $G^+ = G^*(GG^*)^{-1}$ is the Moore-Penrose pseudo-inverse of *G*.

## 2.3.2 SMOS AF-FOV and EAF-FoV

As it has been mentioned in chapter 2, SMOS is a Y-shaped instrument. The length of a baseline (k,j) is calculated as:

$$d_{kj} = \sqrt{\Delta x_{kj}{}^2 + \Delta y_{kj}{}^2} \qquad (2.\ 24)$$

where $\Delta x_{kj} = x_j - x_k$ and $\Delta y_{kj} = y_j - y_k$ are the difference between the x and y coordinates of the receivers k and j. The radiometric integral in (2.17) uses the $(u,v)$ coordinate (normalized antenna positions or spatial frequencies) to describe the baselines. The $(u,v)$ coordinates are defined as the difference between the positions of the two receivers that comprises a given baseline divided by the wavelength at the center frequency of operation:

$$u_{kj} = \frac{x_j - x_k}{\lambda_0}, v_{kj} = \frac{y_j - y_k}{\lambda_0} \qquad (2.\ 25)$$

Figure 2.6 shows the antenna positions of MIRAS and the corresponding u-v samples in the hexagonal grid (also called the spatial sampling frequencies) since $V_{kj}(-u_{kj},-v_{kj}) = V^*_{kj}(u_{kj},v_{kj})$ only half visibility samples need to be measured.

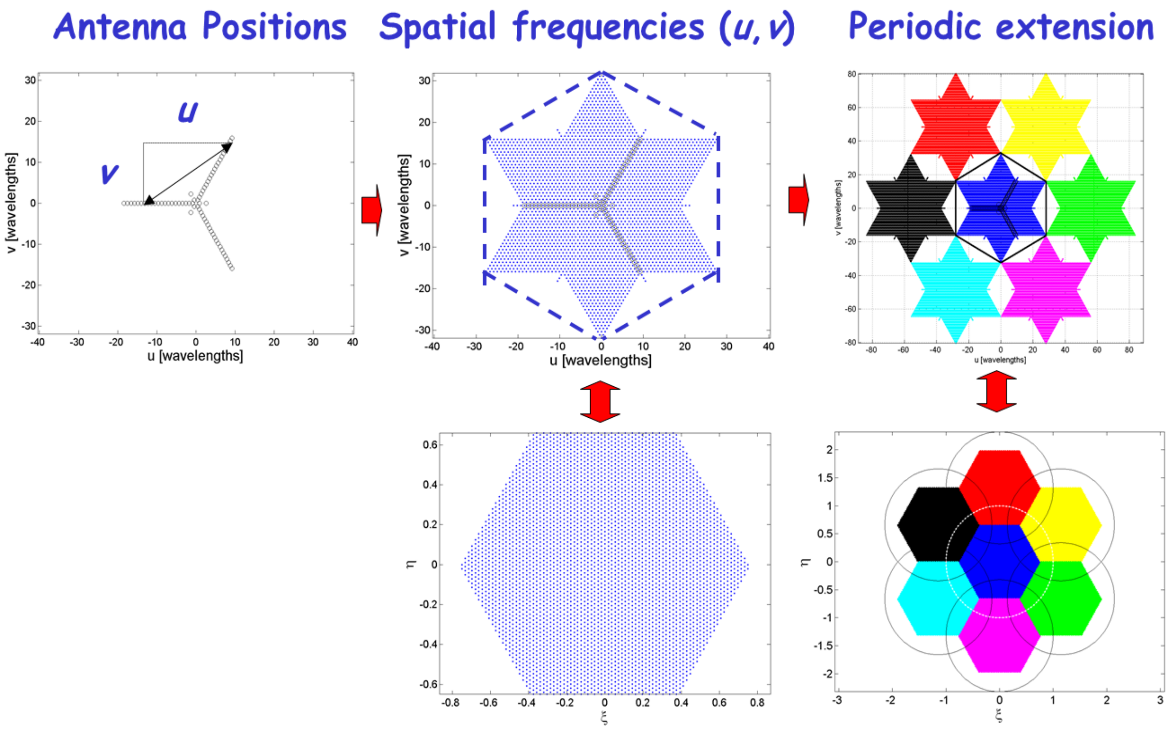

*Figure 2.5 Hexagonal spatial periodicity due to the discrete sampling*

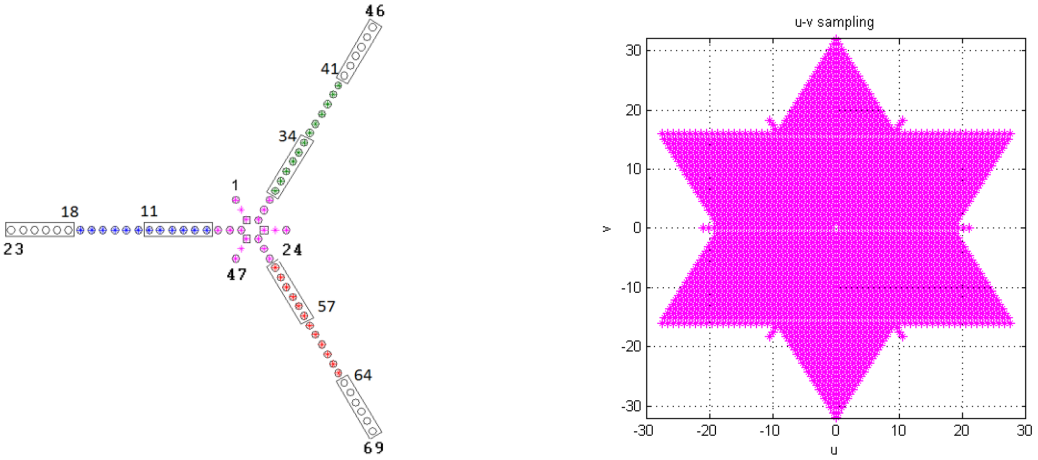

*Figure 2.6 Number related to antennas positions of MIRAS and the corresponding spatial sampling frequencies (u-v domain)*

The points in the star belong to a hexagonal grid. The image reconstruction process can be understood as the discrete-time Fourier transform (DTFT) because of the discrete sampling in the frequency domain *(u-v)*. This discrete sampling produces spatial periodicity: aliases (Figure 2.5 top right).

In the image inversion, the choice of using a $(\xi,\eta)$ grid is necessary in order to apply the FFT routines. The $(\xi,\eta)$ grid is reciprocal to the hexagonal *(u,v)* coverage given by the Y-shape array. For that purpose, it is necessary a change or coordinates from (u – v) to *($k_1$,$k_2$)* and from $(\xi,\eta)$ to *($n_2$,$n_1$)*. [Camps, 1996].

$$u=\frac{(2k_1-k_2)d}{2},v=\frac{k_2d\sqrt{3}}{2} \tag{2. 26}$$

$$\xi=\frac{n_2}{N_Td},\eta=\frac{2n_1+n_2}{\sqrt{3}N_Td} \tag{2. 27}$$

*(u,v)* points can be computed from (2.25), and then *($k_1$,$k_2$)* can be obtained from the equation (2.26) as follows:

$$k_1=\frac{u}{d}+\frac{1}{\sqrt{3}d}v,k_2=\frac{2}{\sqrt{3}d}v \tag{2. 28}$$

As shown in Figure 2.7 all points inside the fundamental hexagon are re-ordered to fit inside a rectangular shape in *(k1,k2)*. The same occurs with the *(n2,n1)* rectangular grid realignment to a hexagonal grid by applying an inverse processing of the similar method used in *k1-k2* re-ordering [Corbella, 2008].

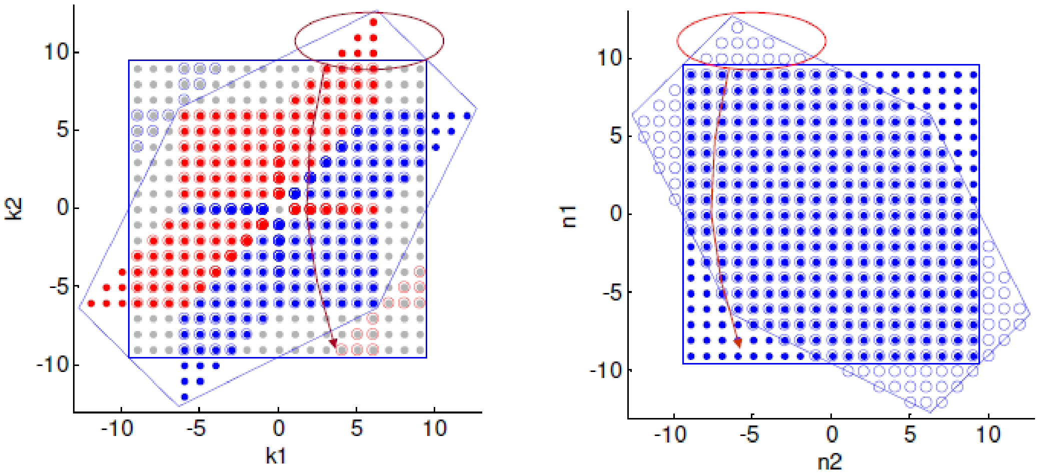

*Figure 2.7 k1-k2 star (left) and n2-n1 hexagon (right) re-ordered to find inside rectangular shapes*

Finally, Figure 2.8 shows the $(\xi,\eta)$ hexagonal grid computed by *(n2,n1)* in the hexagonal grid using equation (2.27).

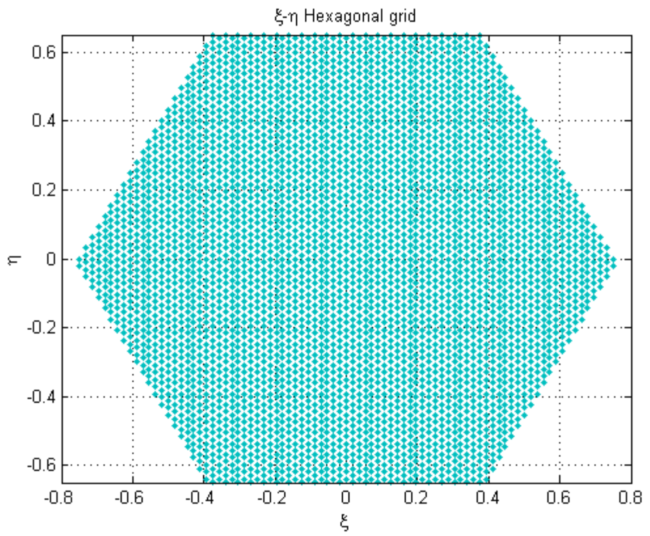

*Figure 2.8 Hexagonal sampling grid in SMOS case*

In the real case of SMOS, the extension of the modified brightness temperature is in all the unit circle. This imposes the condition $\xi^2+\eta^2<1$.In the SMOS real case, this antenna spacing is d=0,875$\lambda$, so it is larger than the Nyquist criterion ($d=\lambda/\sqrt{3}$), so aliasing will appear.

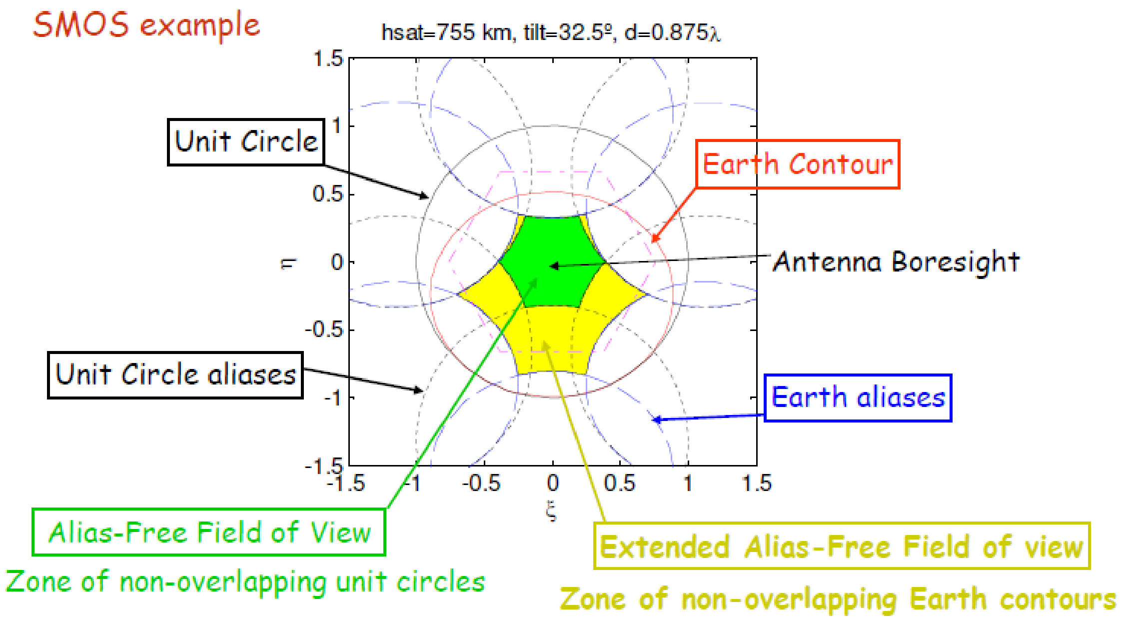

*Figure 2.9 Strict and extended alias-free field of view*

Figure 2.9 shows the resulting AF-FoV is similar to a hexagonal shape with curved sides formed by the unit circle replicas. SMOS measurements are characterized by an Earth-fixed attitude with a constant forward tilt angle of 32.5° between the instrument boresight and the local nadir in the flight direction. It gives an Earth-Sky view in the unit circle. Obviously, this sky region has lower and known brightness temperature than the Earth. So, removing thus known contribution from sky in the unity circle, the contribution of this sky part to aliasing will be zero. After removing the sky contribution AF-FoV can be extended to the so-called Extended AF-FoV (EAF-FoV).

Figure 2.10 shows the EAF-FoV limited by the Earth aliases:

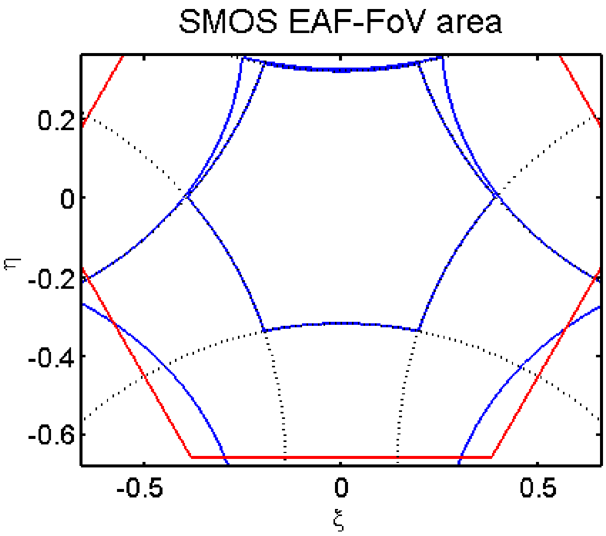

*Figure 2.10 SMOS EAF-FoV*

In Figure 2.10 the red line is the fundamental hexagon, the dotted lines the unity circle alias contours, while the blue lines set the AF-FoV and the extended AF-FoV given by the Earth sky contours of the array.

### 2.3.3 Spatial Bias

The so-called spatial bias (SB) is a standard metric to describe the systematic spatial error of the images. To compute or measure the so-called Spatial Bias (SB) it is necessary a flat and stable scene. The most usual target is the ocean, although some regions of Antarctica can also be used. In order to measure SB over the ocean a large number of consecutive snapshots are taken into account to average down the real noise. When measured over the ocean SB is also called OTT (Ocean Target Transformation) because it is used to measure ocean salinity retrievals.

So, the spatial bias is given by:

$$m_{sb} = \frac{\sum_{i=1}^{Me}\left[T_B^m(\xi_i,\eta_i) - T_{ref}(\xi_i,\eta_i)\right]}{M_e} \tag{2. 29}$$

where:

$$T_B^m(\xi,\eta) = \frac{\sum_{i=1}^{N}\hat{T}_B(\xi,\eta;t_i)}{N} \tag{2. 30}$$

$\hat{T}_B$ is the retrieved brightness temperature. $T_{ref}$ is the truly brightness temperature also called reference image or ground truth, $Me$ are the 1825 pixels inside this region, $N$ is the number of snapshots and $t_i$ the time in seconds. Sections 2.3.5 and 2.3.6 describe two different models used to characterize it.

### 2.3.4 The Stokes parameters at antenna and ground frames

The polarization direction can be defined in different planes: antenna frame (X,Y) or the ground frame (H,V). The measurements in SMOS always are related to the antenna frame but the ground frame is sometimes required because the geophysical parameters are related to (H,V) polarization defined at each pixel on ground.

Figure 2.11 shows the relation between antenna and ground frame with a coordinate rotation.

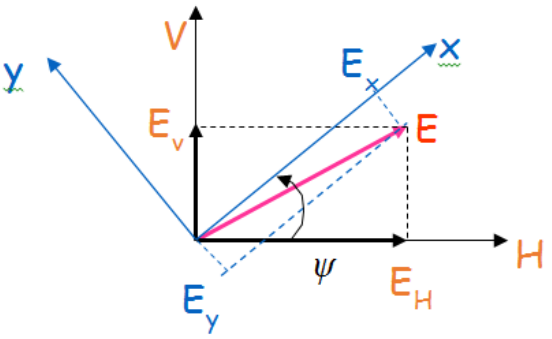

*Figure 2.11 Coordinate rotation in ground frame (H,V) and antenna frame (X,Y)*

$$\begin{bmatrix} T_B^{xx} \\ T_B^{xy} \\ T_B^{yx} \\ T_B^{yy} \end{bmatrix} = \begin{bmatrix} A^2 & AB & AB & B^2 \\ -AB & A^2 & -B^2 & AB \\ -AB & -B^2 & A^2 & AB \\ B^2 & -AB & -AB & A^2 \end{bmatrix} \begin{bmatrix} T_B^{hh} \\ T_B^{hv} \\ T_B^{vh} \\ T_B^{vv} \end{bmatrix} \tag{2. 31}$$

where $A = cos\psi$ and $B = sin\psi$, being $\psi$ the rotation angle between the $(\mathrm{H}, \mathrm{V})$ and $(\mathrm{X}, \mathrm{Y})$ axes including the relative orientation between the pixel's in ground frame and the antenna frame and Faraday rotation effects.

Note that in this thesis, the 3rd and 4th Stokes parameters are very important to verify the quality of the SMOS image and they are defined at the antenna frame:

$$\begin{aligned} A3 &= 2Re\{T_B^{xy}\} \\ A4 &= 2Im\{T_B^{xy}\} \end{aligned} \tag{2. 32}$$

### 2.3.5 Reference brightness temperature images: Fresnel model

This section is devoted to define the reference polarization images used in several simulations undertaken in the following section (e.g. to assess the impact of an error). A reference image widely used is the Ocean.

The emissivity of the ocean mainly depends on:

- Electrical properties of the body which is related to the salinity of the seawater, the frequency and the sea surface temperature.
- Direction of observation
- Roughness of the surface
- Polarization

The emissivity follows the Fresnel reflection theory if the ocean surface is seen as a perfect flat and stable surface. Note that ocean emissivity is the main contribution of the brightness temperature measured by SMOS.

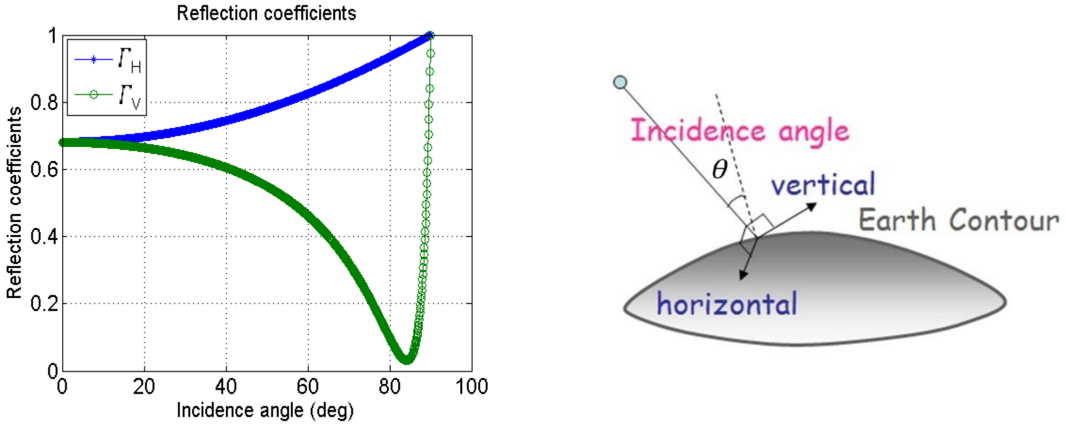

*Figure 2.12 Fresnel reflection coefficients over the ocean [Corbella, 2008]*

It is possible to model the brightness temperature by considering the roughness of the sea surface, the contribution of the atmosphere and also other contributions. In any case, a simplified model of the ocean surface can be computed only considering the flat sea emissivity from the reflection coefficients given in Figure 2.12 (left).

$$\Gamma_H = \left| \frac{\cos\theta - \sqrt{\varepsilon_{r\ eff} - \sin^2\theta}}{\cos\theta + \sqrt{\varepsilon_{r\ eff} - \sin^2\theta}} \right|^2 \qquad (2.\ 33)$$

$$\Gamma_V = \left| \frac{\varepsilon_{r\ eff}\cos\theta - \sqrt{\varepsilon_{r\ eff} - \sin^2\theta}}{\varepsilon_{r\ eff}\cos\theta + \sqrt{\varepsilon_{r\ eff} - \sin^2\theta}} \right|^2$$

where $\theta$ is the incidence angle defined as the angle between the wave propagation direction and the vertical to the surface (Figure 2.12, right) and $\varepsilon_{r\ eff}$ is the Ocean superficial layer relative effective dielectric permittivity.

The emissivity is defined as $e = 1 - \Gamma$. Brightness temperature on the ground frame can be modeled taking into account the sea surface temperature (SST) as:

$$\begin{aligned} T_B^{Hf} &= SST(1 - \Gamma_H) \\ T_B^{Vf} &= SST(1 - \Gamma_V) \end{aligned} \tag{2. 34}$$

Finally, the Fresnel model referred to the antenna frame can be computed as:

$$\begin{bmatrix} T_B^{Xf} \\ 2T_B^{XYf} \\ T_B^{Yf} \end{bmatrix} = \begin{bmatrix} A^2 & B^2 \\ -2AB & 2AB \\ B^2 & A^2 \end{bmatrix} \begin{bmatrix} T_B^{Hf} \\ T_B^{Vf} \end{bmatrix} \tag{2. 35}$$

Figure 2.13 shows the Fresnel model in the SMOS EAF-FoV image used as a reference for all the work of this thesis in antenna frame (L-band) with SSS (Sea surface salinity) 35 psu (practical salinity units) and SST (Sea surface temperature) 294 K. On the other hand, Figure 2.14 shows the reference imagen in the unity circle domain.

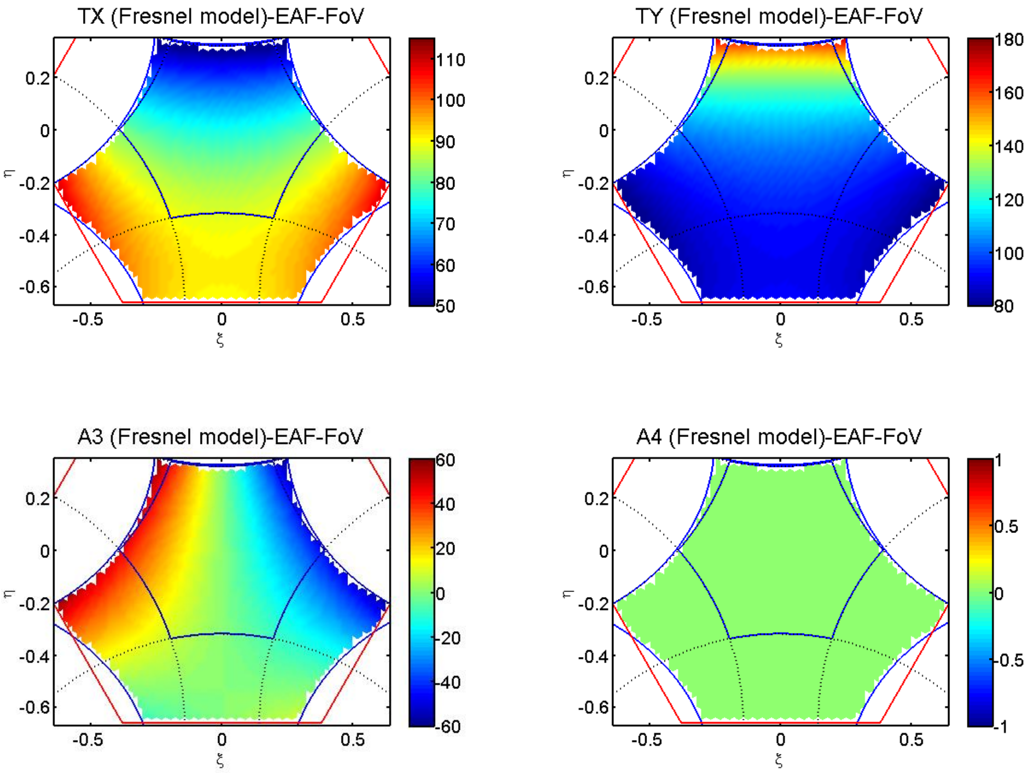

*Figure 2.13. Fresnel Ocean brightness temperature in the antenna frame in EAF-FoV area*

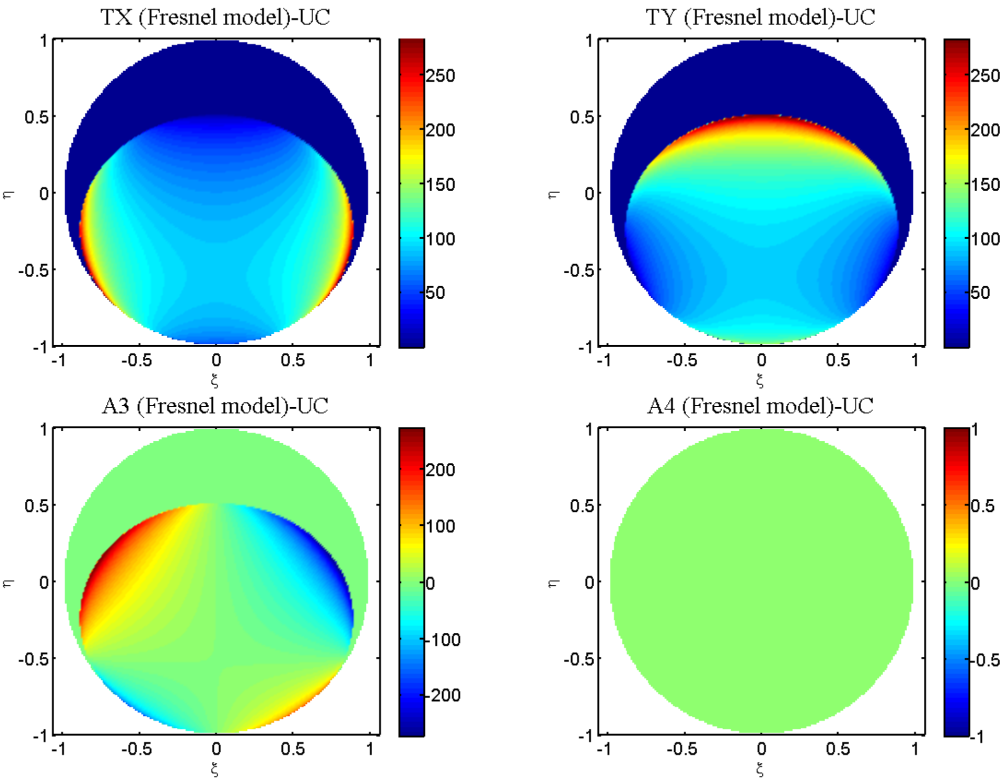

*Figure 2.14 Fresnel Ocean brightness temperature in the antenna frame in Unity circle area (0K in sky area)*

Figure 2.15 shows an example of the spatial bias over the ocean computed with (2.29).

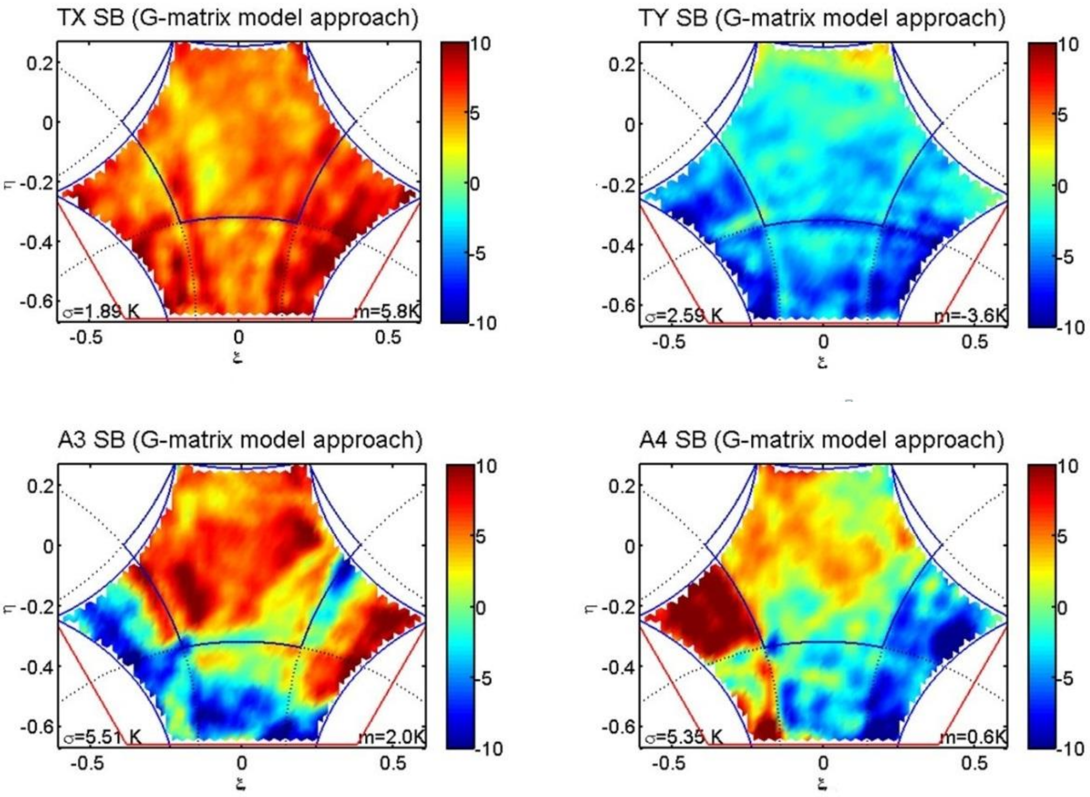

*Figure 2.15 LOCEAN Spatial bias over the ocean for TX and TY (top) and A3 and A4 (bottom)*

### 2.3.6 Accurate ocean models: LOCEAN and J.Tenerelli model

During this thesis other ocean models have been used for comparing SMOS brightness temperature (simulate or measured) with a reference, this is the case of LOCEAN model. It is a model developed by the Laboratoire d'Océanographie et du Climat Expérimentations et approaches Numériques (LOCEAN, France). It is an accurate Ocean model for SMOS validation (Level 1) to assess SMOS performance over the ocean. This is a powerful tool to analyze the instrument systematic spatial errors (also called spatial bias) over the ocean. In that case, the model considers all the possible contribution to the brightness temperature at top of the atmosphere and the Faraday rotation in the earth reference frame. This Faraday rotation is clearly seen since it introduces asymmetries in the images. It is also the responsible for a non-zero mean on A3, if it is not corrected.

Other very accurate models have been used as a model computed by J. Tenerelli from OceanDataLab, in that case this model is used for assessing one of the major problems in SMOS (Land sea contamination) as it will be explained in chapter 7.

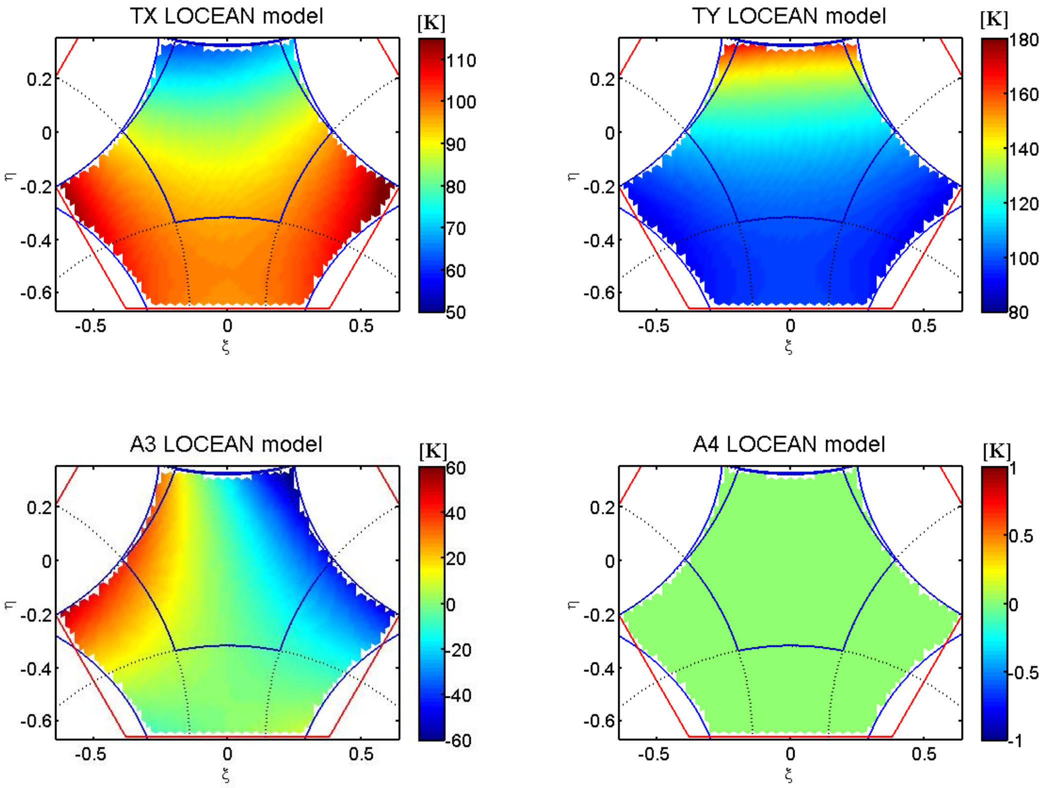

*Figure 2.16 LOCEAN model (TX, TY, A3 and A4) for the SMOS orbit (UTC time from 2011-06-28-01:16:4.8 to 2011-06-28-01:22:43.2)*

## 2.4 Inversion approaches

As it has been explained in 2.3.1 the image reconstruction consists on solving for $T(\xi,\eta)$ in a equation of the type $V(u, v) = F[T(\xi, \eta)]$, where $V(u, v)$ is known.

This can be written as:

$$V(u_{kj},v_{kj}) = \int_{-\infty}^{\infty}\int_{-\infty}^{\infty} T_{kj}^{'}(\xi,\eta) e^{-j2\pi(u_{kj}\xi+v_{kj}\eta)} d\xi d\eta \tag{2. 36}$$

with:

$$T_{kj}^{'} = \begin{Bmatrix} T(\xi,\eta) AP_{kj}(\xi,\eta) \tilde{\bar{r}}_{kj}\left(-\dfrac{u_{kj}\xi+v_{kj}\eta}{f_0}\right), \xi^2+\eta^2<1 \\ 0, \qquad \xi^2+\eta^2 \geq 1 \end{Bmatrix} \tag{2. 37}$$

in which, for consistency, $T(\xi, \eta)$ should only be a function of the director cosines ($\xi$, $\eta$) but not of the specific baseline used. From the beginning of the mission the operational processor is being updated with new techniques or improvements of the different paramenters. Until the version v520 of the operational processor, three different inversion approaches were used in the choice of *V* and *T*, which are summarized in Table 2.1 and described in the following [Corbella *et al.*, 2009b].

1) **Approach #1** uses the visibility directly as obtained from the calibration procedure. To take into account the –*Tr* term, this must be subtracted both at the zero visibility and at the brightness temperature. Note that the term subtracted to TB consists of the average receiver temperature *Tr* in order to comply with the requirement that T does not depend on the specific baseline.

2) In **approach #2** the –*Tr* term is canceled in the visibility before inversion. In this case, the zero visibility is directly the antenna temperature, and the retrieved variable is simply the brightness temperature.

3) Finally, **approach #3** inverts the incremental visibility. Then, the zero visibility vanishes, and the retrieved function is the difference between the brightness and the average antenna $T_A$ temperatures. In any case, the flat-target response is assumed to be known, either from direct measurement using, for example, the cold sky or computed from measured antenna patterns. Alternatively, it can be neglected using simply *FTRkj* = 0, which may be a good option for instruments having large antenna separations in terms of the wavelength.

| # | $V(u_{kj},v_{kj})$ for $u_{kj},v_{kj} \neq 0$ | $V(0,0)$ | $T(\xi,\eta)$ |
|---|---|---|---|
| 1 | $V_{kj}$ | $T_{A_k} - T_{r_{kj}}$ | $T_B(\xi,\eta) - \bar{T}_r$ |
| 2 | $V_{kj} + T_{r_{kj}} FTR_{kj}$ | $T_{A_{kj}}$ | $T_B(\xi,\eta)$ |
| 3 | $V_{kj} - (TA_{kj} - T_{r_{kj}}) FTR_{kj}$ | $0$ | $T_B(\xi,\eta) - \bar{T}_A$ |

*Table 2.1 Inversion approaches*

These approaches have been used in the first stages of this PhD work until more evolved procedures were developed.

### 2.4.1 The co-polar and the full-pol inversion approaches

Up to version 520 of the operational processor the inversion approaches were dealing exclusively with co-polar matrices. In such case, SMOS image reconstruction algorithm neglects the cross-polar antenna pattern terms $\left(\mathrm{C_p} \cong 0\right)$ and takes into account, exclusively, the reference (co-polar) patterns. Hence, each one of the polarimetric brightness temperatures can be retrieved independently as:

$$\begin{aligned} \hat{T}_B^{xx} &\cong (G_{xx}^{RR})^{-1} \cdot \hat{V}_{kj}^{xx} \\ \hat{T}_B^{yy} &\cong \left(G_{yy}^{RR}\right)^{-1} \cdot \hat{V}_{kj}^{yy} \\ \hat{T}_B^{xy} &\cong \left(G_{xy}^{RR}\right)^{-1} \cdot \hat{V}_{kj}^{xy} \end{aligned} \tag{2. 38}$$

where the superscript (-1) stands for the Moore-Penrose pseudoinverse and the hat (^) stands for the measured visibility and retrieved temperature. This basic method, which hereafter is referred to as co-polar G-Matrix (CPG) has been improved in SMOS operational processor to the so-called Model approach (M-CPG) where a theoretical model of the Earth at a constant brightness temperature has been removed at visibility level (before inversion) in order to mitigate the antenna errors as detailed in section 2.4.3.

The antennas that compound the interferometric array can be characterized according to their normalized polarimetric voltage antenna patterns as [*Corbella, 2008*]:

$$\vec{F}_x = R_x\hat{x} + C_x\hat{y}, \quad \vec{F}_y = C_y\hat{x} + R_y\hat{y}, \tag{2. 39}$$

where $R_x$, $R_y$ are the reference (*co-polar*) pattern and $C_x$, $C_y$ are the *cross-polar* antenna patterns at each of the orthogonal polarizations at the antenna frame {x, y}.

Then, the SMOS full-pol equations [Camps *et al.*, 2005] and [Wu *et al.*, 2013], where antenna cross-polar antenna pattern effects have been included, can be written as:

$$\begin{aligned} V_{kj}^{xx} &= G_{xx}^{RR}\left(T_B^{xx}-T_r\right)-G_{xx}^{RC}T_B^{xy}-G_{xx}^{CR}T_B^{yx}+G_{xx}^{CC}\left(T_B^{yy}-T_r\right)\\ V_{kj}^{yy} &= G_{yy}^{CC}\left(T_B^{xx}-T_r\right)+G_{yy}^{CR}T_B^{xy}+G_{yy}^{RC}T_B^{yx}+G_{yy}^{RR}\left(T_B^{yy}-T_r\right)\\ V_{kj}^{xy} &= G_{xy}^{RC}\left(T_B^{xx}-T_r\right)+G_{xy}^{RR}T_B^{xy}-G_{xy}^{CC}T_B^{yx}-G_{xy}^{CR}\left(T_B^{yy}-T_r\right) \end{aligned} \tag{2. 40}$$

## 2.4.2 The basic approach

These inversion approaches listed in Table 2.1 evolved to a more simple one. After version 620 of the operational processor, the approaches were classified in two categories: the basic and the model approach.

In the basic FPG inversion, the FPG matrix is inverted directly without additional pre-processing of the visibility sample. The calibrated full-polarimetric visibility samples can be expressed with the G-matrix operator as:

$$\begin{bmatrix} V^{xx} \\ V^{yy} \\ V^{xy} \\ V^{yx} \end{bmatrix} = \begin{bmatrix} G_{xx}^{RR} & -G_{xx}^{RC} & -G_{xx}^{CR} & G_{xx}^{CC} \\ G_{yy}^{CC} & G_{yy}^{CR} & G_{yy}^{RC} & G_{yy}^{RR} \\ G_{xy}^{RC} & G_{xy}^{RR} & -G_{xy}^{CC} & -G_{xy}^{CR} \\ G_{yx}^{CR} & -G_{yx}^{CC} & G_{yx}^{RR} & -G_{yx}^{RC} \end{bmatrix} \begin{bmatrix} T_B^{xx} \\ T_B^{xy} \\ T_B^{yx} \\ T_B^{yy} \end{bmatrix} \tag{2. 41}$$

The fourth row has been included to take into account the proper antenna patterns in the measurement of $V^{yx}$. The brightness temperature can be retrieved simply as:

$$\begin{bmatrix} \hat{T}_B^{xx} \\ \hat{T}_B^{yy} \\ \hat{T}_B^{xy} \\ \hat{T}_B^{yx} \end{bmatrix} = \begin{bmatrix} G_{xx}^{RR} & -G_{xx}^{RC} & -G_{xx}^{CR} & G_{xx}^{CC} \\ G_{yy}^{CC} & G_{yy}^{CR} & G_{yy}^{RC} & G_{yy}^{RR} \\ G_{xy}^{RC} & G_{xy}^{RR} & -G_{xy}^{CC} & -G_{xy}^{CR} \\ G_{yx}^{CR} & -G_{yx}^{CC} & G_{yx}^{RR} & -G_{yx}^{RC} \end{bmatrix}^{-1} \begin{bmatrix} V^{xx} \\ V^{yy} \\ V^{xy} \\ V^{yx} \end{bmatrix} \tag{2. 42}$$

It is known that the Moore–Penrose pseudoinverse (operator $-1$) gives a least square solution on the linear equation (2.42). From this point of view, even in the case of an instrument perfectly known where the system G-matrix is error free, spatial errors are introduced to the retrieved images.

## 2.4.3 The model inversion approach

In the full-polarimetric model inversion approach, the visibility samples are pre-processed in order to reduce the spatial bias. To do so, since the FPG is a linear system of equations, a common term consisting of an Earth disk at a constant brightness temperature is subtracted from all the visibility terms, before inversion [Corbella *et al.*, 2013].

The elements of the G-matrix include, among other terms, the antenna patterns of the individual elements of the array. This is why, as part of the ground characterization, all MIRAS antenna patterns were measured before launch. The results were used to compute an unique G-matrix that is used throughout the mission. Thus, any differences

between the actual antenna patterns in flight configuration and the ground characterization is a source of error in the retrieved brightness temperature.
Denoting $\hat{G}$ the G-matrix computed from the available antenna patterns, the reconstructed brightness temperature becomes:

$$\hat{T} = \hat{G}^{-1}V \tag{2. 43}$$

where $V$ is the calibrated visibility. To help understanding the intrinsic limitations of this inversion problem, a simulated visibility was computed by using the equation $V = GT$ with $G = \hat{G}$ and $T = T_M$ a known brightness temperature. Equation (2.43) was then used to reconstruct the original brightness temperature. Mathematically, this simulation is expressed as:

$$\hat{T}_M = \hat{G}^{-1}GT_M \tag{2. 44}$$

Since it is deterministic, the floor error of a given model can be subtracted from the reconstructed brightness temperature of measurement. Defining the error as the difference between the reconstructed model and the original one $T_M$, the new reconstructed brightness temperature after subtracting the floor error becomes:

$$\hat{T} = \hat{G}^{-1}V - (\hat{G}^{-1}\hat{G}T_M - T_M) = \hat{G}^{-1}(V - V_M) + T_M \tag{2. 45}$$

where $V_M = \hat{G}T_M$ is the estimated visibility of the model. This equation shows that subtracting the floor error of a given model is equivalent to apply the reconstruction algorithm to the difference between the measured visibility and that computed theoretically from a model and adding the model to the result. In the current SMOS data processing (v520 for co-polar inversion and v620 for Full-pol inversion) a constant brightness temperature over the earth surface is used as model for this purpose. It is called the “model approach” in the SMOS community.

In general, the total reconstruction error is the difference between the recovered brightness temperature and the original one $T$. Taking into account the error can be written as

$$\hat{T} - T = (1 - \hat{G}^{-1}\hat{G})(T_M - T) + \hat{G}^{-1}(G - \hat{G})T \tag{2. 46}$$

This equation shows that the total reconstruction error has two terms. The first one is due to having non-zero floor error and it is scaled by the difference between the model and the true value. The second one is due to the uncertainties in the G-matrix and scales with the brightness temperature. For an inversion method with no floor error that guarantees that $(1 - \hat{G}^{-1}\hat{G}) = 0$, subtraction of the model is not needed. Otherwise, the better the model approaches the actual brightness temperature, the lower the impact of this error.

# 3 The MIRAS payload

MIRAS synthesizes a large aperture from a reasonably sized 2-D array of passive microwave radiometers. By using interferometric techniques, the required coverage and spatial resolution can be achieved without the need for a large antenna and mechanical scanning.

It is the first ever satellite in the world designed both to map sea surface salinity and to monitor soil moisture on a global scale. It features a unique interferometric radiometer that enables passive surveying of the water cycle between oceans, the atmosphere and land.

It was launched on Monday 2nd November 2009 from the Plesetsk Cosmodrome in northern Russia at 01:50 UTC.

The MIRAS instrument consists of a Y-shape synthetic aperture radiometer operating at L-band (1,4 GHz) formed by 72 receivers called LICEFs (Light-Weight Cost Effective Front-End), equally distributed along the three deployable arms, which are connected to a central structure called hub.

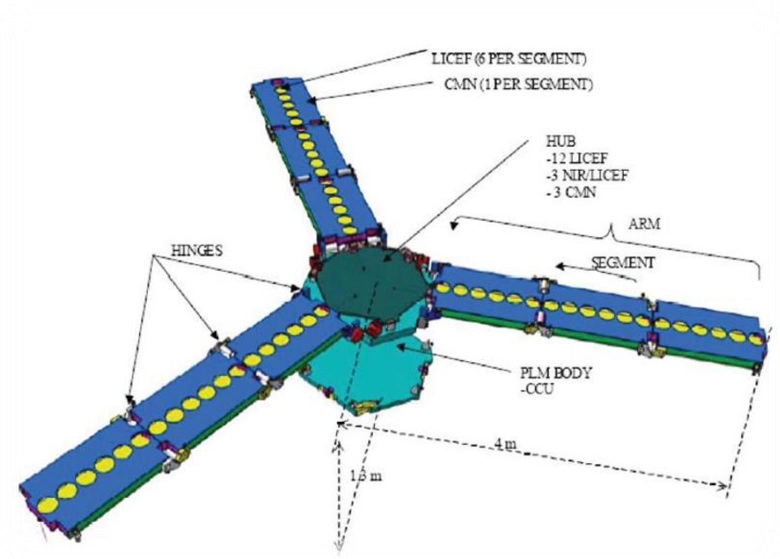

*Figure 3.1 Instrument architecture*

The central hub is 1,3 m in diameter connected to three arms extending up to 8 m in diameter. The arms are equally spaced with an angular separation of 120º. Each arm comprises three segments, each containing six L-band receivers. The line of 18 receivers in each arm is complemented by a further four receivers in the central hub, making a total of 66 receivers, 12 in the hub and 54 in the arms. Due to their design, these receivers are known as LICEFs.

In addition, there are three Noise Injection Radiometers (NIRs) placed in the hub. These NIRs are included to complete the calibration concept. Each NIR also performs as two different LICEFs placed in the same position. In practice, each NIR consists of two LICEF receivers coupled to a single antenna in both polarizations. Thus, in total, the MIRAS comprises 69 antennas (for the 66 LICEFs and 3 NIRs) but 72 receivers (66 LICEFs plus 6 for the NIRs).

The function of the LICEFs and NIRs is to measure the antenna radiometric temperature which represents the radiation noise power delivered by the antenna (corresponding to the brightness temperature of the scene) to the receiver.

Each segment of the instrument also contains a Control and Monitoring Node (CMN) that provides power and a phase locked local oscillator to each LICEF.

## 3.1 MIRAS configuration

This section describes in detail the most important subsystems of the instrument, explaining their main characteristics and their working principles.

### 3.1.1 LICEF and NIR

A LICEF is basically a radiometric receiver integrated with a dual polarization antenna. Figure 3.2 shows a photograph of one LICEF receiver.

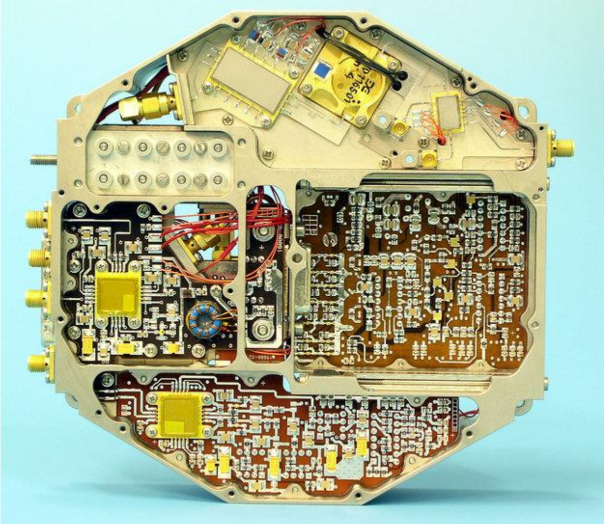

*Figure 3.2 LICEF unit (Credits from Mier)*

Each LICEF has four inputs:

- 2 inputs from the antenna (H and V ports)
- 1 calibration input (C)
- 1 Unmatched load input (U)

There is a switch that allows selecting the two possible observation modes (H and V ports) and the two calibration modes (C input and U-load input). After the switch, there is an isolator and a Low Noise Amplifier (LNA) before the Band-Pass Filter (BPF) which selects the frequencies within the working band (1404-1423 *MHz*) and rejects the rest of them. After that, there is an RF amplifier before the mixer, where the selected frequencies are converted to an intermediate frequency (8-27 *MHz*) by using a Local Oscillator (LO) at 1396 MHz with a clock reference frequency of 55.84 *MHz*. Figure 3.3 shows a block diagram of a LICEF.

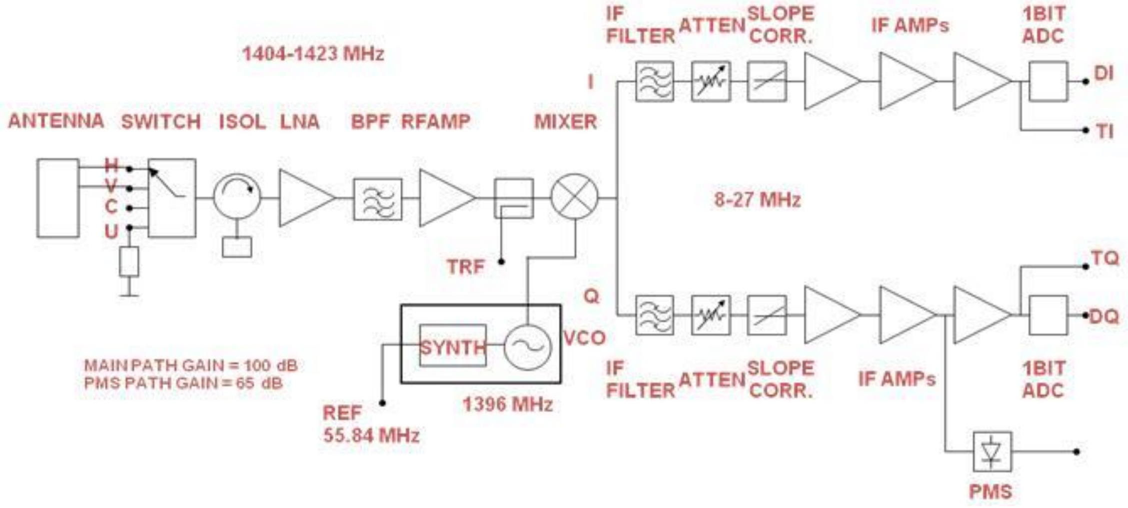

*Figure 3.3 Block diagram of a LICEF (Credits from Mier)*

On the other hand, the instrument carries three NIRs to measure:

- The power of the noise sources, needed in the internal calibration to retrieve the individual power gain of the receivers' PMS (Power Measurement System).
- The scene antenna temperature, which in turn is used for getting the visibility at zero spacing.

The antenna temperature information is required for the retrieval of SMOS brightness temperature map, whereas the calibration of the output level of the centralized noise source is essential to calibrate the power level of the LICEF receivers. Additionally, each NIR will form interferometer baselines (called mixed baselines) with all LICEF units.

Each NIR consists of one NIR controller unit (NIC) and two LICEF receivers, which indicates the flight hardware configuration of the NIR instrument as mounted on the HUB of MIRAS. An antenna identical to that of a LICEF is mounted on the NIC unit, and each polarization (H and V) is routed to one standard LICEF receiver through an "antenna branch". In each antenna branch, a noise pulse of variable length is added via a coupler to measure the antenna temperature. The length of the pulse is adjusted to keep the average input power to the LICEF receivers equal to the physical temperature of the internal LICEF U-matched load.

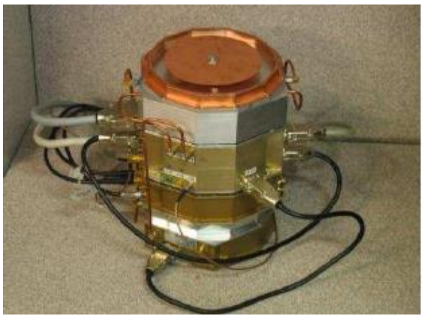

*Figure 3.4 Noise Injection Radiometer (Credits from HUT)*

Figure 3.5 shows a blog diagram of a NIR. During on board calibration, the NIR-LICEF receivers are switched to measure the CAS (calibration system) output, and the noise pulse is injected through a different "reference branch". The reference branch incorporates a reference-matched load in this case. A NIR uses two absolute calibration loads: the internal U-matched load of the LICEF and cold sky. To view the cold sky, the full SMOS satellite pointing is changed from earth fixed to inertial pointing periodically during one orbit.

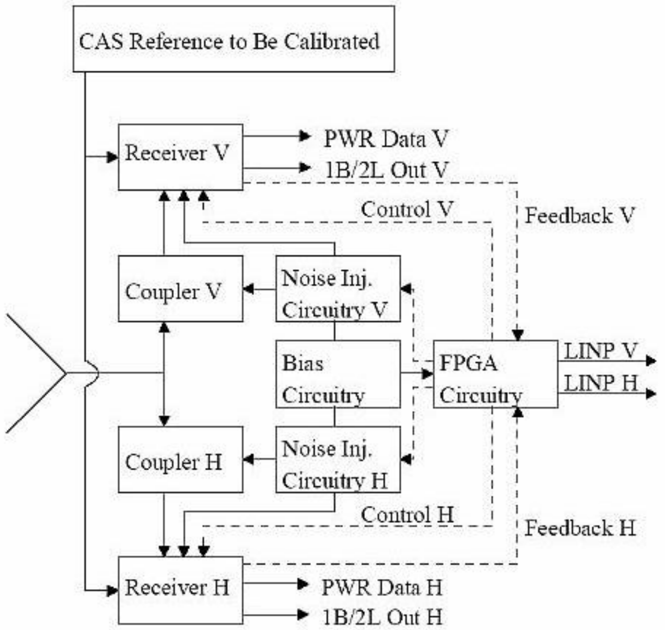

*Figure 3.5 Block diagram of a NIR [McMullan et al., 2008]*

### 3.1.2 PMS

Each LICEF receiver contains a PMS. The PMS of each LICEF converts the received signal into a voltage.

Each power measurement system consists of a diode detector and an integrator and its behavior is equivalent to a total power radiometer. The PMS block diagram is shown in Figure 3.6.

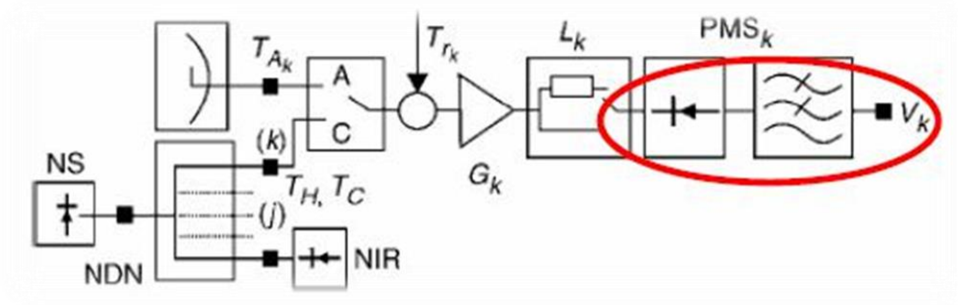

*Figure 3.6 PMS scheme*

The output voltage of PMS can be approximated for the next equation:

$$v_k = G_k \cdot T_{sys_k} + v_{off_k} \tag{3. 47}$$

where $G_k$ and $v_{off_k}$ are the gain and offset of the PMS, respectively and $T_{sys_k}$ is the system temperature. Although the PMS gain and the PMS offset were characterized on ground, they have to be estimated in a PMS calibration routine to track any fluctuation because the system temperature $T_{sys_k}$ is used in the denormalization of the visibilities needed to calculate the brightness temperature.

### 3.1.3 CAS (Calibration System) and noise sources

The onboard CAS provides a correlated noise reference to calibrate the noise temperature and relative phase characteristics between the LICEF receivers. CAS is based on a distributed noise injection. Three Arm Noise Sources (ANS) per arm and one hub Noise Source (HNS) generate two different levels, known as cold noise (75 K) and hot noise (1500 K).

This noise is split using two-by-six port Power Dividers (PD) for a set of 12 LICEFs with an overlap of six LICEFs so that every receiver can receive calibration noise from two adjacent noise sources, one at a time.

CAS is basically a multiport structure with strict requirements on amplitude and phase difference between output ports, port isolation, and port matching. Careful prelaunch characterization and modeling of CAS has been necessary to meet these performance requirements. Moreover, since the physical temperature in-orbit varies between individual components of CAS, it is mandatory to determine CAS characteristics for all possible temperature distribution.

This is accomplished by:

- Measuring, over temperature, the generated noise level and S-parameters of all individual NS units and the S-parameters of the PD units and adjacent cables
- Combining the results in a mathematical model to simulate the behavior of the integrated CAS

*Figure 3.7 Noise source (left) and power divider (right)* [UPC]

### 3.1.4 DICOS (Digital Correlator System)

DICOS is the Digital Correlator System, it is used to correlate the signals produced by the I-Q channels of all the LICEFs. Each correlator is an exclusive NOR gate, so the output is only '1' if the two input signals are equal. The correlation is measured accumulating its output during the integration time using the clock frequency $f_S = 55,84 MHz$.

At the end of the integration time the correlation accounts are read and reset the accumulator for the next period of integration.

Therefore, the correlation accounts of DICOS output for each pair of receivers correspond to the number of bits that matches between the input signals of the correlator during integration time.

MIRAS consists of 72 receivers, and then there are 2556 different baselines (72 I signals, 72 Q signals, and constant channels '1' and '0').

### 3.1.5 CMN (Control and Monitoring Node) and Local Oscillators

The CMN (Control and Monitoring Node) acts as a remote terminal of the CCU (Instrument Central Computer Unit). Each of the three arms of MIRAS contains three identical segments of six LICEFs each. In each segment, there is one CMN responsible for the control and monitoring of that segment. The HUB is divided in three sectors, each equipped with one CMN serving four LICEFs and two NIR-LICEFs. In addition, the CMN is used to control the onboard CAS.

Each CMN, in turn, provides power and a phased local oscillator (LO) signal controlled by the reference clock supplied by the optical link MOHA (MIRAS Optical Harness) to each LICEF.

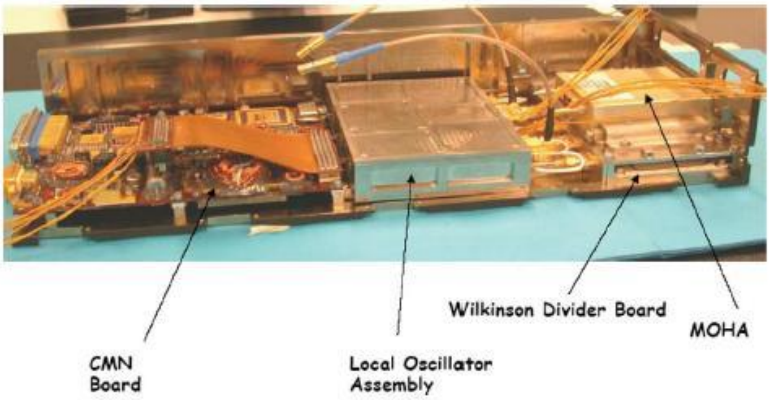

*Figure 3.8 CMN and Local Oscillator [McMullan et al., 2008]*

### 3.1.6 Thermal Control System

The thermal control subsystem (heaters) is designed to minimize the temperature differences between all the LICEF and the NIR units. This is achieved by placing all these units on thermal doublers (aluminum plates used to equalize the temperature of arm-segment and HUB LICEF units) which are controlled in temperature by heaters.

The temperature sensors that are built into the LICEFs and NIRs are read by the CMN units and the data are relayed to the CCU. In the early orbit phases and in any situation where the payload is switched off, these heaters are controlled by thermostats to prevent the instrument from becoming too cold.

## 3.2 Calibration modes

One of the main objectives of any mission is to obtain and provide stable and accurate data (in SMOS case this refers to the radiometric performance). So, a well-calibrated instrument provides the basis for stable measurements. This section provides a summary of the main calibration procedures [Brown *et al.*, 2008], [Torres *et al.*, 2008], [González-Gambau, 2012], [Corbella *et al., 2008*] and [Corbella *et al.*, 2005b].

The calibration of any Earth Observation sensor is a key stage which encompasses those tasks which are necessary to convert the raw measurement data into science data. Calibration is basically the process of quantitatively defining the system responses to known controlled signal inputs.

One of the important prerequisites to the performance verification and the validation of geophysical parameters is calibration which demonstrates that the instrument meets its requirements.

On the one hand, characterization is the measurement of the typical behavior of instrument properties, including subsystems, which may affect the accuracy or quality of its response or derived data products. The characterization activities are mainly performed on-ground before launch but are also performed in-flight thus being a prerequisite for the calibration activities.

On the other hand, verification encompasses the testing and analysis necessary to provide confirmation that all instrument requirements have been met. Finally, validation is the process of assessing the quality of the data products derived from the system outputs. The measured visibility is based on the so-called calibrated visibility given by:

$$V_{kj} = \frac{\sqrt{T_{sys_k} T_{sys_j}}}{G_{kj}} M_{kj} \tag{3. 1}$$

where $M_{kj}$ is the normalized complex correlation between the receivers $k$ and $j$ after the self-calibration procedure, $G_{kj}$ is the fringe washing function at the origin and $T_{sys_k}$ and $T_{sys_j}$ are the system temperatures for the LICEF $k$ and $j$ respectively measured by the PMS units.

To obtain the calibrated visibility, all values in the equation must be also calibrated. The following parameters are used in the calibration to correct these values:

1) Instrument outputs

    - Correlator counts ($N_c$)
    - PMS voltages ($v_k$)
    - NIR noise injection temperatures ($T_N$)

2) On-ground characterized parameters

    - S-parameters of the NDN (Noise Distribution Network) path to the NIR
    - S-parameters of the LICEF switch
    - Antenna efficiency
    - Antenna relative phase
    - Temperature sensitivity of calibration parameters

In the MIRAS instrument, two different types of calibration are performed. These include the injection of noise to the LICEF by the internal calibration system (internal calibration) and looking at a specific known target (such as cold sky that can be accurately estimated) that lies outside the payload module (external calibration).

Figure 3.9 shows both calibrations and the parameters involved in them.

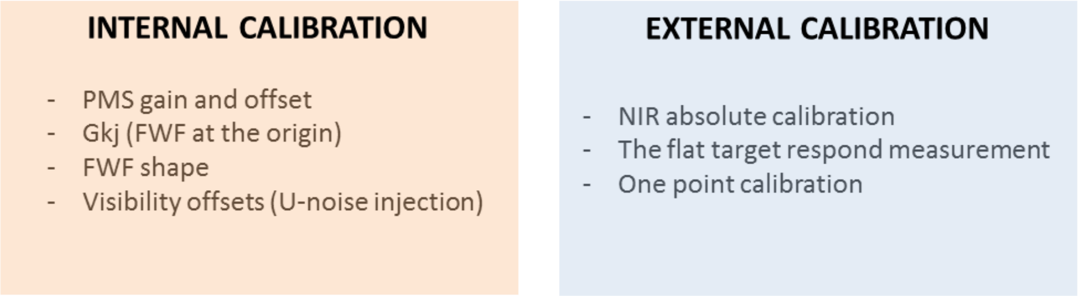

**INTERNAL CALIBRATION**

- PMS gain and offset
- Gkj (FWF at the origin)
- FWF shape
- Visibility offsets (U-noise injection)

**EXTERNAL CALIBRATION**

- NIR absolute calibration
- The flat target respond measurement
- One point calibration

*Figure 3.9 Internal and external calibration scheme*

## 3.2.1 The amplitude calibration

End-to-end calibration of MIRAS radiometer refers to processing the measured raw data up to brightness temperature maps over the Earth's surface. The procedure starts with a self-correction of comparators offset and quadrature errors and it is followed by the calibration procedure itself [Corbella *et al.*, 2005b].

The calibration procedure involves the injection of correlated and uncorrelated noise in the receivers and post-processing on ground the correlation results.

A noise distribution network called the calibration subsystem (CAS) is applied to calibrate the receiver noise temperature and the relative phase characteristics of the receivers. Some ancillary data of different subsystems (such as relative S-parameters of the CAS and of the input switch), measured on ground, are required for the calibration procedure.

The amplitude calibration comprises the estimation of two terms: the system temperatures at the receivers input referred to the antenna plane ($T_{sys_k}$ and $T_{sys_j}$) and the baseline complex gain amplitude referred to the same plane ($G_{kj}$). The computation of the system temperatures requires the PMS internal calibration of each receiver.

Figure 3.10 shows a detailed block diagram of a baseline, which consists of two LICEF receivers and the complex 1-bit correlator. Moreover it includes the reference radiometer (NIR) and the different planes where the calibration equations are defined.

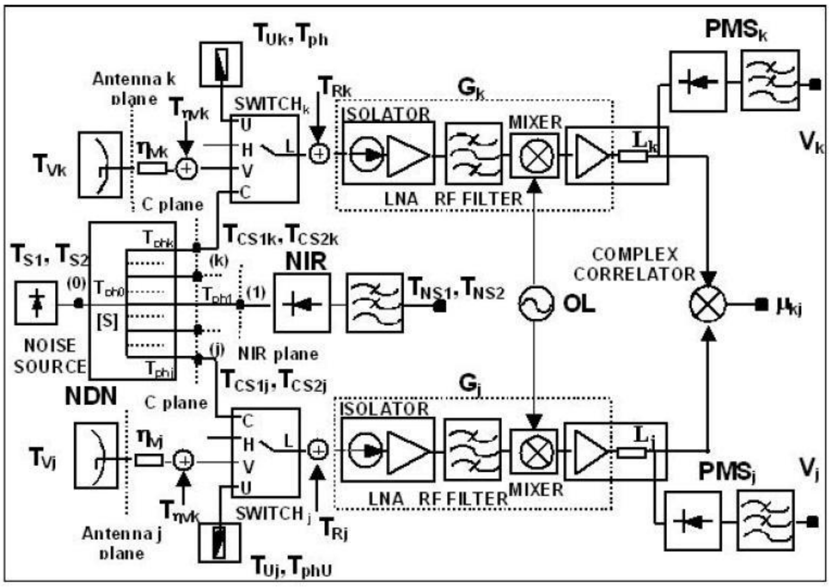

*Figure 3.10 Block diagram of the parts involved in the calibration processes*

Three planes have been defined to clearly express where the values of the variables are referred to. These planes are Calibration Internal Plane (CIP), antenna Plane and NIR Plane.

To calibrate the PMS, two different procedures have been designed: PMS internal calibration and PMS external calibration with a variant called one-point calibration.

#### 3.2.1.1 PMS internal calibration

PMS internal calibration, also known as the two-level four-points method consists of injecting correlated noise at two different temperatures (HOT and COLD) in the C input of the switch of the LICEF.

It is known that the PMS voltage follows:

$$v_k = G_k^C T_{sys_k}^C + v_{off_k} \tag{3. 1}$$

where $v_{off_k}$ is the PMS offset, $G_k^C$ is the PMS gain and $T_{sys_k}^C$ is the system temperature (values referred to CIP). The computation of the system temperatures requires the PMS calibration of each receiver to estimate the gain and offset at the internal calibration plane (CIP):

$$T_{sys_k}^C = \frac{v_k - v_{off_k}}{G_k^C} \tag{3. 2}$$

In the two-level four-points calibration method, two known external noise signals at different temperatures ($T_{s_1} < T_{s_2}$) are generated. $T_{s_1}$ is the so-called COLD temperature and $T_{s_2}$ is the HOT temperature. In addition, the overall system gain can be switched between two values, $G_k^C$ and $G_k^C/L_k$, through an attenuator located in the signal path, which allows to obtain one extra equation for each noise temperature.

The four PMS voltage measurements are given by [*Torres et al., 2006*]:

$$\begin{aligned}
v_{1k} &= v_{off_k} + G_k^C\left(T_{s1_k}^C + T_{r_k}^C\right) \; Cold\ noise, Attenuator\ OFF \\
v_{2k} &= v_{off_k} + G_k^C\left(T_{s2_k}^C + T_{r_k}^C\right) \; Hot\ noise, Attenuator\ OFF \\
v_{3k} &= v_{off_k} + \frac{G_k^C}{L_k}\left(T_{s1_k}^C + T_{r_k}^C\right) \; Cold\ noise, Attenuator\ ON \\
v_{4k} &= v_{off_k} + \frac{G_k^C}{L_k}(T_{s2_k}^C + T_{r_k}^C) \quad Hot\ noise, Attenuator\ ON
\end{aligned} \tag{3. 3}$$

Then PMS gain and offset can be readily computed:

$$v_{off_k} = \frac{v_{2k}v_{3k} - v_{1k}v_{4k}}{(v_{2k} - v_{4k}) - (v_{1k} - v_{3k})} \tag{3. 4}$$

$$G_k^C = \frac{v_{2k} - v_{1k}}{\left(T_{s2_k}^C + T_{r_k}^C\right) - \left(T_{s1_k}^C + T_{r_k}^C\right)} \tag{3. 5}$$

Equation (3. 5) is reduced to:

$$G_k^C = \frac{v_{2k} - v_{1k}}{T_{s2_k}^C - T_{s1_k}^C} \tag{3. 6}$$

The main advantage of this relative calibration approach is that the PMS gain is computed using the difference between both system temperatures, canceling out the noise contribution of the receiver and the NDN contribution itself.

$T_{s_1}$ and $T_{s_2}$ are placed at the port 0 of the NDN. The equivalent noise temperatures present in the equations of the PMS are referred to the calibration plane of LICEF $k$ and can be written as:

$$\begin{aligned}
T_{S_{1_k}}^C &= |S_{k0}|^2 \cdot T_{S_1} + (1 - |S_{k0}|^2) \cdot T_{ph_k} \\
T_{S_{2_k}}^C &= |S_{k0}|^2 \cdot T_{S_2} + (1 - |S_{k0}|^2) \cdot T_{ph_k}
\end{aligned} \tag{3. 7}$$

where $S_{k0}$ corresponds to the S-parameter from the noise source to the $k$ port of the NDN and $T_{ph_k}$ is the physical temperature at $k$ port of the NDN. Similar equations to (3. 7) can be derived for LICEF $j$.

Since the NIR also measures the noise temperature, it can be expressed at NIR plane as following:

$$\begin{aligned}
T_{S_1}^N &= |S_{10}|^2 \cdot T_{S_1} + (1 - |S_{10}|^2) \cdot T_{ph1} \\
T_{S_2}^N &= |S_{10}|^2 \cdot T_{S_2} + (1 - |S_{10}|^2) \cdot T_{ph1}
\end{aligned} \tag{3. 8}$$

where $S_{10}$ is the S-parameter from the noise source to the NIR port of the NDN and

$T_{ph1}$ is the physical temperature at NIR port.

Then by solving the equations (3.7) and (3.8), the difference $T^C_{s2_k} - T^C_{s1_k}$ is independent of the noise contribution from the receiver and the NDN itself:

$$T^C_{S_{2_k}} - T^C_{S_{1_k}} = \frac{|S_{k0}|^2}{|S_{10}|^2} \cdot (T^N_{S_2} - T^N_{S_1}) \tag{3. 9}$$

Substituting expression (3. 9) in (3. 6), PMS gain as a function of the NIR measurement is given by:

$$G^C_k = \frac{v_{2_k} - v_{1_k}}{T^N_{S_2} - T^N_{S_1}} \cdot \frac{|S_{10}|^2}{|S_{k0}|^2} \tag{3. 10}$$

Finally, any system temperature at the calibration plane when correlated noise is injected can be computed:

$$T^C_{sys_k} = \frac{v_k - v_{off_k}}{v_{2_k} - v_{1_k}} \cdot \frac{|S_{k0}|^2}{|S_{10}|^2} \cdot (T^N_{S_2} - T^N_{S_1}) \tag{3. 11}$$

In order to obtain the system temperature at the antenna plane, a plane transformation must be applied by adding the S parameters of the switch of the LICEF and the antenna efficiency.

Therefore, the system temperature at the antenna plane can be computed as:

$$\begin{aligned} T^H_{sys_k} &= T^C_{sys_k} \cdot \frac{|S_{LC_k}|^2}{|S_{LH_k}|^2 \cdot \eta_{H_k}} \\ T^V_{sys_k} &= T^C_{sys_k} \cdot \frac{|S_{LC_k}|^2}{|S_{LV_k}|^2 \cdot \eta_{V_k}} \end{aligned} \tag{3. 12}$$

where $\eta_{H_k}$ and $\eta_{V_k}$are the antenna efficiencies in horizontal and vertical of the LICEF $k$ and $S_{LH_k}$, $S_{LV_k}$, $S_{LC_k}$ are the S-parameters of the LICEF for the H, V and C inputs.

This approach provides a relative calibration, since all measurements are referenced to the NIR measurement of the CAS noise injection temperatures. Internal calibration cannot provide absolute accuracy. External calibration events are needed to calibrate the reference for the internal calibrations (NIR absolute calibration during deep sky views).

### 3.2.1.2 PMS External calibration

External calibration is a method to calibrate the instrument based on a combination of internal and external signals [Torres *et al.*, 2008]. This so-called one point calibration makes use of deep sky views as single external calibration target.

Figure 3.11 shows the one-point calibration scheme. The switch has four positions: antenna (A=H/V), matched load (U) and a port devoted to calibration (C). If the front end is in thermal equilibrium and perfectly matched, injecting noise at the U port by means of a matched load is equivalent to place a perfect absorber in front of the antenna at the same temperature. Note that in order to simplify the scheme only A and U position appears in the figure.

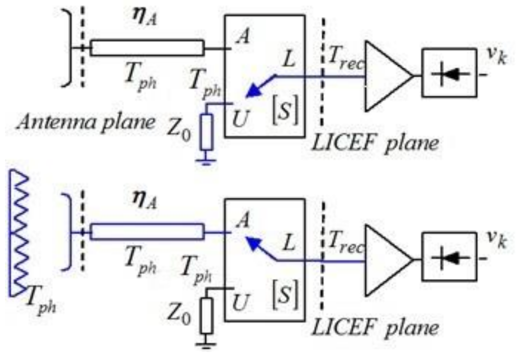

*Figure 3.11 Block diagram of the LICEF/PMS front-end of one-point calibration*

The linear relation between PMS voltage and input temperature can be written either as a function of antenna temperature or system temperature as:

$$\begin{aligned} v_A &= G^A T_{sys_A} + v_{off} = G^A T_A + v'_{off} \\ v'_{off} &= v_{off} + G^A T_R^A \end{aligned} \tag{3. 13}$$

Where $T_R^A$ is the noise receiver temperature at antenna plane. Since there are two unknowns (gain and noise temperature) the PMS requires two known input signals to be calibrated. The payload performs periodic pointing to the deep sky in order to calibrate the reference radiometer. During these cold sky views the PMS units are also switched between the U-load (WARM noise) and the antenna ($T_A = T_{sky}$, COLD noise).

When the U input is selected (WARM noise), the system temperature at CIP plane can be computed using the Friis formula as follows:

$$T^C_{sys_{LOAD}} = T_{ph} + \frac{1-|S_{LU}|^2}{|S_{LU}|^2} \cdot T_{ph} + \frac{T_{rec}}{|S_{LU}|^2} = \frac{T_{ph}+T_{rec}}{|S_{LU}|^2} \tag{3. 14}$$

where $T_{ph}$ is the physical temperature at the U port, $S_{LU}$ is the S-parameter of the switch between the U input and the output and $T_{rec}$ is the noise temperature of the receiver at LICEF plane.

Then the system temperature $T_{sys_{LOAD}}$ in CIP plane can be transformed to antenna plane taking into account the antenna efficiency and the S-parameter of the switch between the A input and the output:

$$T^{A}_{sys_{LOAD}} = T^{C}_{sys_{LOAD}} \cdot \frac{|S_{LU}|^{2}}{|S_{LA}|^{2} \cdot \eta_{A}} = \frac{T_{ph} + T_{rec}}{|S_{LA}|^{2} \cdot \eta_{A}}, \tag{3. 15}$$

where $S_{LA}$ is the S-parameter of the switch between the A input and the output and $\eta_A$ is the antenna efficiency for H and V pol.

When the A input is selected, the system temperature at antenna plane can be expressed:

$$T^{A}_{sys_{SKY}} = T_{sky} + \frac{1-\eta_A}{\eta_A} \cdot T_{ph_2} + \frac{1-|S_{LA}|^{2}}{\eta_A \cdot |S_{LA}|^{2}} \cdot T_{ph_1} + \frac{T_{rec}}{\eta_A \cdot |S_{LA}|^{2}} \tag{3. 16}$$

Then the PMS gain $G^{A}_{k}$ can be computed as:

$$G^{A}_{k} = \frac{v_{LOAD} - v_{SKY}}{T^{A}_{sys_{LOAD}} - T^{A}_{sys_{SKY}}} \tag{3. 17}$$

It is possible to find that the difference of the system temperatures depends only on $T_{ph}$, $T_{sky}$ and $\eta_A$ :

$$T^{A}_{sys_{LOAD}} - T^{A}_{sys_{SKY}} = T_{ph} - T_{sky} \tag{3. 18}$$

Then PMS gain and the receiver noise temperature can be expressed as:

$$\begin{gathered} G^{A}_{k} = \frac{v_{LOAD} - v_{SKY}}{T_{ph} - T_{sky}} \\ T^{A}_{R} = \frac{v_{SKY} \cdot T_{ph} - v_{LOAD} \cdot T_{sky}}{v_{LOAD} - v_{SKY}} \end{gathered} \tag{3. 19}$$

In the case that PMS gain needs recalibration along each orbit the most simple and accurate way that has been foreseen to do it is by U-noise injection (switch to matched load). In such case, the PMS gain, so-called Gain one-point, is retrieved as:

$$G^{A}_{1P} = \frac{v^{U}_{k} - v_{offk}}{T^{A}_{R_k} + T_{ph_U}} \tag{3. 20}$$

where $v^{U}_{k}$ is PMS voltage when the switch is the U position (matched load) , $v_{offk}$ is the offset from internal calibration (with temperature correction), and $T^{A}_{R_k}$ is the receiver noise temperature at the antenna plane at its physical temperature $T_{ph_U}$.

The receiver noise temperature $T_{R_k}^C$ can be computed when the U-noise is injected using the PMS gain obtained in (3. 10) and the U-noise measurement:

$$T_{R_k}^C = \frac{v_k^U - v_{offk}}{G_k^C} - T_{ph_U} \tag{3. 21}$$

## 3.2.2 Flat Target Transformation

External calibration is also used to measure the Flat Target Transformation (FTT), a kind of differential imaging used to eliminate the *Tr* term in 2.17 [Martin-Neira *et al.*, 2008a].

A "flat target" is defined as a completely unpolarized target having an equal brightness temperature from any direction. In a markedly different way to the point target response method used to calibrate other imaging systems, the technique put forward is essentially based on measuring a "flat target" such as the cold sky near the galactic poles. It has been called the "flat target transformation" [Martin-Neira *et al.*, 2008a]. FTR is just the measured Flat Target Response during the cold sky calibration procedure. In theory, FTR is expressed as:

$$FTR_{kj} = \iint_{\xi^2+n^2<1} AP_{kj}\, \bar{\tilde{r}}_{kj}(-\frac{u_{kj}\xi + v_{kj}\eta}{f_0}) e^{-j2\pi(u_{kj}\xi+v_{kj}\eta)} d\xi d\eta \tag{3. 22}$$

For the galactic poles, it has a temperature $T_{FT} = T_{sky} = 3{,}5$K (assuming the sky is a perfect flat target), the corresponding visibility $V^{FT}$ (measured during the External Target Observation (ETO)) can be expressed as [Corbella *et al*, 2009a]:

$$V_{kj}^{FT} = \left(T_{FT} - T_{r_{kj}}(ETO)\right) FTR_{kj} \tag{3. 23}$$

Then the FTR can be computed as:

$$FTR_{kj} = \frac{V_{kj}^{FT}}{T_{sky} - T_{r_{kj}}(ETO)} = \frac{V_{kj}^{FT}}{3.5 - T_{r_{kj}}(ETO)} \tag{3. 24}$$

where $T_{r_{kj}}(ETO)$ is the baseline physical temperature of the receivers during the cold sky calibration. In practice, the cold sky is not a true flat target (galactic noise, moon, back lobe effect and so on) and $T_{sky}$ is not equal to 3.5K, and errors are introduced to the measured FTR.

## 3.2.3 Gkj (Fringe washing function at the origin)

The fringe washing function at the origin $G_{kj}$ is also needed in the visibility denormalization. It is realted to the response of the channels involved in a baseline and can be estimated at the calibration plane by means of the two-level noise injection technique for all receivers sharing a noise source [Corbella *et al.*, 2008].

The normalized correlation when HOT ($T_{S_2}$) and COLD ($T_{S_1}$) noise temperature are injected through the NDN can be written as:

$$\begin{aligned} M_{kj}^{C_2} &= \frac{S_{k0}S_{j0}^{*}(T_{S2}-T_{ph})}{\sqrt{T_{sys_k}^{C_2C}T_{sys_j}^{C_2C}}} \cdot G_{kj}^{C} \\ M_{kj}^{C_1} &= \frac{S_{k0}S_{j0}^{*}(T_{S1}-T_{ph})}{\sqrt{T_{sys_k}^{C_1C}T_{sys_j}^{C_1C}}} \cdot G_{kj}^{C} \end{aligned} \tag{3. 25}$$

where $T_{ph}$ is the physical temperature of the NDN. $G_{kj}^{C}$ can be measured as:

$$G_{kj}^{C} = \frac{\sqrt{T_{sys_k}^{C_2C}T_{sys_j}^{C_2C}}M_{kj}^{C_2} - \sqrt{T_{sys_k}^{C_1C}T_{sys_j}^{C_1C}}M_{kj}^{C_1}}{S_{k0}S_{j0}^{*}(T_{S_2}-T_{S_1})} \tag{3. 26}$$

where T$_{ph}$ is the physical temperature of the NDN, $T_{sys_k}^{C_1C}$ and $T_{sys_k}^{C_2C}$ are the system temperature of receiver k measured using the four-point calibration (3. 11):

$$\begin{aligned} T_{sys_k}^{C_1C} &= \frac{v_{1k}-v_{off_k}}{v_{2k}-v_{1k}} \cdot \frac{|S_{k0}|^2}{|S_{10}|^2}(T_{S_2}^{N}-T_{S_1}^{N}) \\ T_{sys_k}^{C_2C} &= \frac{v_{2k}-v_{off_k}}{v_{2k}-v_{1k}} \cdot \frac{|S_{k0}|^2}{|S_{10}|^2}(T_{S_2}^{N}-T_{S_1}^{N}) \end{aligned} \tag{3. 27}$$

Similar equations can be derived for receiver $j$. From (3. 8), the difference between $T_{S_2}^{N}$ and $T_{S_1}^{N}$ is:

$$T_{S_2}^{N} - T_{S_1}^{N} = |S_{10}|^2(T_{S_2}-T_{S_1}) \tag{3. 28}$$

Finally, $G_{kj}^{C}$ can be expressed in terms of the PMS voltages by substituting (3. 27) and (3. 28) in (3. 26):

$$G_{kj}^{C} = \frac{M_{kj}^{C_2}\sqrt{(v_{2k}-v_{offk})(v_{2j}-v_{offj}))} - M_{kj}^{C_1}\sqrt{(v_{1k}-v_{offk})(v_{1j}-v_{offj}))}}{\sqrt{(v_{2k}-v_{1k})(v_{2j}-v_{1j})}} \frac{|S_{k0}||S_{j0}^{*}|}{S_{k0}S_{j0}^{*}} \tag{3. 29}$$

Applying a plane translation, FWF in antenna plane can be computed as:

$$G_{kj}^{A} = G_{kj}^{C} \cdot \frac{\bar{S}_{LAk}\bar{S}_{LAj}}{\bar{S}_{LCk}\bar{S}_{LCj}} \cdot e^{j(\phi_{Ak}-\phi_{Aj})} \tag{3. 30}$$

where $S_{LCk}$ and $S_{LAk}$ are the S-parameters of the switch from the calibration and antenna ports to the output and the overline means normalized to unit amplitude $\bar{S} = S/|S|$. $\phi_{Ak}$ and $\phi_{Aj}$ are the inter-element phases retrieved during the IVT on-ground measurements (chapter 4).

## 3.3 Measurement mode

MIRAS has two measurements modes that are dual-polarization mode and full-polarization mode.

### 3.3.1 Dual polarization measurement mode

In the *dual-polarization* measurement mode, the brightness temperatures are alternatively measured in each polarization epoch (1.2s). In any epoch, all the LICEFs measure the same polarization, which produces all of the necessary baselines from the receivers in the same polarization (HH or VV), with an additional three measurements from the NIR receivers in the opposite polarization. Figure 3.12 shows the scheme of the pairs of antennas configured in the *dual-polarization* mode.

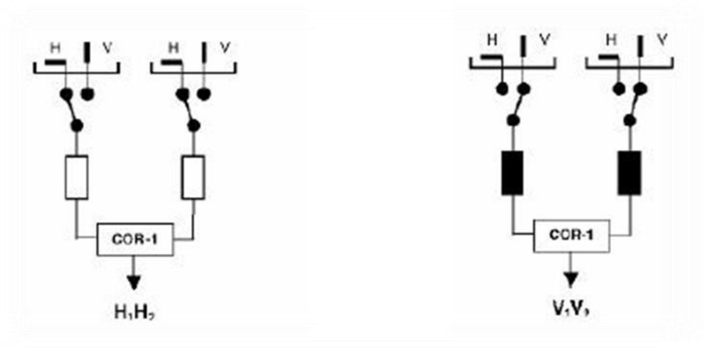

*Figure 3.12 Scheme Dual-polarization mode. HH (left) and VV (right) baselines measurement mode*

### 3.3.2 Full-polarization measurement mode

SMOS-MIRAS has the capability to measure the four Stokes parameters (TH, TV, T3 and T4, respectively). The operation mode is called the full-polarization measurement mode. Note that in this section we use the old nomenclature HV instead of the recent and accurate XY referred to the antenna frame.

In full-polarization mode, the antennas measure all possible combinations of polarizations alternative with an integration time of one epoch for every measurement (HH, HV, VH, VV) by means of the so-called pol-switching scheme. As in the SMOS case, interferometric radiometers have a large number of elements, and the receivers have typically only one channel to save mass and power consumption, as shown in Figure 3.13. Therefore, it is only possible to perform one of the four correlations at any time, regardless of the number of correlators. By properly selecting the H and the V ports of each antenna element through an adequate switching sequence, the four correlations are obtained. Figure 3.13 shows the four steps measurement procedure to measure HH, HV, VH and VV. Table 3.1 shows the measurement configuration given by the pol-switching scheme. This smart sequence interlaces short polarimetric measurements within each epoch (1.2 s) to yield a *full-pol* image every 2 epochs. The pol-switching scheme takes 4 epochs to equalize the radiometric sensitivity for all four polarimetric measurements [Martin-Neira *et al.*, 2002].

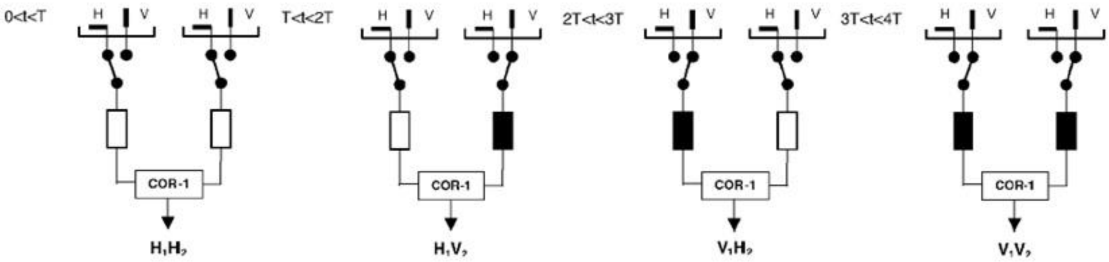

*Figure 3.13 Full-polarization measurement mode*

| Integration period | Arm A | Arm B | Arm C | Integration time (s) |
|---|---|---|---|---|
| First epoch | *H* | *H* | *H* | *1.2* |
| Second epoch | *V* | *H* | *H* | *0.4* |
|  | *H* | *V* | *H* | *0.4* |
|  | *H* | *H* | *V* | *0,4* |
| Third epoch | *V* | *V* | *V* | *1.2* |
| Fourth epoch | *H* | *V* | *V* | *0.4* |
|  | *V* | *H* | *V* | *0.4* |
|  | *V* | *V* | *H* | *0.4* |

*Table 3.1: Full-pol switching sequence*

This kind of technique indeed gives the advantage of saving mass and power consumption when compared to the configuration in which each receiver of the baseline is provided with two parallel channels allowing the measurement of the four Stokes terms in parallel. But obviously, it introduces the disadvantage that the integration time for each step is reduced by a factor of 4 at least compared with the *dual-pol* mode, which introduces degradation on the radiometric sensitivity of the measurement. Additionally the full polarimetric pixel has larger blurring than in case of two fully independent H and V channels.

## 3.4 All-LICEF

As explained in section 3.1, the MIRAS instrument is designed to use three redundant Noise Injection Radiometers (NIR) specifically to measure the antenna temperature. The SMOS Level 1 operational processor (L1OP) uses these three measurements in the image reconstruction part. Nevertheless, in its latest version only one of the three NIRs is used, as it shows improved seasonal and long-term stability with respect to using all three. Additionally, the NIRs are used in the calibration of the power measurement system (PMS) installed in all receivers.

This section describes a different scheme in which SMOS data is entirely processed without using the NIR outputs. In principle it is intended as a backup solution in case of failure or malfunction of all three NIR and it will be included in the next version of the L1OP (v700). It is, however, already implemented in the MIRAS testing software (MTS) and has been called "all-LICEF mode" in reference to the name given to the

MIRAS individual receivers: “LIghtWeight Cost-Effective Front-end” [Corbella *et al.*, 2016].

Figure 3.14 shows a block diagram of the PMS gain calibration strategy, both for the nominal processing (internal calibration plus NIR) and for the proposed all-LICEF mode.

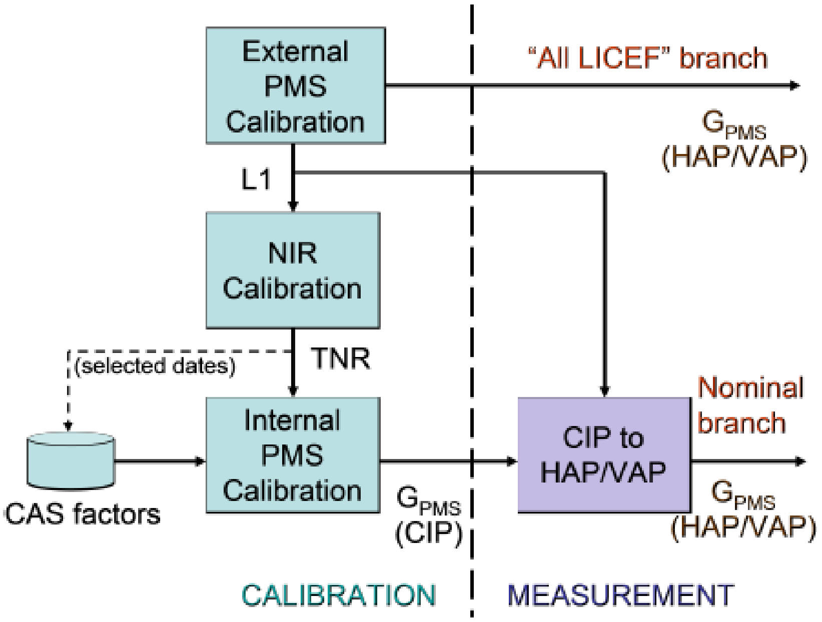

*Figure 3.14 Block diagram of the nominal and “all LICEF” PMS calibration strategies*

In the case of the nominal, internal PMS calibration uses the NIR measurement as a secondary calibration standard, which is in turn calibrated using the sky. To compensate the distribution network unbalance, a correction using the so-called “CAS factors” [Brown, M *et al.*, 2008] is introduced in the processing. In the case of all-LICEF, the PMS gain at HAP/VAP is directly recovered from the values obtained in the external calibration. So, the process is much simpler.

In order to measure the antenna temperature can be carried out directly by each individual LICEF operating as a total power radiometer. This implies a complete calibration of the PMS including both gain and receiver noise temperature by calibration during the cold sky external calibration as explained before.

As a summary, the all-LICEF mode implements the following changes with respect to the nominal processing [Corbella *et al.*, 2016]:

- PMS gains are computed using uncorrelated noise (matched load) instead of correlated noise. CAS factors and NIR are no longer used
- System temperatures at antenna plane use constant values of total front-end attenuation computed once from external calibration data
- Antenna temperature for all LICEF is computed from system temperatures and on-ground characterized receiver noise temperatures
- The visibility at the origin V(0,0) is the average of the selected LICEF antenna temperatures

Measured visibility sample

$$V_{kj} = \frac{M_{kj}}{G_{kj}} \sqrt{\frac{\left(v_k - v_{Offk}\right)\left(v_j - v_{Offj}\right)}{G_k G_j}}$$

MAIN MAGNITUDES

- $V_{kj}$: Denormalized visibility
- $M_{kj}$: Normalized correlation
- $G_{kj}$: complex FWF(0)
- $G_k$, $G_j$: $PMS_{k,j}$ gains
- $voff_{k,j}$: $PMS_{k,j}$ offsets
- $V_{k,j}$: $PMS_{k,j}$ voltage

Measured zero-baseline (antenna temperature)

NIR mode: $T_A = T_U - \eta T_{NA}$

All-LICEFmode: $T_A = \left\langle \frac{v_k - v_{Offk}}{G_k} - T_{Rk} \right\rangle$

- $\eta$: NIR fraction of Dicke cycle
- $T_U$: NIR internal load temperature
- $T_{NA}$: Noise injection temperature
- $T_{Rk}$ : $PMS_k$ receiver temperature

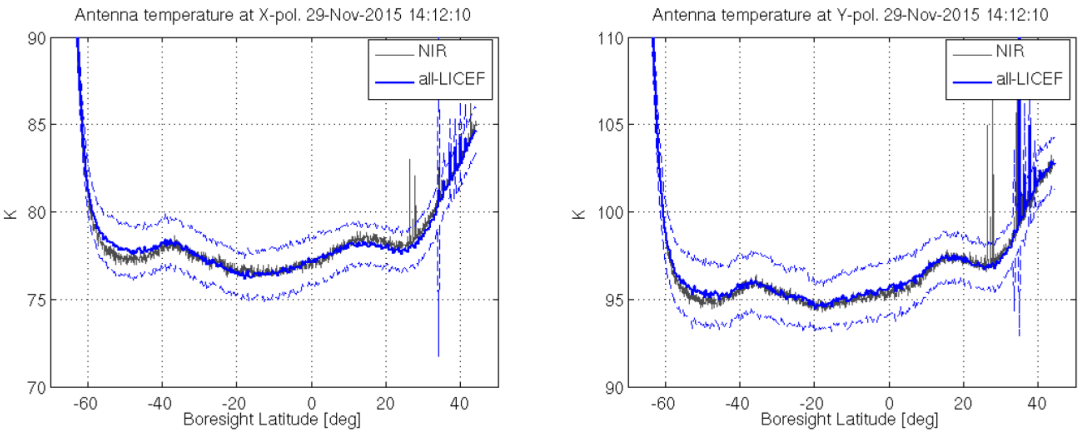

*Figure 3.15 Comparison between antenna temperature from NIR mode (nominal case) and all-LICEF for an orbit over the Pacific*

Figure 3.15 shows the difference between measuring the antenna temperature using NIR mode (nominal case) or by using all-LICEF mode. This will be an important aspect to take into account for the study of the land-sea contamination problem detailed in chapter 7. Figure 3.15 shows the antenna temperatures measured by the NIR and by the LICEF-PMS for an ascending orbit over the Pacific Ocean. In both cases, the average along all the measurements is drawn. As it is seen, both measurements are highly correlated, with some less noise in the case of the LICEF due to averaging. Both cases are affected by RFI (Radio Frequency Interferences) at high north latitudes.

# 4 Improvements in SMOS calibration

As commented in the previous sections, calibration of the instrument is a key stage to provide stable and accurate data.

This chapter is devoted to describe several calibration up-grades that have been undertaken within this PhD work. Also some system performance assessments.

Mainly:

- Improved inter element Full-pol phase calibration
- SLL performance
- PMS improved calibration

Calibration is needed to provide accurate values of visibility for all receiver pairs and antenna temperature for at least one element. Besides, image reconstruction algorithms need the fringe washing function shape and the flat target response. MIRAS uses a combination of both external and internal calibration to estimate all the time varying parameters. Stable parameters such as antenna patterns, S-parameters of noise distribution network and others, are directly used from on-ground characterization. The outcome of the MIRAS calibration system consists of the following parameters: the PMS (Power Measurement System) gain $G_k$ and offset $v_{off}$, the correlation complex gain $G_{kj}$ in amplitude and phase, the NIR source noise temperature $T_{NA}$ and the the normalized fringe washing function. All of them are periodically updated during the mission to account for instrumental drifts. Additionally, the Flat Target Response [Martin-Neira *et al.*, 2008a] is also considered a calibration parameter. The different parameters (described in chapter 3) were accurately characterized on ground, even so these parameters change in orbit because of seasonal temperature variation and can cause very large errors if a suitable calibration is not performed.

## 4.1 Relative phase retrieval in full-pol mode

SMOS single antenna patterns were accurately measured at the Danish Technical University (DTU) [Pivnenko *et al.*, 2007]. In this measurements the antenna pattern phase were normalized to boresight. LICEF phase drift due to aging, temperature or other factors is corrected by correlated noise injection at the calibration port C, as shown in chapter 3. However, the phase term between the calibrated phase (CIP) and the antenna phase center is out of the calibration loop. Due to mechanical and circuital tolerances this term is slightly different in the LICEF antennas and requires calibration. The test called “Inter-element phase retrieval” was performed during the ground tests to set the MIRAS Data Base (assumed to be constant throughout the mission). This section is devoted to review the MDB values to improve SMOS performance by reducing the relative phase contribution to spatial bias.

This work has addressed these objectives in two ways:

1) On-ground MDB values were obtained by blindly averaging the results from several measurement set-up configurations. Now, once SMOS is providing brightness temperatures maps over the ocean, the accuracy provided by each set of measurements can be evaluated to select the best option
2) The initial MDB values were computed to provide two independent sets of values, one for each polarization. However, SMOS full-pol performance requires the two sets to be phase linked to provide accurate A3 and A4 results

In this work the methodology and codes used to retrieved dual-pol inter-element phases during the IVT tests in 2007 have been extended to provide interlaced Hpol and Vpol phases from IVT full-pol tests.

### 4.1.1 Inter-element phase retrieval in IVT (Dual pol case)

SMOS relative phases were measured in the anechoic chamber from the image validation tests (IVT-1 and IVT-2) performed at ESTEC on May-June 2007 [Corbella *et al.*, 2006].

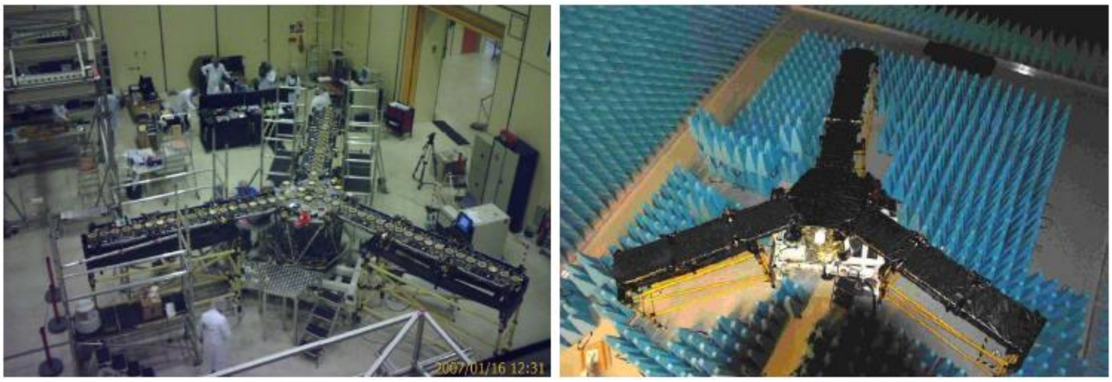

*Figure 4.1 MIRAS at EADS-CASA Spain premises (left) and at Maxwell anechoic chamber in ESTEC, Netherlands (right)*

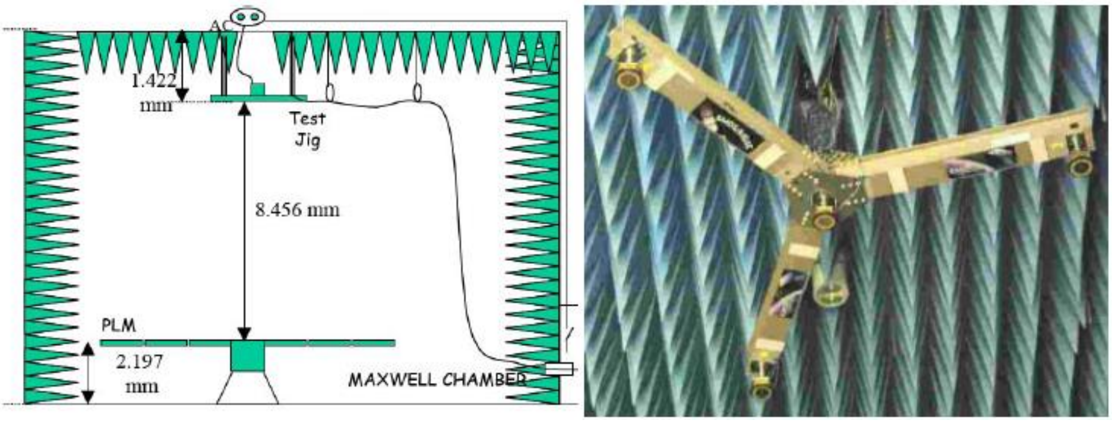

*Figure 4.2 Test setup (left). Radiation probes (test jig) situated at the ceiling of the chamber (right)*

Figure 4.1 (left) shows the instrument at the manufacturer premises in its final assembly process. At right, the radiometer is shown installed at the “Maxwell” anechoic chamber in ESTEC, ready to undergo the image validation and system performance tests. Note the radome covering the antennas.

The phase characterization method is based on measuring the cross-correlation of receivers’ output signals while emitting noise from a probe at known location. The measurement setup is schematically depicted in Figure 4.2 (left): the instrument is deployed horizontally inside the chamber while a point source (probe) in the ceiling is activated. Four probes at different locations with different polarization and power levels were used. Figure 4.2 at right shows the test jig containing all probes. It is also a Y-shape structure made of material transparent to L-band and having one probe at each arm plus one in the center. The probes precise positions were measured with a laser tracker. The antennas used in the probes were of similar design as the ones in the instrument, having a wide beamwidth of about 80º. Noise was generated by a 50 Ω resistor at ambient temperature connected to an amplifier followed by a variable attenuator to set up the power and feed the probes.

A general formulation to compute the inter-element phases takes into account the orientation and polarization of the antennas and the impact of the anechoic chamber radiation [Corbella *et al.*, 2006]. To illustrate the procedure Figure 4.3 shows the phases in the propagation of the signal from the active source (probe) to a given element.

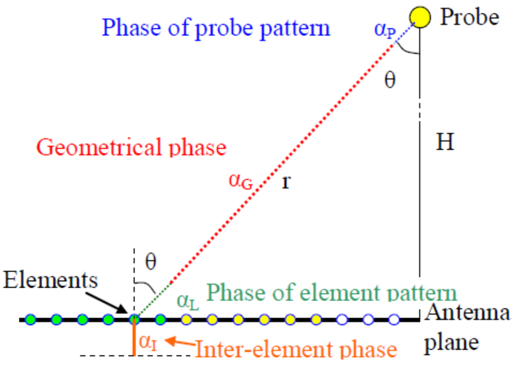

*Figure 4.3 Definitions of phases in propagation from probe to elements*

- $\alpha_P$ : Phase of antenna pattern probe referred to zero in boresight
- $\alpha_G$=-kr . Geometrical phase, where k is the wave-number
- $\alpha_L$ : Phase of element antenna pattern referred to zero in boresight
- $\alpha_I$ : Inter-element phase. The unknown phase to be retrieved

The phase difference between two inter-element phases $(k, j)$ is computed as:

$$\alpha_{kj} = \alpha_I(k) - \alpha_I(j) = \Phi_{kj} - \left\{\left[\alpha_P(k) - \alpha_P(j)\right] + \left[\alpha_G(k) - \alpha_G(j)\right] + \left[\alpha_L(k) - \alpha_L(j)\right]\right\} \tag{4. 1}$$

where $\Phi_{kj}$ is the phase of the complex correlation measured between the corresponding output signals of receivers k and j. Although $\alpha_{kj}$ is the parameter that is actually needed, individual phases can also be obtained for each element by solving the following system of equations:

$$\begin{bmatrix} \alpha_{12} \\ \alpha_{13} \\ \vdots \\ \vdots \\ \alpha_{N-1N} \end{bmatrix} = \begin{bmatrix} 1 & -1 & 0 & 0 & \cdots & 0 & 0 & 0 \\ 1 & 0 & -1 & 0 & \cdots & 0 & 0 & 0 \\ \vdots & \vdots & \vdots & \vdots & \ddots & \vdots & \vdots & \vdots \\ 0 & 0 & 0 & 0 & \cdots & 1 & 0 & -1 \\ 0 & 0 & 0 & 0 & \cdots & 0 & 1 & -1 \end{bmatrix} \begin{bmatrix} \alpha_I(1) \\ \alpha_I(2) \\ \vdots \\ \alpha_I(N) \end{bmatrix} \tag{4. 2}$$

Figure 4.4 shows the IVT phase recomputed according to [Corbella *et al.*, 2006] to reproduce the IVT values stated in the ground MDB. As shown in Figure 4.4, relative phases have a small dispersion between LICEFs units (except those from the NIR units not shown in the plots). The standard deviation of the retrievals for each unit due to the different measurements set-up is around 1,35º.

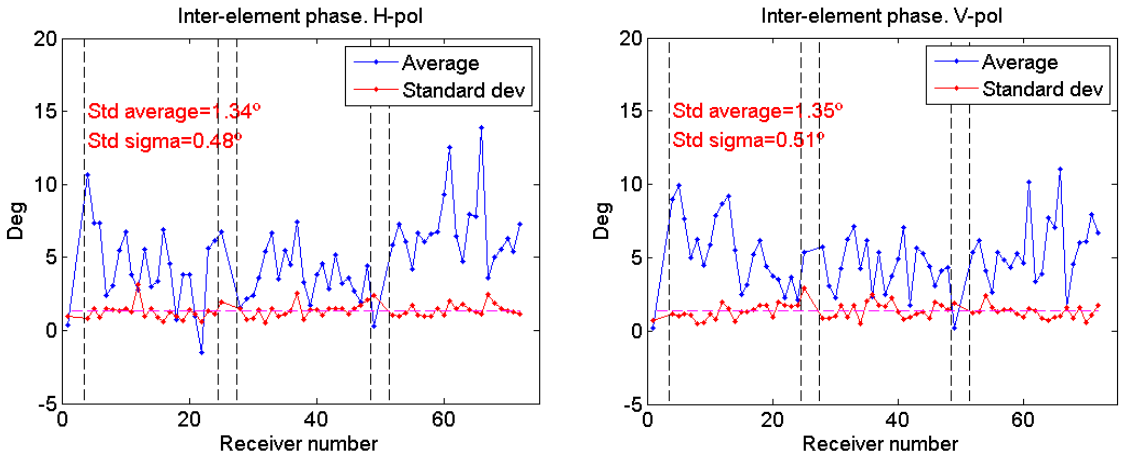

*Figure 4.4 Average and standard dev. of Inter-element phase H-pol (left) and V-pol (right)*

Figure 4.4 reproduces the dual-pol phases stated in the ground MDB, as recomputed in this PhD.

### 4.1.2 IVT SMOS Relative phase for Full-Pol mode

The phase relation between H and V polarization can be obtained from the polarimetric measurements $V_{xy}$ performed during the IVT but never processed before. In the full-pol case the equivalent matrix shown in (4.2) is larger than in dual-pol because it contains both H and V measurements. Since IVT tests provides both HV and VH measurements there are two cases, as shown in Figure 4.5.

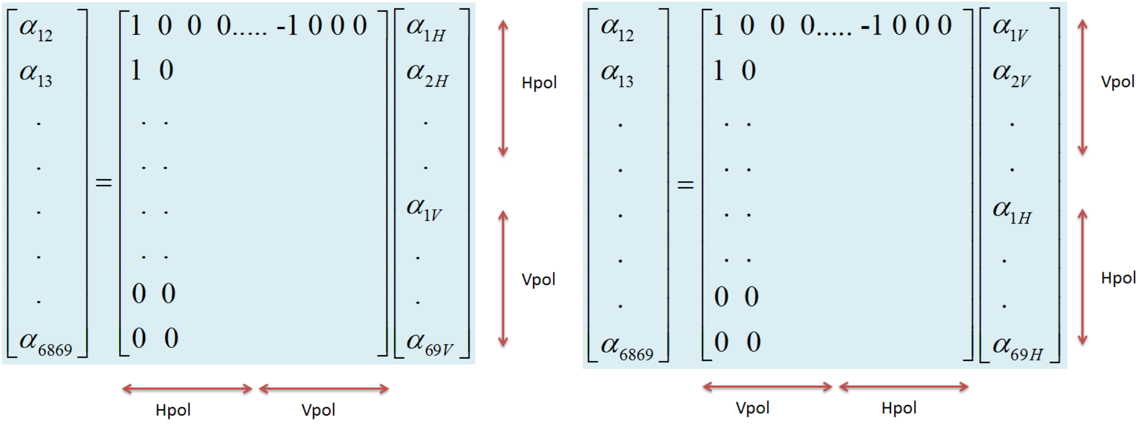

*Figure 4.5 Inter-element phase matrix for HV pol (left) and VH pol (right)*

However the system of equations in Figure 4.5 is under determined. To be solved, it is necessary to add an additional equation for the first receiver (2-1 pair). To solve the system, four new equations have been added to obtain all inter-element phases in the hub as it is shown in the following figure (yellow rows):

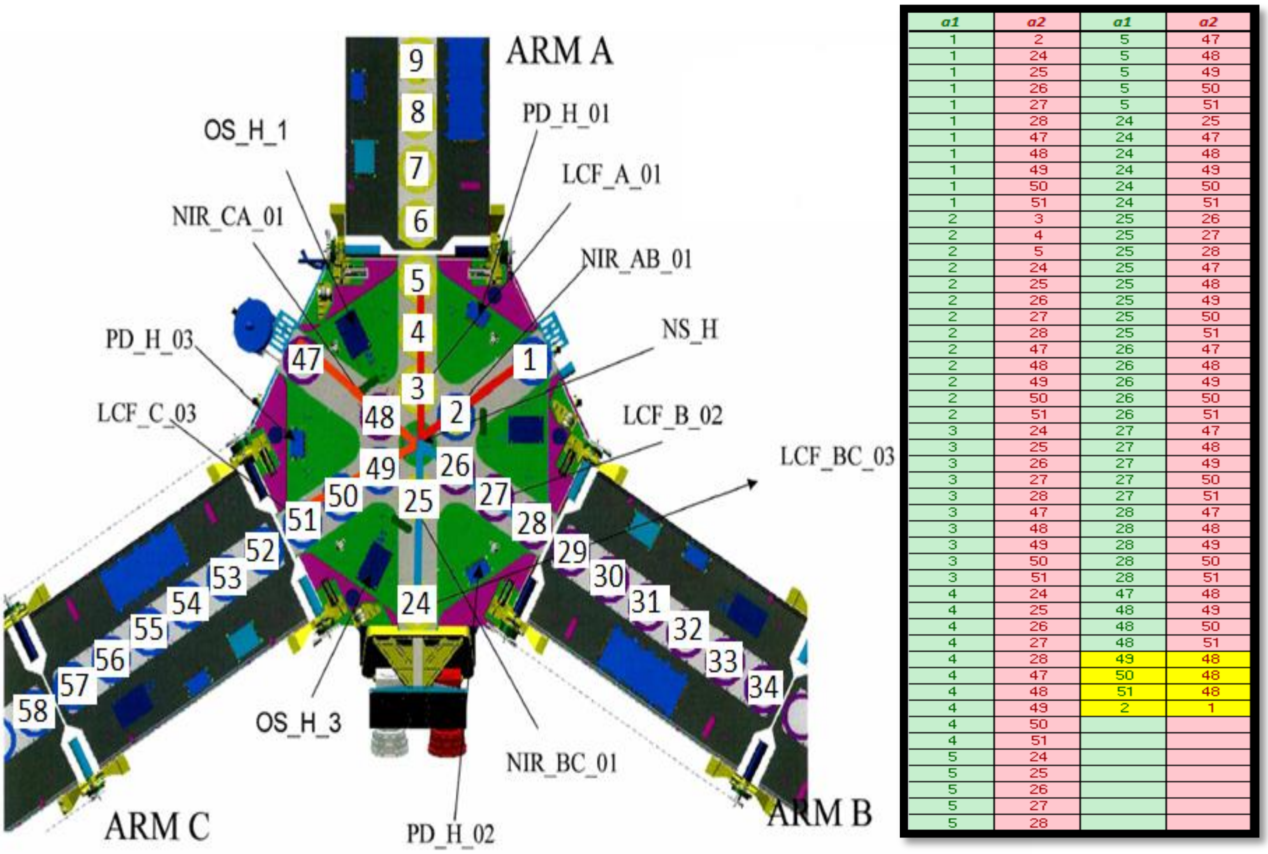

| a1 | a2 | a1 | a2 |
|---|---|---|---|
| 1 | 2 | 5 | 47 |
| 1 | 24 | 5 | 48 |
| 1 | 25 | 5 | 49 |
| 1 | 26 | 5 | 50 |
| 1 | 27 | 5 | 51 |
| 1 | 28 | 24 | 25 |
| 1 | 47 | 24 | 47 |
| 1 | 48 | 24 | 48 |
| 1 | 49 | 24 | 49 |
| 1 | 50 | 24 | 50 |
| 1 | 51 | 24 | 51 |
| 2 | 3 | 25 | 26 |
| 2 | 4 | 25 | 27 |
| 2 | 5 | 25 | 28 |
| 2 | 24 | 25 | 47 |
| 2 | 25 | 25 | 48 |
| 2 | 26 | 25 | 49 |
| 2 | 27 | 25 | 50 |
| 2 | 28 | 25 | 51 |
| 2 | 47 | 26 | 47 |
| 2 | 48 | 26 | 48 |
| 2 | 49 | 26 | 49 |
| 2 | 50 | 26 | 50 |
| 2 | 51 | 26 | 51 |
| 3 | 24 | 27 | 47 |
| 3 | 25 | 27 | 48 |
| 3 | 26 | 27 | 49 |
| 3 | 27 | 27 | 50 |
| 3 | 28 | 27 | 51 |
| 3 | 47 | 28 | 47 |
| 3 | 48 | 28 | 48 |
| 3 | 49 | 28 | 49 |
| 3 | 50 | 28 | 50 |
| 3 | 51 | 28 | 51 |
| 4 | 24 | 47 | 48 |
| 4 | 25 | 48 | 49 |
| 4 | 26 | 48 | 50 |
| 4 | 27 | 48 | 51 |
| 4 | 28 | 49 | 48 |
| 4 | 47 | 50 | 48 |
| 4 | 48 | 51 | 48 |
| 4 | 49 | 2 | 1 |
| 4 | 50 |  |  |
| 4 | 51 |  |  |
| 5 | 24 |  |  |
| 5 | 25 |  |  |
| 5 | 26 |  |  |
| 5 | 27 |  |  |
| 5 | 28 |  |  |

*Figure 4.6 HUB antenna location nomenclature (left) and pairs generation with new equations added in yellow color (right)*

Note that the nomenclature is related to antenna location because it is referred only for H or V polarization. Therefore, instead of having 18 receivers in the hub, the total number of antennas is 15 for H-pol and 15 for V-pol due to the NIRs switch position.

The solution of the full-pol system of equation provides a new set of inter-element phase where both polarization are interrelated. So, the phase difference between both polarization depending on the set of full-pol measurements used in the equation HV or VH measurements is the same.

Both HV and VH measurements provides an estimation of the same set of inter-element phases $\alpha_{H_k}$ and $\alpha_{V_k}$, that are interlaced. Since it is important to set the mean difference between polarization, Figure 4.7 plots the difference $\langle\alpha_H\rangle-\langle\alpha_V\rangle$. The result is about 7.09º. This is consistent with the fact that V-pol antennas include an additional path delay with relation to H-pol antennas.

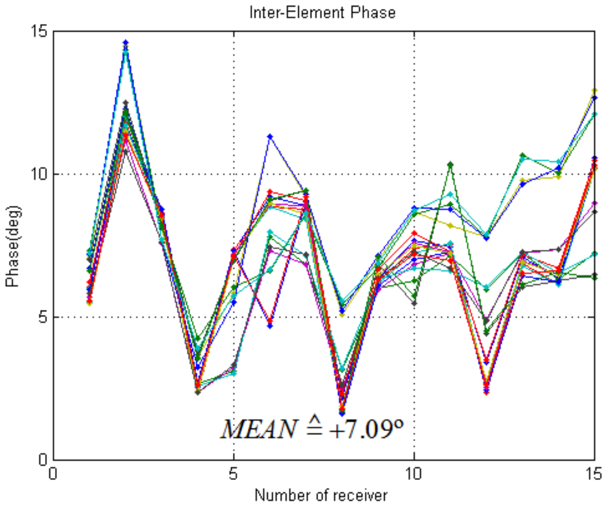

*Figure 4.7 HUB Inter-element phases from SMOS full-pol measurements regarding both HV and VH measurements (this last with a sign change)*

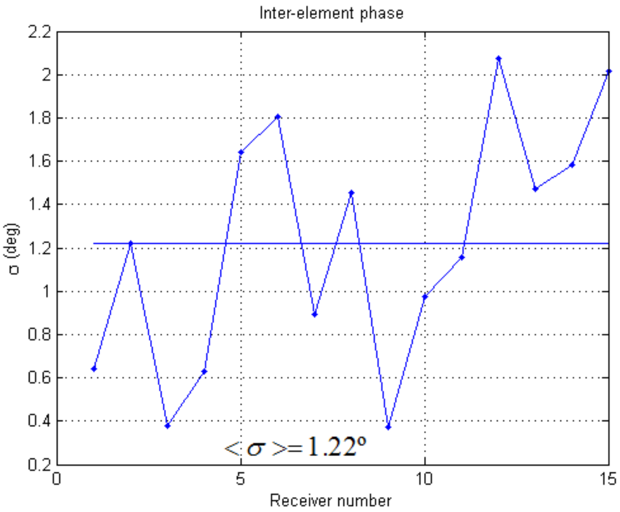

*Figure 4.8 Standard Deviation of Inter-element phases from full-pol measurements HUB*

The standard deviation of the relative phase measured for each antenna (due to the different IVT-1 and IVT-2 tests) is plotted in Figure 4.8. A mean value 1.22º for the standard deviation has been obtained.

### 4.1.3 Computation of inter-element phases in polarimetric mode

Once verified that inter-element phase retrieval in the HUB provides consistent results, the program has been extended to the whole instrument in order to retrieve 69 phases from HV measurements and 69 phases from VH measurements.

The main difference with respect to dual-pol mode is again the fact that equations from arm C receivers cannot be generated because all arms are in the same polarization and pairs condition a1<a2 do not allow to create pairs between these receivers and other arm. So, the program has been extended to introduce additional equations as shown in Figure 4.9.

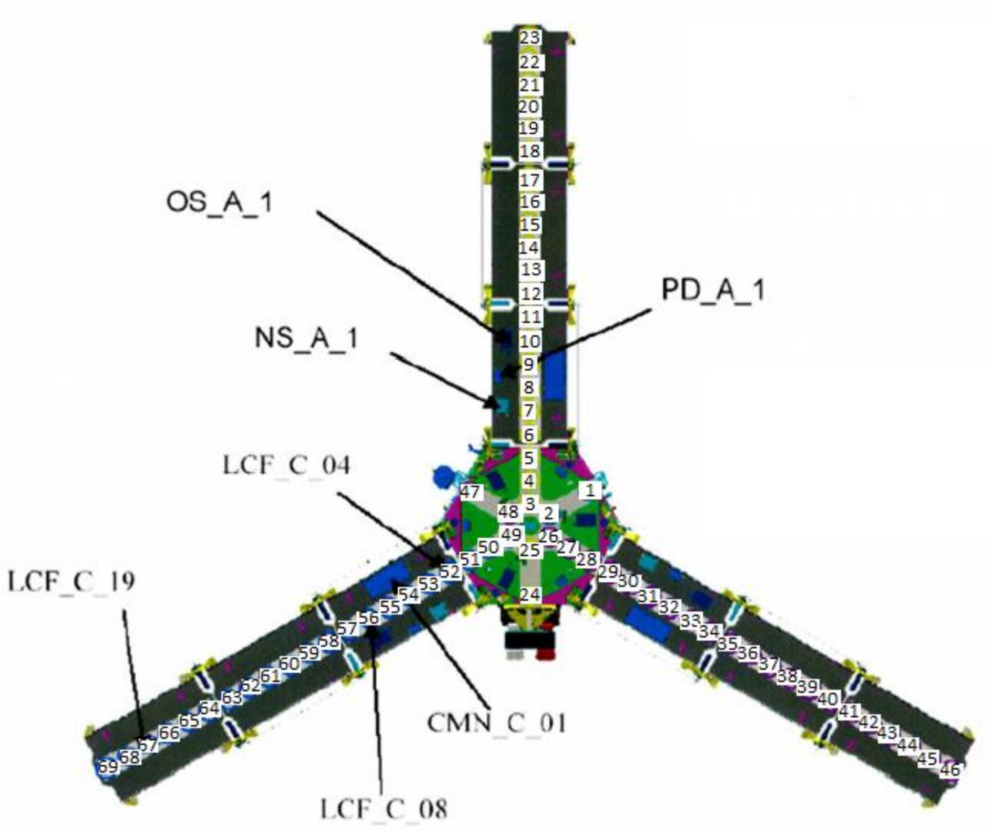

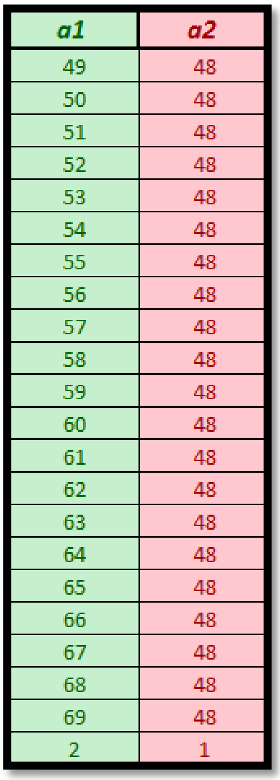

| a1 | a2 |
|---|---|
| 49 | 48 |
| 50 | 48 |
| 51 | 48 |
| 52 | 48 |
| 53 | 48 |
| 54 | 48 |
| 55 | 48 |
| 56 | 48 |
| 57 | 48 |
| 58 | 48 |
| 59 | 48 |
| 60 | 48 |
| 61 | 48 |
| 62 | 48 |
| 63 | 48 |
| 64 | 48 |
| 65 | 48 |
| 66 | 48 |
| 67 | 48 |
| 68 | 48 |
| 69 | 48 |
| 2 | 1 |

*Figure 4.9 SMOS antenna location nomenclature (left) and new equations added to pairs generation (right)*

Note that the nomenclature is related with antenna location because it is referred only for H or V polarization instead of having 72 receivers in the entire instrument, the total number of antennas is 69 for H-pol and 69 for V-pol due to the NIRs switch position. Two sets of interlaced relative phases in H-pol and V-pol are obtained from HV and VH measurements. Figure 4.10 show the results of plotting the difference $\langle \alpha_H \rangle - \langle \alpha_V \rangle$, resulting in a mean difference of 6,8º. Again this is consistent with the fact that V pol antenna includes an extra path delay.

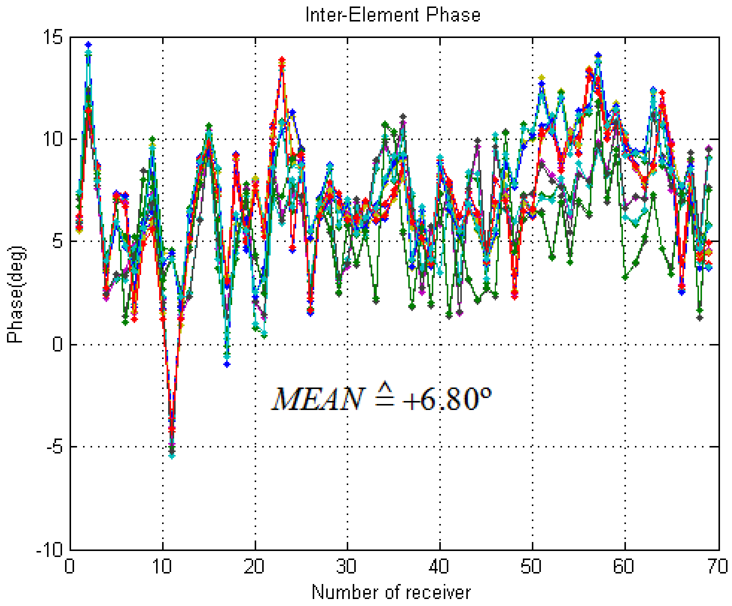

*Figure 4.10 Inter-element phase differences ($\alpha_H - \alpha_V$) from SMOS full-pol HV and VH measurements*

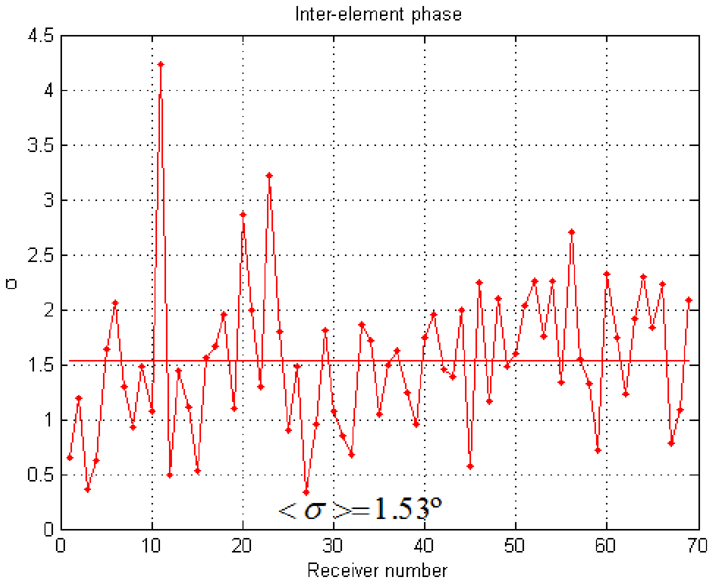

*Figure 4.11 Standard Deviation of Polarimetric inter-element phase measurements*

The standard deviation of each receiver out of the IVT tests is plotted in Figure 4.11 and the mean value obtained is 1.53º.

Figure 4.13 shows the comparison between inter-element phase differences ($\alpha_H - \alpha_V$) from dual and full equations in order to perform the comparison. In the dual results, the mean difference between H and V polarization in full-pol (6,8º) has been subtracted from the V-pol results. The consistency between the two sets of results is very good, thus validating the full-pol set of equations and results.

The difference $\langle \alpha_H \rangle - \langle \alpha_V \rangle = 6.8^{\circ}$ is also consistent with the results obtained by Wu Lin in his PhD work (chapter 6 section 6.2.7). In his work the value obtained for the difference is achieved by minimizing crosstalk between A3 and A4 measurements over the ocean. The value obtained minimizing A4 error was $\langle \alpha_H \rangle - \langle \alpha_V \rangle = 6^{\circ}$. Also a value similar to the result derived from the IVT tests.

When preparing the version, V620 of the processor, it became clear that the two sets of relative phases could have an offset between them which had to be corrected. Such phase bias across the two polarizations was in fact causing distortions in the Stokes-3 and, most clearly, Stokes-4 parameters. Therefore, the IVT data set was re-analyzed to determine the missing phase offset between the two polarizations, which was found to be of -6,8° as shown in this section. This value was verified using Stokes-4 images over the ocean: as shown in Figure 4.12, the error (sigma displayed in the lower left corner) was indeed minimized for a phase offset close to the retrieved one. All phases corresponding to vertical polarization were then reduced by that amount in version V620 of the processor. All these results were presented in the paper “SMOS instrument performance and calibration after 5 years in orbit” [Martin-Neira *et al.*, 2015].

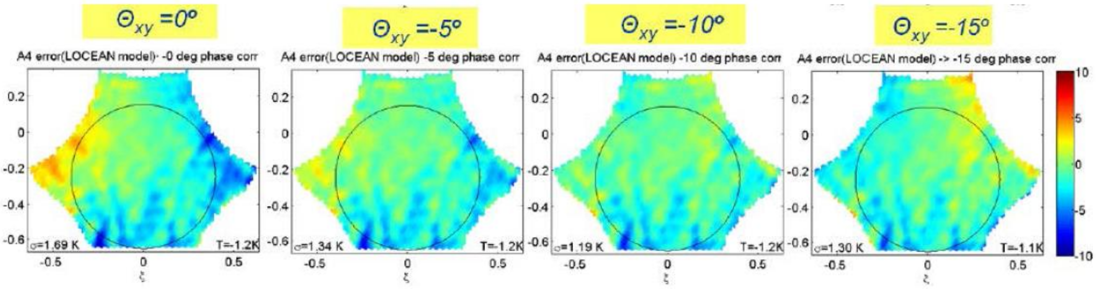

*Figure 4.12 Validation of the relative phase between polarizations using Stokes-4 over ocean*

The previous two sets of relative phases (dual and full equations) are consistent if the 6,8° difference is taken into account in the dual-pol case.

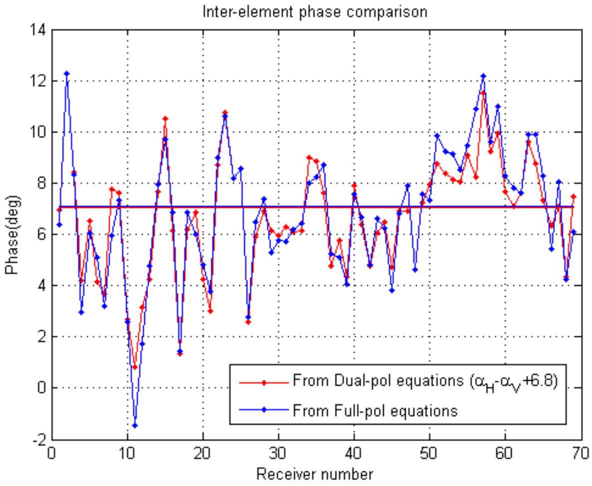

*Figure 4.13 Inter-element H-pol and V-pol phase difference comparison: Dual-pol equations vs Full-pol equations*

The following figures shows MDB (MIRAS Database) phases and the phases re-processed in this work from dual-pol measurements (H/V pol.):

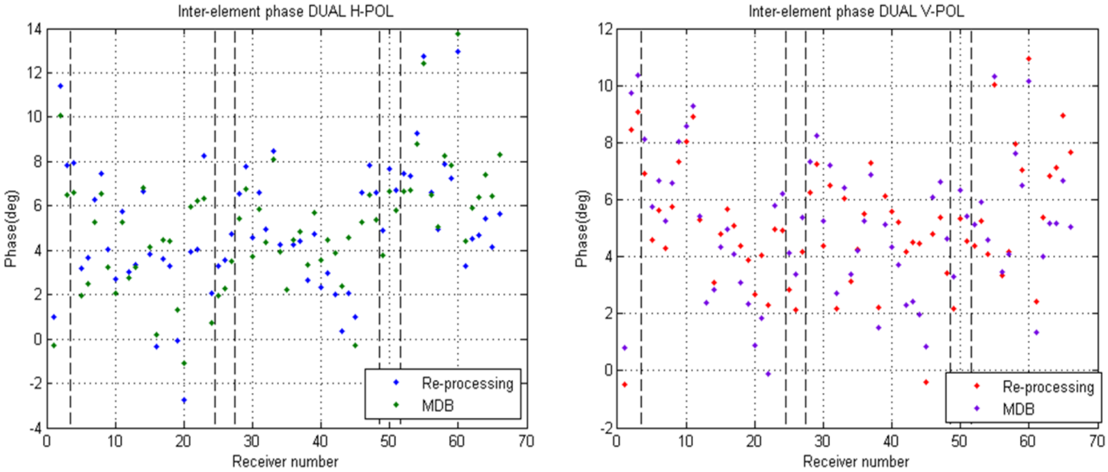

*Figure 4.14 Inter-element phase comparison MDB vs Re-processed H-pol (left) and V-pol (right)*

Note that the values are slightly different due to the fact that MDB phases were computed in 2007 and some parts of the code have slight changes or improvements. It must be pointed out that the NIR phases are computed but not represented in Figure 4.14 since their values are very different (around -110º).

Once all these results have been validated, the MDB inter-element relative phases can be re-computed taking into account the value of the phase error $\theta_{HV}$ obtained after all the polarimetric analysis as:

$$\begin{aligned} \alpha_H^{'} &= \alpha_H \\ \alpha_V^{'} &= \alpha_V - \theta_{HV} \end{aligned} \tag{4. 3}$$

where $\alpha_H$ and $\alpha_V$ are the current MDB inter-element phases obtained in dual pol. mode and $\theta_{HV}$=6,8º is the mean value obtained from re-computing inter-element phases in full-pol mode. This approach was selected by SMOS calibration team to guarantee consistency with all the scientific studies performed so far. It must be pointed that until release of version 620 of the Level 1 operator processor (L1OP), SMOS was delivering data in dual-pol: Since a constant phase added to all vertical channel does not change the results in dual pol, only the mean 6,8º difference is used to update MDB to improve SMOS full-pol performance (reduced spatial bias in A3 and A4) while not changing at all the dual pol radiometric data (thus not producing changes in the scientific results obtained by the international community from previous dual-pol data).

Finally, after applying this new phases in the SMOS calibration a clear improvement for A4 has been obtained in the image:

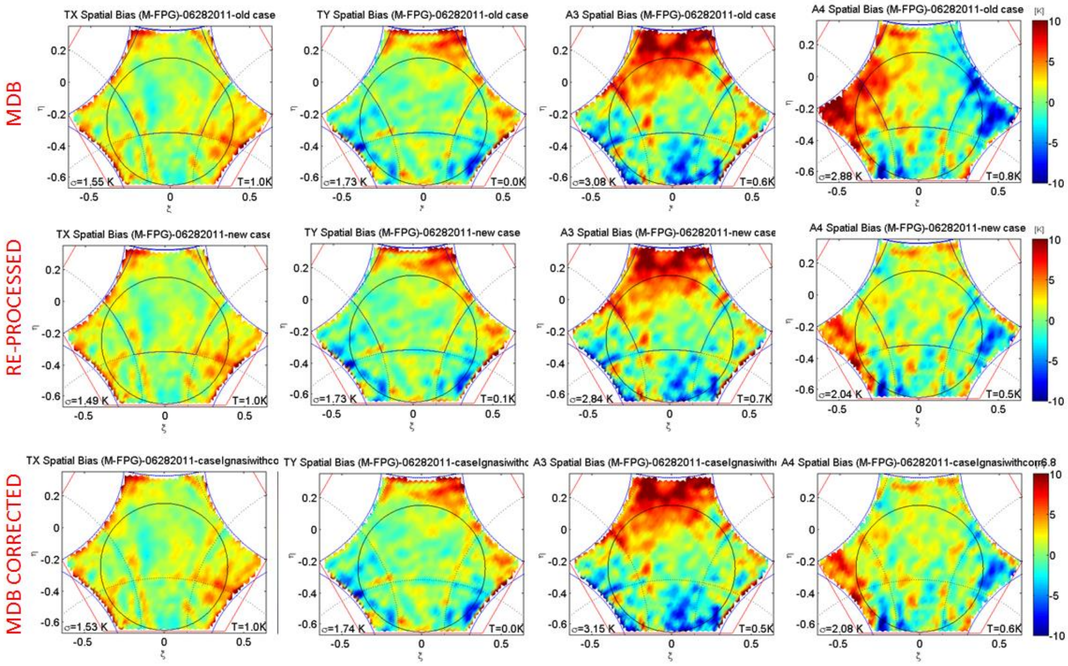

*Figure 4.15 Ocean view image error MDB phases (top) re-processed phases (middle) and MDB corrected phases (bottom) M-FPG (Model approach Full Pol. G-matrix)*

Figure 4.15 shows spatial bias measured over the ocean using the current MDB phases (1st row), re-processed ones (2nd row) and MDB corrected phases (3rd row). Note that MDB inter-element phases (third row in Figure 4.15) provide a large improvement in A4 (standard deviation is reduced from 2,88 K to 2,08 K). The large error in A4 was mainly due to A3 to A4 crosstalk because of the mean error between H-pol and V-pol phases. Additionally, in the left part of the image some red spots have been removed. Results for TX, TY and A3 are very similar as expected, since $\theta_{XY}$ mainly affects A4.

Relative phases retrievals from the single IVT-1 and IVT-2 tests have produce very similar results on pixel bias performance. Therefore, in order to average errors, the mean relative phases from all the tests have been selected to update the MDB values.

After all the previous assessment the best candidate to update inter-element phases is MDB corrected case because it is using current MDB relative phases subtracting the mean obtained from full-pol measurements that is $\theta_{xy}$=6,8º. So, it only introduces changes in the current V-pol values but not in the H-pol. In this case, the changes of the MDB exclusively affects A4 but not the other terms (TX, TY and A3), thus simplifying the validation of the change.

Finally, Figure 4.16 shows the preliminary version of phases re-computed after all the assessment performed in this section:

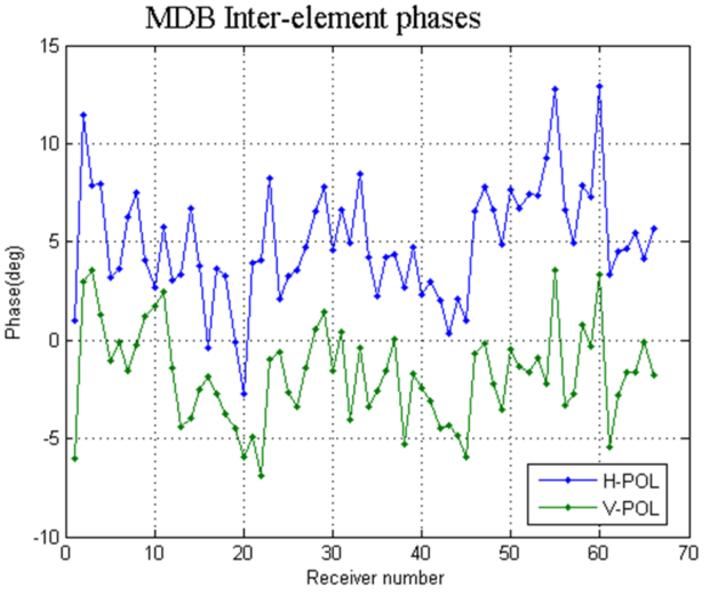

*Figure 4.16 Inter-element phases taking into account full-pol. IVT measurements*

### 4.1.4 Further improvement of inter-element phases

After a first analysis in which inter-element phases have been re-computed from the image validation tests (IVT-1 and IVT-2) performed at ESTEC on May-June 2007 [Durán *et al.*, 2013], it has been detected that some probes introduce systematic errors that can be mitigated by making the same assessment but separating inter-element phases in different groups depending on polarization, radiated power or height of the probe.

Before launch of the instrument inter-element phases were estimated by averaging all measured values in the anechoic chamber. This was done in this way since in the anechoic chamber there was no way to evaluate the quality of each of the tests. However, once SMOS has been launched spatial bias can be measured over the ocean and the performance of inter-element phases from each set of measurement configuration can be tested and evaluated against ground truth data. This section is devoted to recompute inter-element phases by groups depending on the probe (O, A, B or C) in order to obtain a more accurate set of phases to calibrate the instrument. This analysis has been performed by filtering inter-element phases per groups depending on the position, the temperature or the height of the probe located at the ceilings as it is shown in Figure 4.17.

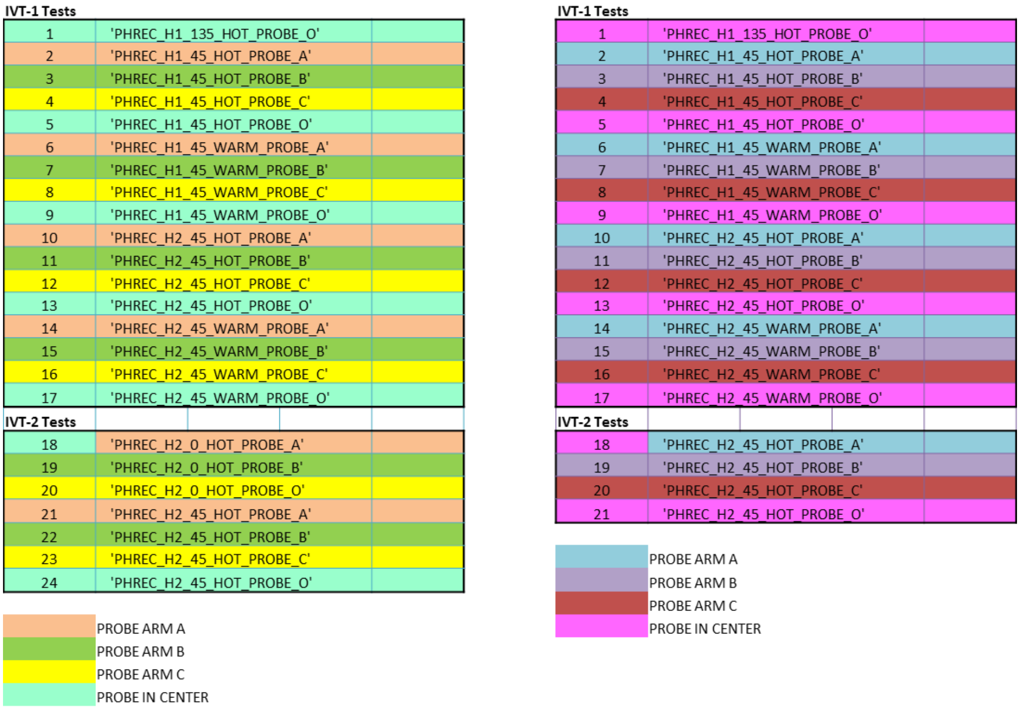

| IVT-1 Tests | |
|---|---|
| 1 | 'PHREC_H1_135_HOT_PROBE_O' |
| 2 | 'PHREC_H1_45_HOT_PROBE_A' |
| 3 | 'PHREC_H1_45_HOT_PROBE_B' |
| 4 | 'PHREC_H1_45_HOT_PROBE_C' |
| 5 | 'PHREC_H1_45_HOT_PROBE_O' |
| 6 | 'PHREC_H1_45_WARM_PROBE_A' |
| 7 | 'PHREC_H1_45_WARM_PROBE_B' |
| 8 | 'PHREC_H1_45_WARM_PROBE_C' |
| 9 | 'PHREC_H1_45_WARM_PROBE_O' |
| 10 | 'PHREC_H2_45_HOT_PROBE_A' |
| 11 | 'PHREC_H2_45_HOT_PROBE_B' |
| 12 | 'PHREC_H2_45_HOT_PROBE_C' |
| 13 | 'PHREC_H2_45_HOT_PROBE_O' |
| 14 | 'PHREC_H2_45_WARM_PROBE_A' |
| 15 | 'PHREC_H2_45_WARM_PROBE_B' |
| 16 | 'PHREC_H2_45_WARM_PROBE_C' |
| 17 | 'PHREC_H2_45_WARM_PROBE_O' |
| **IVT-2 Tests** | |
| 18 | 'PHREC_H2_0_HOT_PROBE_A' |
| 19 | 'PHREC_H2_0_HOT_PROBE_B' |
| 20 | 'PHREC_H2_0_HOT_PROBE_O' |
| 21 | 'PHREC_H2_45_HOT_PROBE_A' |
| 22 | 'PHREC_H2_45_HOT_PROBE_B' |
| 23 | 'PHREC_H2_45_HOT_PROBE_C' |
| 24 | 'PHREC_H2_45_HOT_PROBE_O' |

🟧 PROBE ARM A
🟩 PROBE ARM B
🟨 PROBE ARM C
🟩 PROBE IN CENTER

| IVT-1 Tests | |
|---|---|
| 1 | 'PHREC_H1_135_HOT_PROBE_O' |
| 2 | 'PHREC_H1_45_HOT_PROBE_A' |
| 3 | 'PHREC_H1_45_HOT_PROBE_B' |
| 4 | 'PHREC_H1_45_HOT_PROBE_C' |
| 5 | 'PHREC_H1_45_HOT_PROBE_O' |
| 6 | 'PHREC_H1_45_WARM_PROBE_A' |
| 7 | 'PHREC_H1_45_WARM_PROBE_B' |
| 8 | 'PHREC_H1_45_WARM_PROBE_C' |
| 9 | 'PHREC_H1_45_WARM_PROBE_O' |
| 10 | 'PHREC_H2_45_HOT_PROBE_A' |
| 11 | 'PHREC_H2_45_HOT_PROBE_B' |
| 12 | 'PHREC_H2_45_HOT_PROBE_C' |
| 13 | 'PHREC_H2_45_HOT_PROBE_O' |
| 14 | 'PHREC_H2_45_WARM_PROBE_A' |
| 15 | 'PHREC_H2_45_WARM_PROBE_B' |
| 16 | 'PHREC_H2_45_WARM_PROBE_C' |
| 17 | 'PHREC_H2_45_WARM_PROBE_O' |
| **IVT-2 Tests** | |
| 18 | 'PHREC_H2_45_HOT_PROBE_A' |
| 19 | 'PHREC_H2_45_HOT_PROBE_B' |
| 20 | 'PHREC_H2_45_HOT_PROBE_C' |
| 21 | 'PHREC_H2_45_HOT_PROBE_O' |

🟦 PROBE ARM A
🟪 PROBE ARM B
🟥 PROBE ARM C
🟪 PROBE IN CENTER

*Figure 4.17 IVT tests separated per groups H-pol. (left) and V-pol (right)*

So, four new groups are generated depending on the specific probe to be used in the test:

- *Group 1:* Mean Tests from Probe arm A ON
- *Group 2:* Mean Tests from Probe arm B ON
- *Group 3:* Mean Tests from Probe arm C ON
- *Group 4:* Mean Tests from Probe on hub ON

As described in Figure 4.17 (left table) the IVT-1 and IVT-2 tests measured in H-pol separated by colors that details a different position, temperature and height of the probe. The table on the right represents the tests measured in V-pol. Note that in this case there are 3 tests less than H-pol. because 0º Tests were only measured in the horizontal case.

A simple assessment of the inter-element phases from the different tests has shown that these results were very insensitive to the height and temperature of the probe. The main difference came from the different position of the probes due to geometric uncertainty. Therefore, all the results from the same probe were averaged to minimize the effect of the trend noise and other minor effects [Durán *et al.*, 2013]. Therefore only four different groups of tests are taken into account in this validation exercise:

Probe O (HUB)
- Probe A
- Probe B
- Probe C

The four new sets of inter-element phases computed from the IVT tests are used to calibrate the instrument obtaining the ocean view image error and the spatial bias. Probe B and O provide the larger error and were discarded after a few simulations [Durán *et al.*, 2013]. Therefore a fine comparison of the results provided by probes A and C was undertaken by selecting one ascending and one descending orbit.

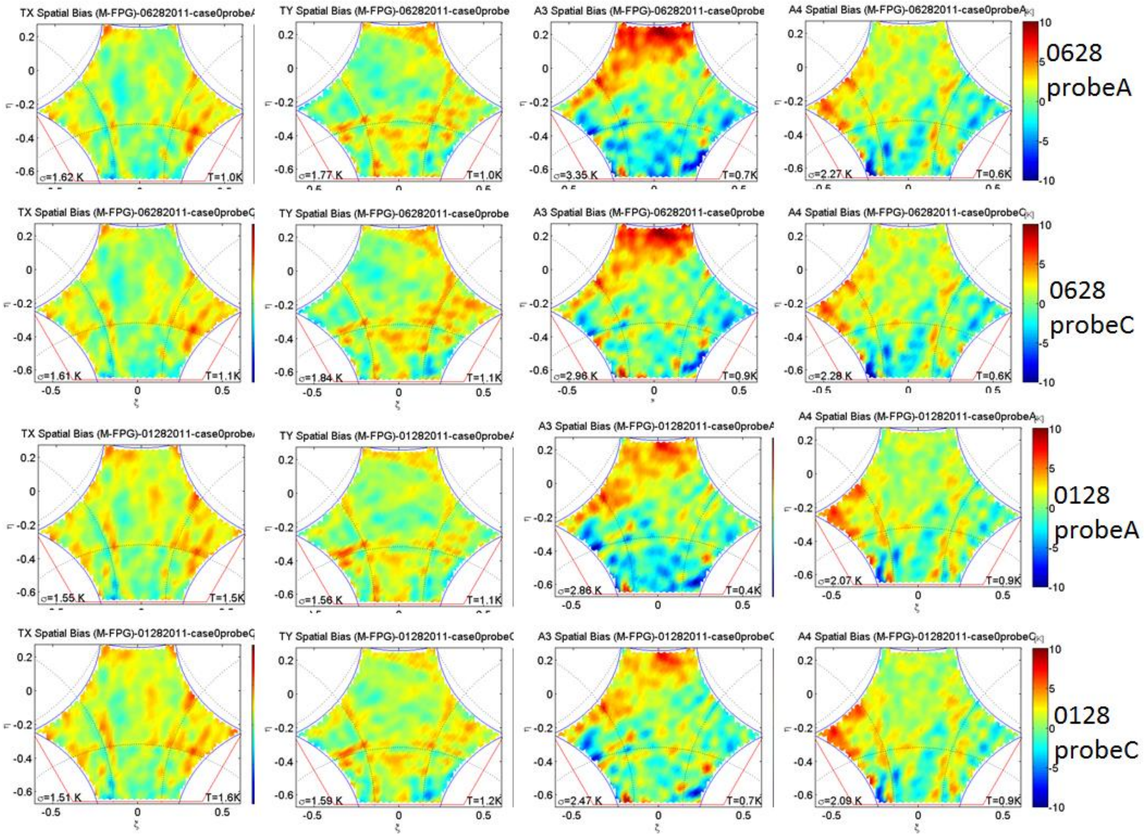

*Figure 4.18 Ocean view image error probe A 28/06 (1st row), probe C 28/06 (2nd row), probe A 28/01 (3rd row) and probe C 28/01 (4th row) M-FPG with Fresnel model*

| PROBE | Std TX | Std TY | Std A3 | Std A4 |
|---|---|---|---|---|
| **A (28/06)** | 1,62 K | 1,77 K | 3,35 K | 2,27 K |
| **C (28/06)** | 1,61 K | 1,84 K | 2,95 K | 2,28 K |
| **A (28/01)** | 1,55 K | 1,56 K | 2,86 K | 2,07 K |
| **C (28/01)** | 1,51 K | 1,59 K | 2,47 K | 2,09 K |

*Table 4.1 Standard deviation Probe A vs Probe C*

Figure 4.18 shows that the results from both probes A and C are very similar. Finally, probe C is selected because it provides slightly better results according to the metric in Table 4.1 especially in A3. In all cases, especially in A3, as shown table Table 4.1.

Therefore as a conclusion of the previous analysis it has been decided that the inter-element phases that provide an improvement in the ocean spatial bias are those that are computed from Probe C measurements in this IVT tests.

Figure 4.19 shows the final version of full-pol inter element relative phases that have been included in the current MTS and in version v620 of SMOS level 1 operational processor (L1OP). Again, in order to keep consistency with the scientific results provided by previous dual-pol version, the MDB has been updated by subtracting 6,2º to all V-pol relative phase in the previous version of the data-base.

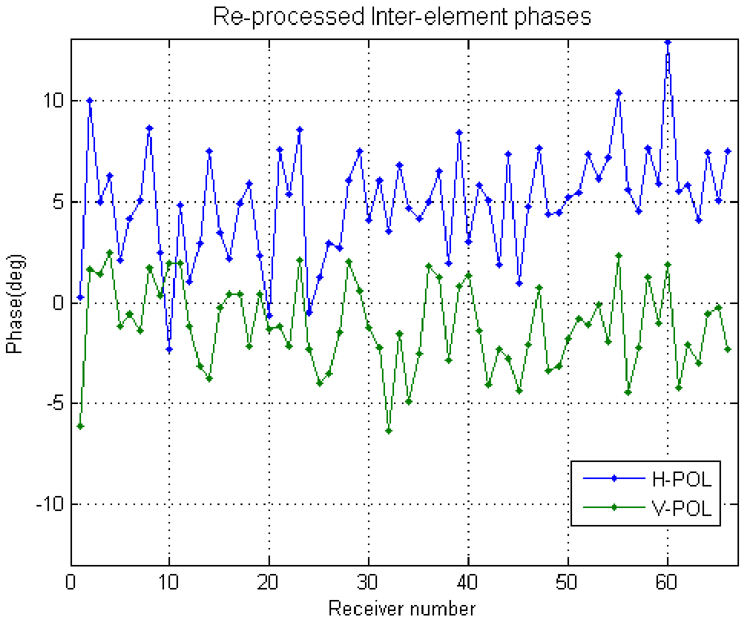

*Figure 4.19 v620 L1OP inter-element phases*

At the end of this section a table with the final inter-element phases obtained in all the receivers for both $\alpha_H$ and $\alpha_V$ is provided.

## 4.1.5 Conclusions

Figure 4.20 shows the 3 main cases performed for this assessment using the following inter-element phases to calibrate the instrument:

1. Original dual-pol SMOS phase (first row)
2. Reprocessed phases (mean of all tests) in full-pol (second row)
3. Reprocessed phases (mean of tests from probe C). MDB for version 620 of the L1OP (third row)

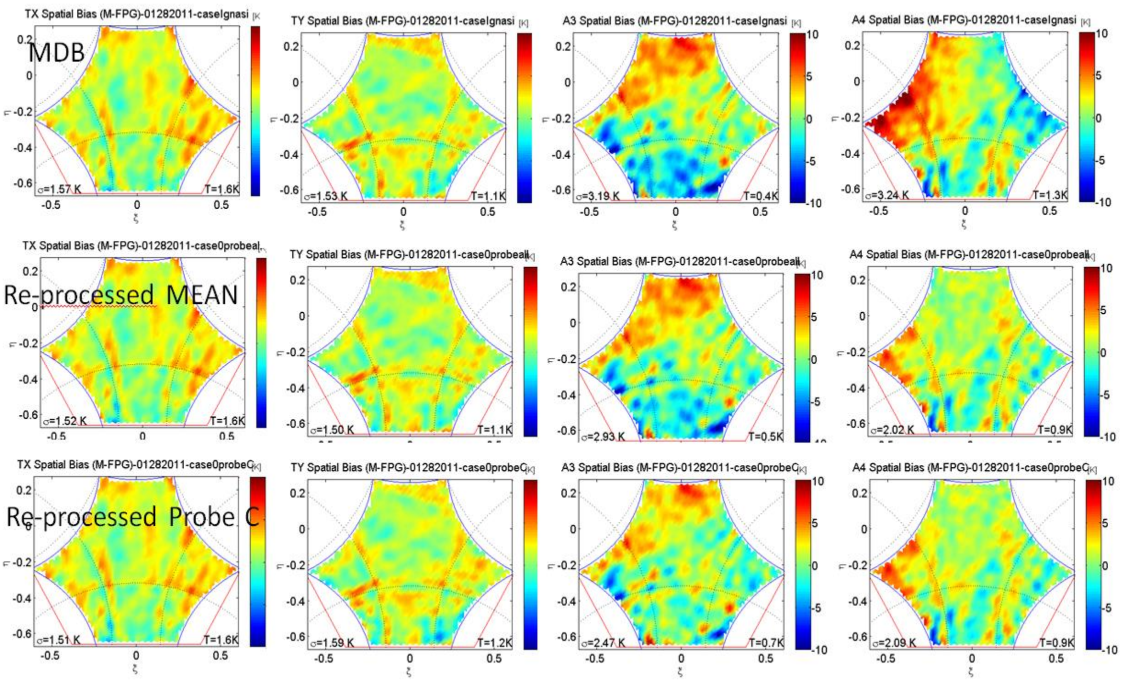

*Figure 4.20 Ocean view image error calibrating with MDB phases (top), calibrating with reprocessed phases mean all tests (middle) and calibrating with reprocessed phases mean of probe C tests (bottom) M-FPG with Fresnel model*

| CASE | Std TX | Std TY | Std A3 | Std A4 |
|---|---|---|---|---|
| **MDB** | 1,57 K | 1,53 K | 3,19 K | 3,24 K |
| **Re-processed MEAN** | 1,52 K | 1,50 K | 2,93 K | 2,02 K |
| **Re-processed Probe C** | 1,51 K | 1,59 K | 2,47 K | 2,09 K |

*Table 4.2 Standard deviation of Original SMOS phases, Re-processed phases (mean) and Re-processed phases (Probe C)*

Note that a clear improvement is obtained in A3 and A4 by using the reprocessed phases computed from the mean of probe C measurements. The spatial bias in A3 using on-ground MDB phases is 3,19 K and calibrating the instrument by using the new set of phases (Re-processed Probe C) is 2,47 K. Moreover, the image shows a clear improvement in the top part (less red spots) and in the bottom (less blue spots).

On the other hand, A4 improves from a spatial bias of 3.24 K to 2.09 K, and especially the error of the left part of the image is reduced.

It must be pointed out that the work in this section was performed during the first stages of this thesis. Some of the artifacts present in the spatial bias plots shown in Figure 4.20 have been revealed to be caused by the floor error and residual Faraday rotation errors. Further improvement of full-pol spatial bias will be addressed in chapter 5.

Summarizing the results of this section:

- Single polarization tests are now more accurate to derive $\alpha_H$ and $\alpha_V$ from dual-pol measurements due to:
    - Discarded measurements from probes that provides large errors (probe B and O).
    - Computation of the mean only from measurements from probe C Tests that provide the best spatial bias in the ocean view image error.
- Reprocessed inter-phases have been updated taking into account the value of the phase error $\theta_{HV}$ obtained after all the polarimetric analysis made per groups. The new phases are computed as:

$$
\begin{aligned}
\alpha_H^{'} &= \alpha_H \\
\alpha_V^{'} &= \alpha_V - \theta_{HV}
\end{aligned}
$$

- where $\alpha_H$ and $\alpha_V$ are the inter-element phases obtained in single mode and $\theta_{HV}$=6,2° (mean value obtained from inter-element phases measured in full pol. from probe C measurements).
- The new set of re-processed inter-element phases provides a significant improvement basically in A3 respect to the previous set of phases. Also A3 to A4 cross-talk has been very much mitigated.
- Note that the mean phase difference between H and V polarization obtained after reprocessing IVT-1 and IVT-2 ground tests (6,8°) is very consistent with the value obtained by minimize the error in A4 as provided in the PhD thesis of Wu, L. [Wu, 2014].
- It must be pointed out that improved inter-element phases together with the development of full-pol G-matrix inversion provided for the first time in the mission operational A3 and A4 brightness temperatures. The quality of this parameters has been good enough to allow direct Faraday rotation correction out of A3 and A4 [Corbella *et al.*, 2015b].

## 4.1.6 Re-processed Inter-element phases table

The following table shows the reprocessed phases for the 69 receivers both H and V polarization; as provided for MTS (database) and L1OP v620.

| *Receiver name* | *αh' (Re-processed)* | *αv' (Re-processed)* |
|---|---|---|
| **'LCF_AB_03'** | 0,24974741 | -6,10867417 |
| **'NIR_AB_01_H'** | -107,23892 | -107,23892 |
| **'NIR_AB_01_V'** | -119,174941 | -119,174941 |
| **'LCF_A_01'** | 10,002393 | 1,64248755 |
| **'LCF_A_02'** | 4,96464536 | 1,39031512 |
| **'LCF_A_03'** | 6,30879221 | 2,50270793 |
| **'LCF_A_04'** | 2,11358385 | -1,17120439 |
| **'LCF_A_05'** | 4,15082724 | -0,53875282 |
| **'LCF_A_06'** | 5,02042265 | -1,38812013 |
| **'LCF_A_07'** | 8,66483942 | 1,7226937 |
| **'LCF_A_08'** | 2,45219152 | 0,32628783 |
| **'LCF_A_09'** | -2,28597368 | 1,93041529 |
| **'LCF_A_10'** | 4,8054111 | 1,90537051 |
| **'LCF_A_11'** | 1,04296693 | -1,17163942 |
| **'LCF_A_12'** | 2,90882841 | -3,13247346 |
| **'LCF_A_13'** | 7,46221163 | -3,75068958 |
| **'LCF_A_14'** | 3,48639472 | -0,23161581 |
| **'LCF_A_15'** | 2,15922566 | 0,44002285 |
| **'LCF_A_16'** | 4,92342994 | 0,41008812 |
| **'LCF_A_17'** | 5,89625474 | -2,18943694 |
| **'LCF_A_18'** | 2,30034513 | 0,43636191 |
| **'LCF_A_19'** | -0,68413465 | -1,34374493 |
| **'LCF_A_20'** | 7,58430369 | -1,20406253 |
| **'LCF_A_21'** | 5,33553381 | -2,1397447 |
| **'LCF_BC_03'** | 8,52331198 | 2,08175595 |
| **'NIR_BC_01_H'** | -105,927185 | -105,927185 |
| **'NIR_BC_01_V'** | -114,345185 | -114,345185 |
| **'LCF_B_01'** | -0,5036984 | -2,34488776 |
| **'LCF_B_02'** | 1,26583232 | -4,01600001 |
| **'LCF_B_03'** | 2,91606912 | -3,52840713 |
| **'LCF_B_04'** | 2,69815808 | -1,45642675 |
| **'LCF_B_05'** | 6,01666402 | 1,98170498 |
| **'LCF_B_06'** | 7,5102953 | 0,54785456 |
| **'LCF_B_07'** | 4,08895444 | -1,23031986 |

| | | |
|---|---|---|
| **'LCF_B_08'** | 6,01830557 | -2,27080495 |
| **'LCF_B_09'** | 3,50563542 | -6,35061115 |
| **'LCF_B_10'** | 6,83155464 | -1,57818907 |
| **'LCF_B_11'** | 4,65606905 | -4,88392743 |
| **'LCF_B_12'** | 4,11109899 | -2,5829912 |
| **'LCF_B_13'** | 4,97047973 | 1,78302699 |
| **'LCF_B_14'** | 6,47733942 | 1,22987592 |
| **'LCF_B_15'** | 1,93110847 | -2,88584587 |
| **'LCF_B_16'** | 8,41036568 | 0,76648411 |
| **'LCF_B_17'** | 2,97438573 | 1,32145905 |
| **'LCF_B_18'** | 5,78174417 | -1,40587512 |
| **'LCF_B_19'** | 5,07776039 | -4,06561351 |
| **'LCF_B_20'** | 1,86179999 | -2,31794971 |
| **'LCF_B_21'** | 7,30576916 | -2,77079756 |
| **'LCF_CA_03'** | 0,92532562 | -4,37045 |
| **'NIR_CA_01_H'** | -113,885057 | -113,885057 |
| **'NIR_CA_01_V'** | -118,933472 | -118,933472 |
| **'LCF_C_01'** | 4,73638914 | -2,06944624 |
| **'LCF_C_02'** | 7,66286403 | 0,69435924 |
| **'LCF_C_03'** | 4,37193584 | -3,36906958 |
| **'LCF_C_04'** | 4,43295046 | -3,1892321 |
| **'LCF_C_05'** | 5,17463941 | -1,77412103 |
| **'LCF_C_06'** | 5,4543066 | -0,80489104 |
| **'LCF_C_07'** | 7,30343721 | -1,12203628 |
| **'LCF_C_08'** | 6,15713638 | -0,14583037 |
| **'LCF_C_09'** | 7,20763459 | -1,95865481 |
| **'LCF_C_10'** | 10,4130872 | 2,30568131 |
| **'LCF_C_11'** | 5,58055217 | -4,41212747 |
| **'LCF_C_12'** | 4,48892425 | -2,22901366 |
| **'LCF_C_13'** | 7,67807184 | 1,28585759 |
| **'LCF_C_14'** | 5,91148485 | -1,04343995 |
| **'LCF_C_15'** | 12,8812066 | 1,86847413 |
| **'LCF_C_16'** | 5,51581712 | -4,23221859 |
| **'LCF_C_17'** | 5,8490049 | -2,12674608 |
| **'LCF_C_18'** | 4,04987668 | -3,00083585 |
| **'LCF_C_19'** | 7,43479813 | -0,56104745 |
| **'LCF_C_20'** | 5,06257038 | -0,23264165 |
| **'LCF_C_21'** | 7,46790555 | -2,35167878 |

*Table 4.3 Re-processed inter-element phases*

## 4.2 Impact of visibility errors on SMOS SLL performance

SMOS moderate Side Lobe Level (SLL) is caused by the limited coverage of the measured visibility samples in the frequency domain. It is responsible for non-negligible radiometric errors at pixels placed close to large brightness temperature transitions (e.g. coastline, ice-sea border, RFI, sun reflection, etc.). In order to mitigate this effect the visibility samples are tapered by means of a Blackman window before the image inversion procedure is undertaken. However, the theoretical SLL performance of such a specific taper is degraded by residual visibility calibration errors. Simulations performed in this work show that SLL performance is very sensitive to calibration errors and that the SLL performance of the rectangular window cannot be improved to a large extend, even in the case that calibration errors are constrained by very stringent requirements. The result of the simulations have been confirmed by SMOS images showing that measured side lobe levels (SLL) of SMOS system response is lower than expected, thus producing undesired effects that degrade the quality of the retrieved geophysical parameters. The two main effects that are observed in the measurements are:

- Longer and larger tails due to RFI or sun response
- Land contamination into the Ocean at a large distance from the coast

This work has been undertaken in the frame of the project "CCN-1 Super MIRAS Study" [UPC team] and is devoted to assess the impact of calibration errors into SMOS side lobes. The main objective is assessing the impact of different calibration errors on SMOS Side Lobe Level performance. That is, to identify the most probable origin of the degradation of SMOS SLL with relation to the theoretical expected performance. The assessment is done by adding different types of errors to an ideal point source visibility set of samples.

The following errors are taken into account in this study:

- Visibility Amplitude errors
    - Separable
    - Non-separable
- Visibility Phase errors
    - Separable
    - Non-separable
- Voltage Antenna pattern errors
    - Amplitude
    - Phase
- Antenna position erros
    - In-plane
    - Off-plane

Figure 4.21 shows the references for the two kinds of analysis performed:

- **Measurement:** A Caribbean RFI image is used to measure the SLL of the instrument.
- **Simulation:** An ideal point source response is generated in order to add different kind of errors and try to reproduce SMOS behavior as yield by the Caribbean RFI.

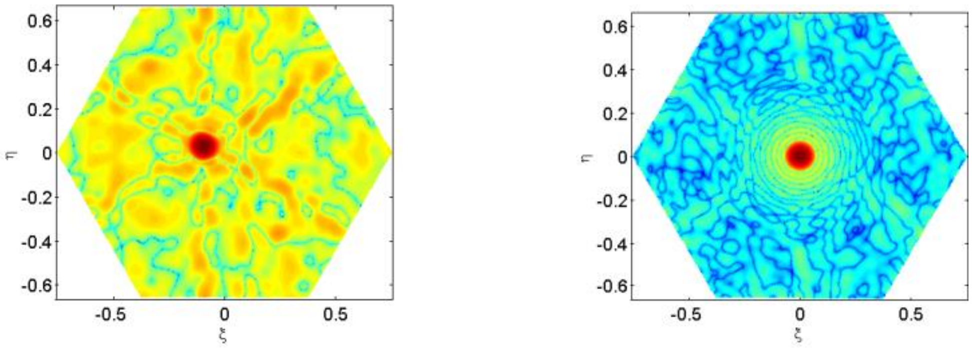

*Figure 4.21 Measured Caribbean RFI image (left) and ideal point source generated by simulation (right)*

An attempt to improve SMOS SLL performance, at the cost of poorer spatial resolution, was undertaken by using the so-called circular window [Corbella *et al.*, 2012c]. In this approach only samples inside a circular area delimited into the so called inner hexagon, that was taken into account in the inversion (see Figure 4.23).

### 4.2.1 Windowing and theoretical Point Source Response (PSR)

SMOS uses a Blackman window in order to improve SLL performance. However, the STAR shape sampled u-v domain, which not covers the full fundamental hexagonal domain, degrades the theoretical Blackman SLL performance Figure 4.22 shows an ideal (error free) point source image that has been recovered by using copolar G-matrix inversion from an ideal point source (blackman+circular window):

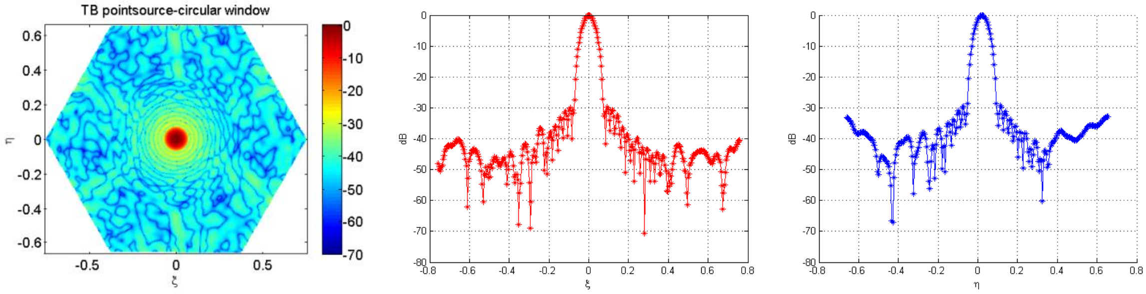

*Figure 4.22 Recovered ideal point source image (left), SLL ξ (middle) and SLL η (right)*

In this case, once the Blackman window has been scaled to this smaller domain, the theoretical performance gives the expected Blackman SLL performance. However, when the technique is applied to SMOS measured data, the performance appears to be much degraded, and side lobes are much larger than theoretically expected.

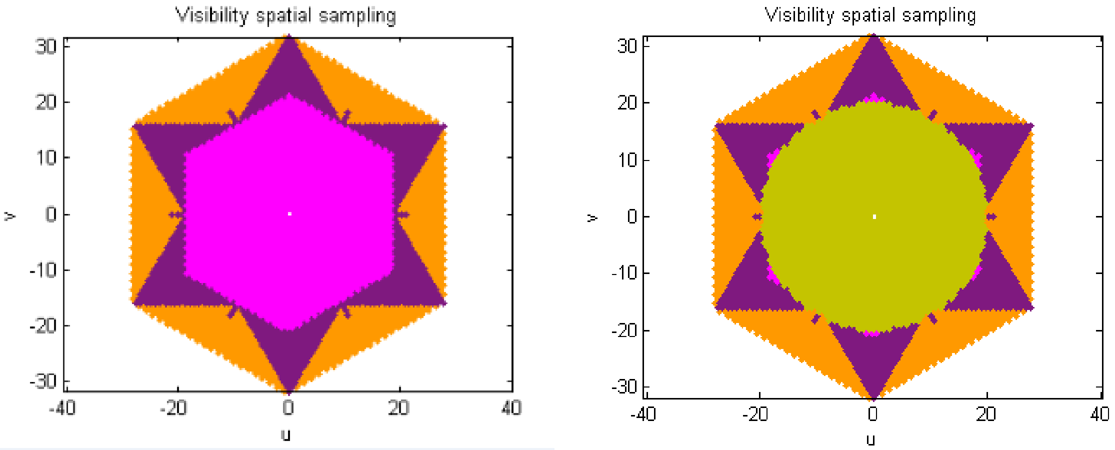

*Figure 4.23 Left: Visibility spatial sampling measured in the star u-v domain (violet), fundamental hexagon (orange) and inner hexagon (magenta). Right: Visibility spatial sampling measured in the star u-v domain including circular window (gold)*

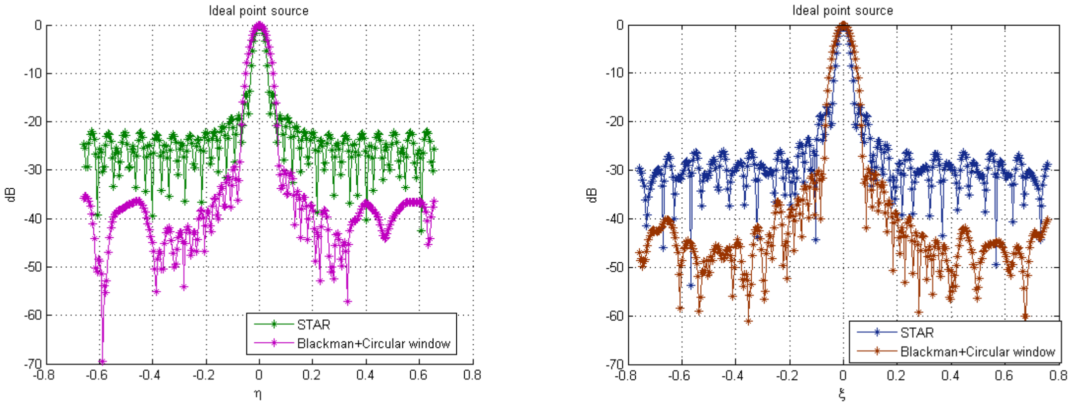

*Figure 4.24 Ideal Point Source star vs Circular window η (left) and ξ (right)*

| | *SLL off-boresight (dB)* | *HPBW (rad)* | *HPBW (deg)* |
|---|---|---|---|
| ***STAR +Blackman (ξ plane)*** | -26 | 0,03886 | 2,22 |
| ***Blackman+Circular (ξ plane)*** | -40 | 0,05986 | 3,42 |
| ***STAR+ Blackman (η plane)*** | -22,7 | 0,03966 | 2,27 |
| ***Blackman+Circular (η plane)*** | -36,5 | 0,05966 | 3,41 |

*Table 4.4 Antenna parameters*

The real SMOS response is tested by means of an isolated point source (PS). The best candidate that has been found is an isolated RFI source at the Caribbean Sea measured on 12th February 2010. The PS response is estimated from the mean by subtracting the visibility corresponding to a Fresnel model of the ocean from measured visibilities.

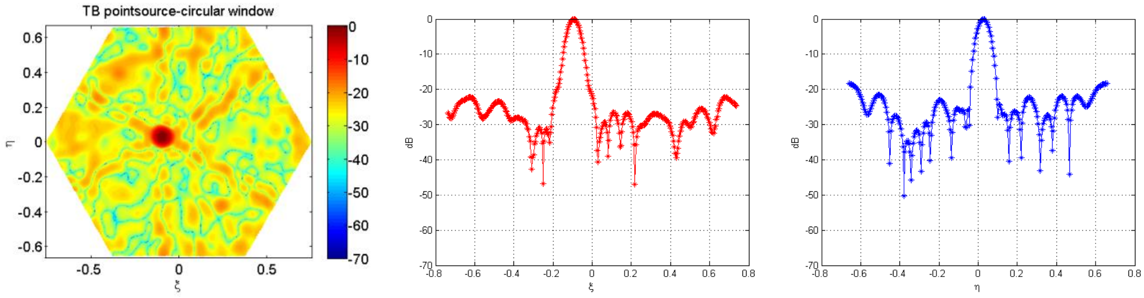

*Figure 4.25 Caribbean RFI (left), η=0 (middle) and ξ =0 (right)*

### 4.2.2 SMOS reference image: The Caribbean RFI

The aim of this section is to assess the real side lobes level of the instrument by means of an image in the Ocean that contains an RFI, possibly from a ship, measured on 12th February 2010 (Figure 4.26).

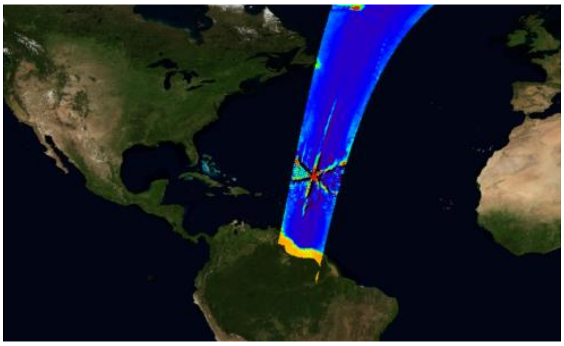

*Figure 4.26 SMOS  Caribbean RFI image*

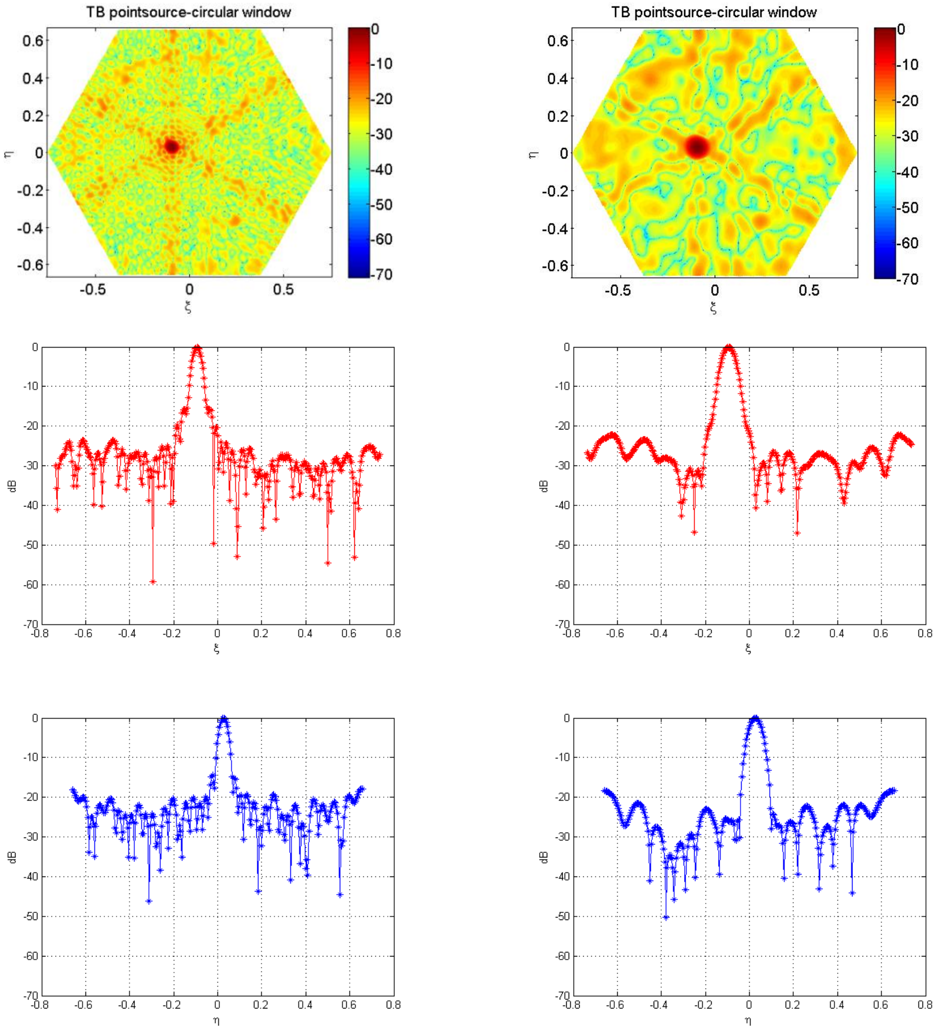

*Figure 4.27 Recovered Caribbean RFI image Blackman+circular window in dB units (top left), recovered Caribbean RFI image blackman+circular window in dB units (top right), SLL Blackman ξ (middle left), SLL blackman+circular window ξ (middle right), SLL Blackman η (bottom left) and SLL blackman+circular window η (bottom right). Note that all the figures are computed using co-polar G-matrix inversion*

In Figure 4.27 it is found that the off-boresight SLL is around 22 dB in the Blackman+circular case.

In the following sections different errors will be added to these ideal point source visibilities samples trying to find what are the main error sources that appear in the real measurements.

### 4.2.3 Impact of simulated errors on SLL

This section is devoted to assess the impact of calibration errors on SMOS SLL performance. In order to identify the dominant source of the error that produces the SLL performance shown in the Caribbean RFI image, the impact of errors is assessed for two points of view:

1. Expected SLL performance given by residual calibration errors as quoted in the Error Budget table ("Analysis of Instrument Requirements"). XMIR-UPC-DD-1B ver 1.0 and “Error budget map to SRD (PRS)”. SO-TN-UPC-PLM-0007 v7.3. March 29th 2007).
2. Required error to theoretically produce the SLL form in the RFI image -22 dB

Since the truncation effect of the star u-v domain already degrades Blackman performance, and probably as a dominant effect over calibration errors, in this assessment, in all cases, the Blackman circular window is used in the simulation.

#### 4.2.3.1 Visibility amplitude errors

The following equations are applied to introduce random amplitude errors to the visibility samples. There are two possible cases: separable where a random error is directly applied to the receivers (4.4) and non-separable where the random error is applied to the baselines (4.5):

$$V_{kj}^{'} = V_{kj}(1+\frac{\Delta_k}{100\cdot\sqrt{2}})(1+\frac{\Delta_j}{100\cdot\sqrt{2}}) \tag{4. 4}$$

$$V_{kj}^{'} = V_{kj}(1+\frac{\Delta_{kj}}{100}) \tag{4. 5}$$

where:

$V_{kj}^{'}$: Visibility with amplitude errors

$V_{kj}$: Ideal visibility

$\Delta_k$: Separable amplitude error in receiver $k$ (%)

$\Delta_j$: Separable amplitude error in receiver $j$ (%)

$\Delta_{kj}$: Non-separable amplitude error in pair $kj$ (%)

Figure 4.28 shows the recovered theoretical PS after applying different amplitude errors in the calibrated visibility (separable and non-separable case).

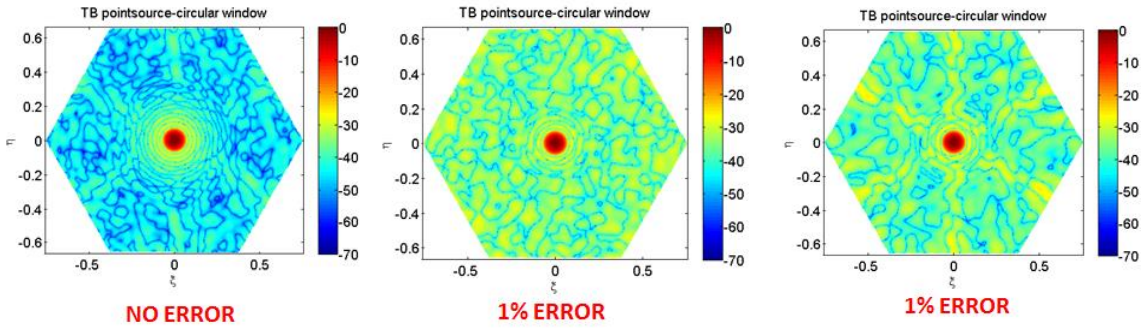

*Figure 4.28 Recovered theoretical PS applying different amplitude errors to visibility (Separable and non-separable case) dB units*

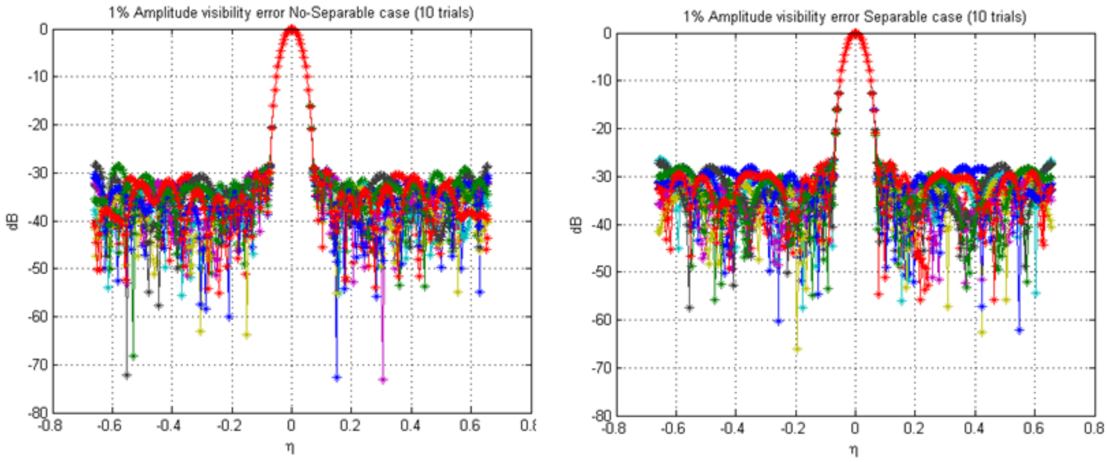

*Figure 4.29 SLL Ideal point source 1% amplitude error non-separable case (left) and separable case (right) 10 trials*

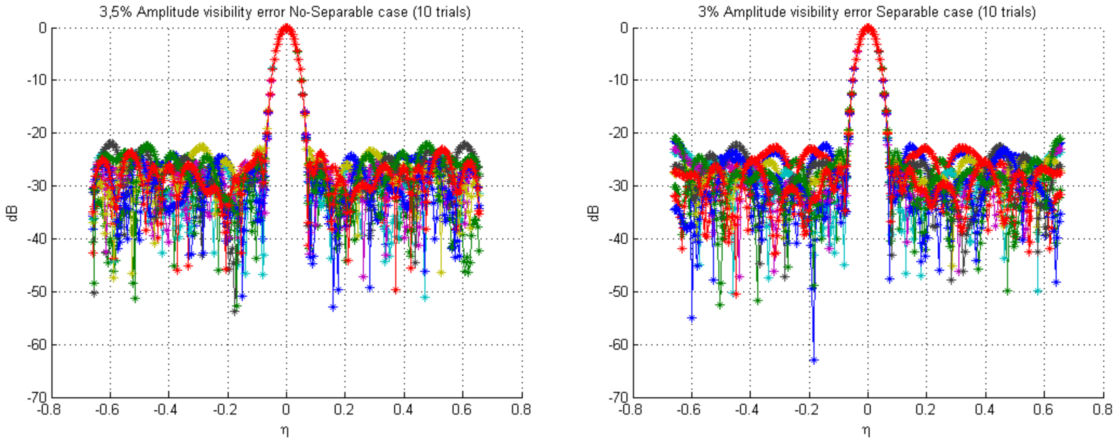

*Figure 4.30 SLL Ideal point source 3,5% amplitude error non-separable case (left) and 3% amplitude error separable case (right) 10 trials*

Figure 4.29 shows that 1% amplitude error achieves -30 dB both in the separable and non-separable case. In order to achieve -22 dB SLL amplitude errors must raise to 3,5% in the non-separable case and 3% in the separable case. These figures are much larger than expected residual calibration error and thus discarded as the source of SLL degradation in SMOS images.

#### 4.2.3.2 Visibility phase errors

Equation (4.6) and (4.7) are applied to introduce random phase errors to the visibility, there are two possible cases: separable error (a random error is directly applied to each receiver in the baseline) and non-separable errors (the error is applied to the baselines).

$$V_{kj}^{'} = V_{kj} e^{j\left(\frac{\phi_k - \phi_j}{\sqrt{2}}\right)} \tag{4. 6}$$

$$V_{kj}^{'} = V_{kj} e^{j\phi_{kj}} \tag{4. 7}$$

where:

$V_{kj}^{'}$ : Visibility with phase errors

$V_{kj}$ : Ideal visibility

$\phi_k$ : Separable phase error in receiver *k* (rad)

$\phi_j$ : Separable phase error in receiver *j* (rad)

$\phi_{kj}$ : Non-separable phase error in pair *kj* (rad)

In these simulations the error is always referred to visibility error. Therefore, the phase error added in the separable case to each receiver is divided by $\sqrt{2}$ as it is shown in (4.6). Figure 4.31 shows the recovered theoretical PS after applying different phase errors in the calibrated visibility (separable and non-separable case).

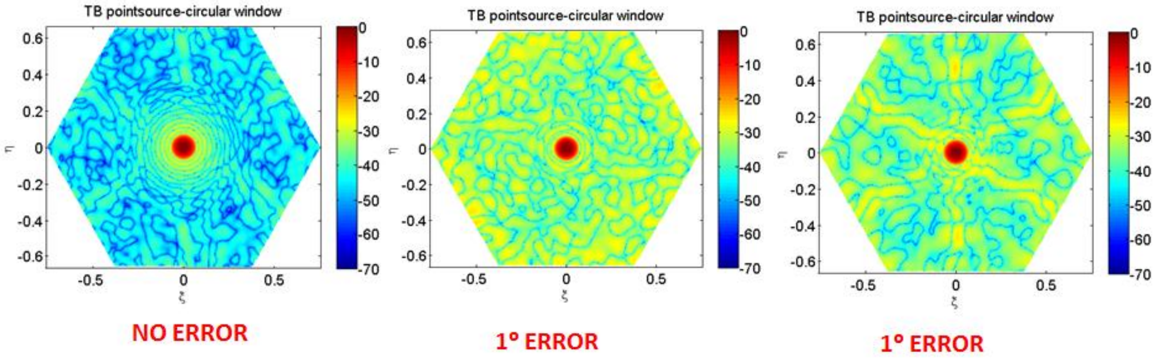

*Figure 4.31 Recovered theoretical PS applying different phase errors to the visibility samples (separable and non-separable case) dB units*

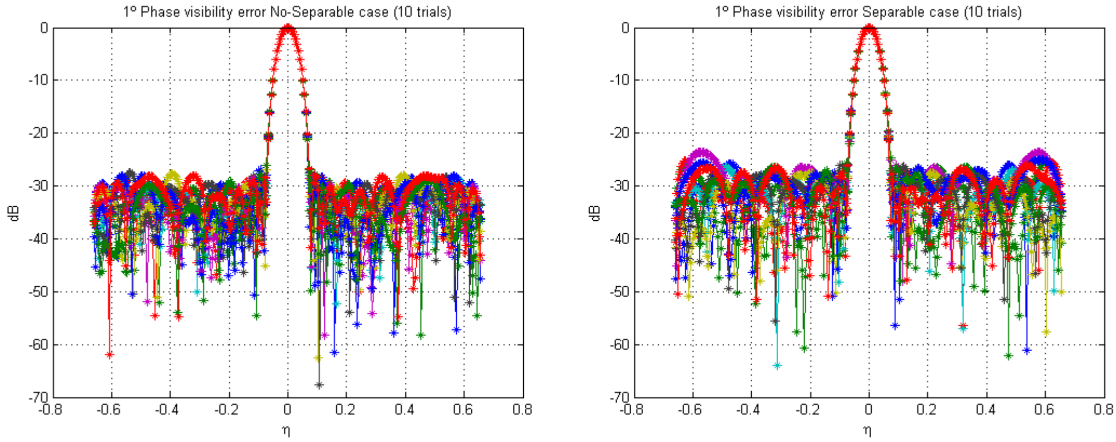

*Figure 4.32 SLL Ideal point source: 1º phase error no-separable case (left) and separable case (right) 10 trials*

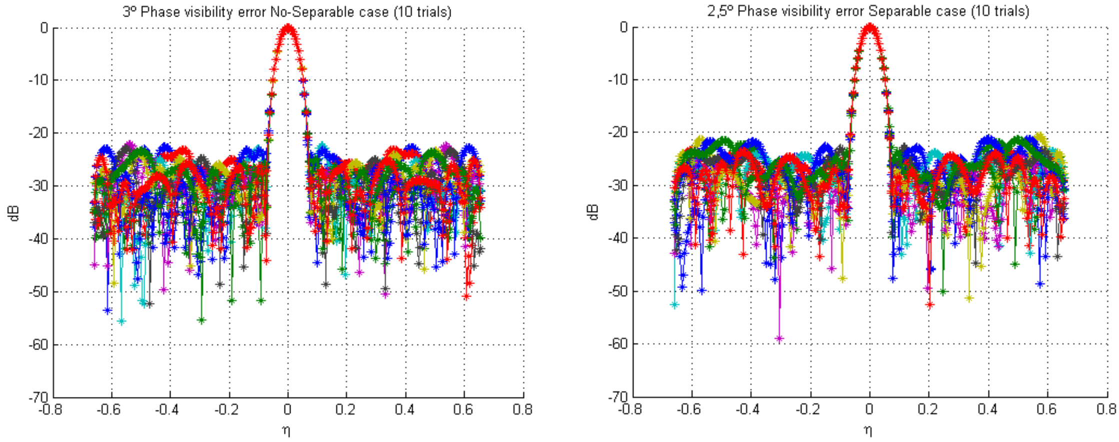

*Figure 4.33 SLL Ideal point source: 3º amplitude error no-separable case (left) and 2,5º amplitude error separable case (right) 10 trials*

Figure 4.32 shows that it is necessary to add 1º phase error to the visibility samples to achieve a -28 dB SLL in the non-separable case and -25 dB in the separable case. Figure 4.33 shows the same plots but now adding 3º phase error in the non-separable case and 2,5º in the separable case in order to reach -22 dB side lobes level (Caribbean RFI level). Clearly, phase errors resulted to have a larger impact on SLL than amplitude errors.

### 4.2.3.3 Antenna pattern errors

In this section different antenna pattern errors are added to the nominal one to assess what is the impact that these kind of errors have in the image. There are two possible cases: amplitude and phase voltage antenna errors.

The error used in the simulations is a random phase ripple as described in the following equations:

$$\Delta F_{nk}(\xi,\eta)=\Delta\phi_{nk}(\xi,\eta)=A_k\cos(16\pi\sqrt{\xi^2+\eta^2}+\phi_k)-A_k\cos(\phi_k) \tag{4. 8}$$

$$F'_{nk}(\xi,\eta)=F_{nk}(\xi,\eta)[1+\Delta F_{nk}(\xi,\eta)] \tag{4. 9}$$

$$F'_{nk}(\xi,\eta)=F_{nk}(\xi,\eta)e^{j\Delta\phi_k(\xi,\eta)} \tag{4. 10}$$

$F'_{nk}$ : Antenna pattern with errors

$F_{nk}$ : Ideal antenna patterns

$\Delta F_{nk}$ : Voltage amplitude and phase errors

$A_k$ : Amplitude ripple

$\phi_k$ : Random displacement in $(\xi,\eta)$ in order to randomize the phase ripple origin

Note that in these equations boresight error has been forced to be zero ($\Delta F_{nk}(0,0)=0$) since the antenna patterns are relative to boresight (0 dB and 0º).

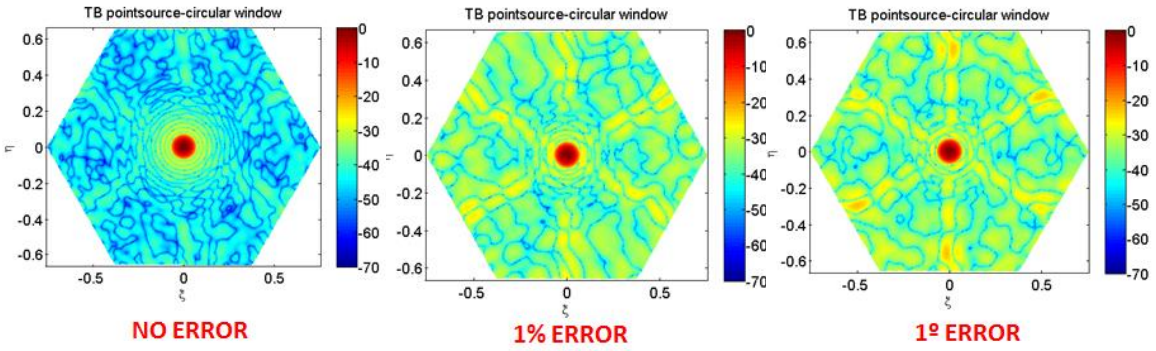

*Figure 4.34 Recovered ideal point source applying different voltage random amplitude/phase antenna pattern errors (dB)*

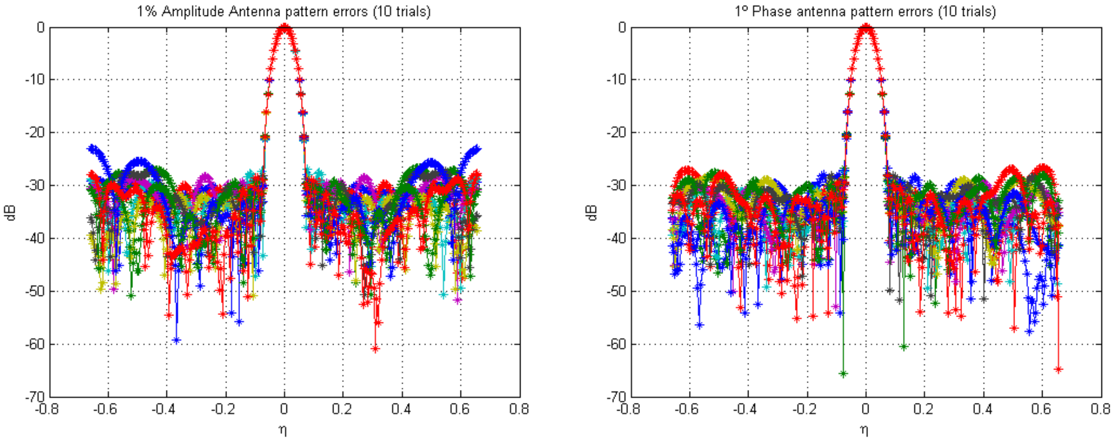

*Figure 4.35 SLL Ideal point source 1% amplitude antenna pattern error (left) and 1º phase antenna pattern error (right) 10 trials*

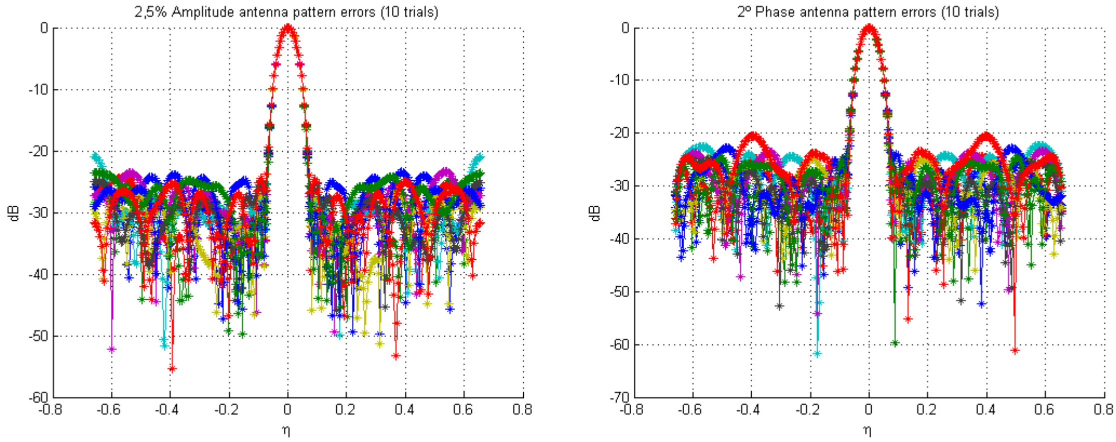

*Figure 4.36 SLL Ideal point source 2,5% amplitude antenna pattern error (left) and 2º phase antenna pattern error (right) 10 trials*

Figure 4.35 shows that in order to achieve -30 dB SLL it is necessary to have 1% amplitude or 1º phase antenna pattern error. Figure 4.36 shows the same plots but now adding 2,5% amplitude antenna pattern error in one case and 2º phase antenna pattern error in the other case to achieve -22 dB SLL (Caribbean RFI level).

These results show that the error required to achieve the Caribbean SLL is significantly larger than expected (value stated in the error budget table). Again, phase antenna pattern errors have more impact than amplitude errors.

### 4.2.3.4 In-plane antenna position errors

The objective of this section is to analyze the impact of array distortion. In the case of in-plane distortion, one arm is slightly rotated and the antenna positions are increasingly shifted from their nominal position along the arm. Equation (4.11) and (4.12) are applied to introduce in-plane antenna position errors.

Note that in this case the point source is shifted to the right because when it is located in the center of the image the error does not have any impact.

The following equations describe the rotation of the arms:

$$Antenna\ \ position = \begin{bmatrix} \vec{r}_0 & \vec{r}_0 e^{-j\frac{2\pi}{3}} & \vec{r}_0 e^{j\frac{2\pi}{3}} \end{bmatrix} \tag{4. 11}$$

$$Antenna\ \ position(errors) = \begin{bmatrix} \vec{r}_0 e^{j\phi_{Ae}} & \vec{r}_0 e^{-j\frac{2\pi}{3}} e^{j\phi_{Be}} & \vec{r}_0 e^{j\frac{2\pi}{3}} e^{j\phi_{Ce}} \end{bmatrix} \tag{4. 12}$$

$\vec{r}_0$ : Original positions in arm A
$e^{j\phi_{Ae}}$ : Error in arm A (CCW rotation)
$e^{j\phi_{Be}}$ : Error in arm B (CW rotation)
$e^{j\phi_{Ce}}$ : Error in arm C (CCW rotation)

Figure 4.37 shows an example of 5º arm C CW rotation; the blue color shows the new position of the antennas after applying the displacement of the arm. Note that 5º is a very large error but it is useful to illustrate the process (Figure 4.37).

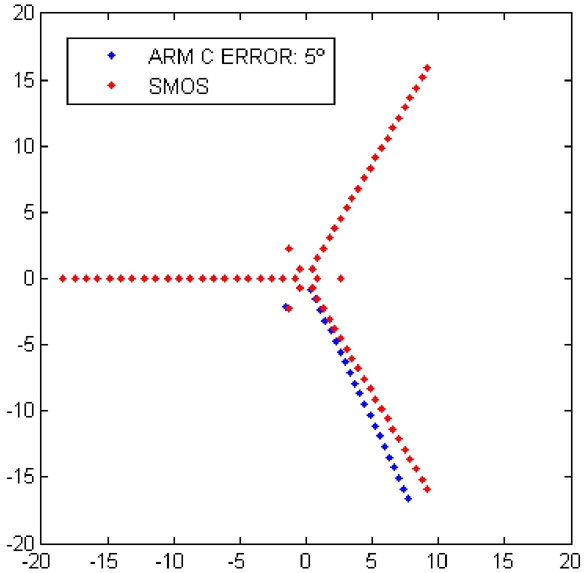

*Figure 4.37 In-plane error example (5º CW arm C rotation)*

Figure 4.38 shows the recovered ideal point source after applying different in-plane antenna position errors to arm C. Moreover, the figure shows the recovered ideal point source after applying a rotation of 3º in each arm separately. Note that in that last case the point source is located in the same coordinates that the real case (Caribbean RFI).

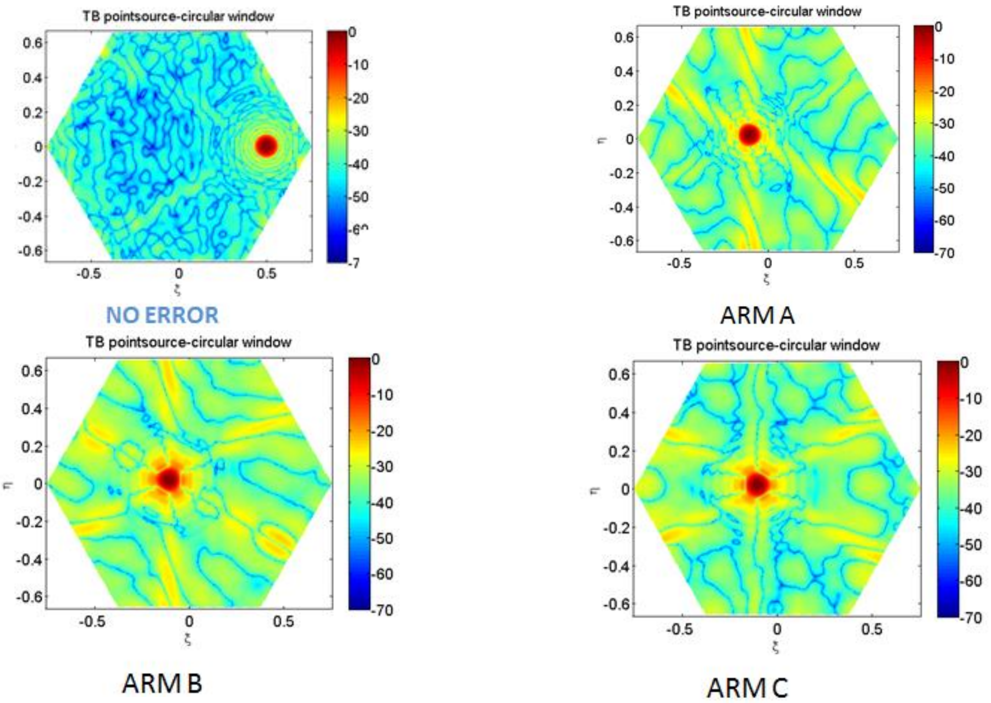

NO ERROR

ARM A

ARM B

ARM C

*Figure 4.38 Recovered ideal point source with different in-plane errors no error (top left), 3º error arm A (top right) 3º error arm B (bottom left), 3º error arm C (bottom right), dB units*

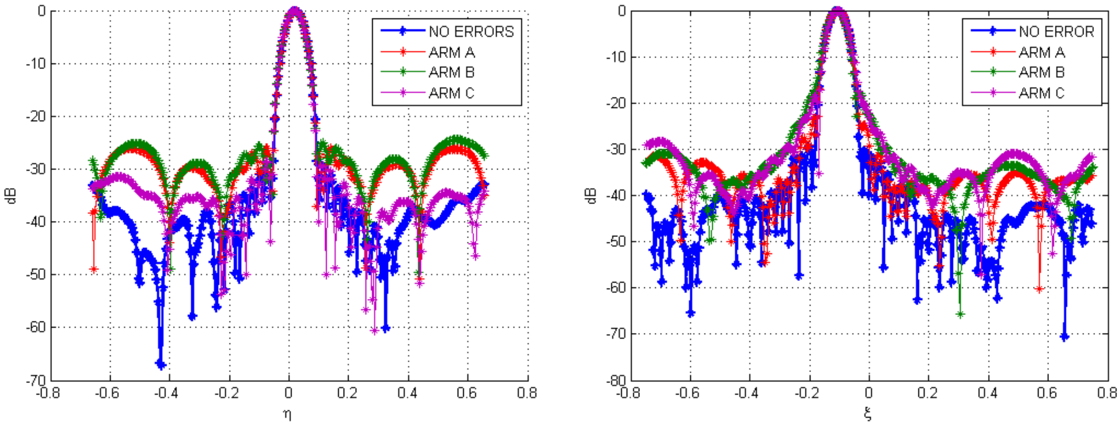

*Figure 4.39 SLL for 3º in-plane antenna position error $\xi$ =0 (left) and $\eta$=0 (right)*

After the previous assessment it is possible to conclude that the Caribbean SLL error is not coming from in-plane antenna position errors when adding a very large error (3º rotation in each arm) the level achieved is on -30 dB, far away than the real case. It can be concluded that in-plane distortion does not contribute significantly to SMOS SLL degradation.

#### 4.2.3.5 Off-plane antenna position errors

The goal of this section is to analyze the impact of off-plane position errors due to array distortion. It will be assessed if a small error in the off-plane position of the antennas over the arms (excluding hub) could cause a considerable error in the recovered image.

Figure 4.40 and Figure 4.41 show the trigonometry used to apply an off-plane error to SMOS antennas. Firstly, Figure 4.40 shows a 2-D representation and Figure 4.41 a 3-D view.

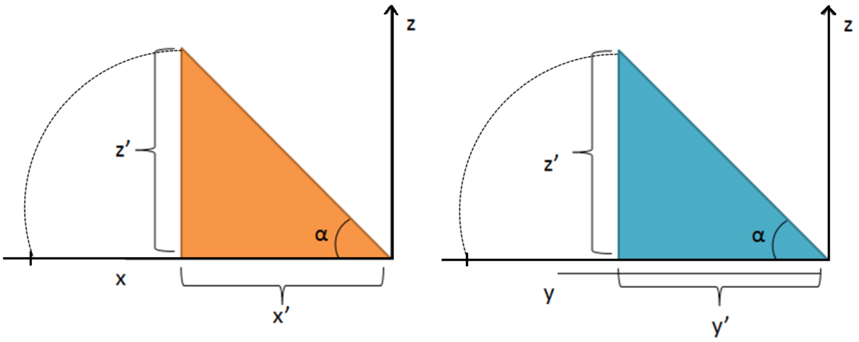

*Figure 4.40 Definitions of off-plane errors (2D case)*

$$x' = x\cos\alpha$$
$$y' = y\cos\alpha \qquad (4.\ 13)$$

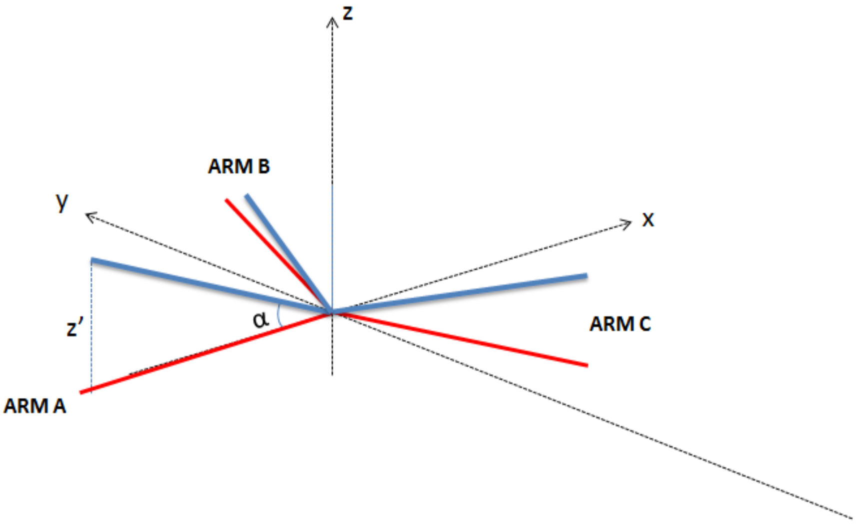

*Figure 4.41 Definitions of off-plane errors (3D case)*

$$z' = \sqrt{x^2 + y^2}\sin\alpha \tag{4. 14}$$

Figure 4.42 shows the trigonometry of how the maximum off-plane error is computed. It takes into account that a reasonable maximum phase error due to path delay can be set to 10º, as described in (4.15):

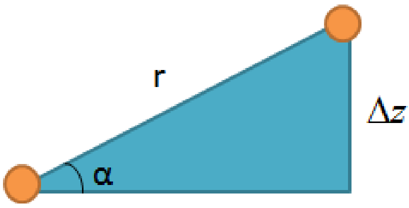

*Figure 4.42 Off-plane error definition*

$$\begin{aligned}
&\frac{\phi}{2\pi} = -\frac{\Delta z}{\lambda} \\
&\phi_{\max} = \left| -\frac{2\pi}{\lambda}\Delta z \max \right| = \left| -\frac{2\pi}{\lambda} sin(\alpha)\cdot 17d \right| \cong \left| -\frac{2\pi}{\lambda}\alpha\cdot 17d \right| \\
&\frac{2\pi}{\lambda}\alpha\cdot 17\cdot 0{,}875\lambda < 10\frac{\pi}{180} \\
&\alpha = \frac{10}{180}\frac{1}{17\cdot 0{,}875\cdot 2} = 0{,}0016 \\
&\boxed{\alpha(\deg) = 0{,}1076^{\circ} \cong 0{,}1^{\circ}}
\end{aligned} \tag{4. 15}$$

The following figures show the recovered point source when the off-plane error is increased from 0,025º to 0,1º:

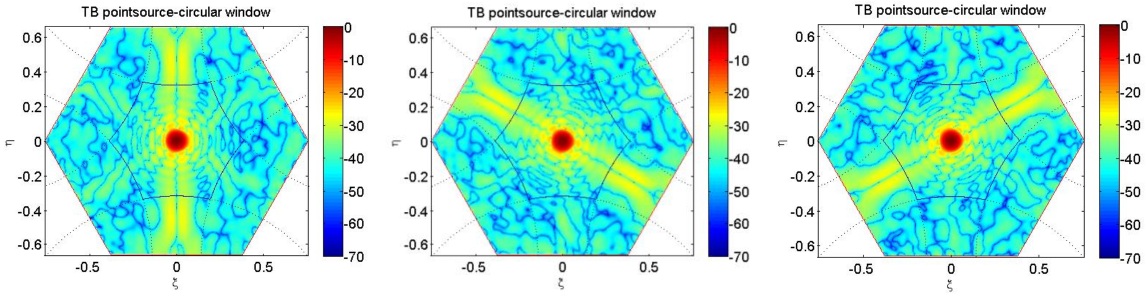

*Figure 4.43 Recovered ideal point source by adding off-plane antenna position errors 0,1º error arm A(left), arm B(middle), arm C(right), dB units*

The following plots show the SMOS sides lobes level when an off-plane is applied from 0,025º to 0,1º:

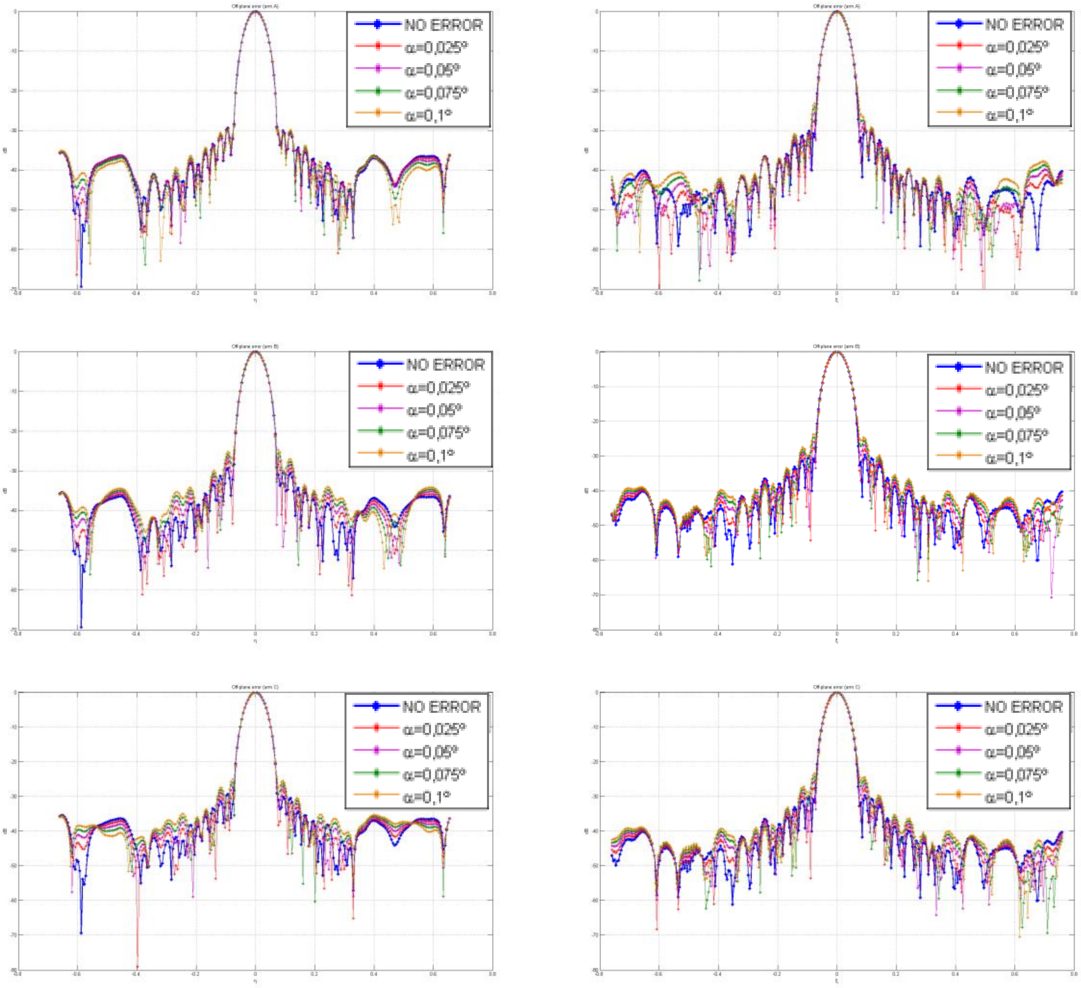

*Figure 4.44 SLL off-plane error $\xi=0$ (left) and $\eta=0$ (right) arm A (1st row), arm B (2nd row) and arm C(3rd row)*

Figure 4.45 shows the recovered point source by adding 0,1° off-plane error in arm A when η cut is shifted to the left reaching the maximum error in order to assess the new SLL.

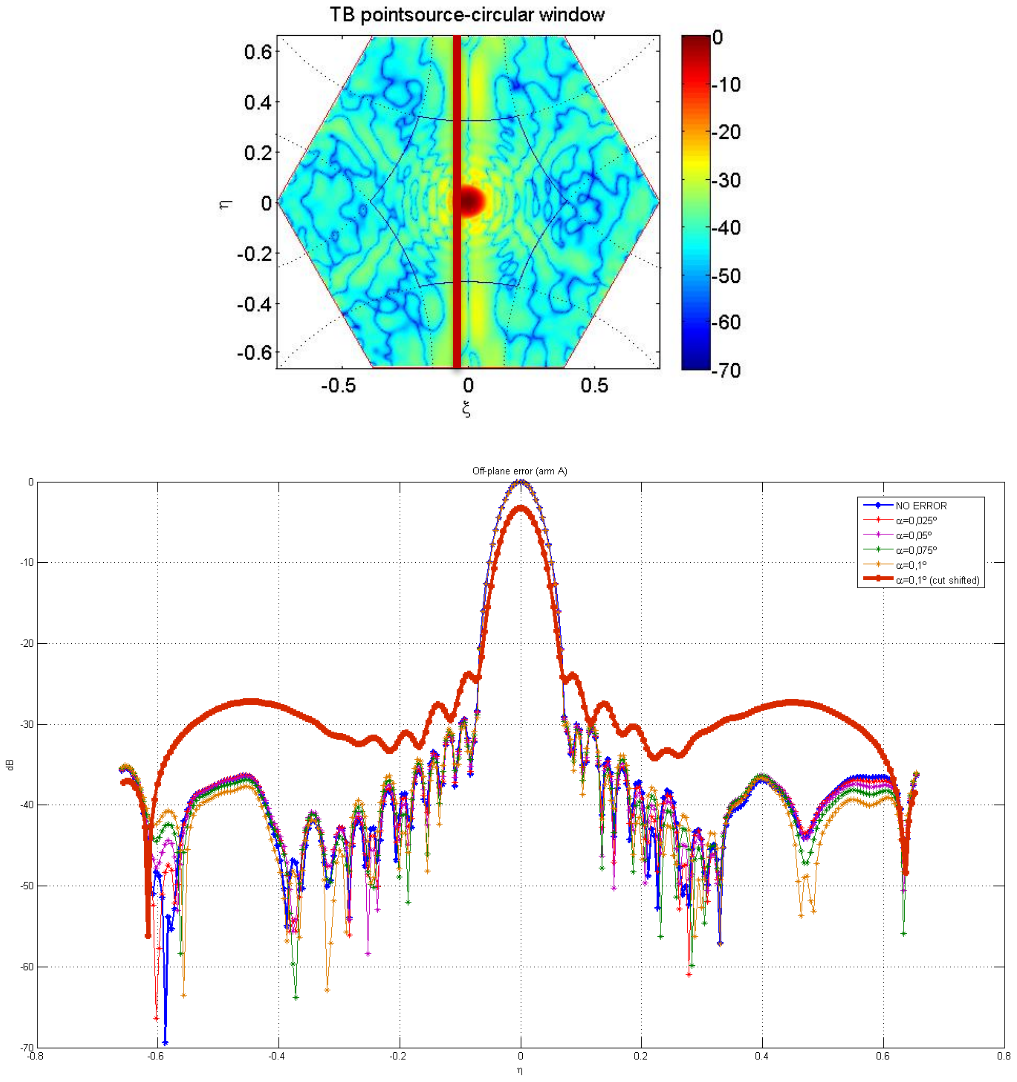

*Figure 4.45 Recovered point source with 0,1° off-plane error in arm A with a cut in η shifted to the left (top) and SLL from the same image compared to other magnitude of errors (bottom)*

The plots in this section show that the SLL is around -30 dB in the case of 0,1° off-plane antenna position error when η cut is shifted to the left in order to consider the maximum error of the image. Note that arm A, B and C have a symmetric error, so it is possible to assess it by making the cut in only one case.

As a conclusion the previous figures show that the error that appears in the real measurement (Caribbean RFI) is far away from this level so it is confirmed that it does not come from a small change in the antenna positions of the instrument.

### 4.2.4 SMOS SLL performance in full-pol

This section is devoted to show that SMOS SLL performance in dual and full-pol modes is basically the same.

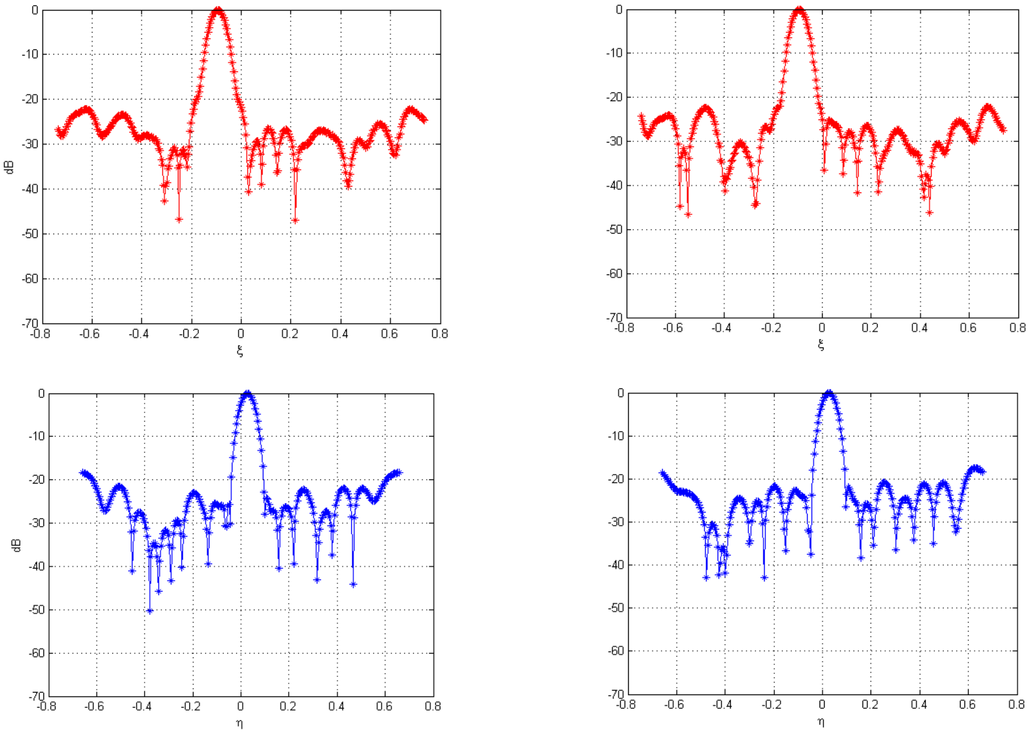

*Figure 4.46 SLL Left: Co-polar inversion Right: Full-pol inversion η=0 (top) and ξ =0 (bottom) Blackman+circular window X-pol*

All results in the previous section were analized by mean of the co-polar G-matrix inversion. In this section the Caribeean RFI image is analyzed in Full-pol. Figure 4.46 show the full-pol G-matrix inversion does not improve SMOS SLL performance in X-pol. Similar results are obtained in Y-pol. Therefore, SLL performance degradation is not related to the inversion in co-polar or full-pol G-matrix.

### 4.2.5 Conclusions

- SMOS SLL performance in dual and full-pol is very similar. In both cases, SLL Blackman performance is degraded by the star-shape u-v domain to about -22 dB. This theoretical degradation due to the limite coverage of the *(u,v)* sampling domain is the dominant source of SLL, over other sources of error (e.g. calibration errors).

- The ideal point source SLL for a Blackman taper over a circular u-v domain is about -34,5 dB in the η plane and -40 dB in the ξ plane. However, simulations show that expected residual calibration errors degrade the SLL of the circular window to about -30 dB. Therefore, there is a theoretical margin for SLL improvement at the cost of poorer angular resolution.

- However, SMOS measured SLL level for the circular window in the case of the Caribbean RFI is about -23 dB, probably due to the degradation effect of calibration errors or array distortion.

- The best candidate for the dominant error source has been found to be the separable phase errors. 1º RMS visibility separable phase errors (0.71 rms phase error in each channel) yields a theoretical SLL of about -28 dB. If 2,5º RMS visibility separable phase errors (1,7º RMS errors in each channel) are taken into account then simulated SLL degrades to 22 dB. Also, if off-plane array distortion is slightly larger than expected, this error can also be a potential source of SLL degradation.

- As a conclusion and from a practical point of view there is very low margin for SLL performance improvement, even at the cost of poorer angular resolution (e.g. circular window) due to the degradation effect of residual calibration errors (even if they are very small). Simulations show that this SLL degradation effect is particularly important for pixels at large distance of the main lobe. This work confirms the results already sketched in [Corbella *et al.*, 2012c].

- It must be pointed out that in an interferometer side lobes have consecutive positive and negative signs. Therefore, the contribution of adjacent pixels to the brightness temperature measured by the mean beam of the synthesized pattern is partially compensated (e.g. This is not the case in a real aperture radiometer the energy contribution of all side lobes to the measured pixel is always positive and their impact in radiometric accuracy is much larger than in an interferometer).

## 4.3 PMS offset improved calibration

As shown in chapter 3 the basic SMOS magnitude is the complex normalized correlation $M_{kj}$ measured out of the signals collected by any pair of antennas “k,j” in the array. Each receiver unit “k” includes a PMS (Power Measurement System) devoted to measure the system temperature at the antenna plane $T_{sysk}$. These measurements are used to denormalize SMOS complex correlations to obtain the visibility samples as:

$$V_{kj} = M_{kj} \frac{\sqrt{T_{sysk} T_{sysj}}}{G_{kj}} \tag{4. 16}$$

The PMS units are simple total power radiometers to provide an output voltage proportional to the noise power present at their input:

$$v_k = G_k T_{sysk} + v_{offk} \tag{4. 17}$$

$G_k$ is the PMS gain and $v_{offk}$ is, basically, a voltage offset added to the PMS output for signal conditioning purposes. During commissioning phase (first six months of SMOS in orbit) it was detected that SMOS heater system were introducing small and random sporadic PMS offset steps (jumps) in several units. In order to track and correct theses jumps a weekly PMS offset calibration was introduced in SMOS calibration schedule just after SMOS commissioning phase. These jumps are randomly distributed within the weekly intercalibration period and produce a measurement error until PMS offset in the affected unit is corrected by the next weekly calibration event. Figure 4.47 shows PMS jump occurrences per unit (bottom) and intercalibration periods (top) along the mission.

This section is devoted to summarize the results of the study that has been conducted to assess and mitigate the impact of this calibration error, initially started by M. Vizcarro [Vizcarro *et al.*, 2016].

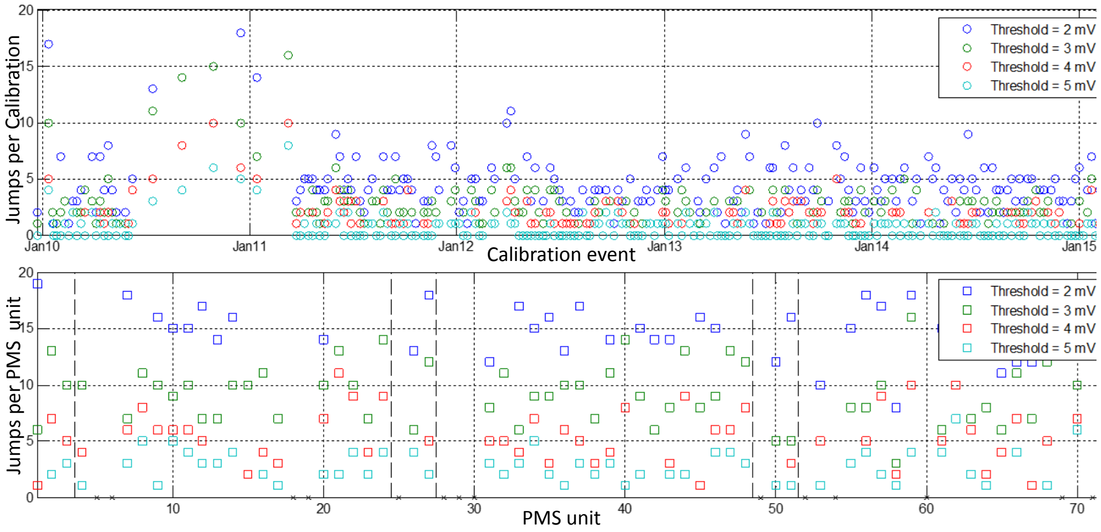

*Figure 4.47 Number of offset jumps in all PMS units per intercalibration period (top) and number of jumps in the 2010-15 period for each PMS unit (bottom)*

The offset jumps are particularly harmfull in the all-LICEF mode since can produce a significant error in the estimation of the antenna temperature (zero baseline). This effect has been mitigated to a negligible impact by the so-called “Dinamic all-LICEF”. In this up-graded approach those units that were identified to have a jump in a given weekly intercalibration period are removed from the set of LICEF units used to measure the antenna temperature. However, these jumps still impact SMOS accuracy through the visibility denormalization process. This impact is assessed in this section.

### 4.3.1 PMS offset jumps assessment

In this section an estimation of the impact of PMS offset errors on the radiometric spatial bias is undertaken. In order to do so, for each PMS unit a record of PMS offset differences between consecutive calibrations is computed. When any of these differences are larger of a given threshold (e.g. $\Delta v_{offk} > 2$ mV) it is assumed that a PMS jump has taken place at an unknown instant within the intercalibration period. Figure 4.47 shows that PMS offset jumps are relatively rare. When the set of 72 PMS units are taken into account (Figure 4.47, top), the mean number of jumps are around five per calibration event when the threshold is set to just above PMS noise level and below one for large jumps (above 5 mV). If the period 2010/15 is taken into account (Figure 4.47, bottom) the mean number of jumps per each PMS unit is around 15 for the 2 mV threshold and around 3 if the largest threshold is taken into account. Figure 4.47 also shows that the jumps distribution is quite uniform along time and units.

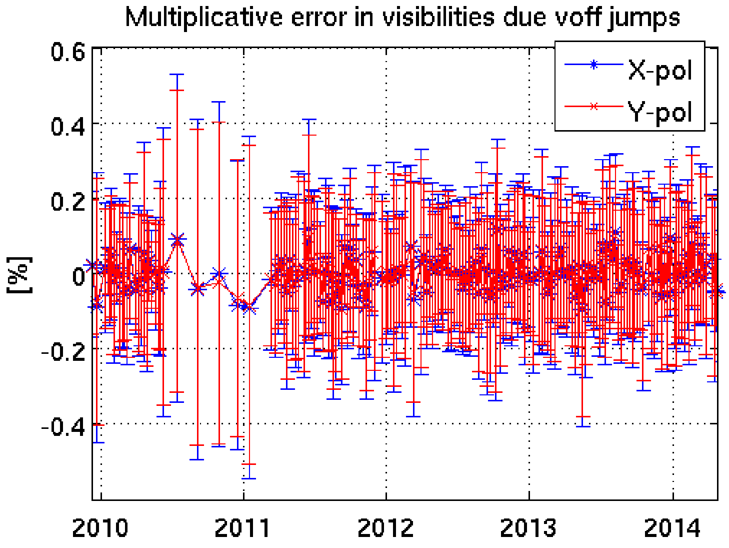

*Figure 4.48 Mean, maximum and minimum multiplicative error in the visibility samples due to PMS offset jumps for each inter-calibration period. The mean standard deviation is around 0,3%, well below the 1% specification given for amplitude errors*

### 4.3.2 Estimation of radiometric spatial error

From the instant that a jump takes place in a PMS unit until the next calibration event (when PMS offset is refreshed) system temperature measured by this PMS unit holds a multiplicative error:

$$\Delta T_{sysk} = \frac{\Delta v_{offk}}{G_k} \tag{4. 18}$$

Now, the error in system temperature translates into a visibility multiplicative error through the denormalization process. In this way, those measured visibility samples affected by a jump can be written as a function of their ideal value as:

$$\hat{V}_{kj} = V_{kj}\sqrt{\left(1+\frac{\Delta T_{sysk}}{T_{sysk}}\right)\left(1+\frac{\Delta T_{sysj}}{T_{sysj}}\right)} \tag{4. 19}$$

This equation can be used to translate into visibility multiplicative errors the set of PMS offset jumps detected in each intercalibration period. Figure 4.48 shows the mean, minimum and maximum visibility multiplicative error for each intercalibration period. Figure 4.48 clearly shows that the weekly PMS calibration starts around March 2011, the commission phase in the first semester of 2010, and the second half of 2010 when only monthly calibrations are available. The mean standard deviation for the multiplicative error along the 2010/15 period is about 0,3%, well below the 1% requirement stablished for this parameter. Figure 4.49 shows a typical example of a multiplicative error distribution in the sampling domain (SMOS u-v star). Any error in one particular PMS unit translate to all baselines that include such unit, yielding clear patterns in the error distribution. To assess the impact of the error distribution given in Figure 4.49, an end-to-end simulation can be performed for a reference image that consists of a pure ocean view (Fresnel emission model at 35 psu and 21 ºC). The error pattern is included in the simulated visibilities before image inversion to yield the radiometric spatial error distribution shown in Figure 4.50. As predicted, on average, the impact of PMS offset jumps on radiometric spatial error is very low (standard deviation below 0,1 K). Moreover, over the ocean, this systematic error is removed by the frequent OTTs (Ocean Target Transformation), a kind of differential imaging [Font *et al.,* 2010]. However, since PMS jumps may produce sporadic non-negligible systematic bias on certain directions of SMOS field of view, a technique to mitigate the impact of this error has been developed and presented in the next section.

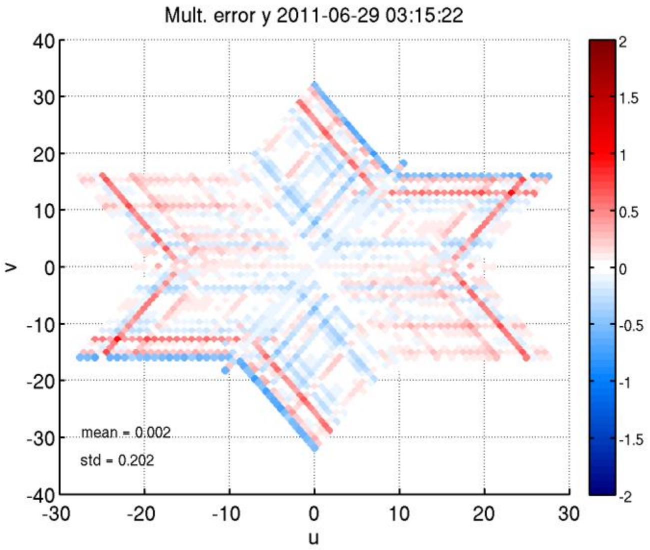

*Figure 4.49 Typical worst case multiplicative error distribution for a weekly inter-calibration period. Any error in one particular PMS unit translate to all baselines that include such unit*

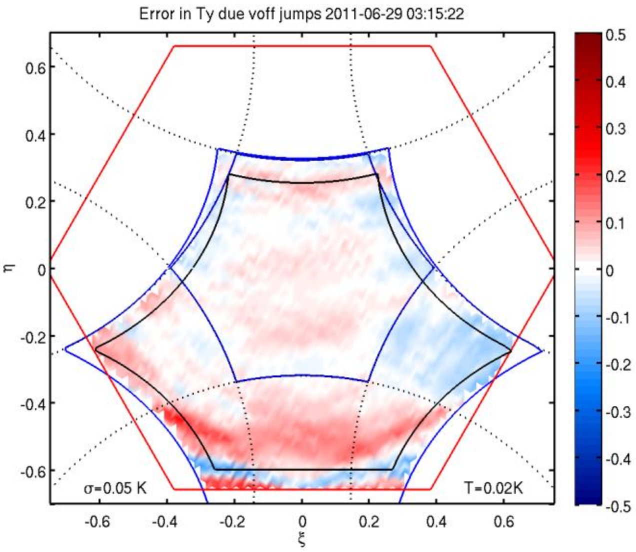

*Figure 4.50 The multiplicative visibility error distribution in Figure 4.49 translate into this radiometric error map. It must be pointed out that, when over the Ocean, this systematic radiometric error is removed by frequent OTTs (Ocean Target Transformation)[Font et al., 2010]*

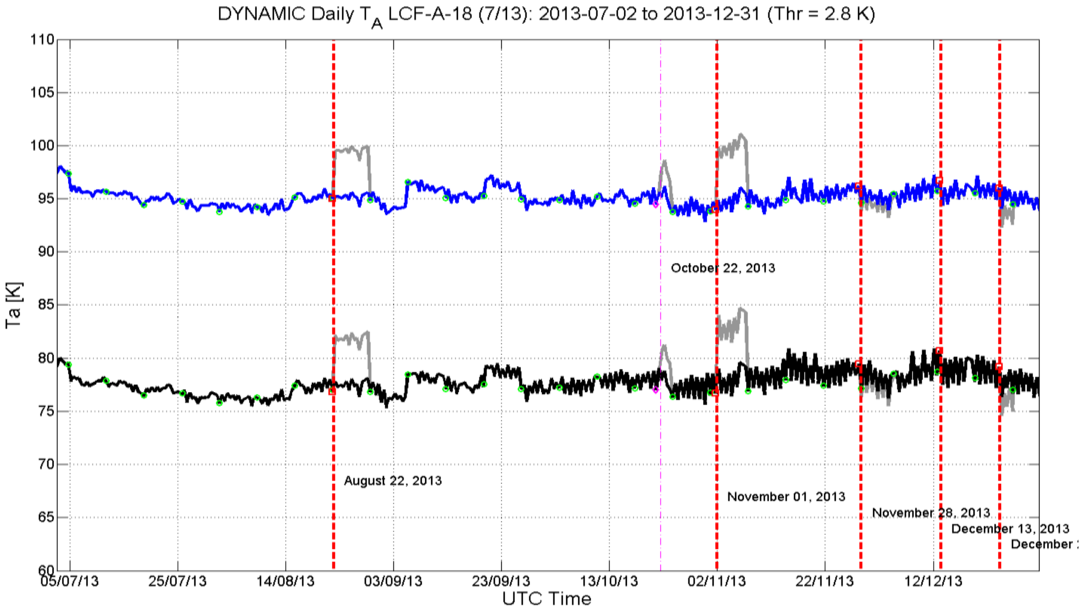

*Figure 4.51 Horizontal (black) and vertical (blue) averaged antenna temperature over the Ocean measured by LICEF unit LCF-A-18 for the 2013 second semester (typical case). The green points are time marks that show the weekly calibrations. When a jump is detected (red line) the next calibration is advanced in time to correct the PMS offset. The grey traces show the measurements before correction*

### 4.3.3 PMS Offset measurements over ocean

Since the PMS units are total power radiometers they can also be used to measure the antenna temperature by each single receiver in SMOS array as:

$$T_{Ak} = \frac{v_k - v_{offk}}{G_k} - T_{Rk} \tag{4. 20}$$

where $T_{Rk}$ is the equivalent receiver noise temperature at the antenna plane of unit “k”. This is the basis of the so-called all LICEF mode [Corbella *et al.*, 2016]. Now, an error in the calibration of PMS offset due to a jump translates into an error in the measurement of the antenna temperature of this unit given by

$$\Delta T_{Ak} = \frac{\Delta v_{offk}}{G_k} \tag{4. 21}$$

Since the antenna HPBW of each single unit in the SMOS array is very large, antenna temperature shows a slow evolution when averaged over large portion of the ocean. This allows the detection of PMS jumps over a certain threshold. Once the instant of a PMS jump is detected, it can be corrected by shifting the PMS offset calibrated in the following calibration event to that time position.

As an example, Figure 4.51 shows horizontal and vertical antenna temperature averaged over a large portion of the Pacific Ocean as given by unit LCF-A-18. Daily ascending and descending orbits give one antenna measurement every twelve hours. The green dots mark the time for PMS offset weekly calibrations while the red lines show the detection of PMS jumps over a 2,8 K threshold. In order to mitigate the impact of a jump, the offset value measured in the next calibration is applied from the instant that the jump is detected. The grey traces in Figure 4.51 represent antenna temperature measurements before applying this correction, clearly showing the impact of uncorrected PMS jumps. The 2,8 K threshold has been adopted after a careful tradeoff that maximizes jumps detection while minimizing the number of false alarms due to noise and ascending vs descending differences.

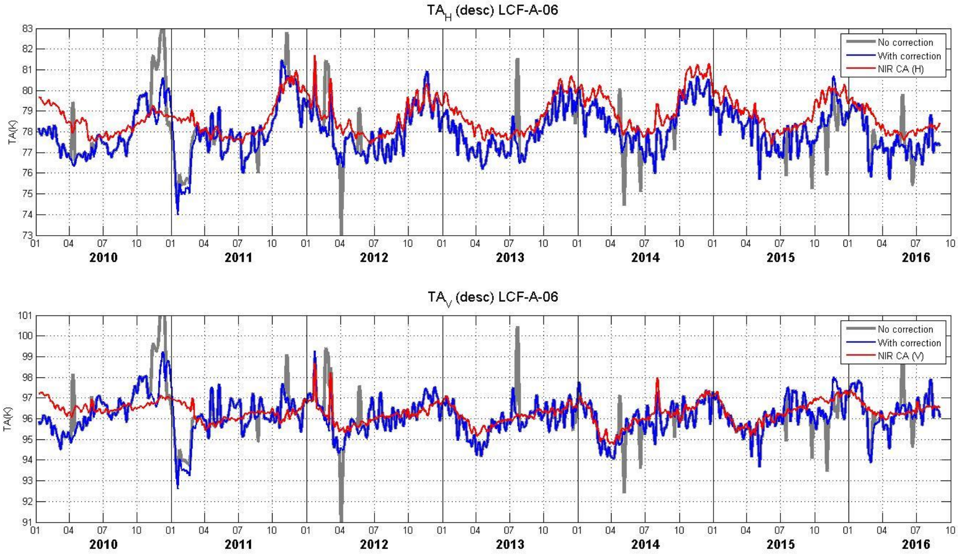

*Figure 4.52 SMOS life-time evolution of averaged antenna temperature for a large area over the Pacific Ocean regarding unit LCF-A-06 before (grey) and after (blue) PMS jump correction, compared to SMOS reference radiometer NIR-CA (red)*

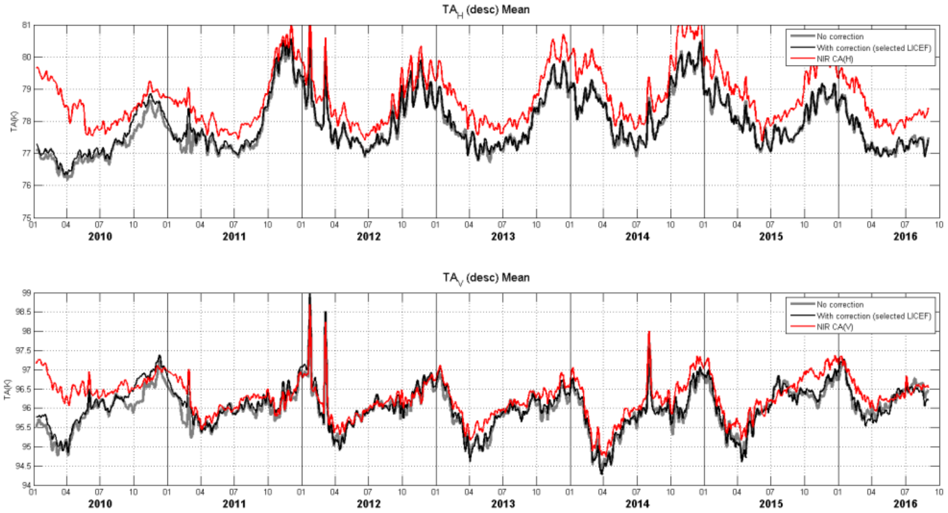

*Figure 4.53 Antenna temperature averaged for a large area over the Pacific Ocean for “all LICEF” mode before (grey) and after (black) PMS offset jump correction compared to SMOS reference radiometer NIR-CA (red)*

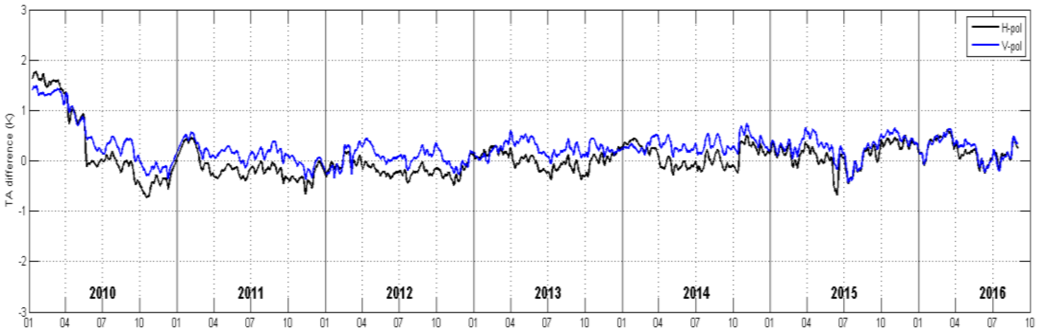

*Figure 4.54 Evolution of the difference between NIR and all LICEF mode antenna temperature (bias removed) showing a seasonal trend: in the winter period H and V show the same difference*

As an example, Figure 4.52 shows how the technique presented in this work is able to remove the larger spikes produced by PMS offset jumps in unit LCF-A-06. Figure 4.52 also shows that a single PMS unit is able to track antenna temperature as SMOS reference radiometer (NIR-CA), although with larger variability. However, Figure 4.53 shows that PMS and NIR yield a similar performance when the “all LICEF” mode is taken into account, that is, when the antenna temperature of all PMS units is averaged [Corbella *et al.*, 2016]. The fact that PMS units and NIR hold a quite independent calibration and measurement principles provides hints to further improve SMOS performance by comparison. As an example, Figure 4.54 shows the evolution of the difference between the NIR and the “all LICEF” antenna temperature (the bias has been removed). A seasonal trend is clearly shown since this difference is the same for the H/V channel in the winter period and drifts by almost half a Kelvin in the intermediate period.

### 4.3.4 Conclusions

This work summarized the main results from a study devoted to assess the impact of PMS offset jumps on SMOS radiometric performance. It has been shown that this error has a low impact at system level when SMOS operational NIR mode is taken into account. However, this correction is important if the “all LICEF” mode is considered.

In any case, a technique to mitigate the effect has been developed and successfully tested. It consists of detecting the PMS jumps by observing the evolution of antenna temperature measured by each single PMS unit when averaged over a large area of the Pacific Ocean. All these results were presented in the international congress IGARSS 2017 (Texas) [Durán *et al.*, 2017].

# 5 Improvements in SMOS modeling

After more than seven years of operation, SMOS has proven to be highly useful for a variety of scientific applications related to soil moisture over land and ocean salinity, as well as specific studies over the ice covered surfaces [Martin-Neira *et al.*, 2017].

Level 2 data is currently used by many institutes around the world to extract relevant information aimed at improving weather forecast and extreme events. This data is derived from Level 1, consisting on maps of full polarimetric brightness temperature over the earth surface. The maps computed in Level 1 are obtained by mathematical inversion of the visibility function measured by MIRAS. Different algorithms for image reconstruction were already developed before launch, but they have been refined afterwards in order to minimize artifacts and systematic errors, as detailed in chapter 6.

The research activities undertaken in the frame of this PhD thesis resulted in some significant contributions. At this point improving visibility inversion requires understanding truncation, aliasing, redundancy, antenna pattern differences and other effects in an undetermined linear system of equations. The aim of this chapter is to investigate on these image reconstruction limitations in order to eventually design an improved methodology able to further reduce the present artifacts on the SMOS images.

## 5.1 Truncation and reconstruction errors

This activity was initially performed as one of the first tasks in this PhD. It was undertaken within the framework of the “XMIRAS” project (see chapter 8). However, due to the impact of the results in the SMOS project the activity was readdressed to improve SMOS performance, in particular by means of assessing the so-called “SMOS floor error” and Gibbs 2 mitigation techniques (described in chapter 6).

As shown in chapter 2, a single snapshot image of brightness temperature is obtained by inverting the visibility equation. This visibility function is measured by MIRAS at a discrete $(u,v)$ points derived from the antenna positions. This discretized visibility equation can be written in a matrix form as:

$$V = GT \tag{5. 1}$$

where $T$ is the real brightness temperature map discretized at each $(\xi,\eta)$ grid points in the unity cercle. $G$ is the so-called “G-matrix”, a linear operator relating the measured visibility to the source brightness temperature. The reconstructed measured brightness temperature $\hat{T}$ is computed by means of the Moore-Penrose pseudo-inverse of $G$. This yields an undetermined system of equation when $G$ is not square as is the case in SMOS [Corbella *et al.*, 2014]:

$$V = GT \rightarrow \hat{T} = G^{-1}V \tag{5. 2}$$

In addition, in the SMOS instrument the G-matrix in the left and right equations above are not identical due to the differences between the actual on-flight antenna patterns and the ones measured on ground. Although this is one of the causes of the reconstruction error in $\hat{T}$, it is not the only one. Even with perfect knowledge of antenna patterns, there is still a residual reconstruction error. It is called “floor error”, defined as the reconstruction error for an error free (no instrumental errors) system.

The floor error can be estimated by a complete forward-backward simulation of a known scene, where the original brightness temperature is not perfectly recovered. There is floor error when $\hat{T} - T \neq 0$. The floor error is a scene dependent image reconstruction error given by:

$$\hat{T} - T = (G^{-1}G - 1)T \tag{5. 3}$$

From a mathematical point of view this is explained by the fact that the problem is under-determined and the solution is not unique. From the point of view of image processing, the result is explained by truncation and aliasing effects.

However, one of the most unexpected features is that differences are observed also in the alias-free field of view, where in principle the problem should be well behaved. In an ideal case when all the antenna patterns are identical and the fringe-washing function can be neglected, the G-matrix becomes a discrete Fourier operator. However, in the following sections it will be shown that for a real case the G-matrix properties do not fully follow the properties of a discrete Fourier inversion.

## 5.2 Impact of antenna pattern differences

The goal of this task is to assess SMOS pixel bias in the EAF-FoV in different scenarios:

- Minimum error due to reconstruction error
- Impact of antenna pattern differences

As reference image, the simulations use the Fresnel model of the Ocean, as seen from the sensor, in order to have a better insight into the impact of antenna errors. Figure 5.1 shows the Fresnel image that has been used as a reference for the forward/backward computation of the brightness temperature. For the sake of simplification in this simulations only co-polar G-matrix inversion is taken into account.

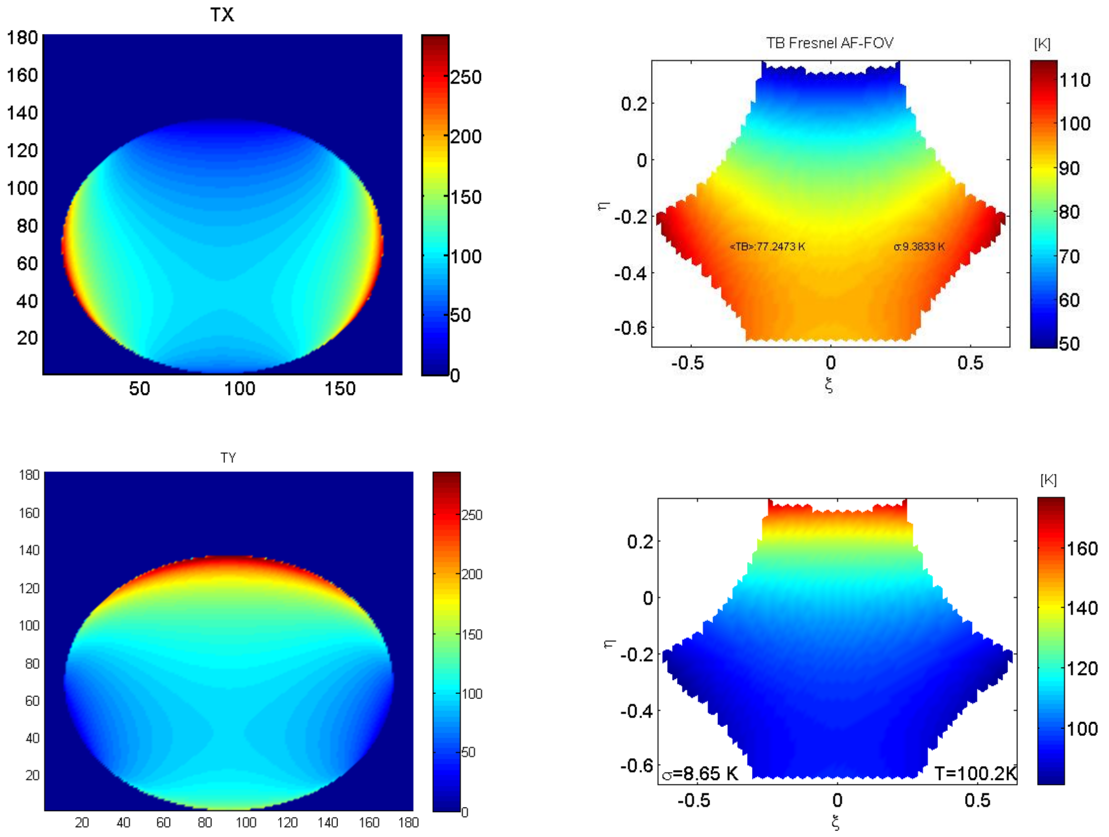

*Figure 5.1 Fresnel reference in the UC (left) and Fresnel reference in the EAF-FOV (right) X-pol case (top) and Y-pol case (bottom)*

The images in the left of Figure 5.1 are used to simulate the measured dual-pol visibility samples as $V = GT$. The plots in the right of Figure 5.1 simulate the real brightness temperature as seen from SMOS, $T(\xi,\eta)$, and are used to simulate the errors in the retrieved image (simulated ground truth).

### 5.2.1 Estimation of SMOS floor error

The first analysis is performed by using the nominal SMOS antenna patterns measured on ground in order to estimate SMOS floor error as:

$$\Delta T_{FE} = \hat{T} - T \tag{5. 4}$$

where $T$ is a Fresnel reference brightness temperature image with Tsky=0 K as seen in Figure 5.1 (right) and $\hat{T}$ is the retrieved brightness temperature. The simulation of the retrieved brightness temperature is performed in the following way:

1. A set of visibility samples is computed taking into account the Fresnel Brightness temperature over the Ocean (Figure 5.1 left) and SMOS measured antenna patterns
2. Since $\Delta T_{FE}$ is an image reconstruction error, the Fresnel image is reconstructed from this SMOS set of visibility samples in the SMOS EAF-FoV by means of different inversion methods

The inversion approaches are described in Table I of [Corbella *et al.*, 2009] and chapter 2 (section 2.4). More than the specific features of the inversion approaches, the important conclusion of these simulations is the fact that, even for the case that the antennas are perfectly known (zero uncertainty in the antenna patterns), the error in the retrieved images is not negligible at all. Figure 5.2 shows the floor error computed for SMOS nominal case using two different approaches in the inversion of the image. As derived from (5.4) the "floor error" depends on the specific image reconstruction algorithm.

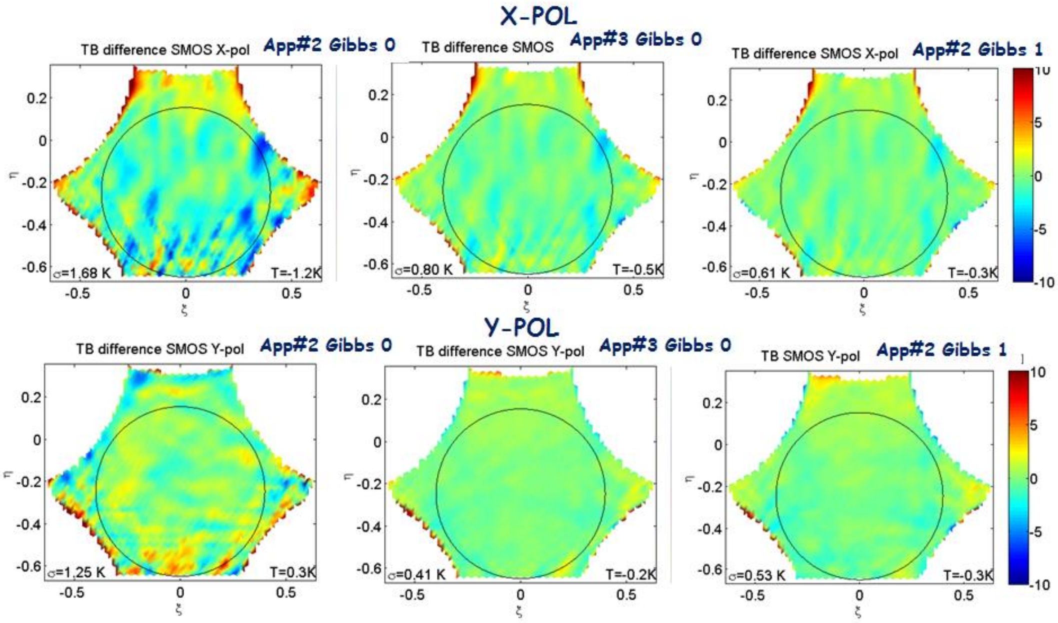

*Figure 5.2 Floor error for X-pol (top) and Y-pol (bottom) for the following inversion cases [Corbella et al., 2009]: App#2 Gibbs 0(left) App#3 Gibbs 0 (middle) and App#2 Gibbs 1 (right) and App#2 Gibbs 0(left) App#3 Gibbs 0 (middle) and App#2 Gibbs 1 (right)*

| Approach | X-pol $\Delta T_{FE}$ | Y-pol $\Delta T_{FE}$ |
|---|---|---|
| **App #2 Gibbs 0** | 1,68 K | 1,25 K |
| **App #3 Gibbs 0** | 0,8 K | 0,41 K |
| **App #2 Gibbs 1** | 0,61 K | 0,3 K |

*Table 5.1 Floor error Standard deviation for different approaches*

### 5.2.2 Floor error in the case of identical antenna patterns

These simulations in this section are aimed to estimate the minimum reconstruction error in the case that all antenna patterns are equal. The following analysis has been performed averaging all the antenna patterns in all the receivers in each arm.

These simulations show that the use of a model to perform a kind of differential image reconstruction procedure reduces the impact of the floor error. This feature will be further confirmed in the following section.

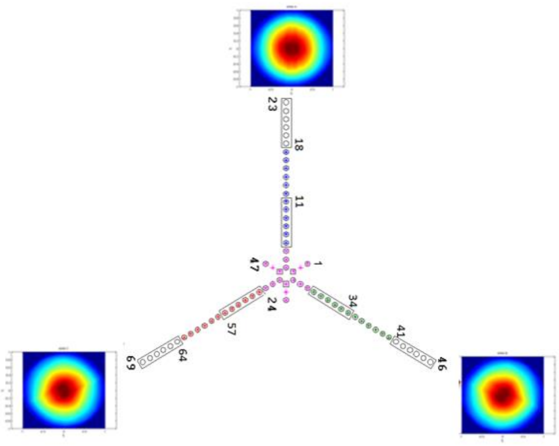

*Figure 5.3 Representation of the mean of all the SMOS antenna patterns per arm X-pol.Antenna patterns are systematically distorted in the direction of the arm*

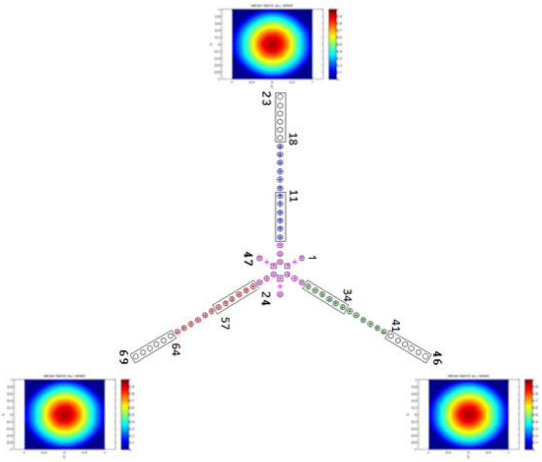

*Figure 5.4 Representation of the mean of all the SMOS antenna patterns X-pol. (circular pattern shape)*

When all the antenna patterns are averaged the result is a smooth circular antenna pattern as it is shown in Figure 5.4.

Figure 5.5 shows the floor error for this particular case. As shown, the floor error is lower than in the previous simulations (Figure 5.2). Moreover, different inversion approaches do not seem to have any impact on it. The major error feature is a ripple, probably due to the truncation of the visibility samples in the *(u,v)* domain to the star-shape shown in chapter 2, as demonstrated in the following sections.

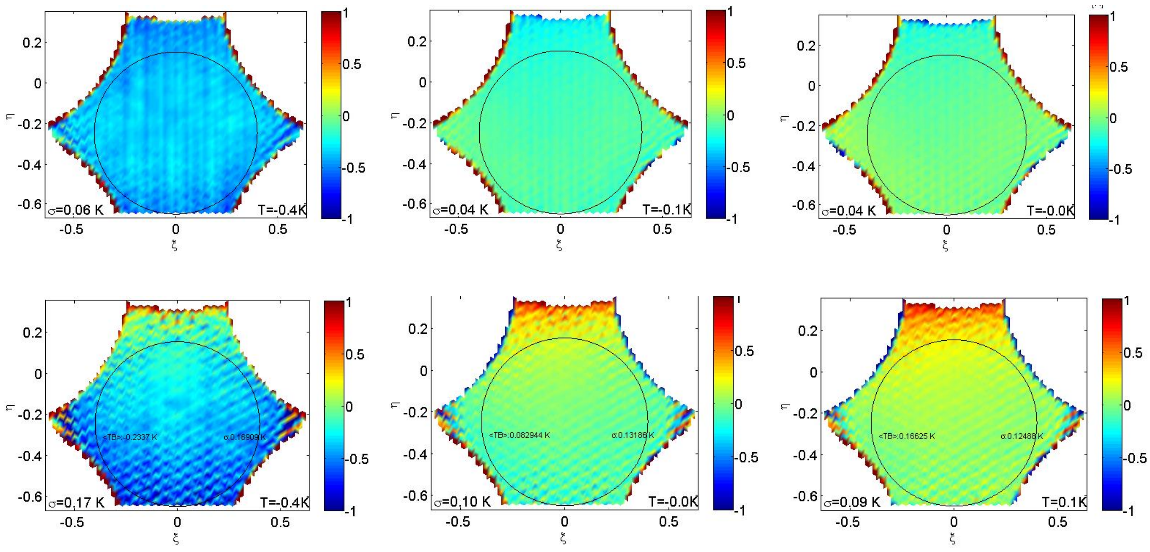

*Figure 5.5.Floor error App#2 Gibbs 0 (left) App#3 Gibbs 0(middle) and App#2 Gibbs 1 (right) for X-pol. (top) and Y-pol. (bottom)*

## 5.2.3 Error using one single SMOS antenna pattern in all elements

In order to evaluate the effect of the truncation error some additional simulations have been performed using an identical antenna pattern. However, in this case the selected antenna patterns correspond to one of the antennas in the array that presents high frequency directional variations (Figure 5.6).

The following analysis has been performed selecting one single SMOS antenna pattern in order to use it in all 69 receivers all the antenna patterns of all the receivers using a Fresnel reference image with a sky temperature of 0 K. These simulations are aimed to assess the minimum reconstruction error in the case that all antenna patterns are equal, but with a larger harmonic content than in the case of the averaged patterns in the previous section.

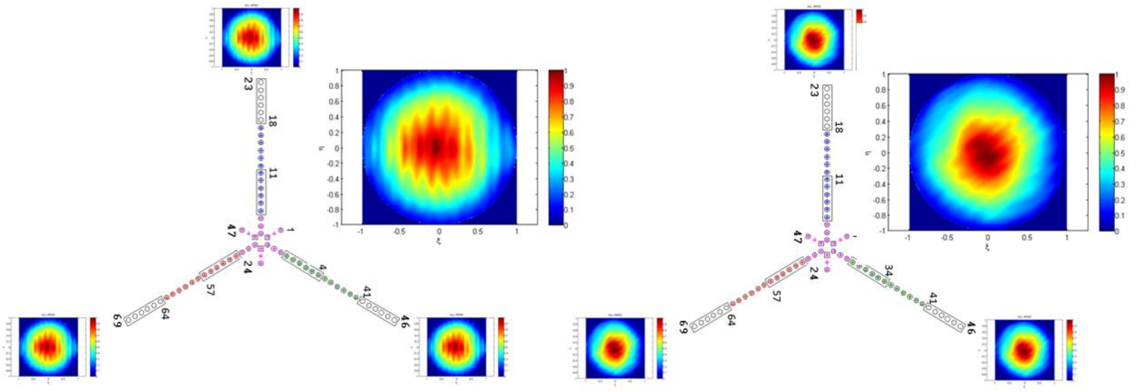

*Figure 5.6 Representation of a single SMOS antenna pattern X-pol. LICEF A-10 (left)and LICEF C-16 (right)*

Figure 5.7 shows the SMOS antenna pattern used in all receivers and the difference between the TB (X-pol) recovered after forward/backward computation of the brightness temperature using the same antenna pattern. Note in Figure 5.7 that the orientation of the error stripes has a clear relation with the spatial frequency content of the original antenna pattern (e.g. vertical bands stripes in the case of LICEF A10).

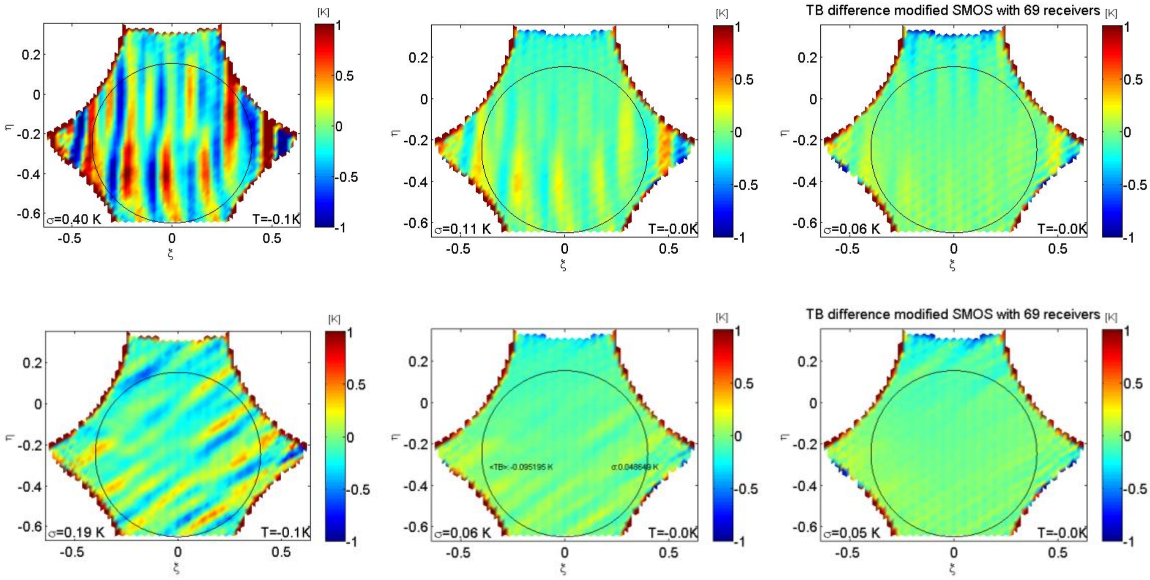

*Figure 5.7.Floor error App#2 Gibbs 0 (left) App#3 Gibbs 0 (left) and  App#2 Gibbs 1 (right) X-pol. case LCF A-10 (top) and Y-pol. case LCF C-16 (bottom)*

## 5.2.4 Error increasing the number of antennas (array size)

In order to confirm that the floor error in the cases analyzed in the previous sections are all related to truncation errors, the size of SMOS arms has been increased in the simulation from 21 elements per arm to 40 (Figure 5.8).

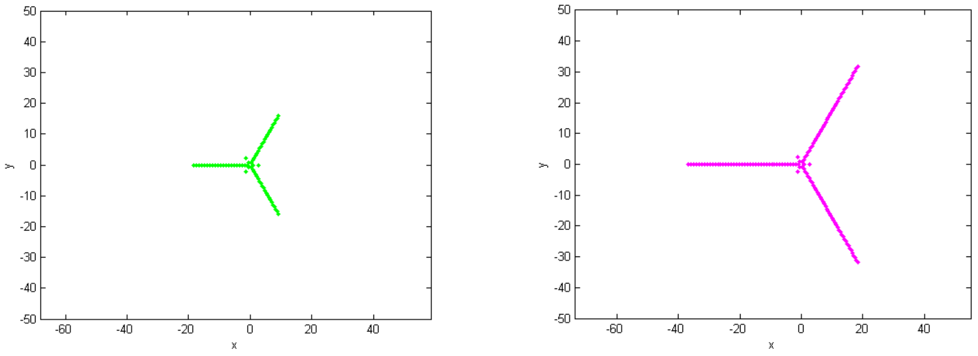

*Figure 5.8. Original SMOS 69 receivers (left) and, modified SMOS 126 receivers (right)*

In this way the spatial coverage of the star in the *(u,v)* domain is significantly larger. Figure 5.9 shows the floor error $\Delta T_{FE}$ for the two cases of LICEF A10 as single antenna pattern. When 126 elements are used the floor error vanishes, thus confirming that in the case of identical antenna patterns the floor error is exclusively dominated by the finite coverage of the visibility samples in the *(u,v)* domain (truncation error).

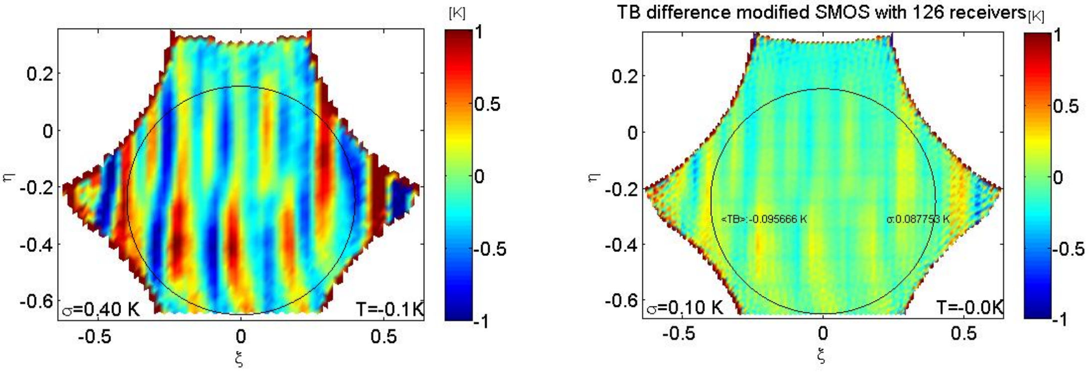

*Figure 5.9 Floor error with the single antenna pattern of  LICEF A-10 used in 69 receivers (left) or 126 receivers (right)*

Figure 5.10 (left) reproduces the floor error for SMOS regarding approach #2 Gibbs 0 for X-pol (Figure 5.2, top left). In this case if SMOS array is increased to 126 elements by using the mean antenna pattern for the additional elements, it resulted that the floor error does not vanish (Figure 5.10 right). The same occurs for the other inversion approaches in Figure 5.2. This demonstrates that the floor error is not dominated by truncation error when different antenna patterns for each element are taken into account as in the SMOS case.

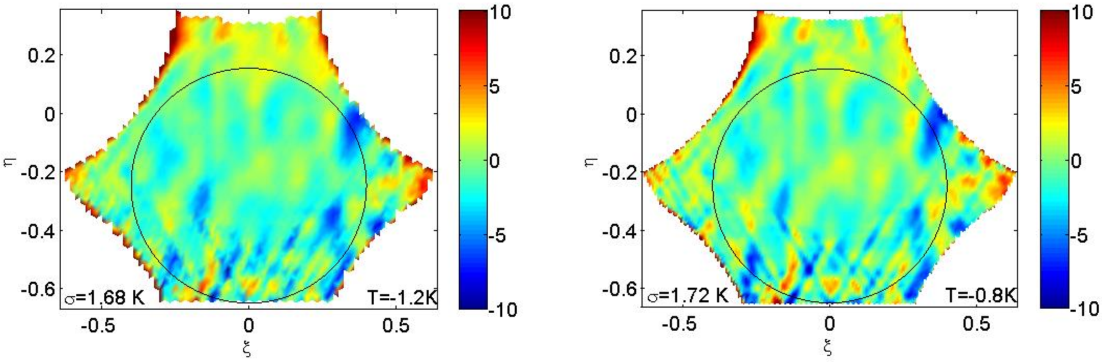

*Figure 5.10 ΔT with the nominal SMOS antenna patterns used in 69 receivers (left) or 126 receivers (right)*

## 5.3 Origin of floor error in SMOS full-pol mode

As defined in the previous section, SMOS “floor error” is defined as the residual error that appears in an error free end-to-end image reconstruction simulation. This section is devoted to identify the origin of this image reconstruction error. The hypothesis is then validated by simulation [Corbella *et al.*, 2014].

If $\hat{G}$ is the matrix computed from the available antenna patterns, and $V$ the visibility samples simulated from a brightness temperature reference scene $T$ defined in the UC. The reconstructed brightness temperature $\hat{T}$ in the fundamental hexagon is given by

$$\hat{T} = \hat{G}^{-1}V \tag{5.5}$$

The floor error is then computed as $\hat{T} - T$ (now T defined in the fundamental hexagon as in Figure 5.11 right), the non-zero error that appears due to the under determined nature of the problem. In a simple case where all receivers and antenna patterns are equal, the G matrix simplifies to a Fourier operator and under determination turns into the well-known aliasing effect that yields an alias free Field of View (AF-FoV) with no-error. However, when the antenna patterns are different, even if they are perfectly known, the properties of the Fourier operator are not fully full-filled by the G-matrix and the energy in the alias regions spreads throughout the AF-FoV. The floor error then, is an image dependent artifact that is affected by the brightness temperature distribution outside the imaged area.

The origin of the floor error can be easily understood by rewriting the columns of the G-matrix split into the principal hexagon $G_H$ and the rest of the unity circle (area outside the hexagon) $G_{NH}$ (Figure 5.11):

$$V = \left[G_H G_{NH}\right]T = G_H T_H + G_{NH} T_{NH} \tag{5.6}$$

Note that the brightness temperature pixels in the unity circle have also been rearranged into these two regions. Since brightness temperature is retrieved exclusively within the fundamental hexagon, from (5.6) the retrieved brightness temperature can be written by means of the G-matrix pseudo-inverse as:

$$\hat{T}_H = \hat{G}_H^{-1}V = \hat{G}_H^{-1}(V_H + V_{NH}) \tag{5.7}$$

where:

$$\Delta\hat{T}_H = \hat{T}_H - T_H = (\hat{G}_H^{-1}G_H - 1)T_H + \hat{G}_H^{-1}[G_{NH}T_{NH}] \tag{5.8}$$

And the floor error is given by the second undesired term:

$$\Delta\hat{T}_{Hfloor} = \hat{G}_H^{-1}\left[G_{NH}T_{NH}\right] \tag{5.9}$$

This error can be mitigated by an inversion approach that consists of a simple Fresnel (specular) model of the Ocean and a constant value over land, exclusively applied to the region outside the fundamental hexagon. The contribution of the undesired term $\Delta\hat{T}_{Hfloor}$

can be estimated at visibility level $\hat{V}_{NH}$ by means of the model, $\hat{T}_{NH}$ , and measured antenna patterns also outside the fundamental hexagon, $\hat{G}_{NH}$ :

$$\hat{V}_{NH} = \hat{G}_{NH}\hat{T}_{NH} \tag{5.10}$$

Now, if $\hat{V}$ are the measured visibility samples, the brightness temperature is retrieved by means of the G-matrix pseudo-inverse as:

$$\hat{T}_H = \hat{G}_H^{-1}(\hat{V} - \hat{V}_{NH}) \tag{5.11}$$

In a general sense, in SMOS nomenclature, this method is referred to as Gibbs 2 approach described in chapter 6 (a brightness temperature model is subtracted from measurements at visibility level before inversion). Note that now, ideally (neglecting calibration and antenna pattern errors) the error in the retrieved brightness temperature is restricted to the truncation error (approximately zero over ocean and Gibbs ringing close to the coast):

$$\Delta\hat{T}_H = \hat{T}_H - T_H = (\hat{G}_H^{-1}G_H - I)T_H \approx T_H \tag{5.12}$$

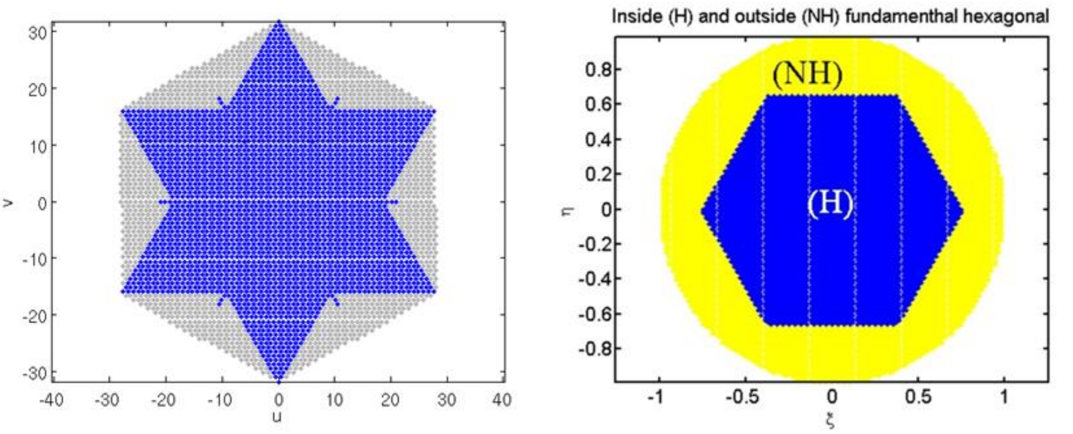

*Figure 5.11 The image is retrieved in the hexagonal area H whereas the visibility samples take into account the image in the full unity circle. (u,v) sampling domain (left) and $\xi,\eta$ imaging domain (right)*

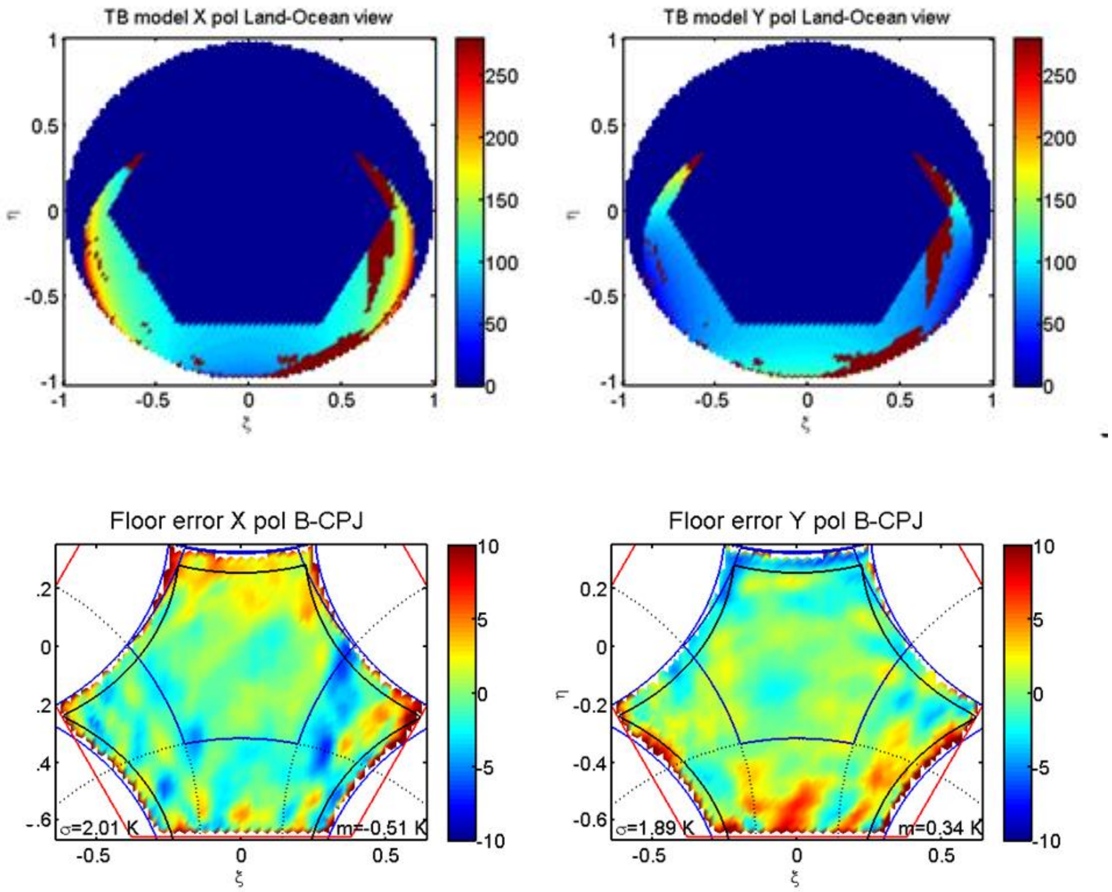

*Figure 5.12 Simulated mixed scene X-pol (top left) and Y-pol (top right) and floor error X-pol (bottom left) and floor error Y-pol (bottom right).*

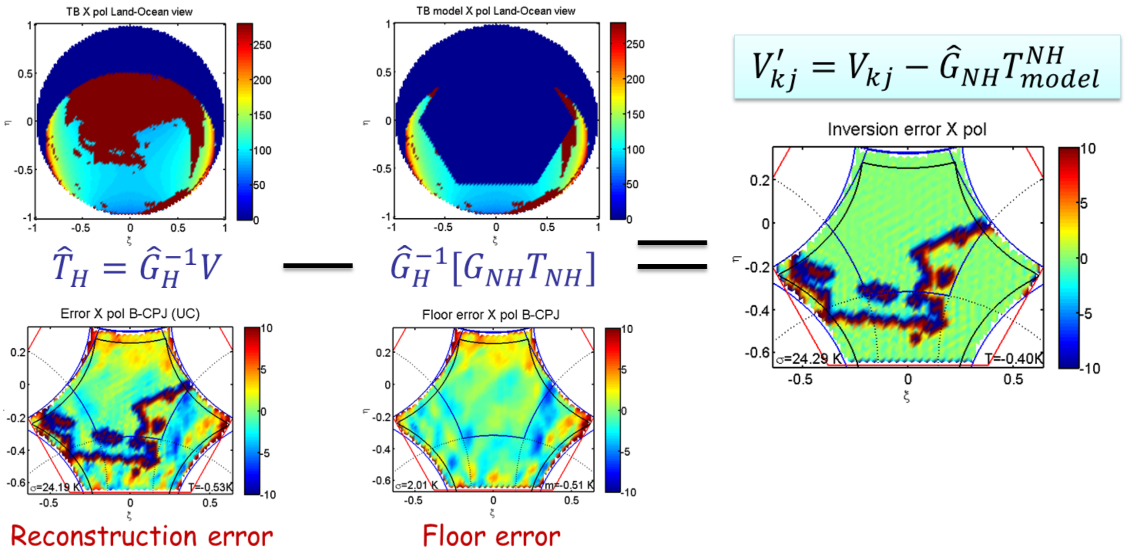

*Figure 5.13 Example of subtracting floor error from a mixed scena (land + sea) Only truncation error in the coast remain. Inversion approach: Gibbs 2*

Figure 5.12 shows a simulated mixed scene (land and sea areas) only in the outside part of the fundamental hexagonal. When the image is reconstructed in the outside part of the fundamental hexagon only floor error is recovered from the original image. This simulation shows that the floor error is an image dependent artifact. Moreover, a function of the energy in the "Alias" region spreads thorough the expected "Alias free" region due to the G-matrix not fully following Fourier properties.

On the other hand, Figure 5.13 shows the model in the complete scene (top left) minus the outside part of the fundamental hexagon referred to the floor error. In the right plot the difference of both images shows that there is not floor error. However, the truncation error remains in the ocean area, in the border of the land. This is a Gibbs effect due to the large increase of brightness temperature from ocean to land. Figure 5.13 is the basis of the so called Gibbs 2 model approach that will be further analyzed in the following sections. All these results were presented in the international congress IGARSS 2014 (Québec) [Corbella *et al.,* 2014].

### 5.3.1 Conclusions

As a main conclusion the differences among antenna patterns produce a residual spatial bias even if they are perfectly known and the G-matrix is used in the image reconstruction process. This minimum error is mitigated by the inversion approaches that are applied to the contrast image (the model approach). Since simulations assume zero error in the visibility samples, this is the minimum spatial bias that can be achieved and it is called "floor error". The assessment in this section has found out that the floor error exclusively depends on the image content outside the fundamental hexagon.

In chapter 6, it is shown that this floor error can be mitigated by smart image reconstruction techniques that are based on differential imaging (Gibbs 2 approach).

## 5.4 Impact of antenna pattern cross-polar terms in spatial bias

This section is devoted to analyze the impact of antenna pattern cross-polar terms. It derived in the full-pol G-matrix inversion, currently incorporated to v620 of the operational processor (L1OP). Part of this work has been done in collaboration with Wu Lin [Wu *et al.*, 2013], [Wu, 2014]. As described in chapter 3, the MIRAS instrument consists of a Y-shape interferometric radiometer formed by 69 coherent receivers in each of two linear orthogonal polarizations (X and Y), placed along the three arms of the array. Cross-correlation of the signals collected by each receiver pair "k, j" in the array gives a sample of the so-called polarimetric visibility function $V_{kj}^{pq}(u_{kj}, v_{kj})$, being $p=\{x, y\}$ and $q=\{x, y\}$ the polarization configuration of the "k" and " j" antennas, respectively; and $(\mathrm{u_{kj}}, \mathrm{v_{kj}})$ the antenna separation in the X-Y plane, measured in wavelengths (baseline). $V_{kj}^{pq}$ develops into a polarimetric brightness temperature map $\mathrm{T_B^{pq}}(\xi, \eta)$ in the direction cosines domain by means of a Fourier based synthesis technique [Corbella *et al.,*2004]. MIRAS can work in two operation modes: In dual-pol mode, MIRAS measures the brightness temperature in horizontal and vertical polarization defined at the antenna frame (X and Y). In full-pol mode, as described in section 3.3, MIRAS uses a pol-switching scheme to measure the samples of the four polarimetric visibilities: $V_{kj}^{xx}, V_{kj}^{yy}, V_{kj}^{xy}$ and $V_{kj}^{yx}$ that allow the retrieval of the four

Stokes parameters [Martin-Neira *et al.*, 2002]. The third and four Stokes parameters are defined at the antenna frame as:

$$A_3 = 2Re\{T_B^{xy}\}, \quad A_4 = 2Im\{T_B^{xy}\} \tag{5. 13}$$

Any single antenna "k" in the interferometric array can be characterized according to its normalized polarimetric voltage antenna patterns as:

$$\vec{F}_x^k = R_x^k\hat{x} + C_x^k\hat{y},\ \vec{F}_y^k = C_y^k\hat{x} + R_y^k\hat{y} \tag{5. 14}$$

where $R_p$ is the reference (co-polar) pattern and $C_p$ is the cross-polar pattern at each of the orthogonal polarization at the antenna frame, *p={x, y}* and *q={x, y}*, defined according to the 3rd Ludwig's polarization definition (*p* corresponds to receiver *k* and *q* to receiver *j*). The polarimetric visibilities $V_{kj}^{pq}(u,v)$ related to each polarimetric temperature $T_B^{pq}(\xi,\eta)$ can be divided into four terms $\Delta V_{pq}^{HS}(u,v)$, each one related to one of the four polarimetric combinations as:

$$\Delta V_{pq}^{HS} = \frac{1}{\sqrt{\Omega_p^k\,\Omega_q^j}} \iint_{UC} H_p^k S_q^j\ T_B^{pq} e^{-j2\pi(u\xi+v\eta)} \frac{d\xi d\eta}{\sqrt{1-\xi^2-\eta^2}}, \tag{5. 15}$$

where $H_p^k(\xi,\eta)$ represents the reference (R) or cross-polar (C) antenna pattern, at polarization p={x, y}, with a solid angle $\Omega_p^k$, of the first receiver, "k" in each baseline; $S_q^j(\xi,\eta)$ represents the reference (R) or cross-polar (C) antenna patterns at polarization q={x, y}, with a solid angle $\Omega_q^j$, of the second receiver, "j" in each baseline; and $T_B^{pq}(\xi,\eta)$ is the pq={xx, xy, yx or yy} polarimetric brightness temperature of the scene, in the direction cosines domain, at the antenna frame X-Y. This radiometric integral $\Delta V_{pq}^{HS}$, which represents one term of the polarimetric visibility $V_{pq}^{HS}$, can be discretized by means of the so called full-pol G-matrix operator.

$$\Delta V_{pq}^{HS} = G_{pq}^{HS} T_B^{pq} \tag{5. 16}$$

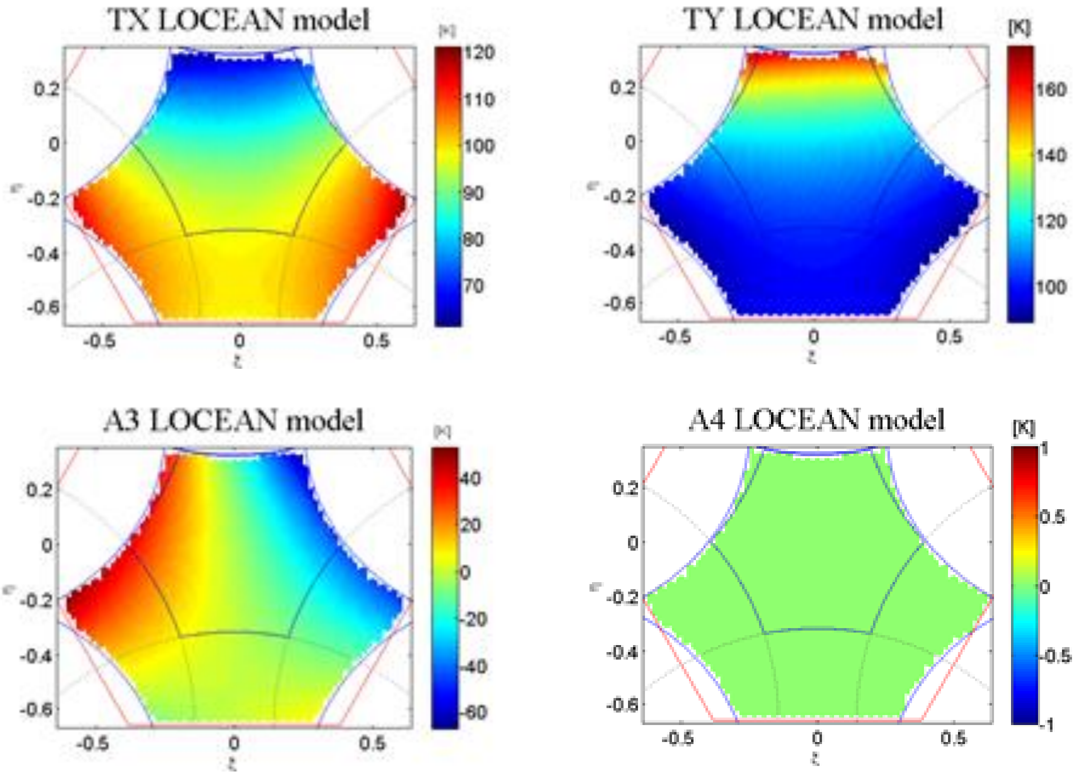

*Figure 5.14 Simulated ocean polarimetric brightness temperatures represented in SMOS synthetic field of view (FoV) at the antenna frame. The alias free (AF) area is given by the six alias of the unity circle (solid line) according to SMOS hexagonal $(u, v)$ sampling and minimum antenna spacing (d=0.875λ)*

SMOS extended alias free (EAF) region is limited by the six Earth aliases, once the contribution of the sky has been removed (dotted lines). The red straight lines gives the fundamental hexagon in the $(\xi, \eta)$ grid. The model for the reference data has been provided by LOCEAN and corresponds to a portion of SMOS descending orbit over the South Pacific ocean corresponding to the 28th June 2011 from 01:07:30 to 01:20:31 UTC times. Note the asymmetry in A3 due to non-zero Faraday rotation.

Then, taking into account this nomenclature convention, SMOS full-pol visibilities given in equation (1) and (10) in [Camps *et al.*, 2005], where antenna cross-polar antenna pattern effects have been included, can be written in a much more compact form as:

$$\begin{aligned} V_{kj}^{xx} &= G_{xx}^{RR}(T_B^{xx} - T_r) - G_{xx}^{RC}T_B^{xy} - G_{xx}^{CR}T_B^{yx} + G_{xx}^{CC}\left(T_B^{yy} - T_r\right) \\ V_{kj}^{yy} &= G_{yy}^{CC}(T_B^{xx} - T_r) + G_{yy}^{CR}T_B^{xy} + G_{yy}^{RC}T_B^{yx} + G_{yy}^{RR}\left(T_B^{yy} - T_r\right) \\ V_{kj}^{xy} &= G_{xy}^{RC}(T_B^{xx} - T_r) + G_{xy}^{RR}T_B^{xy} - G_{xy}^{CC}T_B^{yx} - G_{xy}^{CR}\left(T_B^{yy} - T_r\right) \end{aligned} \tag{5. 17}$$

It must be pointed out that antenna measurements provide the co- (R) and cross-polar (C) antenna patterns with an arbitrary sign convention related to the polarization configuration of the test probes. The terms in (5.17) have been written consistently with SMOS antenna measurements by taking X-pol cross-polar pattern as $-C_x$. SMOS data have validated this assumption since (5.17) has provided consistent A3 and A4 temperatures for the first time, as shown in the following sections.

Additionally, the polarimetric visibility samples $V_{kj}^{pq}$ in (5.17), which are used to feed the image reconstruction algorithms, are obtained from SMOS raw data after a comprehensive calibration and error correction scheme [Corbella *et al.*, 2005b],[Brown *et al.*, 2008] that has been continuously fine-tuned since SMOS launch. It must be pointed out that the, so-called, Corbella term $T_r$ [Corbella *et al.*, 2005a] is removed from (5.17) by means of the FTR (Flat Target Response [Martin-Neira *et al.*, 2008a]) measured during the cold sky calibration [Brown *et al.*, 2008] and will be neglected in the following sections.

An accurate Ocean model developed by LOCEAN for a reference orbit has been used in this work to compare SMOS measured brightness temperature maps and assess spatial errors. In order to perform this comparison, the four expected polarimetric temperatures are given at the antenna frame and according to SMOS synthesized geometry (Figure 5.14). The solid lines draw the alias free (AF) field of view (FoV) constrained by the six unity circle aliases given by SMOS hexagonal sampling. Since the sky brightness temperature is known and can be removed from the measurements, SMOS images are enlarged to the EAF-FoV given by the six Earth aliases (colored area) to yield SMOS nominal swath (approximately 1000 km). LOCEAN model takes into account the expected geophysical features of the reference scene (salinity, roughness, temperature, atmosphere...) and takes into account the geometric rotation of the electrical fields collected by the antennas from the ground frame to the antenna frame, including Faraday rotation (Figure 5.14).

### 5.4.1 Co-polar image reconstruction

Up to version v520 of the operational Level 1 processor (L1OP) SMOS image reconstruction algorithm was neglecting the cross-polar antenna pattern terms $\left(C_p \cong 0\right)$. This procedure took into account, exclusively, the reference (co-polar) patterns. Hence, each one of the polarimetric brightness temperatures in (5.17) can be retrieved independently as:

$$\begin{aligned} \hat{T}_B^{xx} &\cong (G_{xx}^{RR})^{-1} \cdot \hat{V}_{kj}^{xx} \\ \hat{T}_B^{yy} &\cong \left(G_{yy}^{RR}\right)^{-1} \cdot \hat{V}_{kj}^{yy} \\ \hat{T}_B^{xy} &\cong \left(G_{xy}^{RR}\right)^{-1} \cdot \hat{V}_{kj}^{xy} \end{aligned} \tag{5. 18}$$

where the superscript (-1) stands for the Moore-Penrose pseudoinverse and the hat (^) stands for the measured visibility and retrieved temperature. This basic method, which hereafter is referred to as co-polar G-matrix (CPG) has been improved in SMOS operational processor to the so-called Model approach (M-CPG) where a theoretical model of the Earth at a constant brightness temperature has been removed at visibility level (before inversion) in order to mitigate the antenna errors The M-CPG approach also includes a model of the sky brightness temperature to remove the sky alias in the EAF. Figure 5.15a shows the so-called spatial bias given as the difference between the temperatures measured by this SMOS current operational approach (M-CPG) and the reference LOCEAN model given in Figure 5.14.

### 5.4.2 Impact of cross-polar coupling

The neglected cross-polar terms in the current M-CPG approach has been found to produce a large spatial error, mainly in A3 and A4. This cross-pol. error (xpol) can be assessed by inverting an estimation of the neglected cross-polar terms by means of the co-polar (R) antenna patterns as:

$$\begin{aligned}
\Delta T_{xpol}^{xx} &= (G_{xx}^{RR})^{-1} \cdot \left[-G_{xx}^{RC} T_B^{xy} - G_{xx}^{CR} T_B^{yx} + G_{xx}^{CC} T_B^{yy}\right] \\
\Delta T_{xpol}^{yy} &= \left(G_{yy}^{RR}\right)^{-1} \cdot \left[G_{yy}^{CC} T_B^{xx} + G_{yy}^{CR} T_B^{xy} + G_{yy}^{RC} T_B^{yx}\right] \\
\Delta T_{xpol}^{xy} &= \left(G_{xy}^{RR}\right)^{-1} \cdot \left[G_{xy}^{RC} T_B^{xx} - G_{xy}^{CC} T_B^{yx} - G_{xy}^{CR} T_B^{yy}\right]
\end{aligned} \qquad (5.\ 19)$$

The $G_{pq}$ terms in (5.19) are computed from the measured antenna patterns while the forward polarimetric temperature terms $T_B^{pq}$ in (5.19) are simulated by means of a simple Fresnel model. Note that, in the forward case the brightness temperature model is required in the full unit circle. Figure 5.15b shows the error contribution to the four polarimetric temperatures $\Delta T_{xpol}^{pq}$ (5.19). A large radiometric term is clearly seen, mainly in A3 and A4 where the cross-polar contribution from $T_B^{xx}$ and $T_B^{yy}$ is larger. To show the consistency of the test, these cross-polar terms (Figure 5.15b) are subtracted from SMOS M-CPG images (Figure 5.15a) by combining (5.19) and (5.20) as:

$$\begin{aligned}
\hat{T}_B^{xx} &\cong (G_{xx}^{RR})^{-1} \cdot \hat{V}_{kj}^{xx} - \Delta T_{xpol}^{xx} \\
\hat{T}_B^{yy} &\cong \left(G_{yy}^{RR}\right)^{-1} \cdot \hat{V}_{kj}^{yy} - \Delta T_{xpol}^{yy} \\
\hat{T}_B^{xy} &\cong \left(G_{xy}^{RR}\right)^{-1} \cdot \hat{V}_{kj}^{xy} - \Delta T_{xpol}^{xy}
\end{aligned} \qquad (5.\ 20)$$

After this cross-polar correction, spatial bias improves in all cases (Figure 5.15c) yielding a lower rms value and a more random error distribution (the belt and suspenders effect has been mitigated). Since the correction is particularly effective in A3 and A4 (e.g. the large red and blue error spots in A3 have disappeared), these results are an in-orbit validation of the ground cross-polar antenna patterns measurements: they have been measured and kept stable after launch at least with accuracy enough to correct cross polar errors to a large extent, even by means of a simple Fresnel model of the Ocean. Although this correction is a validation of the cross-polar modeling, this is not a general method since it requires a priori information (e.g. Faraday rotation) and in the case of a general scene (e.g. mixed land and ocean) the model may not be accurate enough and introduce unpredictable errors. In the next section, a general approach that provides the four polarimetric brightness temperatures for any scene and does not rely on any a priori knowledge is presented.

### 5.4.3 Full-pol image reconstruction

Since the results in the previous section have shown that both the co- and cross-polar antenna patterns are accurate enough to successfully estimate and remove the non-negligible cross-polar contamination over the Ocean, a general procedure to take into account the cross-polar patterns can be devised to retrieve the polarimetric terms by inverting the full-pol G-matrix (FPG) as given in (5.17). In order to minimize the impact of antenna errors the model approach (M-FPG) is implemented: the contribution of an Earth disk at a constant temperature $T_g = 0{,}5\left(T_A^x + T_A^y\right)$ is removed from all the visibility components in (5.17), being $T_A^x$ and $T_A^y$ the antenna temperature in each polarization. Figure 5.15d shows the spatial bias for the measured polarimetric temperatures regarding the proposed M-FPG approach. The results are very similar to those given in Figure 5.15c demonstrating that the M-FPG method is performing as expected and that the inclusion of the cross-polar antenna patterns in the image reconstruction procedure does yield an enhanced SMOS performance. Table 5.2 summarizes this improved spatial bias performance as provided by the M-FPG with relation to the current M-CPG approach. On the other hand the next section gives further insight into the origin of the residual spatial bias in Figure 5.15d.

| Spatial bias ($m \pm \sigma$) K | | | | |
|---|---|---|---|---|
| | TX | TY | A3 | A4 |
| M-CPG (measured) | 1.6±1.74 | 0.2±2.55 | 2.3±5.25 | -0.7±3.10 |
| M-FPG (measured) | 1.2±1.56 | 0.4±2.21 | 1.2±3.42 | 0.4±2.46 |
| M-FPG (floor error) | 0.0±0.84 | -0.5±1.56 | 0.4±1.71 | -0.1±1.37 |
| Radiometric sensitivity (σ) K | | | | |
| M-FPG (boresight) | 2.6 | 2.8 | 5.5 | 5.5 |

(*) Mean antenna temperatures $T_A^x$=77 K and $T_A^y$=96K.

*Table 5.2 SMOS Full-pol radiometric performance summary*

### 5.4.4 Spatial bias error floor

In this case, in order to assess the minimum theoretical error (floor error) for the M-FPG approach in an error free instrument, a Fresnel model of the ocean has been used to simulate the four polarimetric visibilities in (5.17). Then, these visibilities have been used by the M-FPG approach to retrieve the four polarimetric temperatures. This simulation assumes perfectly known antennas since the SMOS measured antenna co- and cross-polar patterns have been used for both the forward and inverse simulations. Figure 5.14e shows the floor error over the ocean for this technique given as the difference between the temperatures simulated with the M-FPG approach and those derived from the original Fresnel model. The floor error roughly is a factor two lower than the SB for the SMOS M-FPG measurements (Figure 5.15d), as summarized in Table 5.2, thus yielding some margin for further improvement at calibration level. However, some of the SB bias features can be clearly identified both in Figure 5.15d and Figure 5.15e (e.g. the blue spots at the lower right and left edges in $T_B^{yy}$ or the red and blue spots in the lower right edge in A4 as demonstrated previously). As described in section 5.2, The non-zero floor error, even for perfectly known antennas, is caused by the fact that antenna patterns of different elements in the SMOS array are different (e.g. floor error simulation for a hypothetical case where a single co- and cross-polar antenna pattern are used, equal for all elements in the array, shows a negligible spatial bias). The floor error is successfully mitigated to a large extend by means of the so-called Gibbs 2 approach, as thoroughly developed in chapter 6. On the other hand, other spatial bias features still require further investigation either at calibration, image reconstruction or modeling of the reference scene (e.g. the increasing error in η shown in A3, which might be due to a mismodelling of the ionosphere, or the "belt and suspender" traces both in $T_B^{xx}$ and $T_B^{yy}$). All these results were presented in the IEEE Geosc. And Remote Sens. Letters [Wu *et al.*, 2013].

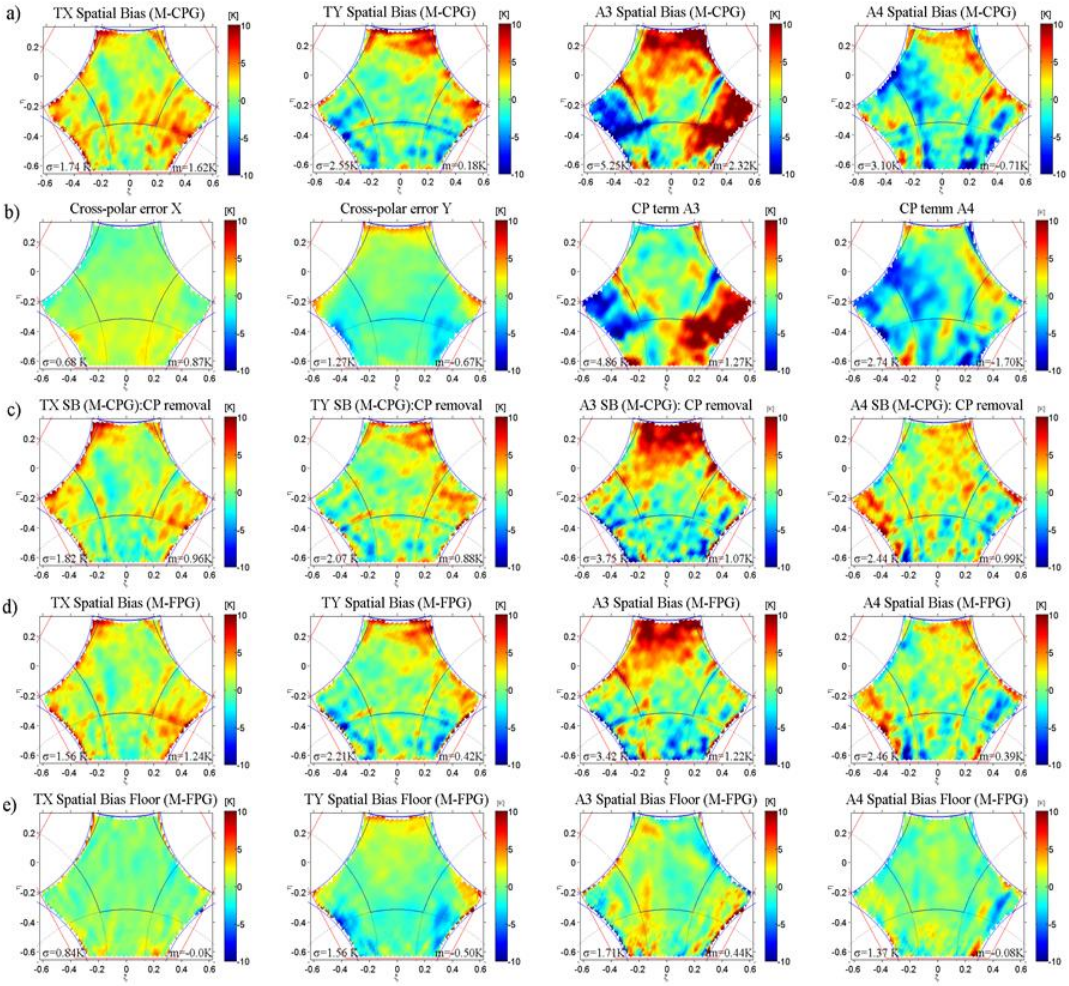

*Figure 5.15 Spatial bias (SB) maps. a) current SMOS M-CPG approach. b) SB contribution of cross-polar terms in the M-CPG approach. c) SB in the M-CPG when the cross-polar contribution is removed. d) SB for the M-FPG approach. e) SB floor error for the M-FPG approach. In all maps, the rms error (σ) and mean error (m) versus the LOCEAN model are plotted in the lower left and right corners, respectively*

### 5.4.5 Conclusions

The work undertaken in this chapter has shown that SMOS full-pol mode provides significantly improved polarimetric images if the full-pol G-matrix reconstruction (M-FPG) is used to take into account the non-negligible cross-polar antenna patterns. In particular the significant improvement in A3 have lead to a better correction of ionospheric effects such as Faraday rotation or attenuation [Corbella *et al.*, 2015b]. In general, the SB improvement opens the door to better geophysical parameter retrievals.

The “floor error” analysis has also shown that improved image reconstruction algorithm, as developed in the current chapter, mainly improve SMOS radiometric performance. Full-pol G-matrix inversion has been operational after release of version v620 of the operational processor. In may 2016 the mainly outcomes of this chapter have been undertaken in col.laboration with Wu Lin and have resulted in several joint publications.

# 6 Improvements in SMOS image reconstruction

The previous chapter has shown that one non-negligible source of error was an image reconstruction error called "floor error". Once its nature was unveiled it became clear that improved image reconstruction algorithm could estimate and mitigate this artifact to a large extended. This conducted to the so called Gibbs 2 full-pol model approach as developed in this chapter.

This chapter is devoted to assess the capability of two inversion methods to mitigate this "floor error". As explained in chapter 5, the instrument has a "floor error" defined as the residual error that appears in an error free end-to-end image reconstruction simulation. In order to reduce this mathematical error, different inversion approaches are implemented (the so-called basic and model approach and Gibbs 2).

The work described in this chapter supported the development by the RSLab team of smarter inversion methods than the ones described in chapter 2 [Corbella *et al.,* 2015a]. It must be pointed out that the activity reported in this chapter was performed in collaboration with Wu Lin [Wu, 2014] and resulted in several publication collaborations.

## 6.1 Mitigation of floor errors: Gibbs 2 approach

The Gibbs 2 approach consists of a brightness temperature model subtracted from measurements at visibility level before inversion. This model is more complex than the model inversion (Gibbs 1) approach (described in chapter 2). The complexity increases because it takes into account land and ocean pixels and the shape of the different areas of the land in each single snapshot, although the model is more sophisticated than in the Gibbs 1 approach, as shown here after it only applies to a fraction of the UC, thus improving memory and computational requirements. In order to implement the Gibbs2 method [Durán *et al.,* 2015], the contribution of the undesired term $\Delta\hat{T}_{Hfloor}$ in (5.9) can be estimated at visibility level $\hat{V}_{NH}$ by means of a model exclusively defined outside the fundamental hexagon $\hat{T}_{NH}$ and measured antenna patterns also outside the fundamental hexagon $\hat{G}_{NH}$ (Figure 6.1). This model can be defined at high resolution to improve the floor error estimation:

$$\hat{V}_{NH} = \hat{G}_{NH}\hat{T}_{NH} \tag{6.1}$$

From a practical point of view it is enough to have $\hat{T}_{NH}$ at the same resolution that the measured antenna patterns. Gibbs2 brightness temperature is now retrieved by means of the G-matrix pseudo-inverse (basic approach) from measured visibility $\hat{V}$ as:

$$\hat{T}_H = \hat{G}_H^{-1}(\hat{V} - \hat{V}_{NH}) \tag{6.2}$$

Note that now, ideally (neglecting calibration or antenna pattern errors) the error in the retrieved brightness temperature is restricted to the truncation error (approximately zero over ocean and Gibbs ringing close to the coast):

$$\Delta\hat{T}_H = \hat{T}_H - T_H = (\hat{G}_H^{-1}\hat{G}_H - 1)T_H \tag{6.3}$$

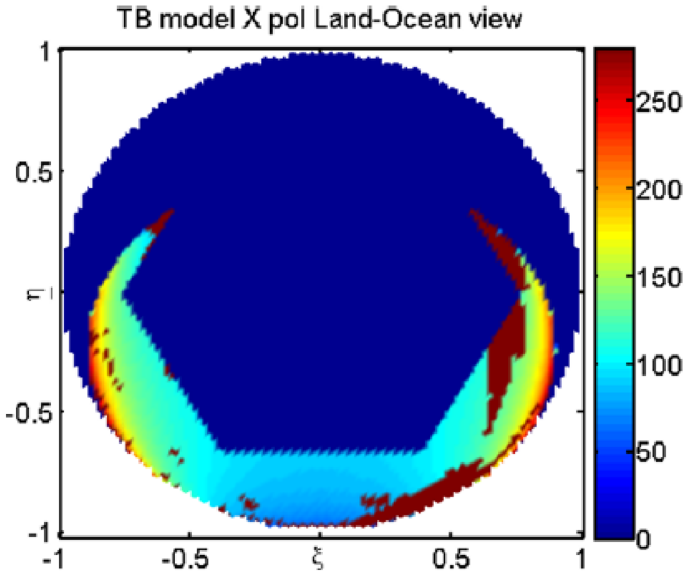

*Figure 6.1 Model for $T_{NH}$ in the brightness temperature domain related to a mixed land-sea scene. It is used to implement the Gibbs2 full-pol G-matrix image reconstruction approach*

Both the co-polar or reference (R) and cross-polar (C) antenna patterns can also be used to better estimate the full-pol floor error in the retrieved polarimetric brightness temperatures given by the contribution of the brightness temperature outside the fundamental hexagon:

$$\begin{bmatrix} V^{xx}_{NH} \\ V^{yy}_{NH} \\ V^{xy}_{NH} \\ V^{yx}_{NH} \end{bmatrix} = \begin{bmatrix} G^{RR}_{xxNH} & -G^{RC}_{xxNH} & -G^{CR}_{xxNH} & G^{CC}_{xxNH} \\ G^{CC}_{yyNH} & G^{CR}_{yyNH} & G^{RC}_{yyNH} & G^{RR}_{yyNH} \\ G^{RC}_{xyNH} & G^{RR}_{xyNH} & -G^{CC}_{xyNH} & -G^{CR}_{xyNH} \\ G^{CR}_{yxNH} & -G^{CC}_{yxNH} & G^{RR}_{yxNH} & -G^{RC}_{yxNH} \end{bmatrix} \begin{bmatrix} T^{xx}_{NH} \\ T^{xy}_{NH} \\ T^{yx}_{NH} \\ T^{yy}_{NH} \end{bmatrix} \tag{6.4}$$

This expression is used to implement the full-pol Gibbs 2 approach that makes use of the full-pol G-matrix pseudo-inverse:

$$\begin{bmatrix} T^{xx}_{H} \\ T^{xy}_{H} \\ T^{yx}_{H} \\ T^{yy}_{H} \end{bmatrix} = \begin{bmatrix} G^{RR}_{xxH} & -G^{RC}_{xxH} & -G^{CR}_{xxH} & G^{CC}_{xxH} \\ G^{CC}_{yyH} & G^{CR}_{yyH} & G^{RC}_{yyH} & G^{RR}_{yyH} \\ G^{RC}_{xyH} & G^{RR}_{xyH} & -G^{CC}_{xyH} & -G^{CR}_{xyH} \\ G^{CR}_{yxH} & -G^{CC}_{yxH} & G^{RR}_{yxH} & -G^{RC}_{yxH} \end{bmatrix}^{-1} \begin{bmatrix} V^{xx} - V^{xx}_{NH} \\ V^{yy} - V^{yy}_{NH} \\ V^{xy} - V^{xy}_{NH} \\ V^{yx} - V^{yx}_{NH} \end{bmatrix} \tag{6.5}$$

where the vector $\hat{V}$ stands for the SMOS measured polarimetric visibilities and an estimation of the contribution of the energy outside the fundamental hexagon is removed before inversion by means of the $V_{NH}$ term.

The main advantage of this method with relation to Gibbs 1 or other Gibbs 2 implementation approaches is given by the fact that the fundamental hexagon is not affected by the model since no signal is subtracted from the fundamental hexagon there is no need to add back any image to the retrieved brightness temperature, thus avoiding artifacts due to resolution, miss pointing, etc.

Both the co-polar or reference (R) and cross-polar (C) antenna patterns can be used to estimate the full-pol floor error in the retrieved polarimetric brightness temperatures given by the contribution of the brightness temperature outside the fundamental hexagon:

$$\begin{aligned} V_{NH}^{xx} &= G_{xxNH}^{RR}T_{NH}^{xx} - G_{xxNH}^{RC}T_{NH}^{xy} - G_{xxNH}^{CR}T_{NH}^{yx} + G_{xxNH}^{CC}T_{NH}^{yy} \\ V_{NH}^{yy} &= G_{yyNH}^{CC}T_{NH}^{xx} + G_{yyNH}^{CR}T_{NH}^{xy} + G_{yyNH}^{RC}T_{NH}^{yx} + G_{yyNH}^{RR}T_{NH}^{yy} \\ V_{NH}^{xy} &= G_{xyNH}^{RC}T_{NH}^{xx} + G_{xyNH}^{RR}T_{NH}^{xy} - G_{xyNH}^{CC}T_{NH}^{yx} - G_{xyNH}^{CR}T_{NH}^{yy} \end{aligned} \qquad (6.6)$$

Some considerations are worth to be highlighted:

- The contribution of the sky to the measured visibilities (included $V_0$) are assumed to be subtracted in advance.
- $\hat{T}_H$ is simply retrieved by applying a G-matrix pseudoinverse. There is no need to invert a zero mean image ($V_0$=0) since the image content outside the fundamental hexagon is zero (negligible residual error after removing $\hat{V}_{NH}$).
- The Gibbs 2 term $V_H - \hat{V}_{NH}$ also includes the zero visibility. Therefore, from the point of view of inversion, since a direct G-matrix pseudoinverse is used, there is no need to optimize the mean value of the ocean or the constant TB applied to land. Obviously, floor error mitigation is better as the model outside the fundamental hexagon, $\hat{T}_{NH}$ and antenna patters are more accurate.

In order to increase computation speed, when required, a simplified Gibbs-2 full-Pol G-matrix image reconstruction procedure can be implemented if only the dominant sources of co- and cross polar error terms are taken into account. The polarimetric floor error term impact on brightness temperatures can be computed in full-pol from (6.5) by setting measured visibilities $\hat{V}$ to zero:

$$\begin{bmatrix} \Delta T_{Hfl}^{xx} \\ \Delta T_{Hfl}^{xy} \\ \Delta T_{Hfl}^{yx} \\ \Delta T_{Hfl}^{yy} \end{bmatrix} = \begin{bmatrix} G_{xxH}^{RR} & -G_{xxH}^{RC} & -G_{xxH}^{CR} & G_{xxH}^{CC} \\ G_{yyH}^{CC} & G_{yyH}^{CR} & G_{yyH}^{RC} & G_{yyH}^{RR} \\ G_{xyH}^{RC} & G_{xyH}^{RR} & -G_{xyH}^{CC} & -G_{xyH}^{CR} \\ G_{yxH}^{CR} & -G_{yxH}^{CC} & G_{yxH}^{RR} & -G_{yxH}^{RC} \end{bmatrix}^{-1} \begin{bmatrix} V_{NH}^{xx} \\ V_{NH}^{yy} \\ V_{NH}^{xy} \\ V_{NH}^{yx} \end{bmatrix} \qquad (6.7)$$

Now, the contribution of each single antenna pattern co- and cross-polar terms to the floor error can also be easily estimated by setting to zero all other terms in (6.7) and computing the polarimetric error term $\Delta T_{Hfe}$ This leads to the following simplified expression to compute the Gibbs-2 visibility term, where only the dominant sources of floor error are taken into account:

$$\begin{bmatrix} V_{NH}^{xx} \\ V_{NH}^{yy} \\ V_{NH}^{xy} \\ V_{NH}^{yx} \end{bmatrix} \simeq \begin{bmatrix} G_{xxNH}^{RR} & 0 & 0 & 0 \\ 0 & 0 & 0 & G_{yyNH}^{RR} \\ G_{xyNH}^{RC} & 0 & 0 & -G_{xyNH}^{CR} \\ G_{yxNH}^{CR} & 0 & 0 & -G_{yxNH}^{RC} \end{bmatrix} \begin{bmatrix} T_{NH}^{xx} \\ 0 \\ 0 \\ T_{NH}^{yy} \end{bmatrix} \tag{6.8}$$

Note that the dominant sources of floor error in the polarimetric term $\hat{V}_{NH}^{xy}$ are the co-polar temperatures outside the fundamental hexagon ($T_{NH}^{xx}$ and $T_{NH}^{yy}$) through the cross-polar antenna pattern components. This simplified full-pol floor error terms derived from (6.8) are the following:

$$\begin{aligned} \hat{V}_{NH}^{xx} &\cong G_{xxNH}^{RR} T_{NH}^{xx} \\ \hat{V}_{NH}^{yy} &\cong G_{yyNH}^{RR} T_{NH}^{yy} \\ \hat{V}_{NH}^{xy} &\cong G_{xyNH}^{RC} T_{NH}^{xx} - G_{xyNH}^{CR} T_{NH}^{yy} \end{aligned} \tag{6.9}$$

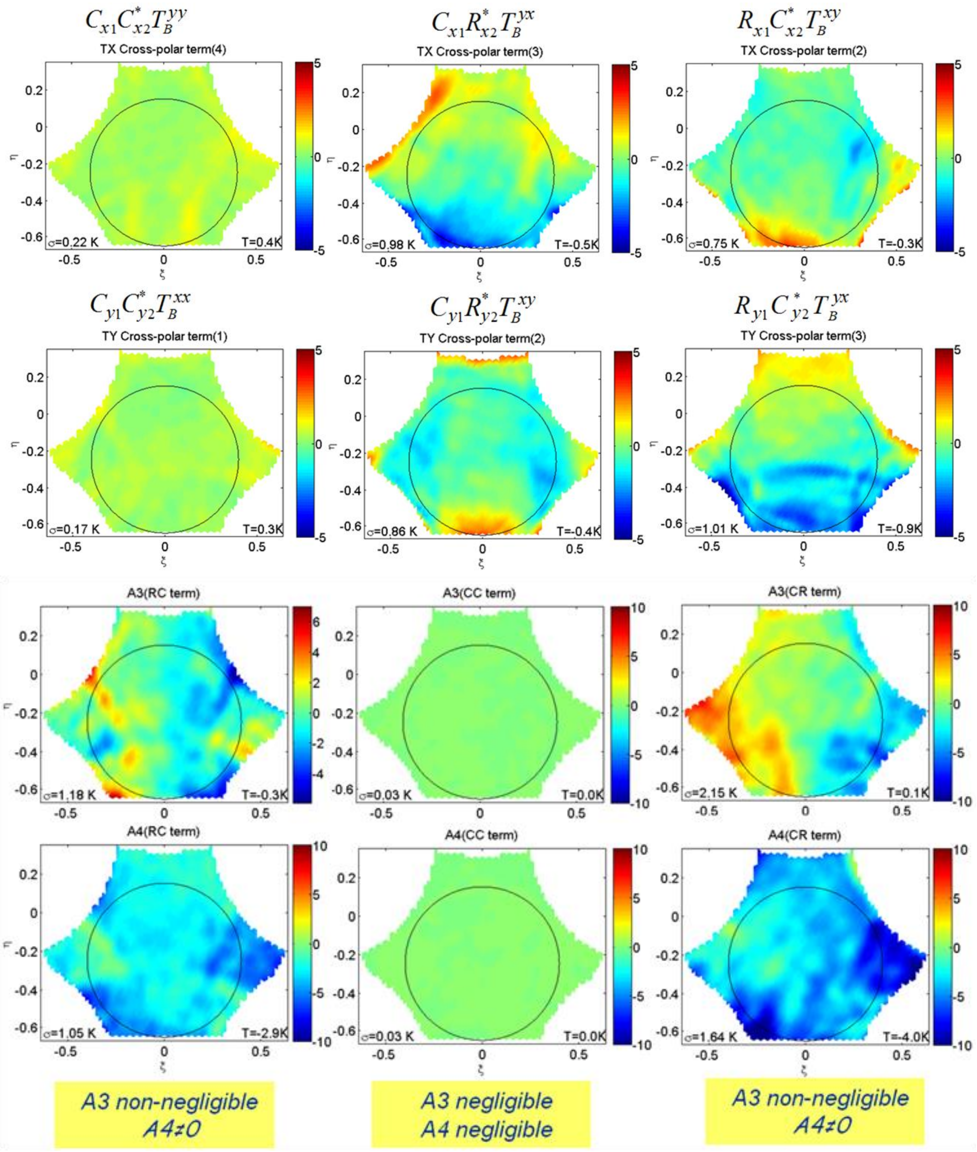

A3 non-negligible
A4≠0

A3 negligible
A4 negligible

A3 non-negligible
A4≠0

*Figure 6.2 Impact of each single cross-polar measured antenna pattern terms on SMOS polarimetric brightness temperatures over the Ocean*

This also shows that the contribution of the polarimetric brightness temperature outside the fundamental hexagon $T_{NH}^{xy}$ can be safety neglected to compute a good estimation of the full-pol Gibbs-2 model. It must also be pointed out that in the case of the G-matrix pseudo-inverse computed for the fundamental hexagon all terms are taken into account in (6.5) and (6.7). A preliminary assessment performed without the Gibbs-2 mitigation approach shows that the CC terms in (6.5) and (6.7) could also have been neglected. However, this simplification has a minimum impact on memory and computational time requirements and has not been implemented in this work.

Figure 6.3 shows that when using Gibbs 2 instead of Gibbs 1, X and Y pol have a more similar standard deviation. In X and Y polarization the impact of the Gibbs 2 approach is low as detailed in Table 6.1. The fact that spatial error distribution in X-pol and Y-pol are similar is consistent with the fact that both antennas are built and measured with the same technology and approach, and there is no reason to have different performance as displayed in the Gibbs 1 approach.

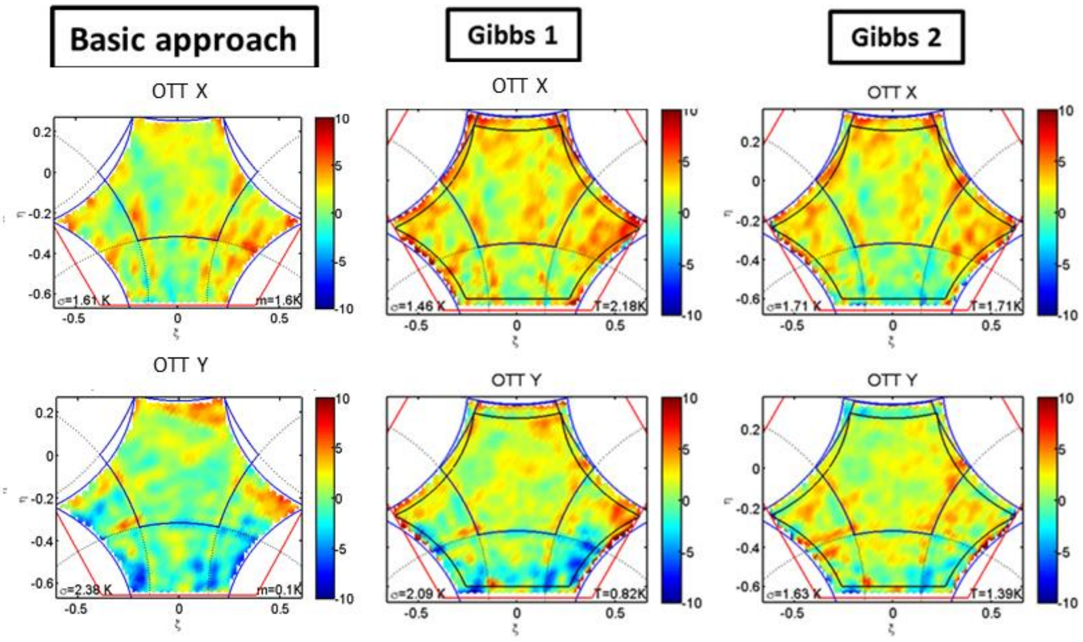

*Figure 6.3 Comparison between spatial bias in X and Y pol using Basic app., Gibbs 1 or Gibbs 2*

However, Figure 6.4 shows that when using Gibbs 2 A3 and A4 clearly improve with respect to Gibbs 1 because the floor error is very much reduced. This is because the dominant sources of co- and cross polar error terms as found in Figure 6.2 are taken into account in the inversion of the image. The results are summarized in Table 6.2.

| INVERSION APPROACH | Std X-pol | Std Y-pol |
|---|---|---|
| **CPG** | 1,61 K | 2, 38 K |
| **Gibbs 1 FPG-M** | 1,46 K | 2,09 K |
| **Gibbs 2 FPG-M** | 1,71 K | 1,63 K |

*Table 6.1 Summary of the results shown in Figure 6.3*

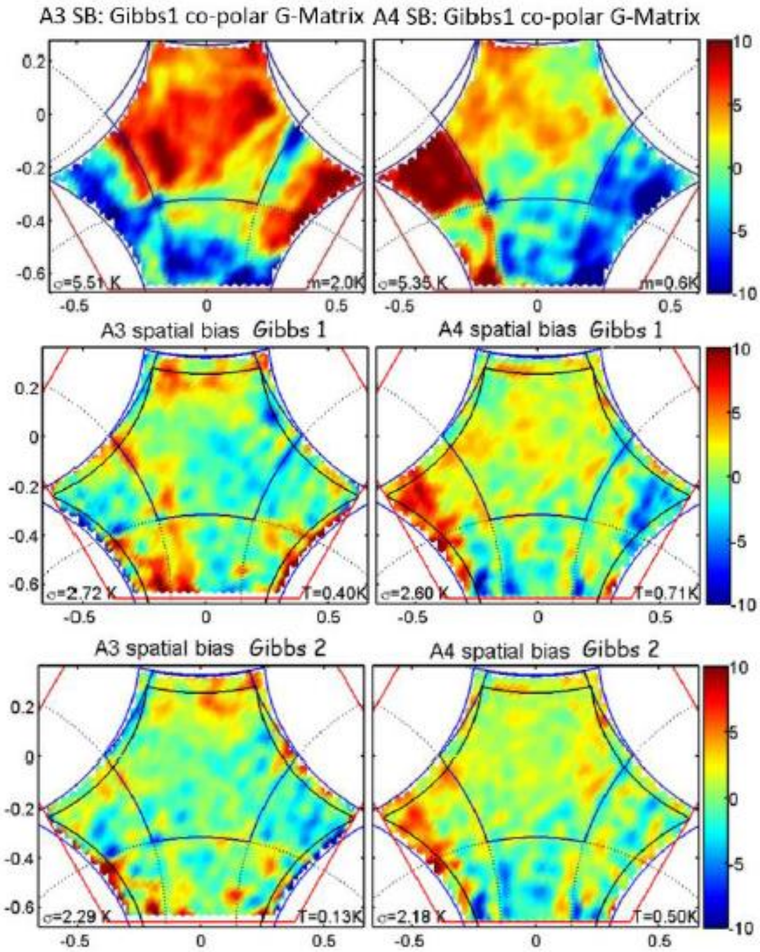

*Figure 6.4 Spatial bias comparison between A3 and A4 reconstructing by using Gibbs 1 or Gibbs 2*

| INVERSION APPROACH | Std A3 | Std A4 |
|---|---|---|
| **CPG** | 5,51 K | 5,35 K |
| **Gibbs 1 FPG-M** | 2,72 K | 2,60 K |
| **Gibbs 2 FPG-M** | 2,29 K | 2,18 K |

*Table 6.2 Summary of the results shown in Figure 6.4*

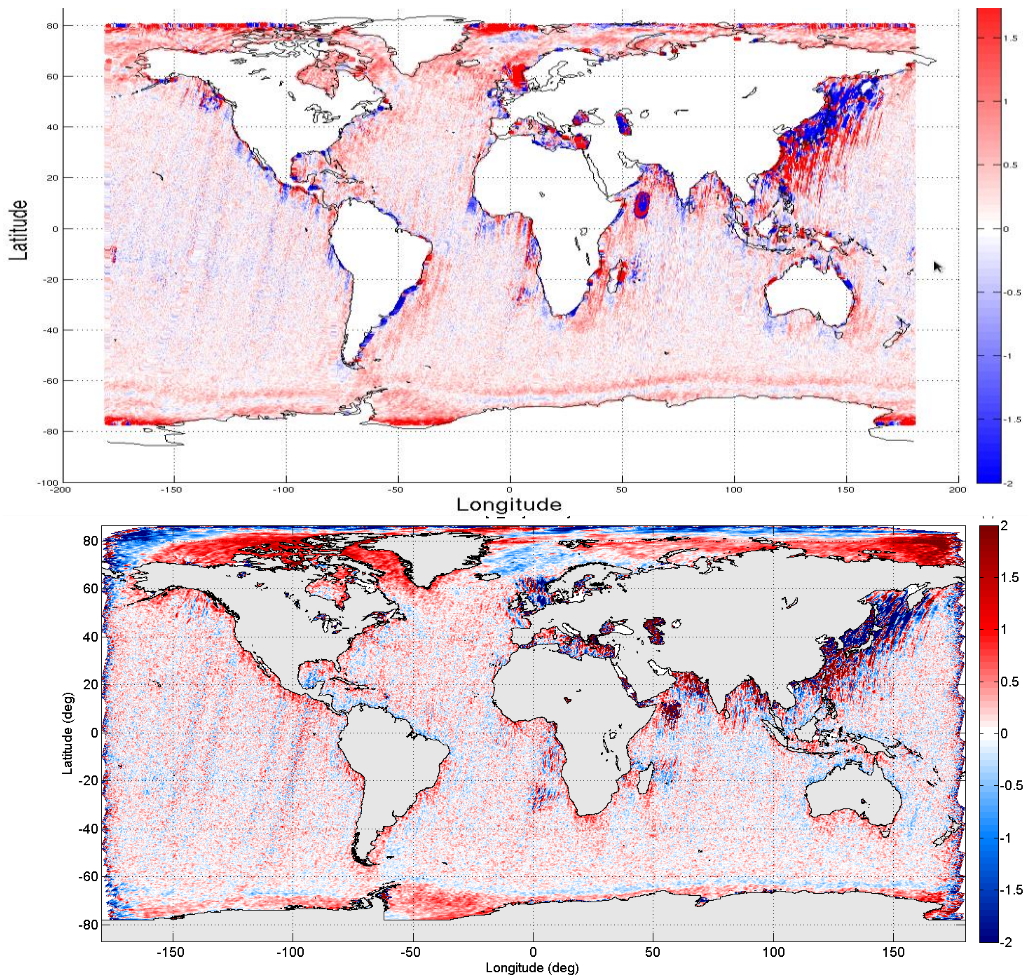

*Figure 6.5 A4 global map using Gibbs 0 (top) or Gibbs 2 (bottom) approach*

As shown previously, a Gibbs 2 image reconstruction approach provides a better A3 and A4 floor error mitigation over pure ocean scenes. However, it must be pointed out that the improvement of Gibbs 2 in front of the current SMOS Gibbs 1 approach is much larger when mixed land-sea scenes are taken into account. In the case of mixed scenes, the impact of land masses outside the fundamental hexagon can produce a large scene-dependent floor error that can very much contribute to the well-known Land-Sea contamination (LSC artifact) in A3 and A4 as will be further developed in chapter 7. That is, whereas on Tx and Ty polarizations LSC is mainly produced by an inconsistency between the error in the zero baseline and all other visibilities [Corbella *et al.*, 2015a], [Corbella *et al.*, 2015b], on A3 and A4 the image contrast between land and ocean is much lower and the main contribution to LSC is the floor error. One of the main improvements of the Gibbs 2 approach is precisely the improved A3 and A4 performance close to the land masses.

In order to assess and validate the performance of the Gibbs 2 model approach, Figure 6.5 shows a global error map of the 4th stokes parameter for descending orbits over the ocean. A4 is averaged from 1st to 10th May 2011 and 0-60º incidence angle. The ideal A4 is assumed to be zero. Although this is a preliminary result, A4 error is low and homogeneously distributed. Large artifacts close to the continents (LSC), that were present in the Gibbs 1 image reconstruction approaches, have disappeared. However, a faint halo close to land can still be seen in some regions and requires further analysis.

A4 has been selected to test the performance of the full-pol Gibbs 2 approach because it is extremely sensitive to any image reconstruction artifact. All these results were presented in IGARSS 2014 (Milán) [Corbella *et al.*, 2013].

## 6.2 Simplified Gibbs 2

The performance of the simplified Gibbs 2 method can be assessed by estimating the spatial bias from SMOS data. Spatial bias is defined as the difference between measured and real polarimetric brightness temperatures in the (ξ, η) direction cosines domain.

From a practical point of view, spatial bias is defined as the difference between the reconstructed complete polarimetric brightness temperature image in an ocean reference area and the ground truth as predicted by J. Tenerelli. It is also known as OTT (Ocean Target Transformation) since these error maps are used to improve the accuracy of salinity retrievals.

The comparison between the two implementations of the Gibbs 2 approach is given in Figure 6.6, where it can be seen that the simplified case yields a small radiometric degradation, especially in Y polarization. Table 6.3 summarizes the radiometric metrics for the two implementations.

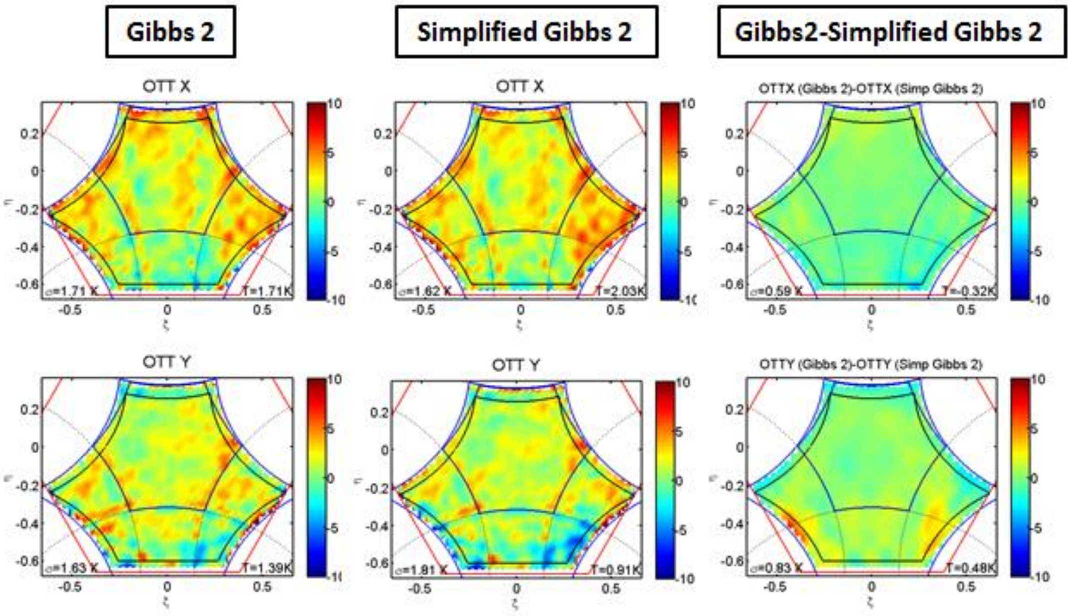

*Figure 6.6 X and Y Spatial bias (OTT) comparison for the full-pol Gibbs 2 approach (left), full-pol simplified Gibbs 2 (middle,) and the difference between the two cases (right).*

| Pol | Gibbs 2 | Simp. Gibbs 2 | Difference |
|---|---|---|---|
| XX | σ =1,71 K m=1,71 K | σ =1,62 K m=2,03 K | σ =0,59 K m=-0,32 K |
| YY | σ =1,63 K m=1,39 K | σ =1,81 K m=0,91 K | σ =0,83 K m=0,48 K |

*Table 6.3 Summary of the results shown in Figure 6.6*

Spatial bias comparison for the 3rd and 4th Stokes is given in Figure 6.7. Note that in this case the approximation given in (6.8) does not result in any significant performance degradation. Table 6.4 gives the metrics regarding Stokes 3 and 4 parameters.

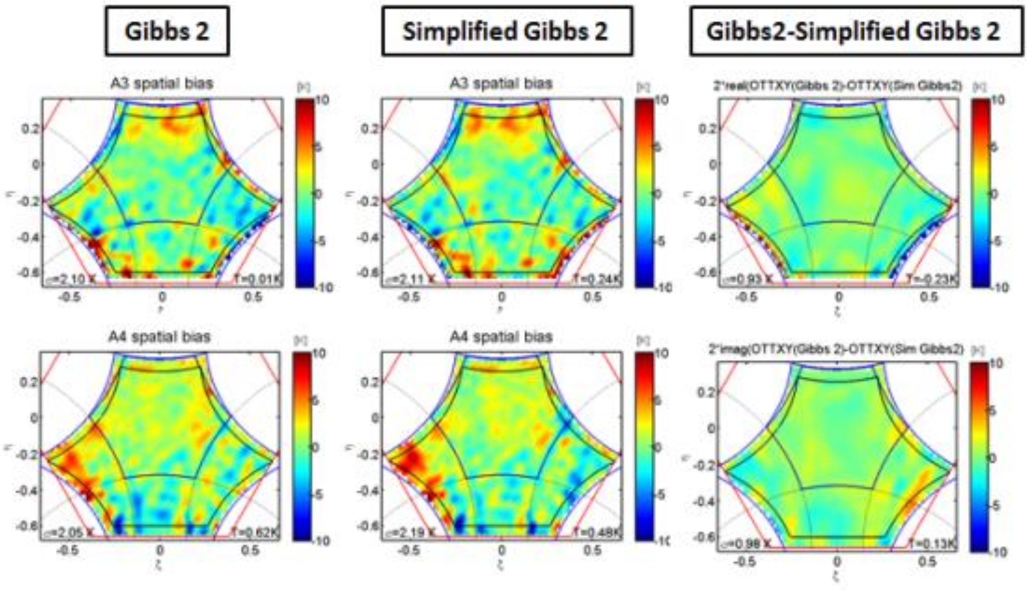

*Figure 6.7 3rd and 4th Stokes Spatial bias (OTT) comparison for the full-pol Gibbs 2 approach (left), full-pol simplified Gibbs 2 (middle,) and the difference between the two cases (right)*

| Pol | Gibbs 2 | Simp. Gibbs 2 | Difference |
|---|---|---|---|
| A3 | σ =2,10 K m=0,01 K | σ =2,11 K m=0,24 K | σ =0,93 K m=-0,23 K |
| A4 | σ =2,05 K m=0,62 K | σ =2,19 K m=0,48 K | σ =0,98 K m=0,13 K |

*Table 6.4 Summary of the results shown in Figure 6.7*

An estimation of the computation time per day of SMOS data acquisition is given in Table 6.5. In our workstation, processing a full orbit takes about 16 hours in the case of Full-Pol G-matrix Gibbs 2 image reconstruction and about 11 hours when the simplified case is taken into account. Therefore, there is a 31% reduction on computation time just by neglecting the second order terms in (6.4).

| Inversion approach | Computational time per day of SMOS data |
|---|---|
| Full-pol G-matrix Gibbs 2 | 16 hours approx. |
| Full-pol G-matrix Simplified Gibbs 2 | 11 hours approx.(-31%) |

*Table 6.5 Computational time per day for the different approaches*

All these results were presented in the international congress MicroRad 2016 (Espoo) [Durán *et al.*, 2016].

## 6.3 Iterative SMOS full-pol image reconstruction

An iterative method that makes use of the approximated term in (6.9) can be developed to further reduce computation time at the cost of a small radiometric performance degradation [Wu, 2014], [Font *et al.*, 2010]. The first attempts to use the iterative method were not successful due to the contribution of the floor error, especially harmful in the computation of the $T_H^{xy}$ term. However, in this work this problem is overcome by implementing a co-polar G-matrix Gibbs2 approach that exclusively makes use of the terms in (6.9). This iterative method consists of the following steps:

The first step is devoted to mitigate the "floor error" in the co-polar terms. That is, a first estimation of the terms $\hat{T}_H^{xx}$ and $\hat{T}_H^{yy}$ is given by means of the co-polar G-matrix pseudo-inverses where the error contribution from the temperatures outside the fundamental hexagon, estimated from (6.9), are subtracted from SMOS measurements before inversion (Gibbs 2 approach):

$$\begin{aligned} \hat{T}_H^{xx} &= (G_{xx}^{RR})^{-1}(V^{xx} - V_{NH}^{xx}) \\ \hat{T}_H^{yy} &= (G_{yy}^{RR})^{-1}(V^{yy} - V_{NH}^{yy}) \end{aligned} \tag{6.10}$$

The second step is devoted to mitigate the cross-polar contribution in the co-polar brightness temperatures, taking into account the estimation provided by the previous step:

$$\begin{aligned} \hat{T}_H^{xx}\,' &= \hat{T}_H^{xx} - (G_{xx}^{RR})^{-1} G_{xx}^{CC} \hat{T}_H^{yy} \\ \hat{T}_H^{yy}\,' &= \hat{T}_H^{yy} - (G_{yy}^{RR})^{-1} G_{yy}^{CC} \hat{T}_H^{xx} \end{aligned} \tag{6.11}$$

Note that $G_{xx}^{CC}$ and $G_{yy}^{CC}$ are defined exclusively in the hexagonal area. Note also that the four steps defined in (6.10) and (6.11) can be reduced to three steps to avoid one matrix multiplication and further improve computational speed.

Finally, the last step is devoted to measure the polarimetric term $\hat{T}_H^{xy}$, if required. In this last case, both the floor error and the cross-polar error contributions are removed at visibility level, before inversion, taking into account the results yielded by the previous steps and the last term in (6.9) as:

$$\hat{T}_H^{xy} = (G_{xy}^{RR})^{-1} \cdot (V^{xy} - V_{NH}^{xy} - V_{CP}^{xy}) \tag{6.12}$$

where:

$$V_{CP}^{xy} = G_{xy}^{RC} \hat{T}_H^{xx} - G_{xy}^{CR} \hat{T}_H^{yy} \tag{6.13}$$

Note that the terms $G_{xy}^{RC}$ and $G_{xy}^{CR}$ are defined in the hexagonal area and that the visibilities in (6.12) implicitly include the zero baseline. One additional advantage of this method is that the terms $T_H^{xx}$, $T_H^{yy}$, and $T_H^{xy}$ can be computed independently further reducing computation load in some application where not all terms are required (e.g. calibration fine tuning, L1 tests, monitoring, etc…).

Figure 6.8 shows the comparison between co-polar spatial bias computed with the different methods. Note that the simplified full-pol G-Matrix Gibbs 2 method and the iterative approach performances are very similar. In both cases there is a small radiometric degradation with relation to the full-pol Gibbs 2 approach, especially in Y polarization. Regarding the iterative approach, it must be pointed that additional iterations do not yield any significant improvement on radiometric performance, as shown in [Wu, 2014].

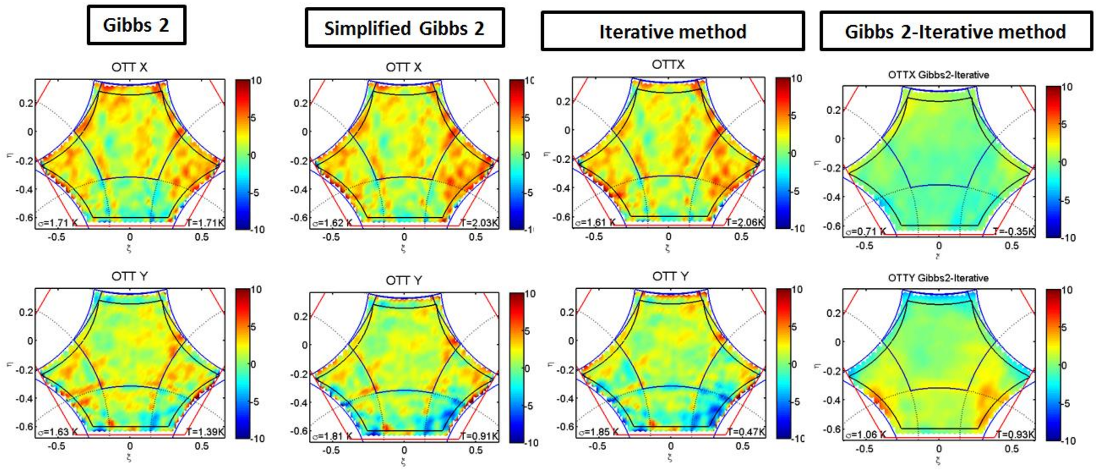

*Figure 6.8 Spatial bias (OTT) comparison for the full-pol Gibbs 2 approach (left), full-pol simplified Gibbs 2 (middle, left), iterative method (middle right) and the difference between the first and last cases (right)*

| Pol | Gibbs 2 | Simp. Gibbs 2 | Iterative method | Difference |
|---|---|---|---|---|
| XX | σ =1,71 K<br>m=1,71 K | σ =1,62 K<br>m=2,03 K | σ =1,61 K<br>m=2,06 K | σ =0,71 K<br>m=0,35 K |
| YY | σ =1,63 K<br>m=1,39 K | σ =1,81 K<br>m=0,91 K | σ =1,85 K<br>m=0,47 K | σ =1,06 K<br>m=0,93 K |

*Table 6.6 Summary of the results shown in Figure 6.8*

Figure 6.9 shows spatial bias comparison for the 3rd and 4th Stokes regarding the same cases given in Figure 6.8. Note that in this case the approximation given in (6.9) does not result in significant performance degradation.

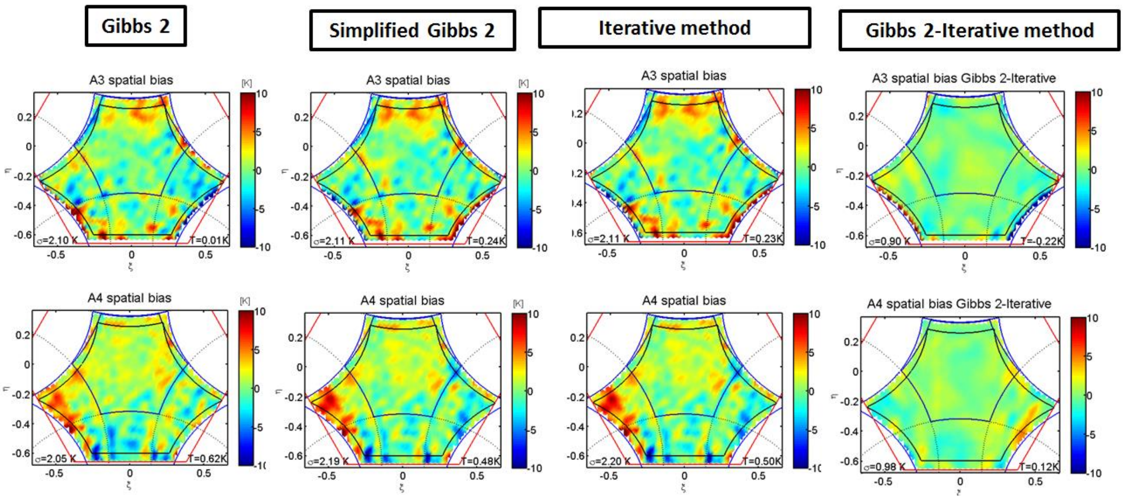

*Figure 6.9 Spatial bias (OTT) comparison 3rd and 4th Stokes*

| Pol | Gibbs 2 | Simp. Gibbs 2 | Iterative method | Difference |
|---|---|---|---|---|
| A3 | σ =2,10 K<br>m=0,01 K | σ =2,11 K<br>m=0,24 K | σ =2,11 K<br>m=0,23 K | σ =0,90 K<br>m=0,22 K |
| A4 | σ =2,05 K<br>m=0,62 K | σ =2,19 K<br>m=0,48 K | σ =2,20 K<br>m=0,50 K | σ =0,98 K<br>m=0,12 K |

*Table 6.7 3rd and 4th Stokes spatial bias*

An estimation of the computation time per one day SMOS data acquisition is about 16 hours by using Full-Pol G-matrix Gibbs 2 image reconstruction and about 11 hours with the simplified Full-Pol G-matrix Gibbs 2 case based on (6.9). Therefore, there is a reduction of 5 hours per day just by neglecting the second order terms in (6.6). In the particular case where only TX or TY are required (e.g. for monitoring or L1 support), computational time is further reduced from 16 hours to 8 hours by using the co-polar G-matrix iterative approach, at the cost of a small performance degradation.

| Inversion approach | Computational time per day of SMOS data |
|---|---|
| Full-pol G-matrix Gibbs 2 | 16 hours approx. |
| Full-pol G-matrix Simplified Gibbs 2 | 11 hours approx. |
| Co-polar G-matrix Iterative (all terms) | 12 hours approx. |
| Co-polar G-matrix Iterative (Only Tx or Ty) | 8 hours approx. |

*Table 6.8. Computational time per day for the different approaches*

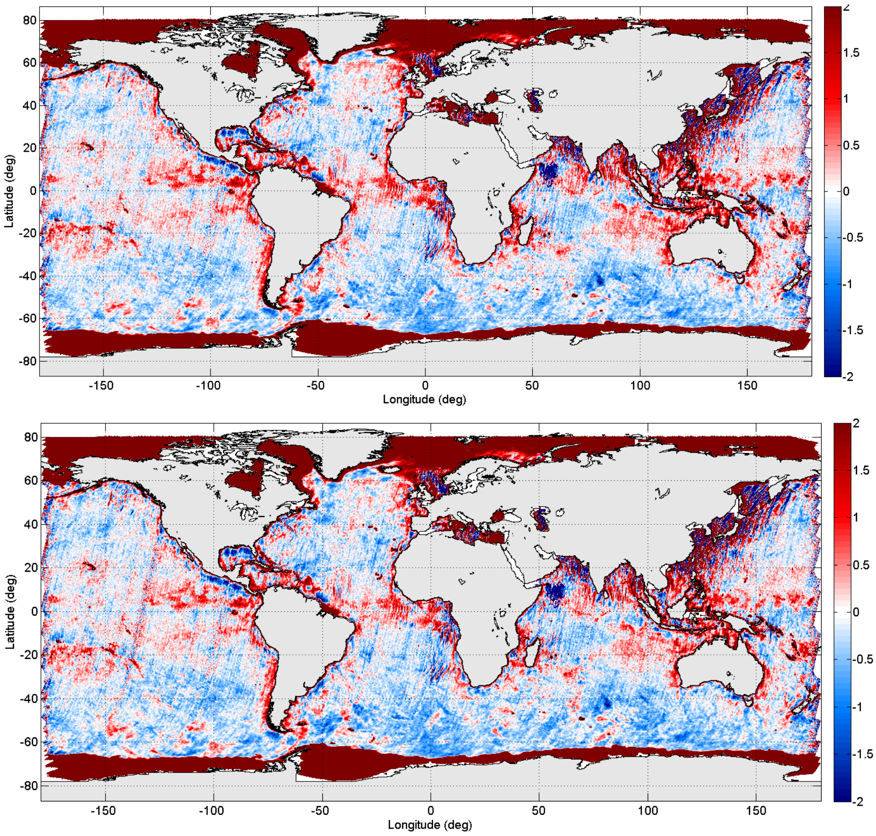

*Figure 6.10 1st Stokes SMOS global error map (10 days data). Full-pol G-matrix Gibbs 2 (top) and Simplified Full-pol G-matrix Gibbs 2 (bottom)*

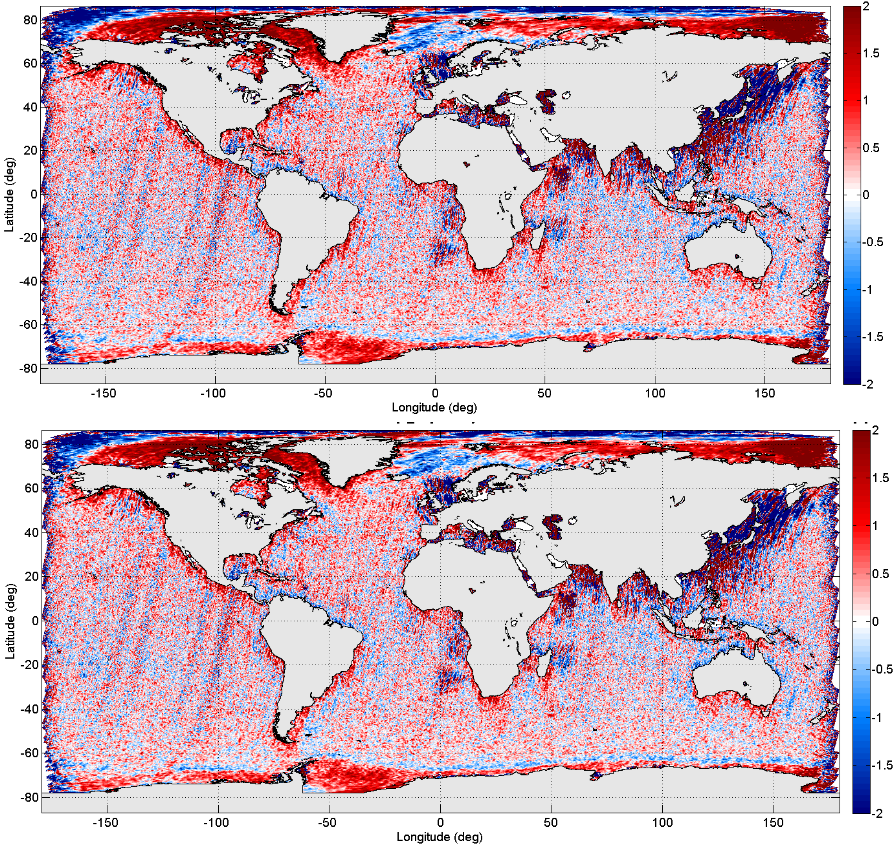

*Figure 6.11 4th Stokes SMOS global error map (10 days data). Full-pol G-matrix Gibbs 2 (top) and Simplified Full-pol G-matrix Gibbs 2 (bottom)*

In order to further assess the impact of the approximation given in (6.9), several 1st and 4th Stokes global error maps have been computed from SMOS real data (orbits from 1st May to 11th May 2011). In this case, the full-pol G-matrix Gibbs 2 image reconstruction is compared to the simplified full-Pol G-matrix Gibbs 2 case. In both approaches the LSC (land-sea contamination) artifact has been mitigated by applying a 2% correction factor on measured correlation efficiency [Corbella *et al.*, 2015a], [Corbella *et al.* 2015b]. In addition, an OTT (Ocean Target Transformation) computed over the Pacific Ocean has been applied to all sea pixels to reduce spatial bias. Figure 6.11 shows that the differences between the two cases are hardly seen in a ±2 K scale 1st Stokes global error map (0-60º incidence angle averaging). A similar conclusion is derived from Figure 6.11regarding 4th Stokes error map.

From the previous figures (global error maps) it can be concluded that simplified Full-pol G-matrix Gibbs 2 provides very similar results to the case without simplification but the computational time is reduced in around a 30%.

All these results were presented in the international congress IGARSS 2016 (China) [Durán *et al.,* 2016].

## 6.4 Conclusions

The work described in this chapter show that, once the cross-polar antenna patterns are taken into account by means of the full-pol G-matrix, the dominant source of spatial bias on A3 and A4 is the floor error. This last is dominated by $T_x$ and $T_y$ brightness temperature outside the fundamental hexagon that leaks into A3 and A4 AF-FoV through antenna cross-polar antenna patterns and a G-matrix inversion that does not fulfill Fourier alias properties. It has been shown that this floor error can be very much mitigated by a simple Gibbs 2 model approach, exclusively defined outside the fundamental hexagon [Corbella *et al.,* 2014], [Corbella *et al.,* 2015b]. Moreover, this chapter has analyzed two simplified image reconstruction methods to retrieve SMOS full-polarimetric brightness temperatures: a simplified full-pol G-matrix and a co-polar G-matrix iterative method. In both cases the inversion is simplified by exclusively taking into account the dominant terms in the full-polarimetric equation. These methods have been compared to the full-pol G-matrix case where all terms are included in the computation of the Moore-Penrose pseudo-inverse. To perform the comparison a Gibbs 2 approach has been implemented to mitigate the so-called “floor error” in the retrieved brightness temperature images. It has been shown that the simplified image reconstruction methods can reduce computation time up to 50% at the cost of a small radiometric performance degradation. These simplified methods are useful to the L1 teams to fine tune the calibration of the instrument or for monitoring purposes, when processing a large amount of data is required [Durán *et al.*, 2016a], [Durán *et al.*, 2016b]

# 7 Land Sea Contamination (LSC) in SMOS

## 7.1 Introduction to the LSC problem

Since its launch in November 2009, the European Space Agency’s (ESA) Soil Moisture and Ocean Salinity (SMOS) mission has provided a large amount of valuable and consolidated geophysical data over land, ice, and ocean. Since there is still room for refinement, the SMOS mission operation relies on “Expert Support Laboratories” (ESL) responsible of defining new algorithms and methodologies to further improve the quality of SMOS products. This activity is crystallized in the periodic development of data processor versions at different levels. For example, the latest Level-1 operational processor (L1OP v620) become nominal in spring 2015 and has been used in the second mission reprocessing completed in September 2015. Among other calibration enhancements described in chapter 5 and chapter 6, this version includes a fully polarimetric image reconstruction scheme.

Preliminary analysis of the reprocessed data confirms an important improvement in the data quality, particularly in the third and fourth Stokes parameters. Discretization of the visibility equation converts it to a system of linear equations, which is solved by standard linear algebra as summarized in section 2.3 [Camps *et al.*, 2008]. This process, often referred to as “image reconstruction,” is much more involved than at first glance would seem. Antenna pattern differences between elements, antenna characterization uncertainties, calibration errors, aliasing, solar and galactic radiation, and other effects produce non negligible artifacts that have to be mitigated using specific techniques.

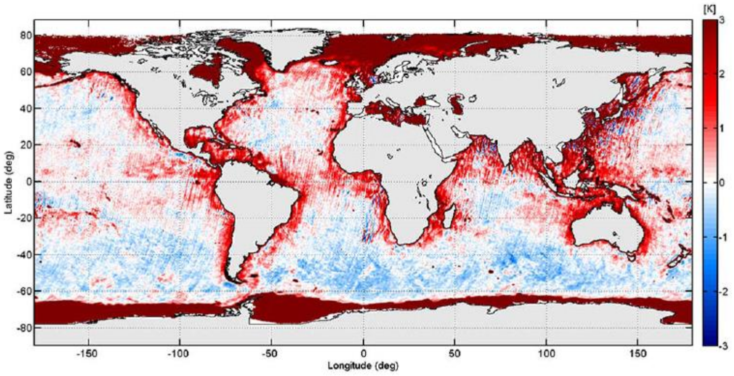

*Figure 7.1 SMOS $T_B$ map showing LSC*

This chapter is devoted to one residual error that persists, it is called “land–sea contamination” (LSC) and consists fundamentally of a slight increase in brightness temperature of water in zones near large land areas [Corbella *et al.*, 2015a], [Corbella *et al.*, 2015b]. This contamination extends to distances much larger than the relatively low resolution that the instrument would predict. It was reported early in the mission by the SMOS ocean science team to be associated generally with both positive and negative biases, and it has been, so far, the most important limitation in using SMOS data for coastal areas. It is important for salinity retrieval since the first Stokes parameter varies by only about 1 K/psu. Part of the LSC can be attributed to the so-called floor error and can be slightly reduced by using differential techniques before visibility inversion as Gibbs 2 presented in chapter 6. However, no image reconstruction method has yet been able to fully cancel this artifact. This chapter presents an analysis of the problem, describes a second mechanism that produces LSC, and proposes a method to mitigate this contribution as developed by the RSlab team.

## 7.2 Origin of LSC

As shown in chapter 2 for a given antenna pair, *(u,v)* are defined respectively as the relative *(x, y)* coordinates of one antenna with respect to the other normalized to the center wavelength. The particular case of the origin u=v=0 corresponds to both antennas collapsing in a single location. In this case, the visibility becomes equal to the antenna noise temperature for this particular element $V_0=T_A$. MIRAS uses three redundant noise-injection radiometers (NIRs) to measure the visibility at zero spacing and digital correlators to measure the rest of the visibility samples. As it will be seen in the following paragraphs, this different implementation is important in the assessment of the LSC problem. Since the zero-spacing visibility is the average antenna temperature of the scene measured with antennas having a very wide pattern, it has contributions from all the sources in front of the instrument. When the boresight travels from ocean to land, the antenna temperature starts increasing as soon as the main lobe of the antenna pattern reaches the coast. Due to the large antenna beamwidth, it starts when the instrument boresight is still at large distances from the coast. This feature itself would not produce LSC, since the image reconstruction synthesizes a narrow pattern at each pixel, and those pointing to the ocean would not be affected. LSC would be observed if an error scaling with antenna temperature is present in the retrieved image. The purpose of the analysis presented as follows is to demonstrate that this error is present and to find its origin.

As shown in chapter 3, brightness temperature is a function of two variables named ξ and η defined as the direction cosines with respect to the instrument reference frame *(x, y)*. It is obtained in the retrieval process as a column vector having as many rows as *(ξ, η)* grid points. Specifically, it is the result of multiplying the pseudoinverse of the G-matrix, i.e., $G^+$, by the vector of measured visibility samples, including the ones at zero spacing and the rest. This means that $G^+$ has as many columns as measured visibility samples in the *(u, v)* plane and as many rows as *(ξ, η)* grid points. The matrix multiplication $T = G^+V$ can then be rewritten as

$$T = G_0^+V_0 + G_{kj}^+V_{kj} \tag{7.1}$$

Where $G_0^+$ is the column of $G^+$ corresponding to *u=v=0* and $G_{kj}^+$ the other columns of the matrix. This equation is useful to introduce errors separately in the zero-spacing visibility $V_0=V(0,0)$ and in the other samples $V_{kj}$ . Errors in these two terms are different because measurement techniques are also different in both cases. For the following error analysis, the measured magnitudes (represented with a hat) are assumed to be related to the error free ones, taking into account a constant multiplicative error $\varepsilon$. The three cases that are taken into account are the following:

a) Error affecting only the zero-spacing visibility (antenna temperature). In this case, $\hat{V}_0 = V_0(1+\varepsilon)$, which substituted into (7.1) results in:

$$\hat{T} = G_0^+ V_0(1+\varepsilon) + G_{kj}^+ V_{kj} = T + G_0^+ V_0 \varepsilon \tag{7.2}$$

b) Error present only in the nonzero-spacing visibility samples. In this case, $\hat{V}_{kj} = V_{kj}(1+\varepsilon)$, and the brightness temperature vector (7.1) becomes:

$$\hat{T} = G_0^+ V_0 + G_{kj}^+ V_{kj}(1+\varepsilon) = T(1+\varepsilon) - G_0^+ V_0 \varepsilon \tag{7.3}$$

c) Error in all visibility samples. In this case, the separation into two types of visibility samples has no effect. Directly from the general equation:

$$\hat{T} = G^+ V(1+\varepsilon) = T(1+\varepsilon) \tag{7.4}$$

That is, the retrieved brightness temperature is simply affected by a scale factor with the sole effect of degrading absolute accuracy. Cases a) and b) show an error term (the second one) that scales with the zero-spacing visibility $V_0$, which is the antenna temperature; hence, they will give rise to LSC error. Note the sign difference of this term in both cases. This error term is also weighted by the zero-spacing column of the inverse G-matrix $G_0^+$. This is a function of $(\xi, \eta)$ approximately equal to the reciprocal of the power antenna pattern $|Fn(\xi,\eta)|^2$ normalized with respect to the antenna solid angle $\Omega_p$ and the obliquity factor as follows:

$$G_0^+ V(\xi,\eta) \approx \frac{\Omega_p \sqrt{1-\xi^2-\eta^2}}{|F_n(\xi,\eta)|^2} \tag{7.5}$$

When drawn as function of *(ξ, η)*, it shows a kind of "bowl shape" being minimum at boresight and growing continuously to the extremes of the field of view. The error terms in both (7.2) and (7.3) should inherit this shape. In conclusion, only cases a) and b) produce LSC due to the presence of an error term depending on the antenna temperature. Contributions from one or the other are opposite in sign. Case c) does not yield any LSC. Additionally, cases b) and c) have a multiplicative error at each spatial direction (a scale factor).

## 7.3 Modeling the LSC artifact at L1

An end-to-end simulation using a Fresnel (specular) model of the ocean has been carried out to confirm the theoretical findings. First, an instrument model (G-matrix) is used to compute the expected visibility; then, a multiplicative error is applied either to antenna temperature or to the nonzero-spacing visibility samples, and finally, image reconstruction is performed using the inverse of the G-matrix. No other source of error has been included; in particular, the floor error has been eliminated by setting to zero the brightness temperature at points outside the principal hexagon. Figure 7.2 (left) shows that a 5% amplitude error on the zero-spacing baseline, i.e., case a), produces a similar bowl-shaped spatial error distribution in brightness temperature than a negative 5% amplitude error only affecting the set of nonzero-spacing visibility samples, i.e., case b), Figure 7.2 (right).

Although the error distribution is similar in both plots, in the second case, the retrieved image has a positive 5% scale factor that leads the overall scene mean error to be zero. This is consistent with the fact that there is no error in the zero baseline (zero spatial frequency). Note that both color bars have the same 4,5 K range, centered at their mean error value.

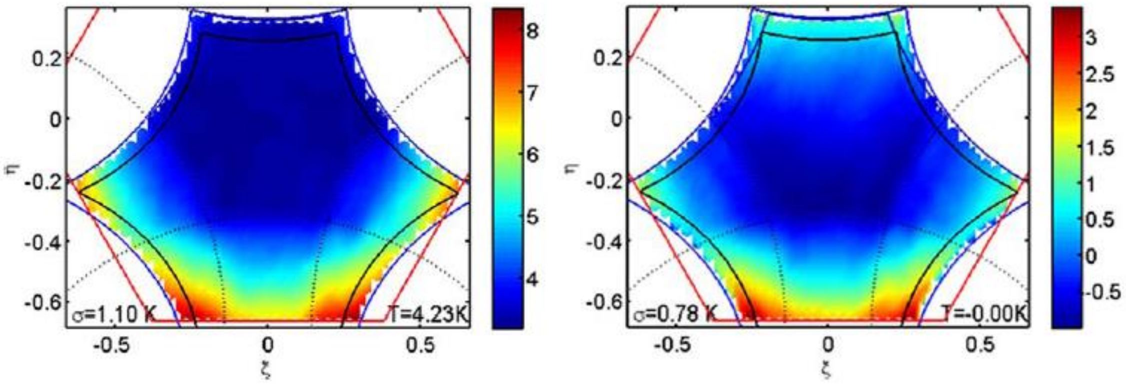

*Figure 7.2 Simulation of the spatial error (horizontal polarization) over pure ocean (Fresnel model) due to a 5% amplitude error on TA (left) and a negative 5% error on the visibility samples (right)*

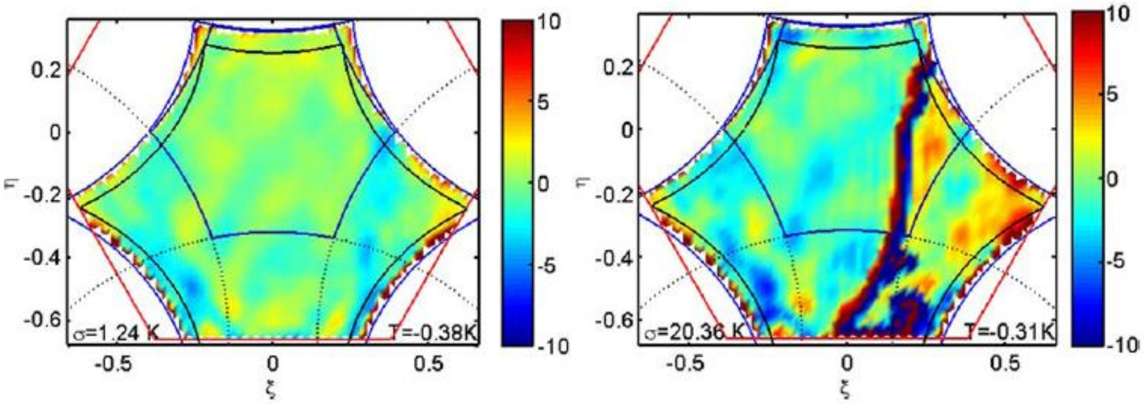

*Figure 7.3 Simulation of the expected spatial error in the first Stokes parameter divided by two due to the combined effect of floor error and a 2% amplitude error on the visibility samples over ocean (Fresnel model) for a pure ocean scene (left) and a mixed land–sea scene (right). Land is modeled at a constant Tb = 280 K. In the mixed scene, LSC is dominated by the contribution from the floor error*

The simulations in Figure 7.3 show the predicted error in the first Stokes parameter divided by two for pure (left) and mixed land–sea (right) snapshot scenes. In the whole UC ocean is modeled as in the previous simulation and land as constant brightness temperature at 280 K. In this case, a 2% amplitude error has been artificially included, but no error reduction mechanisms have been applied; hence, the spatial biases and floor error artifacts are also present. Comparing both images, it is apparent that the error in the ocean part changes in the presence of nearby land masses. The error image at the left is not zero because of the floor error, which is the spread of aliasing into the alias-free zone due to having non identical antenna patterns as shown in chapter 5. In practice, this error can be evaluated and subtracted to all measurements, in order to produce cleaner images. This technique is commonly used by the SMOS ocean science team to correct data and retrieve salinity with higher accuracy, and it is usually referred to as "OTT correction" [Font *et al.,* 2010]. With this definition, the image at the left in Figure 7.3 is the OTT simulated from the pure ocean scene. If it is used to correct the ocean pixels in the mixed scene (see Figure 7.3, right), the error does not cancel but becomes proportional to the antenna temperature difference between the pure ocean and the mixed land–sea scene, thus producing LSC. The simulations in Figure 7.4 clearly show this effect when a negative 2% error in the visibility samples other than $V_0$ is taken into account, i.e., case b). Three snapshots along a descending orbit over the Pacific (leftmost figure) are selected in this example. The pure Fresnel ocean scene in Figure 7.3 (left) is selected as reference (OTT) to correct for spatial errors. Obviously, when applied to this reference image, the OTT corrects for all errors (see Figure 7.4, center-left). However, for mixed land–sea scenes, when the sea pixels are corrected with the OTT, the mean error increases as the land masses enter into the single antenna beamwidth (see Figure 7.4, center-right and rightmost). The bowl shape effect over the ocean is also clearly seen in the last case.

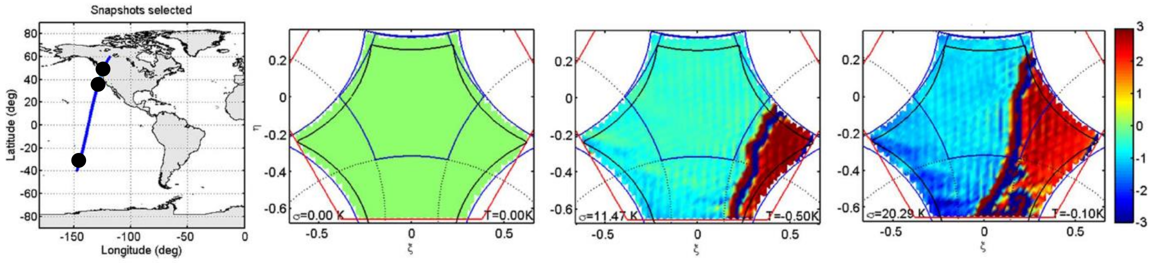

*Figure 7.4 Simulation of the expected spatial error, after applying the OTT, due to a 2% error on the visibility samples for three snapshots in a descending orbit (leftmost). The OTT corrects both spatial bias and mean error in the reference snapshot (center-left). As land enters into the single antenna beamwidth, the amplitude error yields an incremental bias proportional to antenna temperature difference with respect to the reference scene that affects the ocean pixels (center-right and rightmost)*

The ripple is related to the Gibbs effect due to the sea–land transition. In order to better highlight the impact of the LSC, the floor error has been eliminated in these simulations (Figure 7.4) by setting to zero the brightness temperature of the forward model at points outside the principal hexagon, as described in chapter 5, section 5.3 (in a real case the Gibbs 2 model approach produces a similar effect).

The visibility sample measured by a pair of MIRAS receivers k and j is computed from the measured magnitudes according to

$$V_{kj} = \frac{M_{kj}}{G_{kj}} \sqrt{\frac{v_k - v_{offk}}{G_k} \frac{v_j - v_{offj}}{G_j}} \tag{7.6}$$

where the raw measurements are the normalized complex correlation $M_{kj}$ (measured by the digital correlator) and the voltages $v_{k,j}$ measured by the power measurement system (PMS) implemented in each receiver as described in chapter 3, section 3.1.2. The other terms are calibration parameters: the correlator efficiency $G_{kj}$ and the PMS gains and offsets $G_{k,j}$ and $v_{offk,j}$, respectively. During normal operation, the instrument goes periodically into calibration mode to measure and update them [Brown *et al.*, 2008]. In the absence of antenna temperature error, multiplicative errors in $v_{k,j}$ contribute to LSC, i.e., case b). This can be only produced by PMS gain and/or correlation efficiency calibration errors. On the other hand, the zero-spacing visibility is the antenna temperature measured by the NIR units. For each one, it is retrieved (neglecting second-order corrections) using:

$$T_A = T_U - \eta T_{NA} \tag{7.7}$$

where $\eta$ is the measured fraction of the Dicke cycle, and $T_U$ and $T_{NA}$ are the internal load physical temperature and the noise diode injected temperature, respectively, both of them referred to the antenna reference plane [Corbella *et al.*, 2005b], [Colliander *et al.*, 2007]. This last parameter ($T_{NA}$) is periodically measured and updated during instrument calibration operation, and $T_U$ is measured by a thermal sensor. Equations for conversion to antenna reference plane use nominal on-ground characterized parameters. In the latest version of the L1OP, only one of the three NIRs is used since it shows improved seasonal and long-term stability. LSC is caused by a multiplicative error in $T_A$, which can only be present if there is a calibration error of $T_{NA}$. In other words, the calibration error contribution to LSC is a multiplicative error in $T_A$. Amplitude calibration errors on the visibility and on the antenna temperature are decoupled; hence, both contribute to LSC in a different proportion. It even may happen that an empirical correction in one of them, adding a positive error for example, compensates a negative error in the other, yielding good performance in terms of LSC but poor calibrated science data due to increased absolute amplitude error.

In order to identify the origin of LSC, antenna temperature has been recomputed using the PMS of each of the individual receivers (all LICEF mode), which is calibrated by the same gains and offsets as in (7.6) as described in chapter 3, section 3.4. In this mode, SMOS data are processed from level 0, in order to bypass the calibration procedures of the L1OP. The zero-spacing visibility is then computed as the mean antenna temperature measured by the 69 power detectors in each single receiver, according to the one-point calibration scheme as follows [Torres *et al.*, 2006]:

$$T_A = \left\langle \frac{v_k - v_{offk}}{G_k} - T_{Rk} \right\rangle \tag{7.8}$$

where $T_{Rk}$ is the noise temperature of receiver k. Calibration errors on $v_{offk}$ and $T_{Rk}$ are discarded as the source of LSC since they produce a scene-independent additive (constant) error on the antenna temperature that is removed by the OTT. According to (7.6) and (7.8), a common power detector gain calibration error affecting all units $\hat{G}_k = G_k(1+\Delta G)$ produces the same amplitude error in both antenna temperature and visibility samples. In consequence, using the receivers' antenna temperatures for estimating the zero-spacing visibility should not produce LSC, unless the visibility error comes from the term $G_{kj}$ in (7.6). Since LSC has been observed in this case, the conclusion is that there is a calibration error affecting the correlator efficiency. If the amplitude error is related to the correlator efficiency $\hat{G}_{kj} = G_{kj}(1+\Delta G)$, this impacts only the visibility samples measured through correlation, yielding the LSC effect described in (7.3)-(case b). In the all LICEF mode, this happens to be the only source of LSC, and this feature has been used to identify a 2% mean overestimation of correlator efficiency as the source of LSC. The value and origin of this 2% error is investigated in the following sections. Correlation efficiency is periodically measured onboard using the procedures described in chapter 3 (section 3.4) , but some underlying assumptions, such as dominant RF filter response, in-phase/quadrature branches' similarity, or quadrature error correction, induce small but relevant uncertainties that degrade the accuracy of the retrieval.

However, it has been concluded that the decorrelation effect that this imperfection could produce would have been corrected by the selfcalibration procedure that yields decomplex, quadrature corrected normalized correlations $M_{kj}$ [Corbella *et al.*, 2005b]. Other possible causes of this decorrelation are investigated in the following section.

## 7.4 Mitigation of LSC at L1

This section is devoted to estimate the optimum $G_{kj}$ factor to mitigate LSC. In order to perform this analysis several geophysical scenarios have been taken into account. The main scenario is the so called “Vancouver orbit” (Figure 7.5).

The metric for the Land-sea contamination is defined by using the orbit of 2 may 2011 in the Vancouver area using the following procedure [ESA, 2015]:

1. Obtain brightness temperature of the two polarizations
2. Compute OTT for X and Y as the difference between the brightness temperature and the ocean forward model provided by J.Tenerelli averaging snapshots in the range of nadir latitudes from -40º to -5º
3. Remove the OTT above from all snapshots
4. Compute the first Stokes divided by 2
5. Keep only the values of T1 corresponding to xi-eta grid points within extended alias-free field of view
6. Subtract to T1 the model for each snapshot
7. Select a polygon in longitude and latitude around the coast and make the average of all values that fall inside

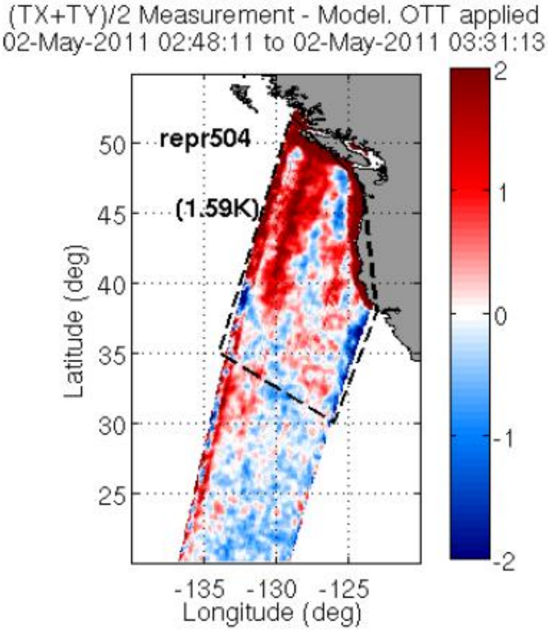

*Figure 7.5 Vancouver orbit (reference)*

Figure 7.6 shows the Vancouver orbit using different correction factors in order to find the optimum one, it is possible to assess that the candidate is around 2% that corresponds to the 0,98 factor.

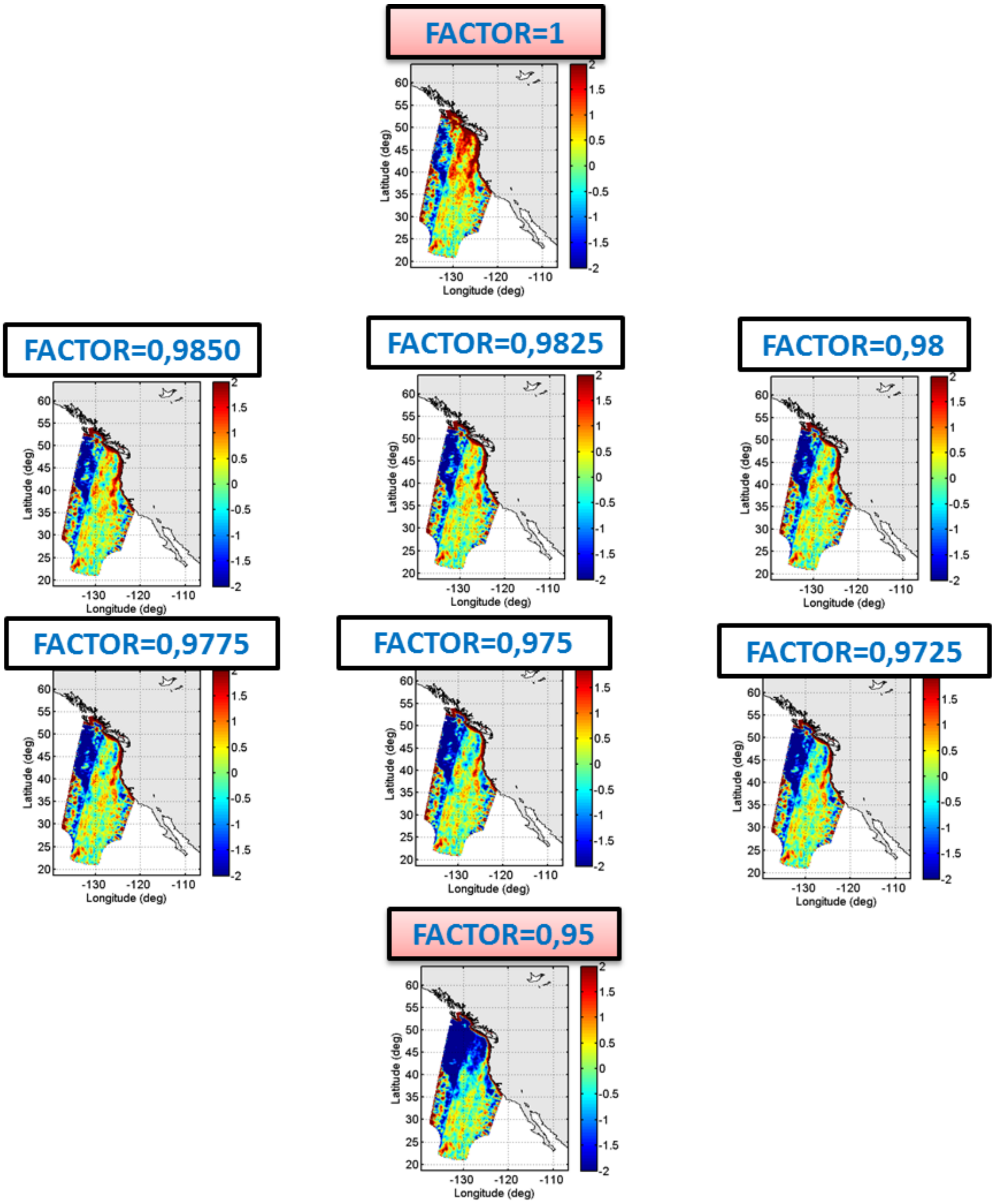

*Figure 7.6 Vancouver orbit using different $G_{kj}$ correction factors*

Figure 7.7 shows an orbit over Chile using different correction factors in order to find the optimum one, it is possible to assess that the candidate is around 2% that corresponds to the 0,98 factor.

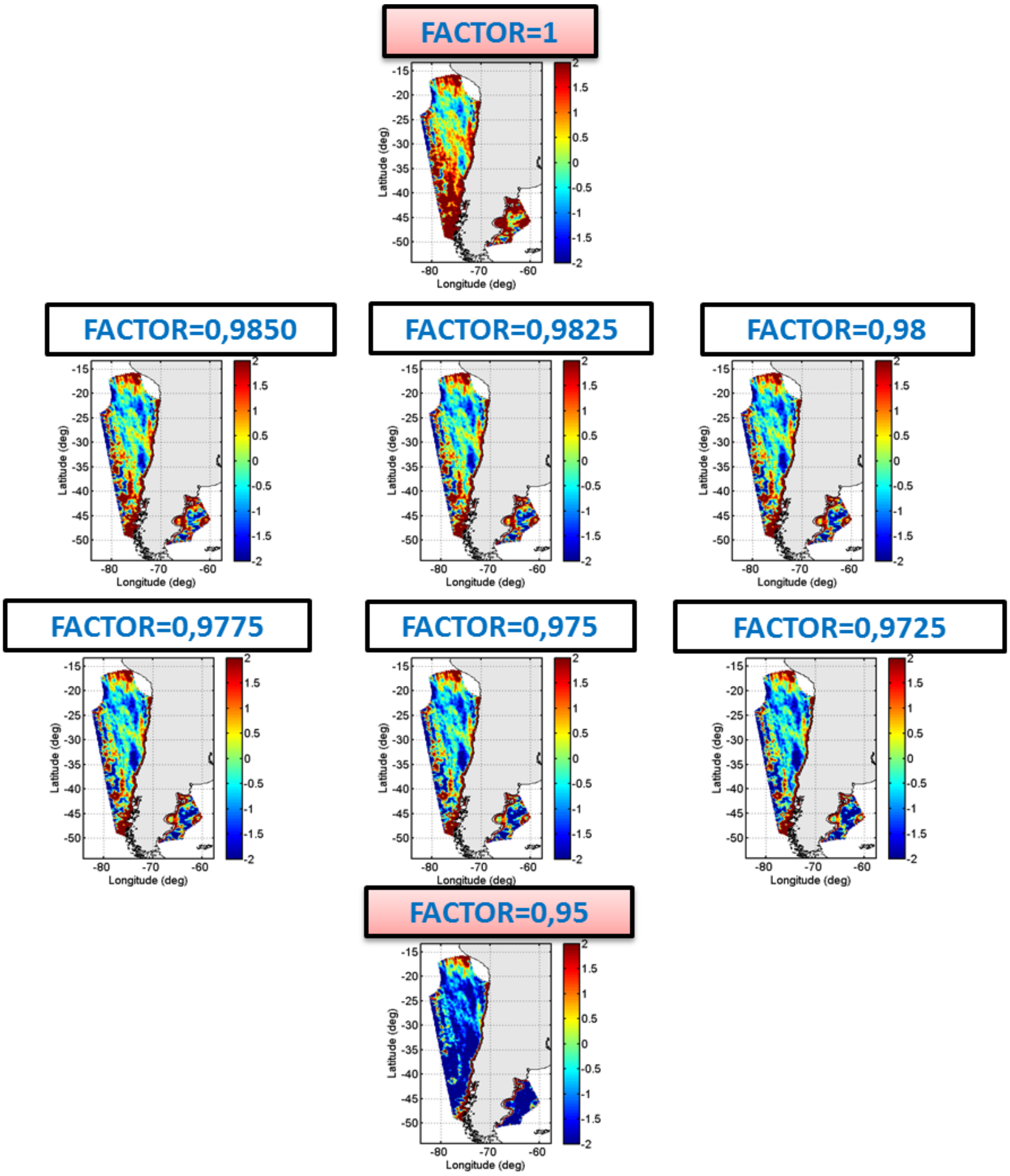

Figure 7.7 Chile orbit using different $G_{kj}$ correction factors

Figure 7.8 shows another representation of Figure 7.7 but in this case taking into account that the best candidate for the factor is around 2% and doing the difference of both.

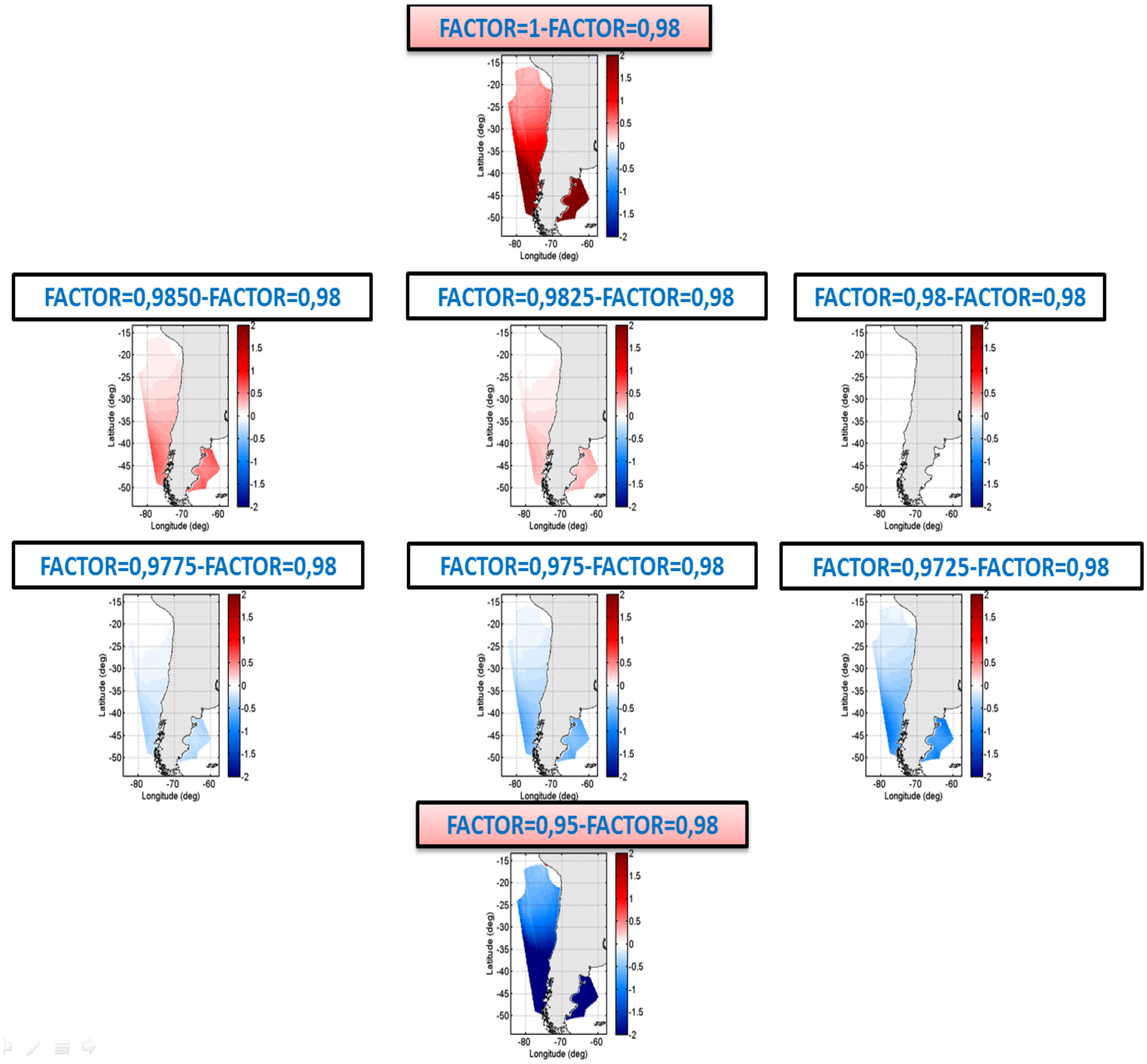

*Figure 7.8 Chile orbit (checking $G_{kj}$ factor)*

Some other orbits are assessed to confirm the validation of the 2% factor for different areas of the earth map. Figure 7.9 shows an orbit that cross Chile, in that case the factor is around 1,8%. Validation and further refinement of the 2% $G_{kj}$ factor requires a close interaction with the OS scientific teams to select the appropriate scenarios and discard unexpected geophysical contributions that may make the result (river discharge, high current, wind, etc).

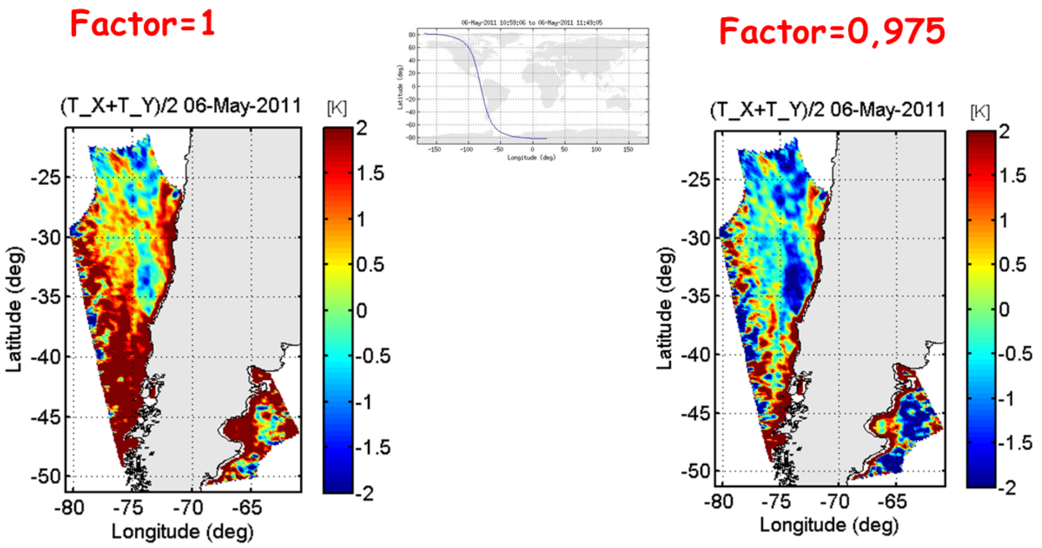

*Figure 7.9 Chile orbit*

Figure 7.10 shows an orbit in Australia, in that case the optimum factor is around 1,8%.

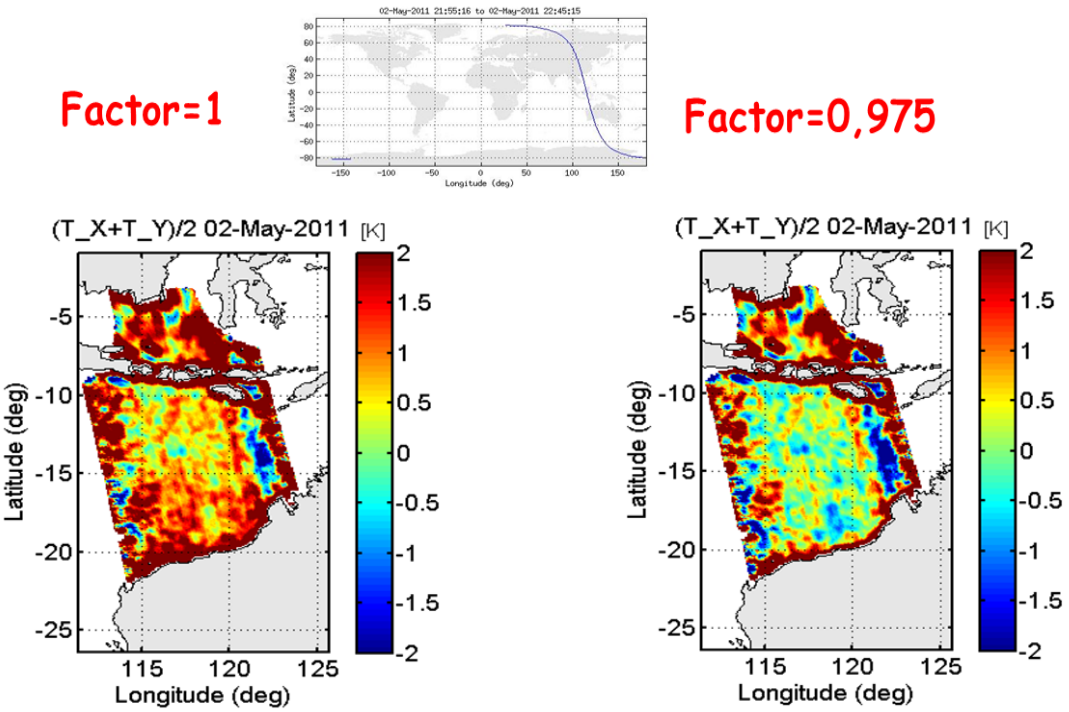

*Figure 7.10 Australia orbit*

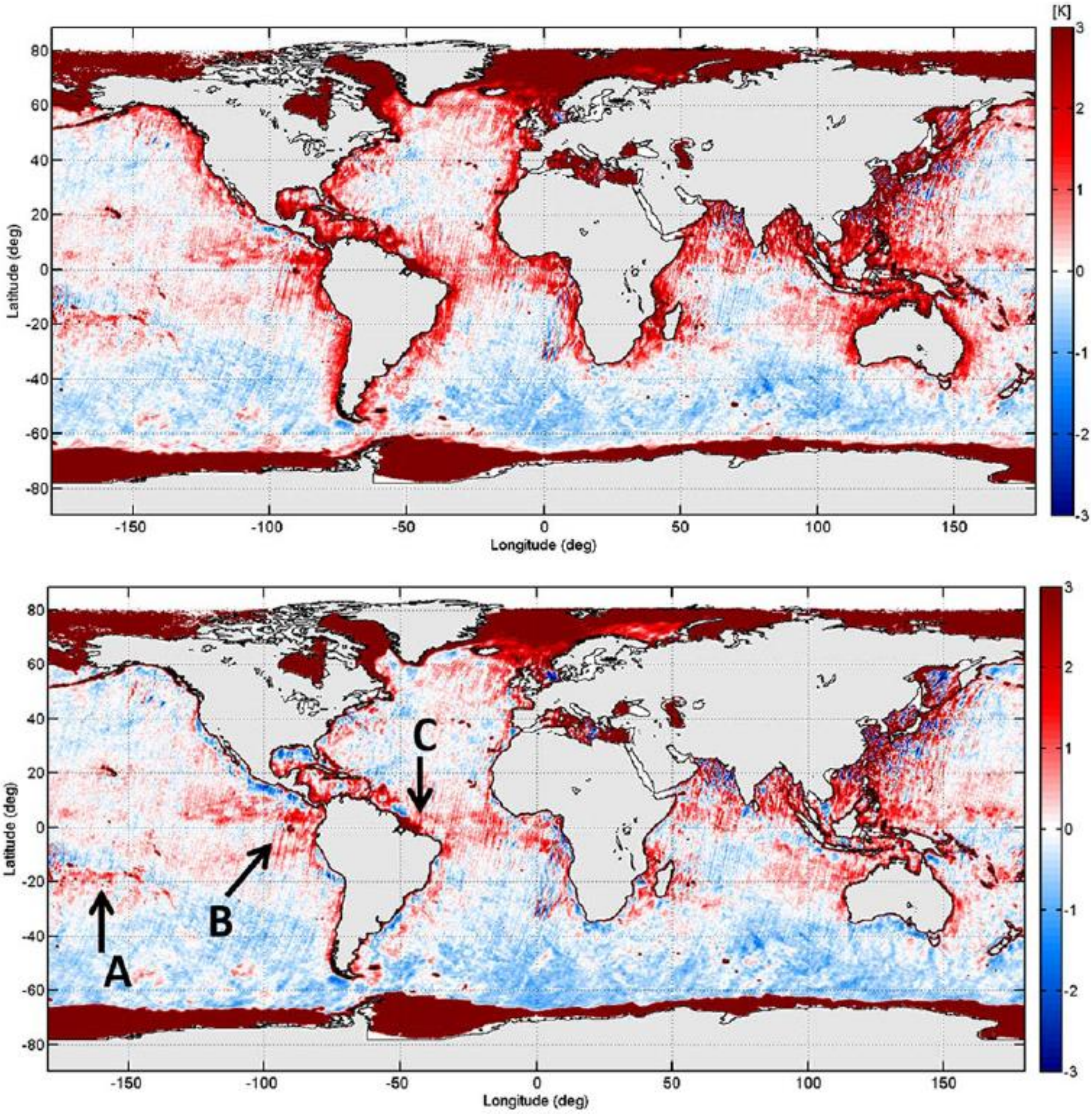

*Figure 7.11 Global error map of first Stokes parameter divided by two for descending orbits over the ocean after applying the OTT before (top) and after (bottom) applying a 2% correction on the measured correlation efficiency. Averaging: May 1–10, 2011; 0–60 ◦ incidence angle. Error relative to the ocean model provided by J.Tenerelli*

Figure 7.11 (top) shows a composite error map (measurement minus model) of the first Stokes parameter divided by two for descending orbits. Data are processed using the all LICEF mode, subtracting to all snapshots a single OTT computed from amid-Pacific set of consecutive snapshots. The global reference map has been provided by the SMOS ocean science team using the salinity reference of the World Ocean Atlas 2009 [Antonov *et al.*, 2009] and a model similar (but not identical) to that described in [Zine *et al.*, 2008]. Spatial and time averaging has been applied to yield the final global map (10 days: May 1–10, 2011; 0º–60º angle of incidence). In this map, the LSC effect is clearly seen as a region of warmer brightness temperature surrounding the land masses. However, as shown in the same composite map, after applying a 2% correction on correlator efficiency (see Figure 7.11, bottom), LSC contamination is very much mitigated while keeping geophysical features, e.g., the mid-Pacific warmer area (A), the Panama upwelling (B), or the Amazon River Plume (C). Figure 7.12 plots the difference between the two maps in Figure 7.11, showing that, as expected, the correlator efficiency correction exclusively affects the areas close to the land masses. The residual LSC still observed in Figure 7.12 is probably due to the floor error contribution, which has not been removed (these simulations were performed using the Gibbs 1 approach) or near coast geophysical signatures not taken into account by the model (e.g. river plumes).

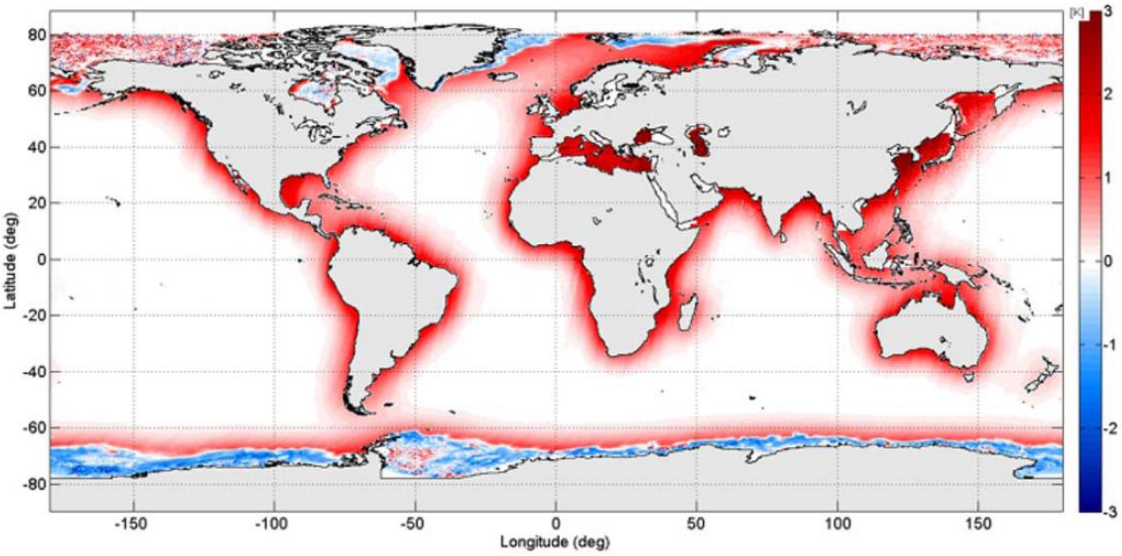

*Figure 7.12 Difference between the two all LICEF maps in Figure 7.11 to show that the 2% correction on correlation efficiency exclusively affects the regions close to land masses*

All these results were presented in a Geoscience and Remote Sensing Letters, IEEE , “Impact of correlator efficiency errors on SMOS land-sea contamination” [Corbella *et al.*, 2015a] and in the international congress IGARSS 2015 (Milán) [Corbella *et al.*, 2015b].

## 7.5 Validation of LSC mitigation in OS retrievals

This section is devoted to validate at brightness temperature and OS retrievals level the LSC artifact mitigation procedure developed in the frame of this PhD.

This section summarizes the work developed in the SMOS BEC (Barcelona Expert Center) [González-Gambau *et al.*, 2017] by the OS team to assess the benefits retrieving salinity maps in coastal regions while applying two correction techniques that enhance the quality of brightness temperature measurements: the correction of residual multiplicative errors at calibration level (method proposed in the previous section of this chapter) and the nodal sampling at imaging level (for the reduction of Gibbs-like contamination) developed by the SMOS BEC team [González-Gambau *et al.*, 2017] called nodal sampling.

Nodal sampling allows to deal with the Gibbs-like contamination produced by any abrupt change in the brightness temperature images. Salinity retrievals from these corrected brightness temperatures were validated with in-situ measurements (Argo floats), showing a clear improvement in open ocean [González-Gambau *et al.*, 2015], [González-Gambau *et al.*, 2016]. The main conclusion of that work was that the application of nodal sampling leads to an increase in the number of valid measurements and to a general reduction of the error in salinity retrievals.

However, in regions close to land, the application of nodal sampling leads to a systematic increase of brightness temperatures around the coasts. This is probably a consequence of the removal of the oscilating, Gibbs-like errors that highlights the systematic deviation of land-sea contamination

In the work presented in [González-Gambau *et al.*, 2017], these systematic biases are mitigated using the 2% correction presented in the previous sections. It is showed that the LSC comes from two main contributors: the floor error, that is, the inherent error associated to the image reconstruction procedure and the residual multiplicative errors affecting differently the zero-spacing visibility and the rest of the visibilities (dominant contribution). In [Corbella *et al.*, 2015a], the use of the all LICEF mode allowed to investigate the origin of these residual multiplicative errors because it is insensitive to any antenna temperature error (e.g. due to orbital or seasonal drift). As demonstrated in the previous section, a common power detector gain calibration error affecting all units produces the same amplitude error in both antenna temperature and visibility samples. In consequence, using the receivers antenna temperatures for estimating the zero-spacing visibility should not produce land sea contamination, unless the visibility error comes from an overestimation of the efficiency of MIRAS correlators. In particular, it is shown in the previous section that applying a 2% multiplicative correction through the correlator efficiency led to an improved calibration and a significant reduction of the main contributor to the LSC. It is important to remark that this correction is applied globally, independently of the scene which is being measured by the instrument.

The impact of introducing the proposed corrections has been assessed in [González-Gambau *et al.*, 2017] by the SMOS BEC team at brightness temperature level. Four TB datasets have been compared to the modeled ones to analyze the effect of each technique individually:

- **Approach 1:** Nominal image reconstruction (no nodal-sampling, no $G_{kj}$ correction)
- **Approach 2:** Image reconstruction by applying nodal sampling
- **Approach 3:** 2% $G_{kj}$ correction errors, nominal image reconstruction
- **Approach 4:** 2% $G_{kj}$ correction, image reconstruction by applying nodal sampling

Figure 7.13 shows that the correction of residual multiplicative errors leads to a reduction of the systematic biases in regions close to land, while preserving those anomalies due to geophysical features, such as the Amazon River plume or the presence of the Eastern Pacific Fresh Pool. As expected, this correction is essentially affecting the areas around the landmasses, as shown in the differences of both maps (before and after applying the correction). The effect is similar when nodal sampling is used in the reconstruction of brightness temperatures. The structures of the anomaly (SMOS TB minus modeled TB) are in agreement to the ones observed in the nominal case, but smoother in the case of using NS. Some residual LSC can be still observed after applying the correction in both cases, probably due to the floor error contribution [Corbella *et al.*, 2014], which has not been corrected in this study (probably Gibbs 2 has not been applied).

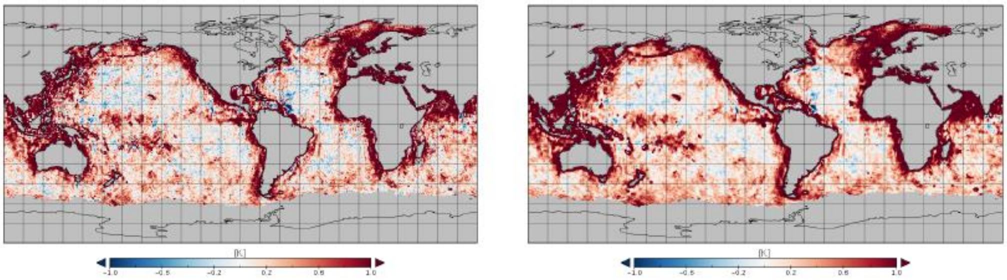

(a) Approach 1 (b) Approach 2

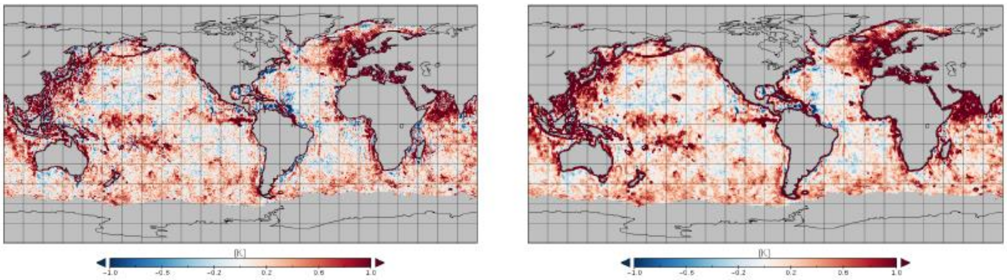

(c) Approach 3 (d) Approach 4

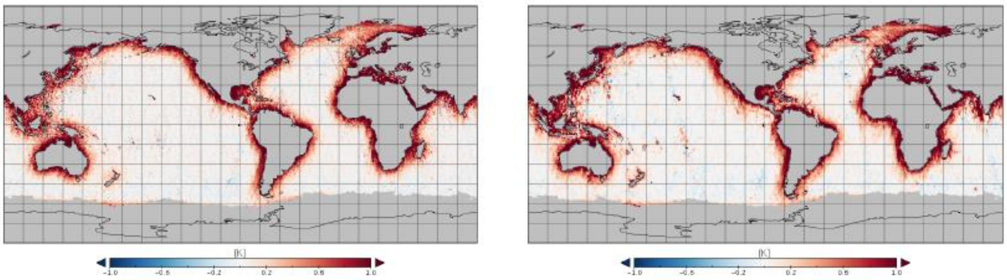

(e) Difference between approaches 1 and 3 (f) Difference between approaches 2 and 4

*Figure 7.13 9-day map 0.25° spatial resolution map of the first Stokes parameter divided by two: difference between the measurements (SMOS OTT-corrected TB) and the modeled TB for (a) the nominal image reconstruction, (b) the TBs reconstructed using nodal sampling, (c) the nominal image reconstruction once the multiplicative errors have been corrected, (d) the reconstructed TBs using nodal sampling once the multiplicative errors have been corrected, (e) impact on LSC of residual multiplicative errors in nominal image reconstruction and (f) impact on LSC of residual multiplicative errors when the nodal sampling is used to reconstruct the TB*

The improvement by using a combination of both, nodal sampling and $G_{kj}$ correction can be also observed in the SSS retrieval performed by the SMOS BEC team [González-Gambau *et al.*, 2017]. SSS maps have been generated from the different TB datasets and compared to an ocean global model to study the errors found in SSS retrievals as a function of their distance to land. The validation of these maps has been performed against in-situ measurements using Argo floats (global validation) and SSS measurements from thermosalinographs along ship tracks [González-Gambau *et al.*, 2017].

The improvement in quality of the brightness temperatures when applying the proposed corrections can be inferred from the characteristics of the SSS distributions. The standard deviation of the SSS distribution per each gridpoint is shown in the global map of Figure 7.14 regarding approaches 1 to 4.

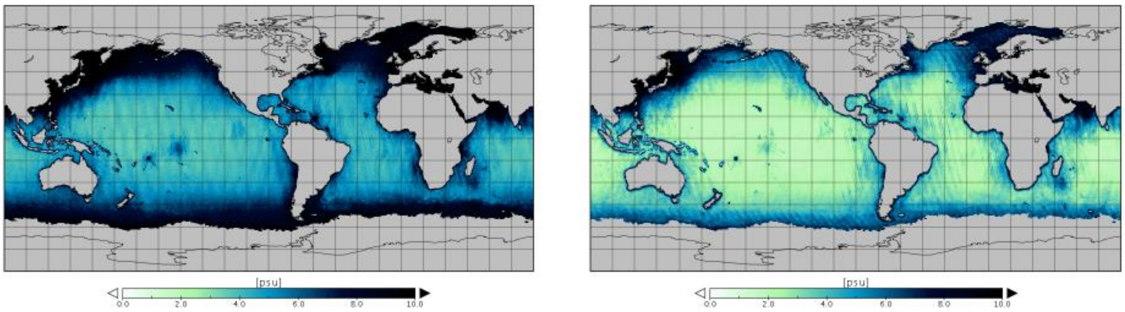

(a) Approach 1 (b) Approach 2

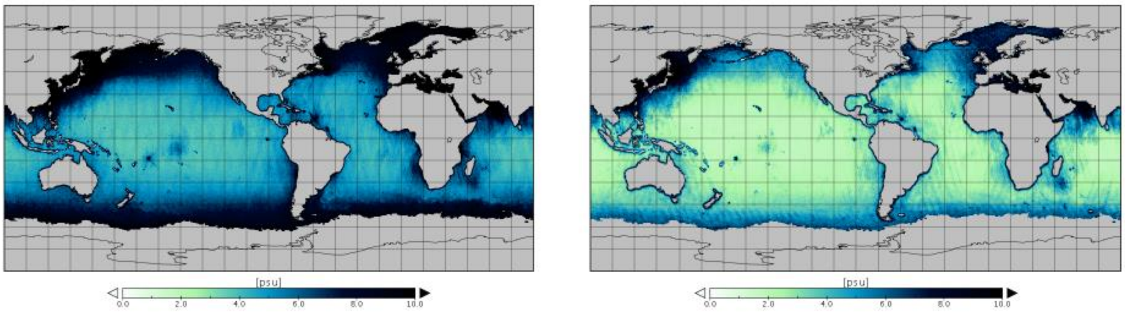

(c) Approach 3 (d) Approach 4

*Figure 7.14 Standard deviation of the SSS distribution per each gridpoint in the map (3rd-12th June, 2014). The error reduction is given by the application of nodal sampling, obtaining the lowest errors when the residual multiplicative errors are mitigated and the NS is used to reconstruct TB (approach 4)*

On average, the standard deviation of the error is reduced around 35% when nodal sampling is applied (approaches 2 and 4) with respect to the nominal case. This error reduction has also been analyzed in several regions specially affected by RFI and LSC. The joint application of the correction of residual multiplicative errors (LSC reduction) and nodal sampling approaches provides the higher reduction of the error in the SSS distributions, especially in coastal regions.

When the LSC is corrected in the nodal sampled SSS, biases are significantly reduced in the first 800 km offshore but also in open ocean. The improvement makes possible to obtain better quality SSS retrievals close to the coasts or even retrieving salinities in areas where this was not feasible when using nominal approaches. These results clearly validate the 2% $G_{kj}$ correction technique as proposed in this PhD thesis.

All these results were presented in the IEEE GRS Transaction "New approach for the improvement of SMOS salinity retrievals in coastal regions" [González-Gambau *et al.*, 2017].

## 7.6 Investigation of the $G_{kj}$ error

One important aspect for further work is assessing the origin of the $G_{kj}$ error and understanding this 2% measurement overestimation of the correlation efficiency. Some preliminary assessments have been performed in order to understand this phenomenon.

### 7.6.1 External $G_{kj}$ measurement

It must be pointed out that the correlation efficiency is periodically measured on-board by means of an internal noise injection scheme [Corbella *et al.*, 2005b]. Since antenna frequency response is not included in the noise injection loop, this section is devoted to assess its potential impact in SMOS end-to-end increased correlation loss. These results were presented in the international congress IGARSS 2016 (China) [Torres *et al.*, 2016].

SMOS on-ground characterization tests can be used to have an estimation of the end-to-end correlation efficiency. In particular, the "relative phase retrieval tests" performed inside Maxwell anechoic chamber, at ESA premises in Holland, include a set of four external probes to feed the instrument from its ceiling. Note that these tests were used in chapter 4 (section 4.1) in order to retrieve relative phases by using full-pol measurements.

As described before, $G_{kj}$ is the complex correlation efficiency (Fringe Washing Function at the origin) and $T_{sys}$ are system temperatures for the pair of baseline receivers *(k,j)*, measured at the antenna plane by a dedicated PMS. In the so-called "all LICEF" mode (described in chapter 3, section 3.4), the zero baseline visibility (antenna temperature) is measured out of an average of these system temperatures:

$$V_{kj}(0,0) = T_{sys_{k,j}} - T_{R_{k,j}} \tag{7.9}$$

As described in section 4.1 of this thesis, the probes were fed with two noise levels (hot and warm) and placed at two different heights (a quarter of a wavelength apart) to minimize the impact of systematic errors. The set-up measurement geometry was accurately measured by means of a laser positioning system to correct for path delay and phase patterns of each LICEF antennas and probes. Differential near field distance between the probes and each LICEF, as large as one meter, is corrected for path delay decorrelation as:

$$\left|(\tilde{\bar{r}}(\Delta\tau_{kj})\right| = A\cdot \mathrm{sinc}\left[B(\Delta\tau_{kj} - C)\right] \tag{7.10}$$

where $\Delta\tau_{kj} = (\tau_k - \tau_j)$ is the differential delay.

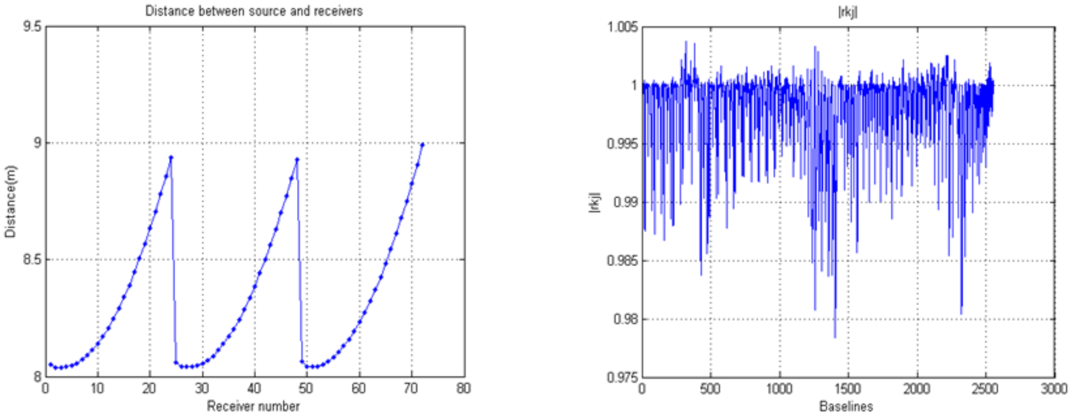

*Figure 7.15 Distance from probe O to each LICEF antenna (left). Estimated correlation loss due to differential path delay for each baseline to correct external* $G_{kj}$ *measures*

Figure 7.15 shows the correction factor for probe O, placed at boresight (set-up center). Now, the external correlation efficiency is computed from (7.10) as:

$$G_{kj}^{EXT} = \frac{G_{kj}}{\left|(\tilde{\bar{r}}(\Delta\tau_{kj})\right|} \tag{7.11}$$

where the values $M_{kj}^{C_2}$ and $M_{kj}^{C_1}$ used to compute $G_{kj}$ are expressed at the antenna plane after correcting for path delay and antenna pattern phases (both LICEF and probe). Figure 7.16 shows correlation efficiency measured with different methods. The red trace shows $G_{kj}$ measurement by internal two-level noise injection (3.26). The green trace, shows correlation efficiency using the same expression, but now the two-level noise injection is performed by one of the external probes (this includes antenna frequency response and differential path delay decorrelation). Finally, the blue trace gives correlation efficiency at the antenna plane after correcting for differential propagation decorrelation. The other probes provide similar results. All measurements are very close and far from the expected $G_{kj} \cong 0{,}97$ mean value that cancels out the LSC effect. It can be concluded that decorrelation is not produced (at least to a large extend) in –between the antenna phase center and the internal calibration plane at the switch (CIP).

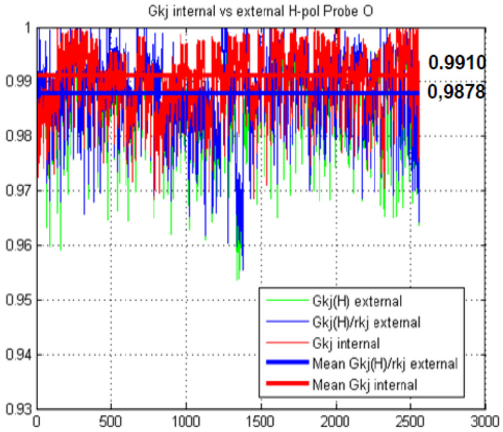

*Figure 7.16 Correlation efficiency measurements using different techniques*

## 7.6.2 Phase antenna pattern errors

In order to find the origin of this 2% measurement overestimation in the correlation efficiency a question was asked: “What errors produce LSC?” or in other words “What errors impact $V_{kj}$ amplitude but not antenna temperature?”.

As it is explained in chapter 8, a program was coded in order to obtain the Error Budget of the instrument, which was useful to compute the radiometric accuracy (or pixel bias) for a new instrument configuration and hardware. This was done by adding different types of errors in the visibility phase, amplitude or in the antenna patterns.

This tool was reused in this section to answer the proposed question by computing spatial bias using two flat references (150 K and 300 K) and adding different errors to investigate which ones produced a scene multiplicative bias (Figure 7.17). Note that all the results are simulations by using Gibbs 2 approach to avoid the floor error. Some part of this work was undertaken during the PhD stay (april-june 2016) with the research team of CESBIO (Centre d'Etudes Spatiales de la BIOsphère) in Toulouse (France).

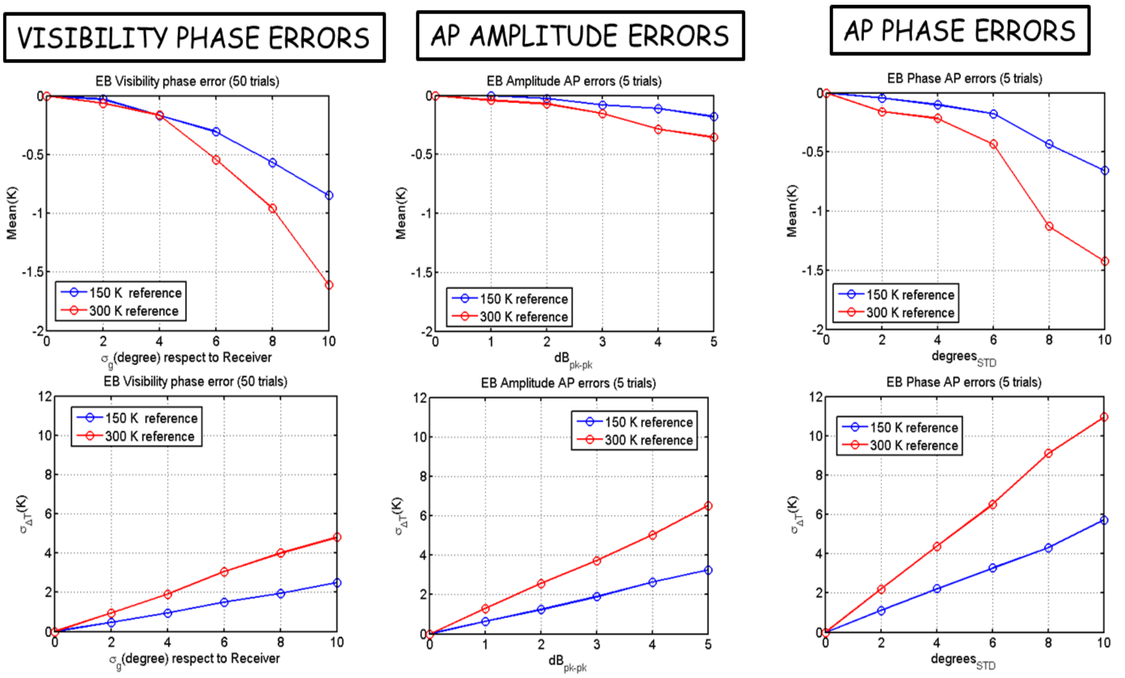

*Figure 7.17 Spatial bias after applying visibility and AP errors*

Figure 7.17 shows that the visibility and AP phase errors produce a similar negative multiplicative bias (decorrelation). Spatial bias (pixel bias) is also multiplicative. AP phase errors have a larger impact on spatial bias. So, these two are candidates for generating this inconsistency between $V_{kj}$ and antenna temperature.

Figure 7.18 shows the impact of adding a 1° random phase error in the visibility samples.

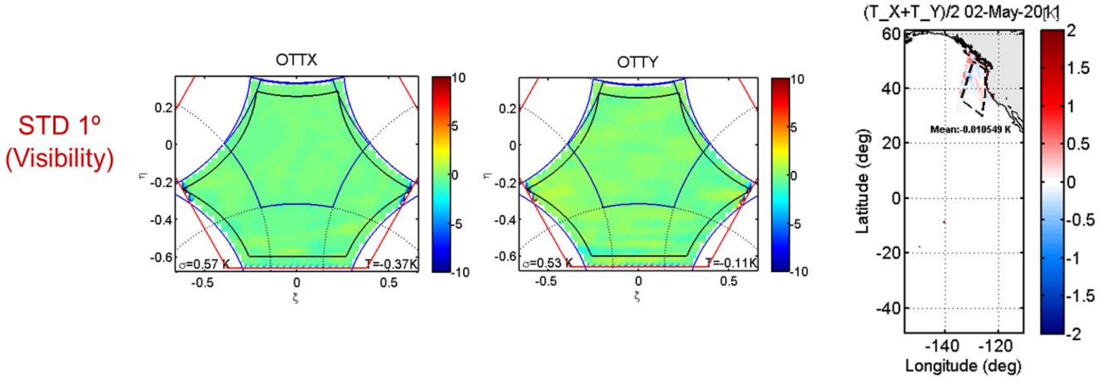

*Figure 7.18 OTT and Vancouver orbit after applying 1° random phase error in visibility*

As it is shown, at this error level, impact on LSC is negligible both in OTT and in the Vancouver orbit after subtracting OTT to the measured brightness temperature. So, the error was increased to 5° and 10° as shown in Figure 7.19 to produce a significant LSC in the Vancouver scenario.

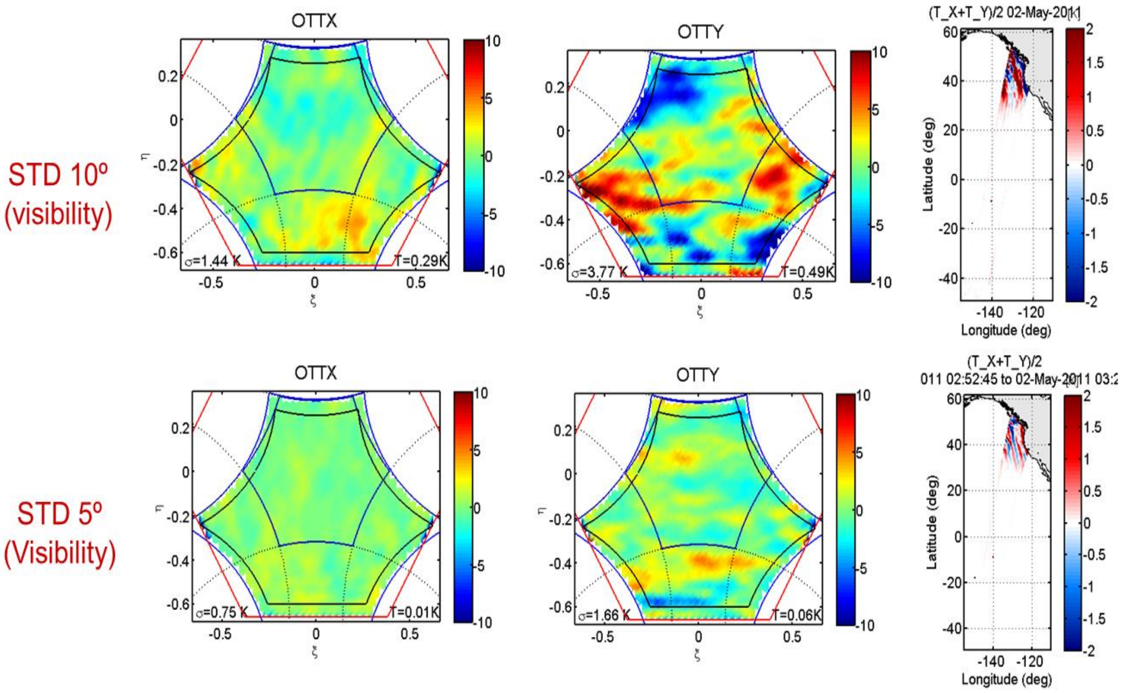

*Figure 7.19 OTT and Vancouver orbit after applying 5º and 10º random phase error in visibility*

However, large visibility phase errors (to induce the measured LSC) degrade impulse response and would produce a large ringing close to the coast line, not observed in the real images. For this reason in the visibility samples are discarded as the origin of LSC.

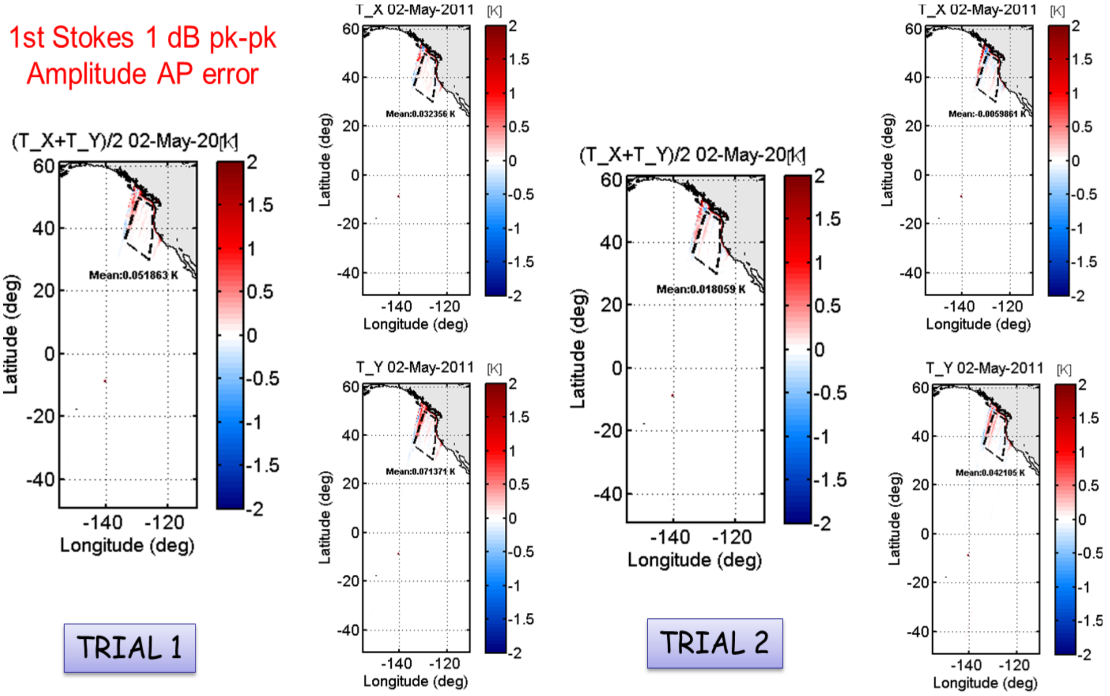

*Figure 7.20 Vancouver orbit after applying amplitude AP errors*

As expected Figure 7.20 shows that reasonable amplitude antenna pattern errors do not generate LSC. Again, larger amplitude errors would introduce a large mean error in the retrieved images and that is not the case.

After this previous analysis, AP phase errors have been identified as the main candidate to explain the origin of LSC because they yield a distributed loss of correlation as sketched in Figure 7.21.

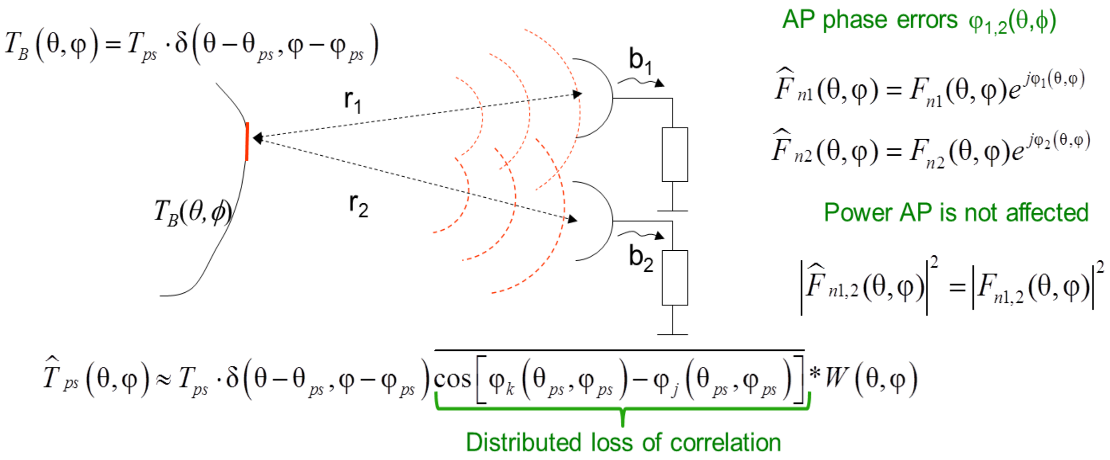

*Figure 7.21 Scheme of the impact of antenna pattern phase errors on point source response*

Since the cosine is an even function, decorrelation on $V_{kj}$ samples due to AP phase errors accumulates when all directions are integrated. LSC appears because antenna temperature $T_A$ is not affected by AP phase errors and LSC due to AP phase errors is mixed with a residual Gibbs 2 floor error. This theoretical assessment has been validated by simulation.

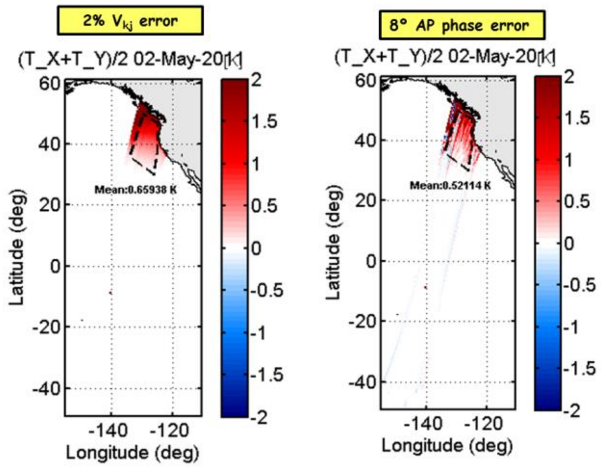

*Figure 7.22 Vancouver orbit 2% $V_{kj}$ error (left) and 8º AP phase error (right)*

Figure 7.22 shows that adding random phase AP errors LSC appears and it is in the order of the real case simulated by adding a 2% error in the amplitude of $V_{kj}$. So, in order to assess if it occurred in all the continents Figure 7.23 shows a complete map when this 8º AP phase error is taken into account.

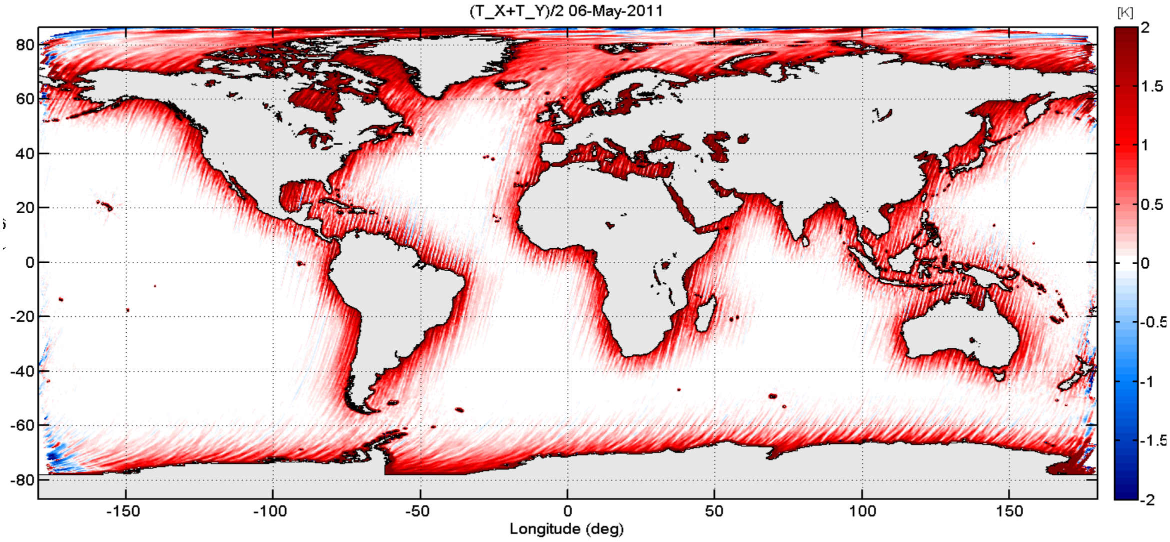

*Figure 7.23 Simulated global map of 9 days by adding 8º AP random phase errors*

The result shows that there is a similarity between this plot and measured data from the real SMOS case (Figure 7.11). In any case, this task needs further assessment because the error applied was not totally realistic.

## 7.7 Conclusions

Once the major sources of spatial bias in SMOS imagery have been successfully mitigated using averaging (spatial and temporal) and enhanced imaging techniques, global error maps still show an anomalous increase in the oceans' brightness temperature near large land masses, this artifact is the so-called Land Sea contamination (LSC). It has been shown in this chapter that LSC is related to residual multiplicative errors affecting, in a different way, the visibility at the origin and the other visibility samples. The all-LICEF mode improves the calibration consistency between both kind of error, reducing the possible differences to only one single calibration parameter: the correlator efficiency $G_{kj}$. A 2% overestimation of this parameter has been found to be the dominant contributor to the observed LSC. Using the all-LICEF mode, LSC is insensitive to any antenna temperature error (e.g., due to orbital or seasonal drift) and is corrected only by adjusting the correlator efficiency. This property might consolidate a decision to operate SMOS in all-LICEF mode in a future version of the processor or used as nominal mode in future sensors (e.g. SMOS ops). Different validation exercises of the $G_{kj}$ correction procedure shows how complementary calibration routines together with image synthesis autoconsistency properties provide a very robust SMOS performance.

From the SMOS salinity point of view, this correlation efficiency correction has been applied by the OS groups of the SMOS BEC [González-Gambau *et al.,* 2017] in combination with different approaches for the improvement of the LSC. The combination of two techniques, nodal sampling and the correction of the LSC at calibration level, has shown to significantly improve the quality of brightness temperatures over the ocean. This enhacement is also reflected in the quality of SSS retrievals from retrievals SMOS measured data [González-Gambau *et al.,* 2017].

The validation against an assimilation model of the global ocean has allowed to characterize the errors in SSS retrievals as a function of the distance to landmasses for the different approaches. In terms of biases, the correction of the residual multiplicative errors translates into a reduction of the positive systematic biases in proximity to land.

As a conclusion, it can be said that the work performed by the SMOS BEC team in [González-Gambau *et al.,* 2017] has validated the LSC mitigation technique developed in this thesis. These results have been confirmed by the comparison against in-situ measurements (both global validation with Argo and transects).

While a 2% correction on $G_{kj}$ has been proved to be very successful in mitigating the LSC artifact and, thus, providing better near coast SSS retrievals, the origin of this error is still not fully understood.

A comprehensive evaluation of the possible error source at calibration level has not revealed a miscalibrated intermediate parameter. The most probable candidate has been found to be antenna pattern phase errors, although this hypothesis require further investigation.

# 8 Future sensors

This chapter is devoted to assess the impact of instrumental errors on the radiometric accuracy (pixel bias) of one of the selected array configurations of the so-called Super-MIRAS instrument. This activity was performed early in this PhD research activity. Some of the relevant advances resulted in improvements to the SMOS mission and have been further developed in other chapters. For instance, the X-MIRAS study on the impact of antenna pattern differences conducted to the origin and model of the so-called "floor error" and proved the way to develop a specific image inversion procedure that mitigates its impact on SMOS retrievals to a large extend.

## 8.1 The Super-MIRAS concept

Super MIRAS is a tentative SMOS follow on mission currently under discussion by the European Space Agency [Corbella *et al.,* 2012a]. UPC Remote Sensing group has assessed the main performance parameters of this instrument within X-MIRAS contract. This project is focused on the assessment of different array geometries and instrument architectures of future L-band synthetic aperture radiometers to improve spatial resolution while maintaining radiometric sensitivity.

The work performed in this thesis, within the framework of the X-MIRAS project, is devoted to the analysis that have been performed about this new concept of instrument oriented to analyze different array geometries and instrument architectures. The work in this thesis is mainly focused to develop the radiometric error budget regarding the selected X-MIRAS array topology.

Figure 8.1 shows a comparison between SMOS and X-MIRAS architecture in the x-y domain:

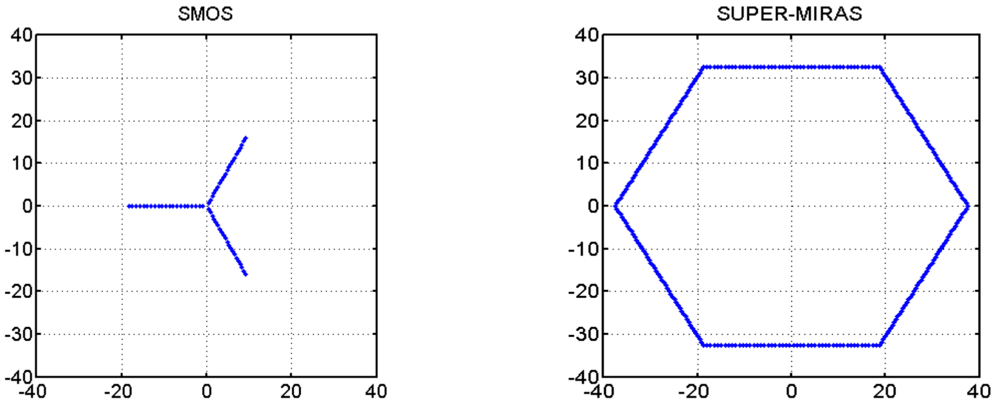

*Figure 8.1 SMOS configuration with 21 antennas per arm (left) and Super MIRAS hexagonal array with 294 antennas (right)*

A first Super MIRAS design would be a 2-D interferometric radiometer with optimal array geometry of a 16m diameter hexagon with 49 antennas per arm.

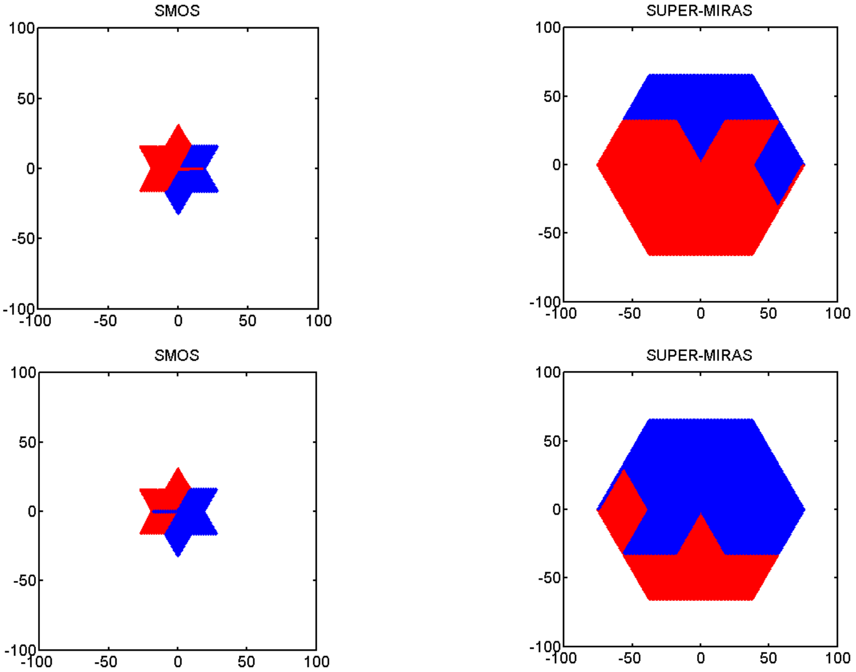

*Figure 8.2 X-MIRAS (right) and MIRAS-SMOS (left) baselines in the u-v domain. The baselines related to measured visibilities are plotted in red (top) while their symmetric ones (conjugated visibilities) are plotted in blue (bottom). In order to analyze redundancy, both measured and symmetric baselines must be taken into account. Note that the errors are introduced in the measured visibilities before computing their conjugates and then the redundant baselines are averaged*

In particular, the following instrument configuration has been proposed by the Remote Sensing laboratory research group [Corbella *et al.*, 2013]:

- **Geometrical array configuration:** Hexagon (to increase redundancy and reduce side lobes)
- **Overall size:** 16 meters in diameter (to achieve the required spatial resolution)
- **Minimum antenna spacing:** 0.767λ at 1413.5 MHz (to achieve a large alias-free field of view for increased swath)
- **Number of antennas per arm:** 49
- **Tilt angle:** 19º (to achieve the required range of incidence angles)
- **Snapshot integration time:** 1 second
- **Frequency:** Protected L-band (1400-1427 MHz)

The most important difference with respect to MIRAS is that the geometrical distribution of the antennas is a hexagon instead of a Y-shape.

Figure 8.3 shows a simulation of the retrieved brightness temperature at the antenna frame for SMOS and X-MIRAS (Super MIRAS) in an ideal case (no instrumental errors). Moreover, the error respect to the original image is computed in order to assess the improvement of spatial bias in X-MIRAS case.

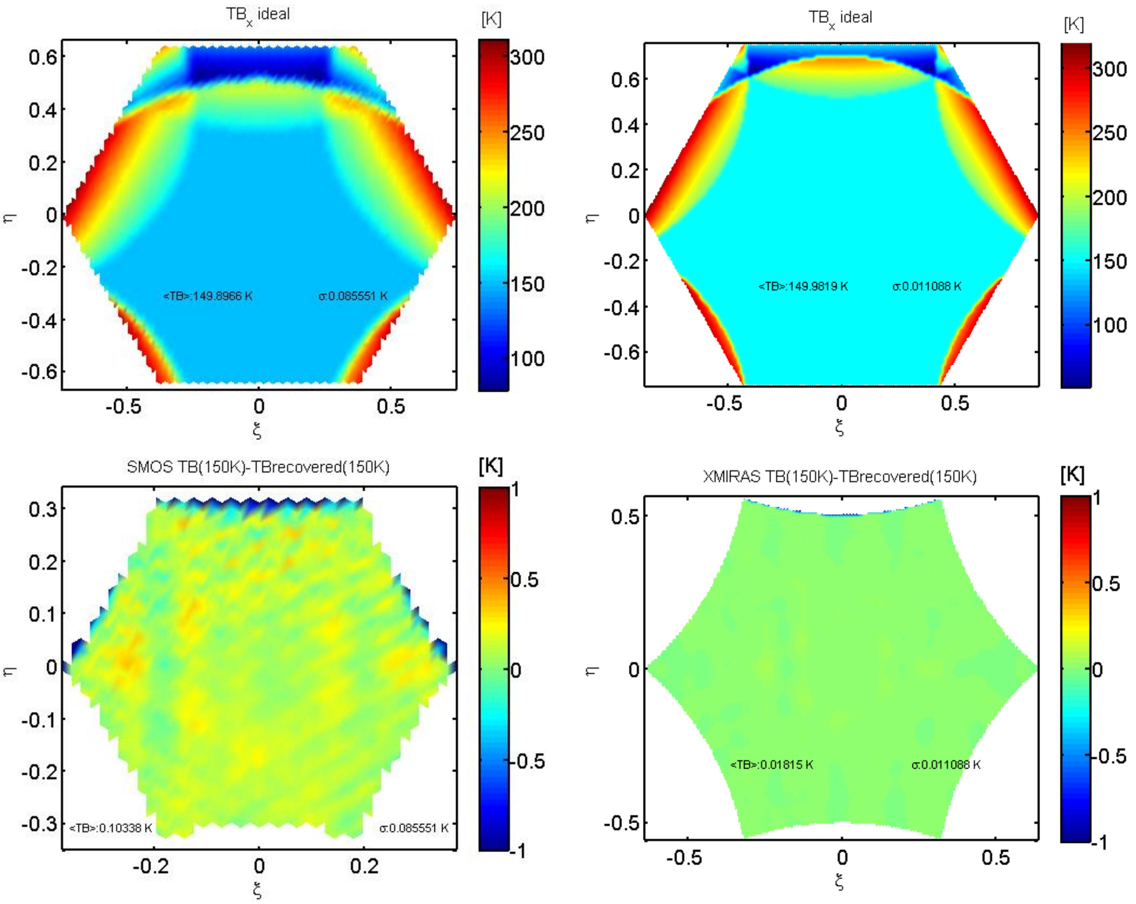

*Figure 8.3 Simulation of retrieved brightness temperature at the antenna frame for SMOS (top left) and X-MIRAS (top right) and simulation of the error (TB recovered-TB reference) for SMOS (bottom left) and X-MIRAS (bottom right)*

Figure 8.3 shows that the floor error is much lower in the X-MIRAS case when compared to the current SMOS topology because the FoV occupies a larger fraction of the fundamental hexagon.

### 8.1.1 X-MIRAS calibration definition

X-MIRAS calibration fundamentals are taken from the MIRAS/SMOS mission [*UPC team*]. This basic approach has been updated after calibration improvements undertaken within SMOS Commissioning and Operational Phases [Martin-Neira, 2010]. Some clear improvements in SMOS calibration performance were also already foreseen in the frame of the SMOSop project [UPC, 2008].

X-MIRAS calibration is based on SMOS heritage and this section is focused just to describe the main changes and/or improvements in the SMOS calibration scheme.

### 8.1.1.1 Classification of errors

As in the SMOS project all, the parameters that are used to describe system performance have been divided into different categories in order to systematize the calibration procedures. These categories are summarized in Table 8.1.

| CLASSIFICATION OF PARAMETERS ACCORDING TO CALIBRATION STRATEGY | | |
|---|---|---|
| PAR. | INITIAL VALUE: | It is calculated at the orbital position at which correlated noise injection takes place to take into account physical temperature at which calibration parameters have been retrieved. |
| P1 | Parameters which are not calibrated. | The initial value is calculated as a function of absolute physical temperature at calibration orbit position. |
| P2 | Parameters which are calibrated by means of ground characterization | The initial value is given by ground measurement uncertainty throughout the operating temperature range. |
| P3 | Parameters which are calibrated by the self-calibration procedure | The initial value is given by the residual calibration error after applying the self-calibration procedure. |
| P4 | Parameters which are calibrated by frequent noise injection (short inter-calibration period). | The initial value is given by the residual calibration error after applying the in-orbit correlated noise injection calibration procedure. |
| P5 | Parameters which are calibrated by means of deep-sky observation and/or long inter-calibration periods. | The initial value is given by the residual calibration error after deep-sky and/or "long" calibration procedures. |

*Table 8.1 Classification of system parameters according to their calibration treatment.*

As clearly seen, Table 8.1 is used to calculate the error budget just after the instrument has been operated in calibration mode. This gives the so-called initial error. Since, all parameters present some degree of drift along the orbit and from orbit to orbit, calibration parameters will present some degradation once they have been measured. It is clear then, that the initial error gives system performance error floor. That is, the better system performance is achieved for a measurement placed just after or before calibration, and will degrade as the lapse of time between measurements and calibration increases. SMOS approach minimizes intercalibration errors by using ad-hoc in-orbit calibration sequences at different rates (minutes, weeks, months,...) to match the different dynamic behavior of the calibration parameters (e.g. LO phase, PMS offset, PMS gain, U-offset, FWF, antenna coupling,...).

The fundamentals of X-MIRAS calibration strategy and the parameters that are required in the calibration procedures are described in Table 8.2 and Table 8.3. Finally it must be pointed out that the calibration strategy has a fundamental impact on system performance, since it determines which parameters must be retrieved and to what level of accuracy as clearly stated by the block diagram in Figure 8.4.

| FUNDAMENTALS OF X-MIRAS CALIBRATION STRATEGY | | |
|---|---|---|
| PAR | CALIBRATION TREATMENT | ERROR TREATMENT&CALIBRATION STRATEGY |
| P1 | Parameters that are not calibrated. | ♦ The parameter is constrained by proper HW design and engineering.<br>♦ Parameter deviation from nominal is leaved as residual error |
| P2 | Parameters that are calibrated by means of ground characterization | ♦ The parameter is measured on-ground.<br>♦ Ground characterization and ancillary data is applied to measured data to correct the effect of this parameter in observation mode.<br>♦ Measurement uncertainty gives the residual error. |
| P3 | Parameters that are calibrated by the self-calibration procedure | ♦ The parameter is corrected making use of intrinsic properties of the measurements<br>♦ Error correction parameters are obtained in a measurement by measurement basis, in both observation and calibration modes. |
| P4 | Parameters that are calibrated by frequent internal noise injection (short inter-calibration period). | ♦ The parameter is estimated by means of measured on-board internal calibration standards and ancillary data.<br>♦ The parameter is corrected by applying a two-step procedure (only drift due to temperature is taken into account):<br>1. Determination of initial value of parameter<br>2. Determination of parameter drift between calibrations. |
| P5 | Parameters that are calibrated by means of deep-sky meas and/or "long" inter-calibration period | ♦ The parameter is estimated by means of measured on-board internal calibration standards, external known targets and ancillary data.<br>♦ The parameter is corrected by applying a two-step procedure:<br>1. Determination of initial value of parameter<br>2. Determination of parameter drift in-between calibrations, if apply. |

*Table 8.2 Summary of calibration procedures according to parameter classification.*

| COD. | PAR. | EB parameter | CAL | CALIBRATION STRATEGY |
|---|---|---|---|---|
| FUNDAMENTAL LIMITATIONS | | | | NATURE OF ERROR SOURCE |
| FL1 | P1 | Discretization and truncation | NO | Estimated theoretical error |
| FL2 | P1 | Thermal noise (Dual-Pol teff=0.7 s) | NO | Estimated/measured value |
| ANTENNA ERRORS | | | | |
| ANT1 | P2 | Antenna voltage pattern phase ripple | YES | Residual error after on-ground characterization |
| ANT2 | P2 | Antenna voltage pattern amplitude ripple | YES | Residual error after on-ground characterization |
| ANT3 | | Antenna XP | | Included in ANT 15 |
| ANT4 | | Switch isolation | | Included in ANT 15 |
| ANT5 | P1 | Antenna mismatch | NO | Included in CAS/LICEF mismatch |
| ANT6 | P1 | Geometric position uncertainty (x-y) | NO | Ground characterization. |
| ANT7 | P1 | Geometric position uncertainty (z) | NO | Ground characterization. |
| ANT8 | P1 | Array arm thermo-elastic deformation:In-plane | NO | Ground characterization. |
| ANT9 | P1 | Array arm thermo-elastic deformations:Off-plane | NO | Ground characterization. |
| ANT10 | P1 | Hub arm thermo-elastic deformation:In-plane | NO | Ground characterization. |
| ANT11 | P1 | Hub arm thermo-elastic deformation:Off-plane | NO | Ground characterization. |
| ANT12 | P1 | Antenna rotation(3) | NO | Not calibrated in-orbit. Left as residual error |
| ANT13 | P1 | Pointing accuracy | NO | Ground characterization |
| ANT14 | P1 | Antenna voltage pattern dependency on frequency | YES | Ground characterization. Weigthed average with 3 frequencies. |
| ANT15 | P2 | Antenna-LICEF XP measured via TRFOP | YES | Ground characterization |
| AMPLITUDE ERRORS:ALL-LICEF | | | | |
| | | | | |
| AMP1 | P1 | All-LICEF: Sensitivity: STD: Tsys/sqrt(B·tef·Nant) | NO | Estimation |
| AMP2 | P5 | All-LICEF: Bias error: [ pk-pk] 1,1/sqrt(Nant) | YES | Residual error after in-orbit deep-sky calibration |
| AMP3 | P5 | All-LICEF: Gain error [ pk-pk] | YES | Residual error after in-orbit deep-sky calibration |
| | | | | |
| AMP10 | P4 | Amplitude calibration residual error due to noise | YES | Residual error after in-orbit self-calibration |
| AMP11 | P2 | NDN Sij relative amplitude | YES | Not apply to All-LICEF |
| AMP12 | P1 | PMS sensitivity due to thermal noise | NO | Theoretical error |
| AMP13 | P1 | Low-frequency PMS random gain fluctuation | NO | Estimated from Allan Variance measurements |
| AMP14 | P2 | PMS linearity error: | YES | Residual error. Ground characterization |
| AMP15 | P2 | Reciever input path Sij relative amplitude | YES | Not apply to All-LICEF |
| AMP16 | P2 | Antenna losses relative amplitude | YES | Residual error. Look-up table. Ground/in-orbit characterization |
| AMP17 | P5 | Error in the relative noise injected by CAS | YES | Not apply to All-LICEF |
| AMP18 | P1 | Amplitude error due to mismatch at calibration planes | NO | Ground characterization |
| AMP19 | P4 | FWF(0) modulus error on distributed calibration | YES | Residual error after in-orbit distributed calibration and estimation. |
| PHASE ERRORS | | | | |
| PHA10 | P4 | In-phase cal. residual error due AM/PM conversion | YES | Residual error after phase calibration by noise-injection |
| PHA11 | P2 | NDN Sij relative phase uncertainty | YES | Residual error. Look-up table. On-ground characterization as *f(Tph)* |
| PHA12 | P2 | Receiver input path Sij relative phase uncertainty | YES | Residual error. Look-up table. On-ground characterization as *f(Tph)* |
| PHA13 | P2 | Path antenna plane to antenna geometric center | YES | On-ground characterization (IVT tests include overall phase error) |
| PHA14 | P3 | Residual quadrature error | YES | Residual error after in-orbit self-calibration |
| PHA15 | P1 | Phase error due to mismatch at calibration planes | NO | On-ground characterization. |
| PHA16 | P1 | In-band freq dependent quadrature error | NO | On-ground characterization. |
| PHA17 | P2 | FWF(0) phase error on distributed calibration | YES | Residual error after in-orbit distributed calibration. |
| OTHER SOURCES OF ERROR | | | | |
| OS1 | P1 | Sampling skew error | NO | Ground characterization |
| OS2 | P1 | Sampling jitter error | NO | Ground characterization |
| OS3 | P4 | Comparators threshold and U-noise injection correction | YES | Residual error after in-orbit self-calibration & U-noise injection correction |
| OS4 | P1 | Antenna coupling | YES | Residual error after deep-sky imaging and FTR correction |

*Table 8.3 Classification and calibration treatment of every single entry in the EB table based on the SMOS approach. Cells in blue correspond to items where changes are expected for the X-MIRAS case. The column labeled "cal" indicates if this parameter is calibrated by any means or just constrained by proper HW design and implementation*

## 8.2 Error Budget

This section is devoted to the SMOS error assessment methodology that has been applied to analyze X-MIRAS performance. The results are compared to the current SMOS error budget since one of the main objectives of XMIRAS is to improve SMOS performance.

The radiometric error budget [Durán *et al.*, 2012], [Corbella *et al.*, 2000] is a simple way to compute the radiometric accuracy (or pixel bias) for a given instrument configuration and hardware. Figure 8.4 shows a simplified diagram that explains the fundamentals and methodology used to compute the error budget and define the calibration scheme. In a first step, the radiometric error sensitivity to basic errors in the visibility samples (phase, amplitude, offset, antenna patterns,..) is computed by intensive simulation. On the other hand, since mission scientific requirements set the maximum radiometric error in the measured images, this allows to set the maximum value for each one of the basic errors. In a second step, the sensitivity of the basic errors in the visibility samples to the errors in the calibration parameters is used to set the specifications for the instrument subsystems in a way that can be easily translated to the hardware developers.

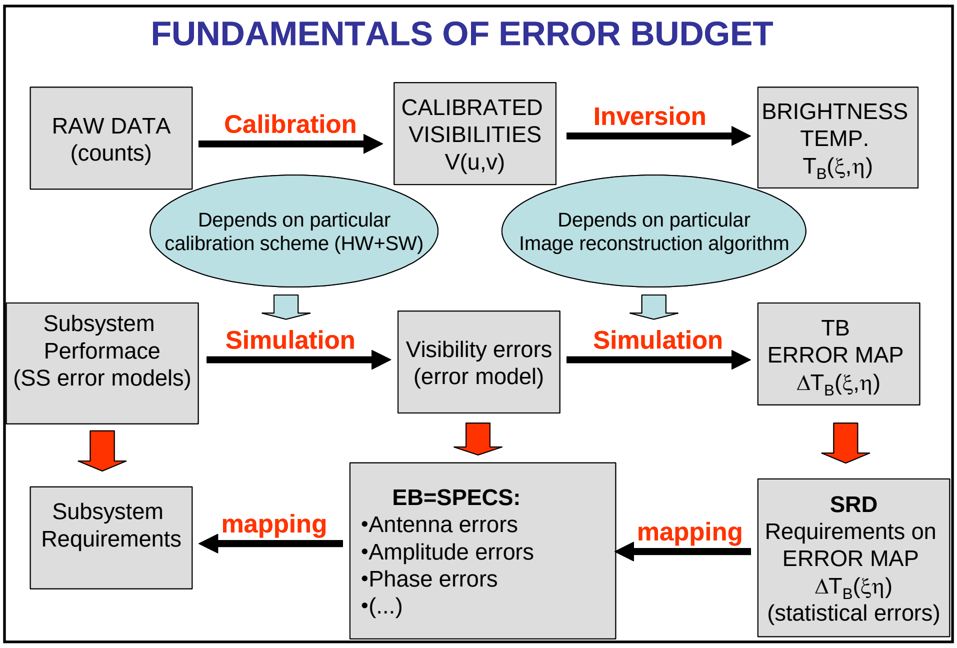

*Figure 8.4 Fundamentals of the error budget assessment*

This section is devoted to compute the error budget related to the basic errors in the visibility samples. In this preliminary analysis the reference image is a constant brightness temperature scene at TB=150K measured at the antenna frame. The spatial error (pixel bias) is computed as the RMS error with relation to the ideal scene for all the pixels within a circle of radius 0,3 in the $(\xi,\eta)$ domain.

The analysis of errors is split into:

- Internal errors (instrumental errors): directly added to the ideal visibility samples:
    - Phase: separable and non-separable errors
    - Amplitude: separable and non-separable errors
    - Offset
    - ALL LICEF error in $V_0$ that is the antenna temperature
- External errors (voltage antenna pattern errors): Corrupted visibilities computed by means of the G-matrix method:
    - Amplitude ripple
    - Phase ripple
    - In-plane antenna position uncertainty
    - Off-plane antenna position uncertainty

In all the cases the sensitivity to error is computed with and without redundancy to clearly illustrate the impact of averaging redundant baselines, a clear improvement of X-MIRAS in front of SMOS.

### 8.2.1 Internal errors

This section is devoted to internal errors. The procedure to assess the pixel bias is the following:

1 The ideal visibility samples are computed from the reference image by means of a Fast Fourier Transform. This samples are computed for each antenna pair in the array to include the redundant baselines.

2 Instrumental errors are included to generate a set of corrupted visibility samples. The error distribution is zero mean Gaussian with a given standard deviation $\sigma_e$.

3 The visibility samples related to the symmetric baselines are computed as the conjugate of the corrupted ones to reproduce SMOS measurement procedure.

4 If redundancy is taken into account, the redundant visibilities are averaged to average the errors. If not, a single redundant baseline is taken into account to fill the nominal u-v domain and instrumental errors are not averaged.

5 The brightness temperature at the antenna frame is computed by an inverse FFT (iFFT) of the corrupted visibilities

6 Pixel bias is computed as the standard deviation $\sigma_T$of the radiometric error $\Delta T$ for each pixel within a circle or radius r=0,3 in the $(\xi,\eta)$ domain. To reduce the uncertainty in the computation of the standard deviation $\sigma_T$ this is computed as the average $\sigma_T$ from 50 trials per error value $\sigma_e$.

The cases that have been assessed are listed in Table 8.4.

| Visibility amplitude error | | | |
|---|---|---|---|
| Non-separable | | Separable | |
| Redundant | Non-redundant | Redundant | Non-redundant |
| Visibility phase error | | | |
| Non-separable | | Separable | |
| Redundant | Non-redundant | Redundant | Non-redundant |
| Visibility offset error | | | |
| Redundant | | Non-redundant | |

*Table 8.4 List of cases to perform the Error Budget (EB) in the case of internal instrumental errors*

In all the cases the error $\sigma_e$ is related to the baseline error. That is, in the case of separable errors, a zero mean error with standard deviation $\sigma_e/\sqrt{2}$ is added to each receiver to have an equivalent $\sigma_e$ at baseline level. The radiometric error sensitivity to each instrumental error is defined as

$$S_{\sigma_e}^{\sigma_T} = \frac{\sigma_T}{\sigma_e} \tag{8. 1}$$

It is computed as the slope of the radiometric error plots. An ad-hoc program has been coded in MATLAB based in some of the routines already used in the MIRAS Testing Software (MTS) developed by UPC. This program automatically generates the radiometric error plots and computes the radiometric sensitivity to each of the instrumental errors (Figure 8.5). Both in the radiometric error sensitivity and in the x-axes of the radiometric error plots, the standard deviation of the error $\sigma_e$ *is* given at baseline level.

*Figure 8.5 Flow graph of the MATLAB program used to compute the Error Budget for the X-MIRAS configuration*

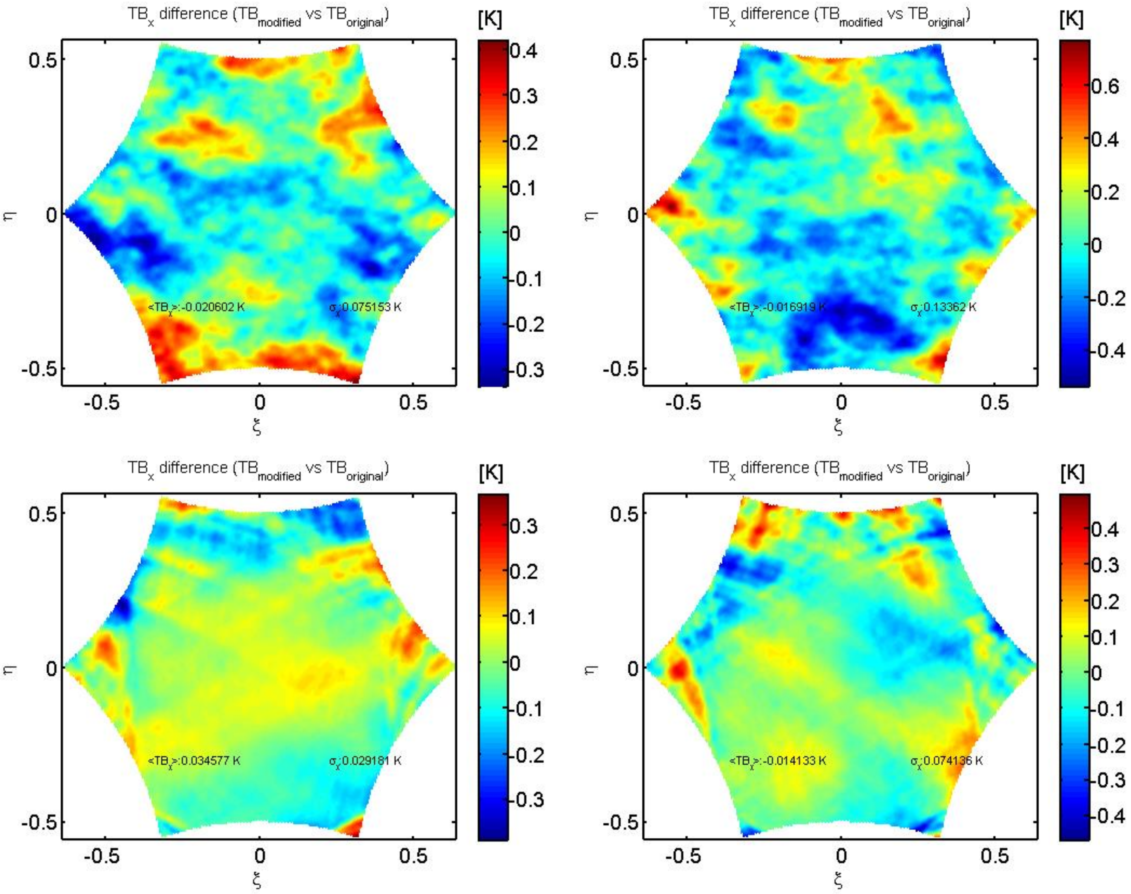

*Figure 8.6 Example of error maps for one of the trials regarding the following internal visibility errors: non-separable amplitude error $\sigma_e$ = 1% (top, left), non-separable phase error $\sigma_e$ = 1º (top, right),separable amplitude error $\sigma_e$ =1% (bottom left) and separable phase error $\sigma_e$ =1º (bottom, right). Redundancy is taken into account in all cases*

In the case of separable errors, the error at baseline level presents a certain degree of correlation since the error distribution in the brightness temperature maps is more random in the case of non-separable errors. Figure 8.6 shows some error maps that clearly show this correlation effect.

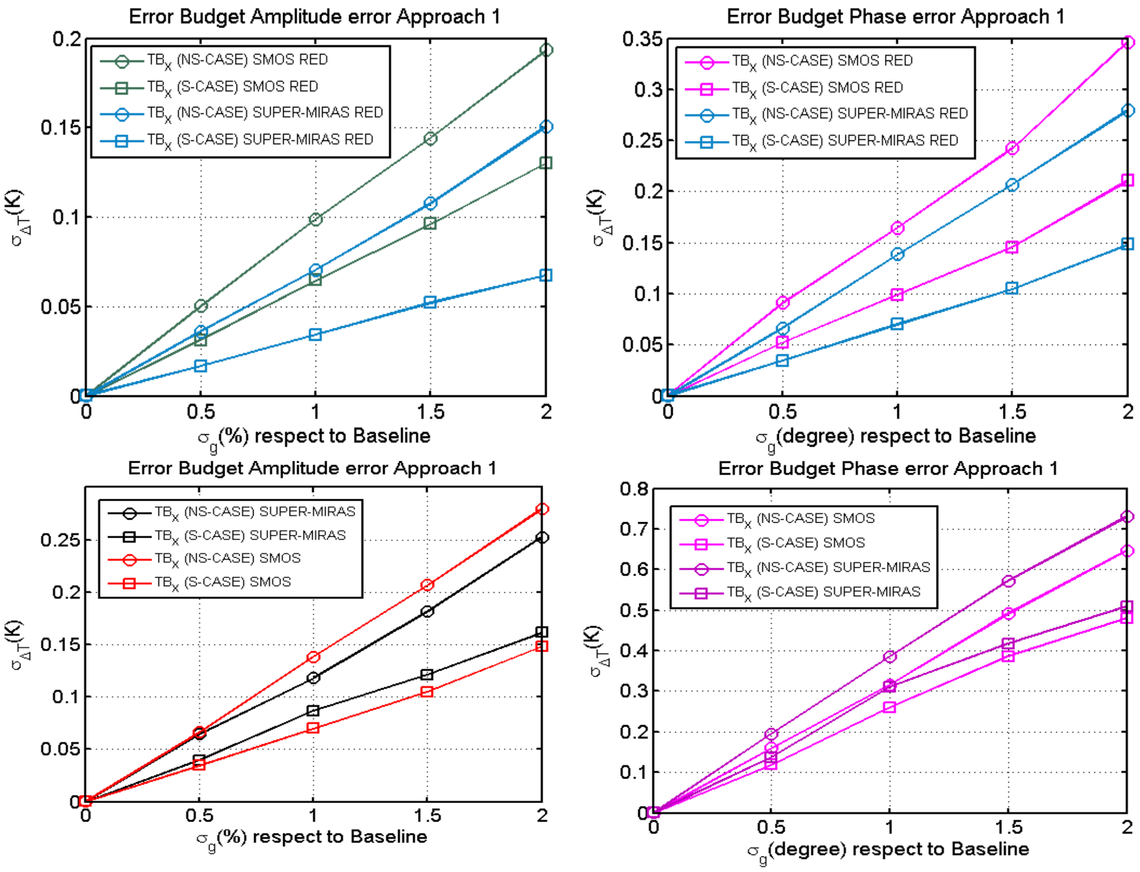

*Figure 8.7 Comparison of pixel bias between X-MIRAS and SMOS for separable and non-separable amplitude (left) and phase (right) internal errors. X-MIRAS radiometric error is significantly lower than in the SMOS configuration when redundancy (top) is taken into account. In the non-redundant case (bottom) radiometric sensitivity to error is comparable in both array configurations*

In order to compute the radiometric error $\Delta T$ produced by a certain instrumental error, a differential image is computed by subtracting the error free image from the corrupted one. In this way, the floor error is removed and only the spatial bias caused by the instrumental error is used to estimate the radiometric error.

Figure 8.7 and Figure 8.8 show the error sensitivity analysis for different causes. The radiometric error sensitivity to each instrumental error is the slope of the lines in the figures. The results are summarized and commented in section 8.2.3.

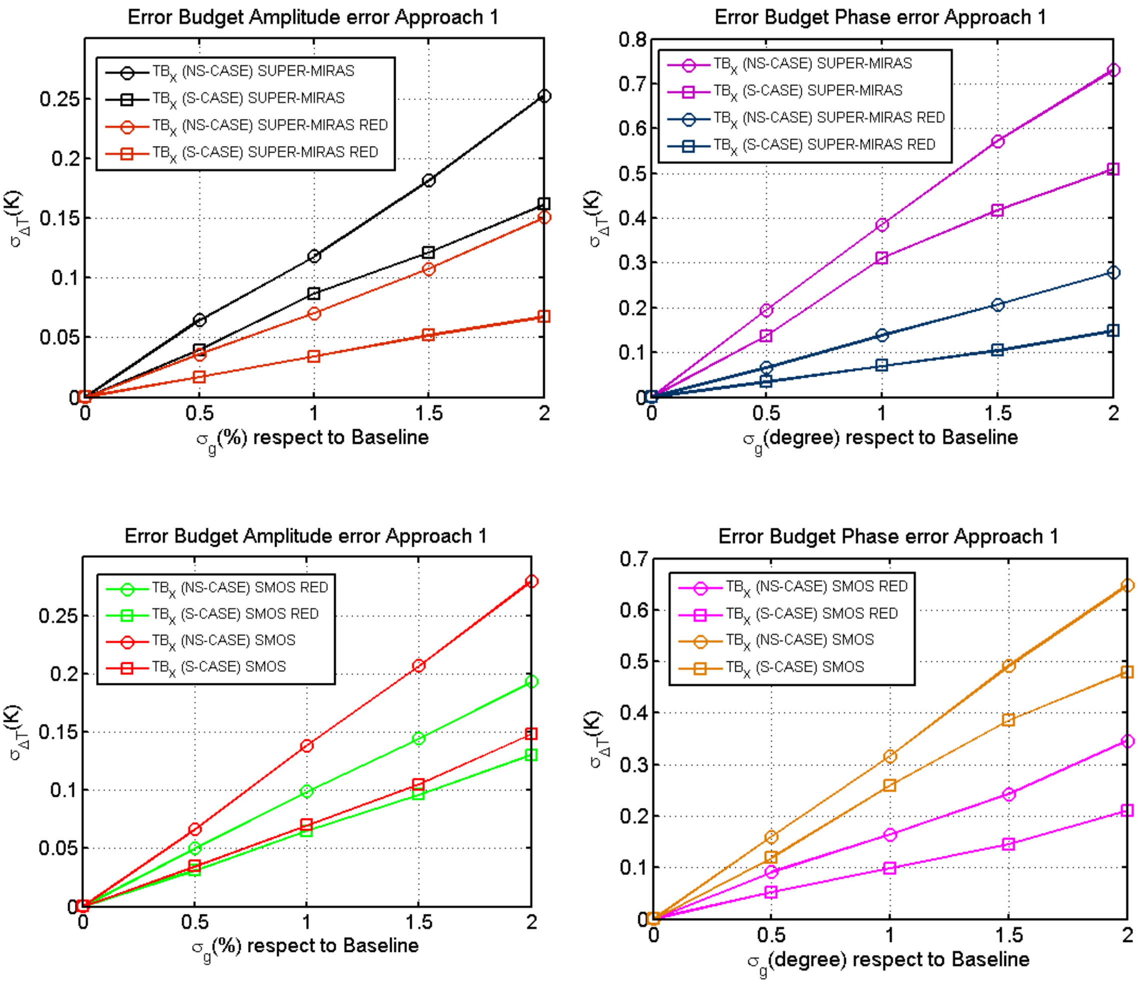

*Figure 8.8 The improvement by averaging redundant baselines is significantly better in X-MIRAS (top) than in the SMOS configuration (bottom) for both amplitude (left) and phase (right) errors, both in the separable and non-separable cases*

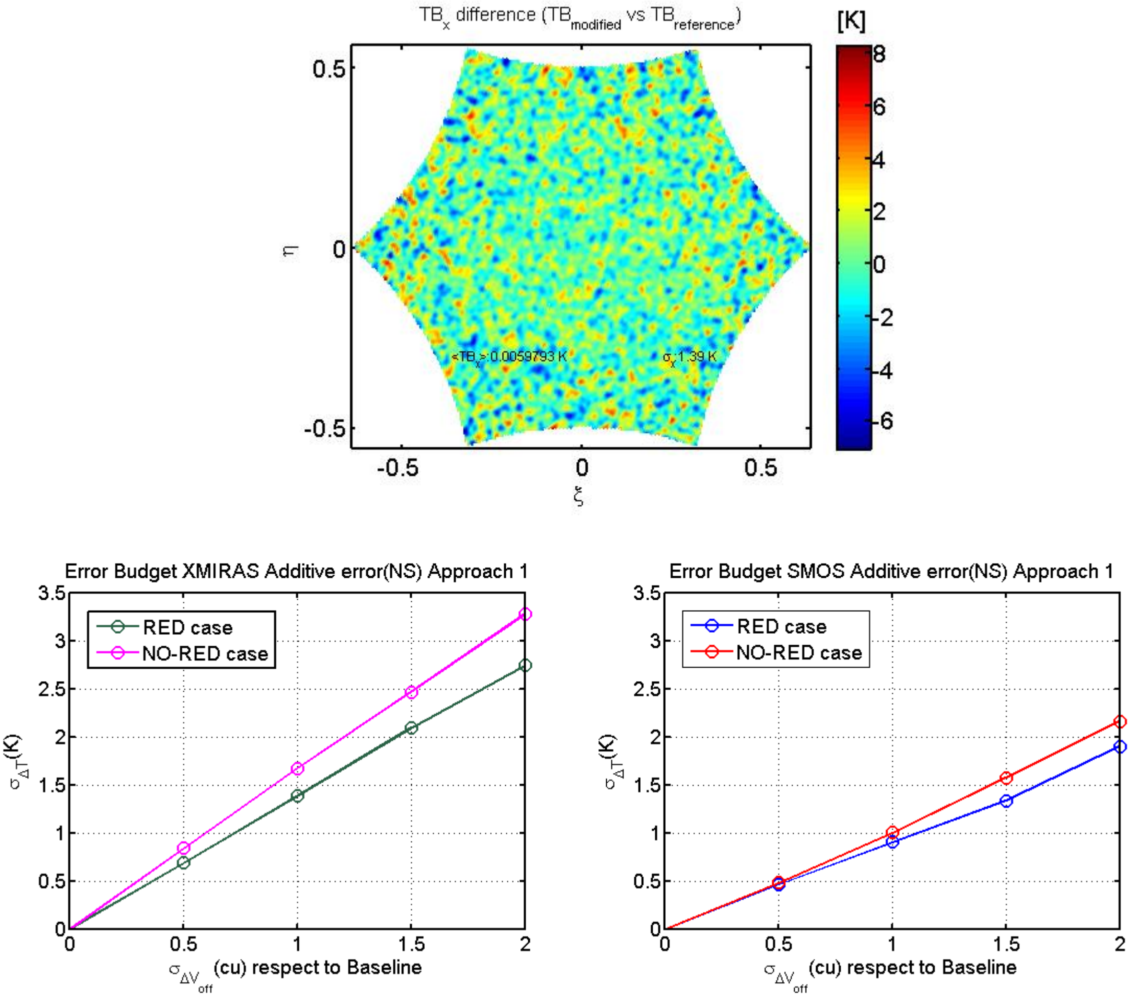

*Figure 8.9 Example of error map for one of the trials regarding an additive error of 1 cu (top). Comparison of pixel bias between X-MIRAS (bottom, left) and SMOS (bottom, right) for visibility offset errors (redundant and non-redundant case). Note that X-MIRAS radiometric error is larger than in the SMOS configuration due to the larger number of visibilities. The additive error (units of Kelvin) added to both the real and the imaginary parts of the visibility samples have the same standard deviation $\sigma_{\Delta v}$ ( x-axis in the plots), expressed in correlation units (c.u) after dividing the error by the system temperature ($T_{sys}=T_R+T_A$, $T_R$=150 K and $T_A$=131,86 K)*

### 8.2.1.1 Radiometric sensitivity

The systematic visibility offset error has exactly the same behaviour than the random noise due to the finite integration time (radiometric sensitivity). The only difference is that this last averages for different snap-shots (decorrelated in time). In the case of X-MIRAS the additive noise in the real and imaginary parts of the normalized correlations are given by:

$$\Delta M_{kj}^{real} = \Delta M_{kj}^{imag} = \frac{1}{\sqrt{2B\sigma_{ef}}} = 1{,}94\ cu \tag{8. 2}$$

where the X-MIRAS parameters have been taken from [UPC team]: B=19 MHz and $\sigma_{ef}$=0,7 s. To perform the simulations the offset added to the ideal visibilities is obtained by multiplying the normalized correlation noise by the system temperature: Tsys=$T_R$+$T_A$ being $T_R$=150 K and $T_A$=131,86 K, this last computed from an earth disk at TB=150 K at the antenna frame (to allow comparison with the SMOS error budget).

Taking into account X-MIRAS sensitivity to additive errors, radiometric resolution is

$$\begin{aligned} \sigma_{\Delta T}^{red} &= 1{,}38 * 1{,}94 = 2{,}68\ K \\ \sigma_{\Delta T}^{nonred} &= 1{,}67 * 1{,}94 = 3{,}24\ K \end{aligned} \tag{8. 3}$$

Note that X-MIRAS improvement due to redundancy is 0,827, slightly larger than the value predicted in [UPC team] (0,697) due to the correlation of errors (in [UPC team] the errors were assumed to be fully uncorrelated).

## 8.2.2 External errors

The assessment of external errors (or antenna errors) is very computationally intensive because for each set of corrupted visibilities an ad-hoc G-matrix might be used. Retrieval of the corrupted brightness temperature map can be performed by means of the inverse Fast Fourier Transform (iFFT). This procedure has been adopted to speed the assessment. In a real case, for an ideal error free instrument, the forward model can be computed by means of an FFT and error intruced in the G-matrix to perform the image retrieval. However, this would have implied to computed and invert a G-matrix for each trial. On the other hand, it has been found that, for theses preliminary analysis, there is no need to perform a large number of trials to estimate pixel bias sensitivity to antenna errors.

The cases that have been assessed are listed in Table 8.5. Note that in the case of antenna errors only the case related to separable errors must be taken into account.

| | |
|---|---|
| Voltage antenna pattern amplitude error | |
| Redundant | Non-redundant |
| Voltage antenna pattern phase error | |
| Redundant | Non-redundant |
| In-plane antenna position uncertainty | |
| Redundant | Non-redundant |
| Off-plane antenna position uncertainty | |
| Redundant | Non-redundant |

*Table 8.5 List of cases to perform the Error Budget (EB) in the case of external (antenna) errors*

#### 8.2.2.1 Voltage antenna pattern errors

Voltage antenna pattern errors are modeled as in the SMOS case: a phase and amplitude ripple as a function of the radius to boresight. Simulations show that the radiometric error is not very dependent on the number of ripples included in the modeling. The error maps presented in Figure 8.10 show that these error produce a radiometric error very randomly distributed in the $(\xi, \eta)$ domain, very similar to that produced by random additive errors.

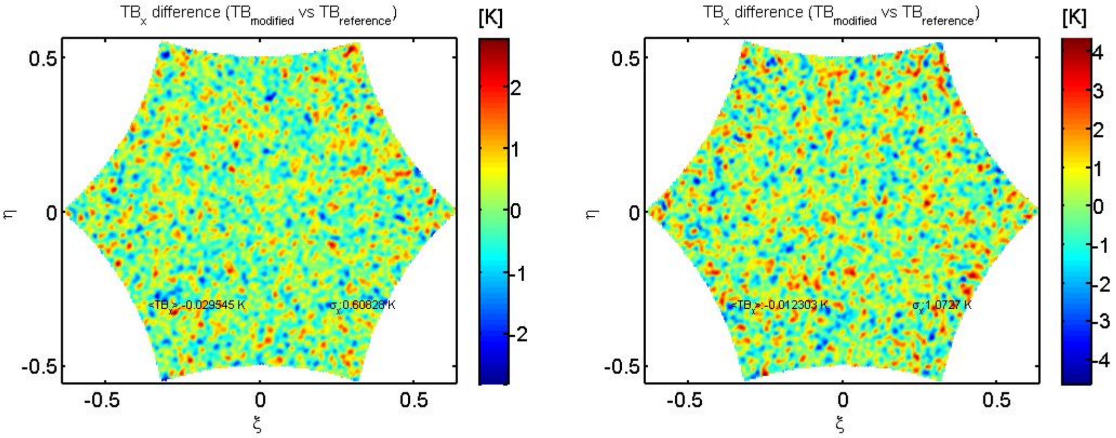

*Figure 8.10 Example of error maps for one of the trials regarding voltage antenna pattern amplitude ripple 1% (left) and phase ripple 1º (right)*

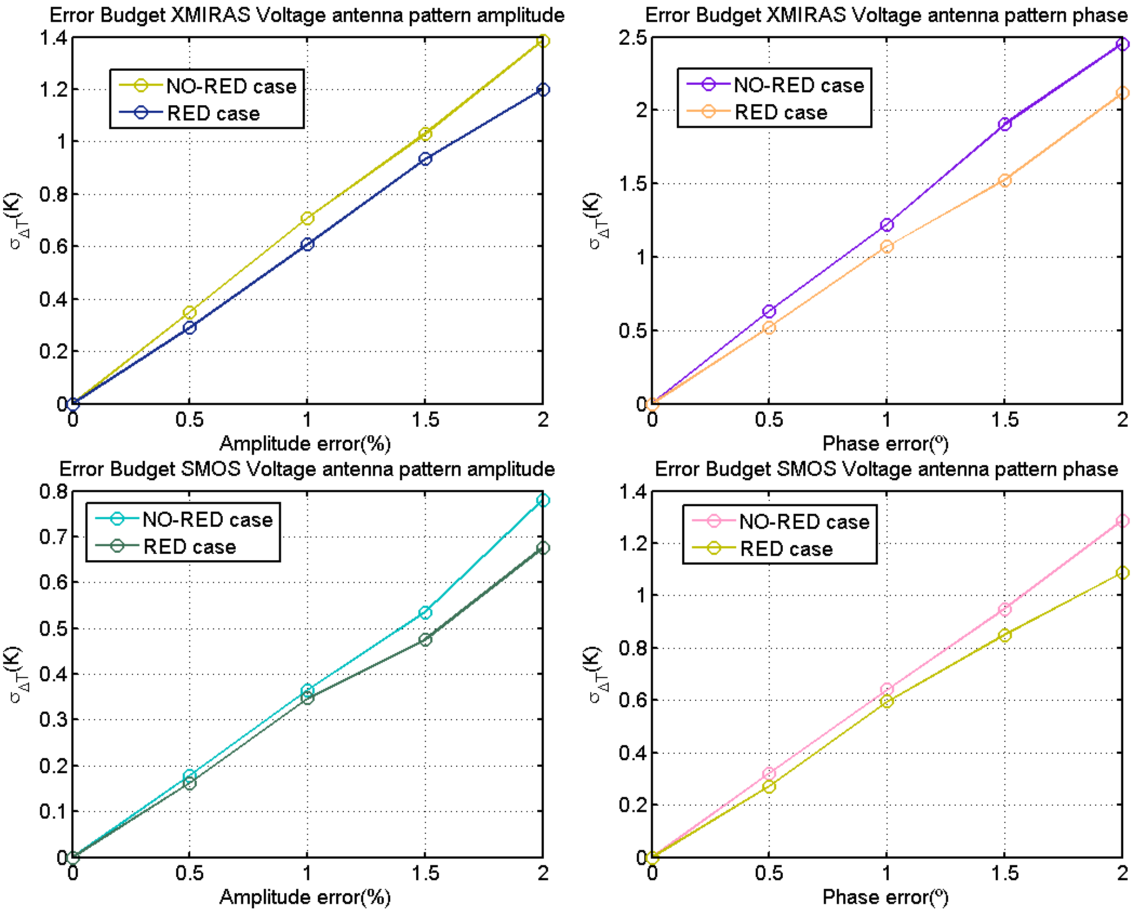

*Figure 8.11 Pixel bias between X-MIRAS Voltage antenna pattern amplitude ripple (left) and phase ripple (right) for redundant and non-redundant cases. SMOS cases are also included for comparison (bottom)*

### 8.2.2.2 Antenna position uncertainty

This section is devoted to analyze the impact of random errors in the estimation of the nominal antenna position in the array. This simulation is also very computationally intensive but with the use of a Workstation the error in the estimation of the standard deviation of the radiometric error has been performed by averaging the result of 600 trials in SMOS case and 300 in X-MIRAS case.

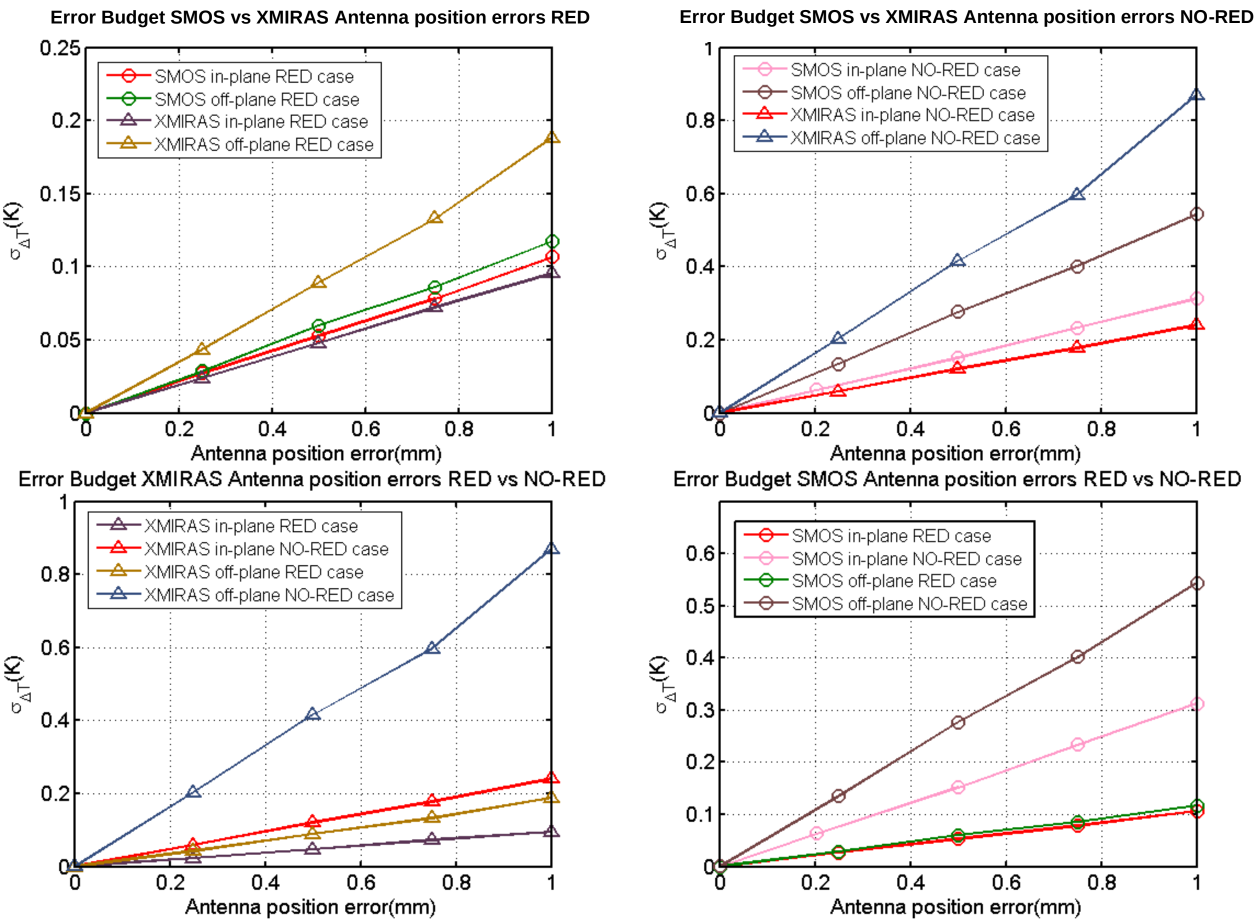

*Figure 8.12 EB X-MIRAS antenna position errors RED vs NO-RED case (left) EB SMOS antenna position errors RED vs NO-RED (right)*

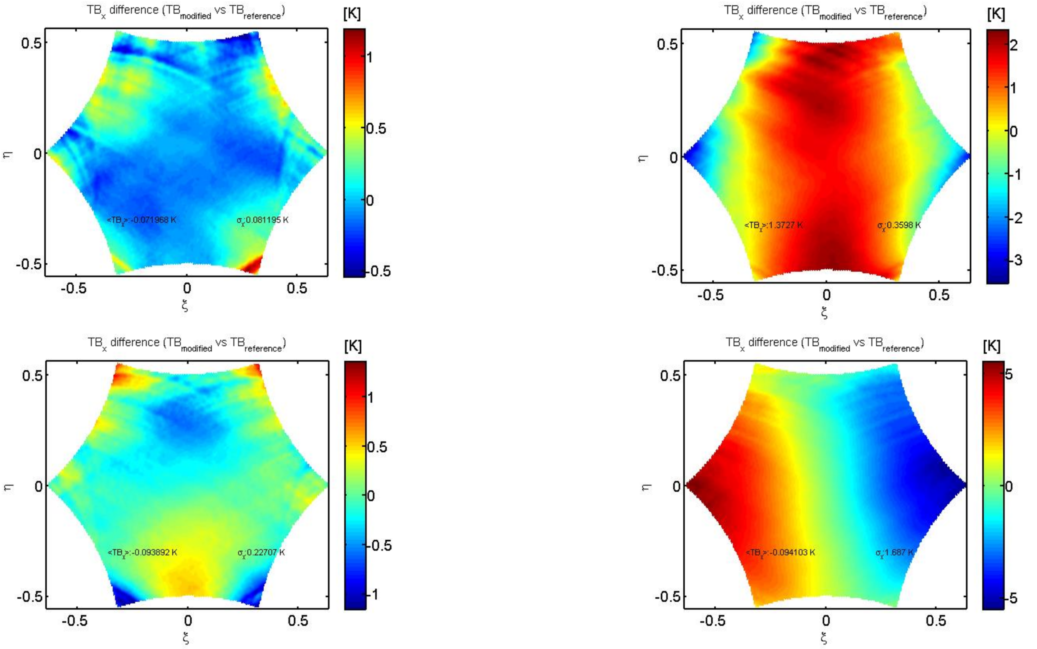

*Figure 8.13. Difference X-MIRAS TB(corrupted)-TB(reference) Antenna position error in-plane 1 mm RED case(top left) and NO-RED case (top right). Difference X-MIRAS TB(corrupted)-TB(reference) Antenna position error off-plane 1 mm RED case(bottom left) and NO-RED case (bottom right)*

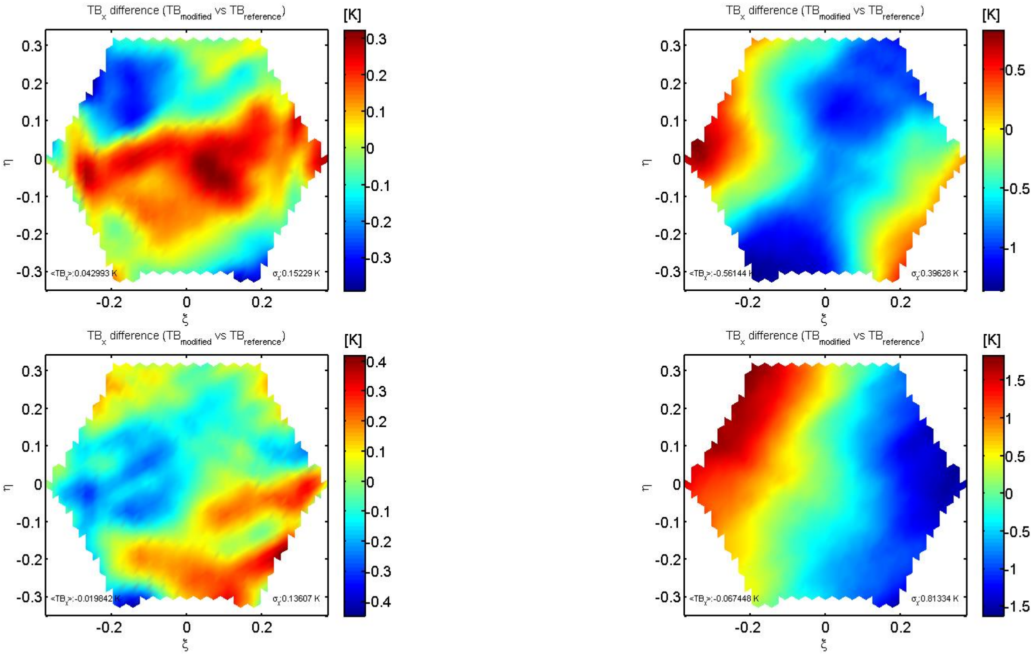

*Figure 8.14. Difference SMOS TB(corrupted)-TB(reference) Antenna position error in-plane 1 mm RED case(top left) and NO-RED case (top right). Difference SMOS TB(corrupted)-TB(reference) Antenna position error off-plane 1 mm RED case(bottom left) and NO-RED case (bottom right)*

### 8.2.3 Radiometric sensitivity to error

This section summarizes the error analysis by providing a list of radiometric sensitivities to instrumental errors. In this analysis, the sensitivity values are the radiometric error when the instrumental error value is one, thus value has been obtained by a linear regression of the simulations performed in this chapter.

| | SMOS | X-MIRAS |
|---|---|---|
| **Amplitude NS RED case** | 0,10 K/% | 0,07 K/% |
| **Amplitude S RED case** | 0,06 K/% | 0,03 K/% |
| **Phase NS RED case** | 0,16 K/° | 0,14 K/° |
| **Phase S RED case** | 0,10 K/° | 0,07 K/° |
| **Amplitude NS NO-RED case** | 0,14K/% | 0,12K/% |
| **Amplitude S NO-RED case** | 0,07 K/% | 0,09K/% |
| **Phase NS NO-RED case** | 0,31 K/° | 0,39K/° |
| **Phase S NO-RED case** | 0,26K/° | 0,31 K/° |

*Table 8.6 SMOS vs X-MIRAS EB table amplitude/phase visibility errors (baselines as reference and 50 trials)*

| | SMOS | X-MIRAS |
|---|---|---|
| **Additive RED case** | 0,90 K/cu | 1,38 K/cu |
| **Additive NO-RED case** | 1,00 K/cu | 1,67 K/cu |

*Table 8.7 SMOS vs X-MIRAS EB table additive errors (5 trials)*

| | SMOS | X-MIRAS |
|---|---|---|
| **Antenna errors amplitude RED case** | 0,35 K/% | 0,61 K/% |
| **Antenna errors amplitude NO-RED case** | 0,37 K/% | 0,71 K/% |
| **Antenna errors phase RED case** | 0,59 K/° | 1,07 K/° |
| **Antenna errors phase NO-RED case** | 0,64 K/ o | 1,21 K/ o |

*Table 8.8 SMOS vs X-MIRAS EB Voltage antenna pattern amplitude/phase (1trial)*

| | SMOS | X-MIRAS |
|---|---|---|
| **Antenna position errors in-plane RED case** | 0,10 K/mm | 0,09 K/mm |
| **Antenna position errors in-plane NO-RED case** | 0,31 K/mm | 0,24 K/mm |
| **Antenna position errors off-plane RED case** | 0,11 K/mm | 0,18 K/mm |
| **Antenna position errors off-plane NO-RED case** | 0,54 K/mm | 0,87 K/mm |

*Table 8.9 SMOS vs X-MIRAS EB Antenna position errors (SMOS 600 trials X-MIRAS 300 trials)*

### 8.2.4 X-MIRAS Error budget

The error budget can be estimated once the sensitivity coefficients are assessed. X-MIRAS error budget is based on the procedure already used in the MIRAS/SMOS mission. However, the following considerations are taken into account:

- This preliminary EB is performed for a constant TB=150 K at the antenna frame to allow comparison with the MIRAS/SMOS case.
- If not otherwise stated, the instrumental error values are taken from the MIRAS/SMOS mission. However, the sensitivity to such errors has been updated for the X-MIRAS case. The main changes with relation to MIRAS/SMOS mission are highlighted in blue and commented.

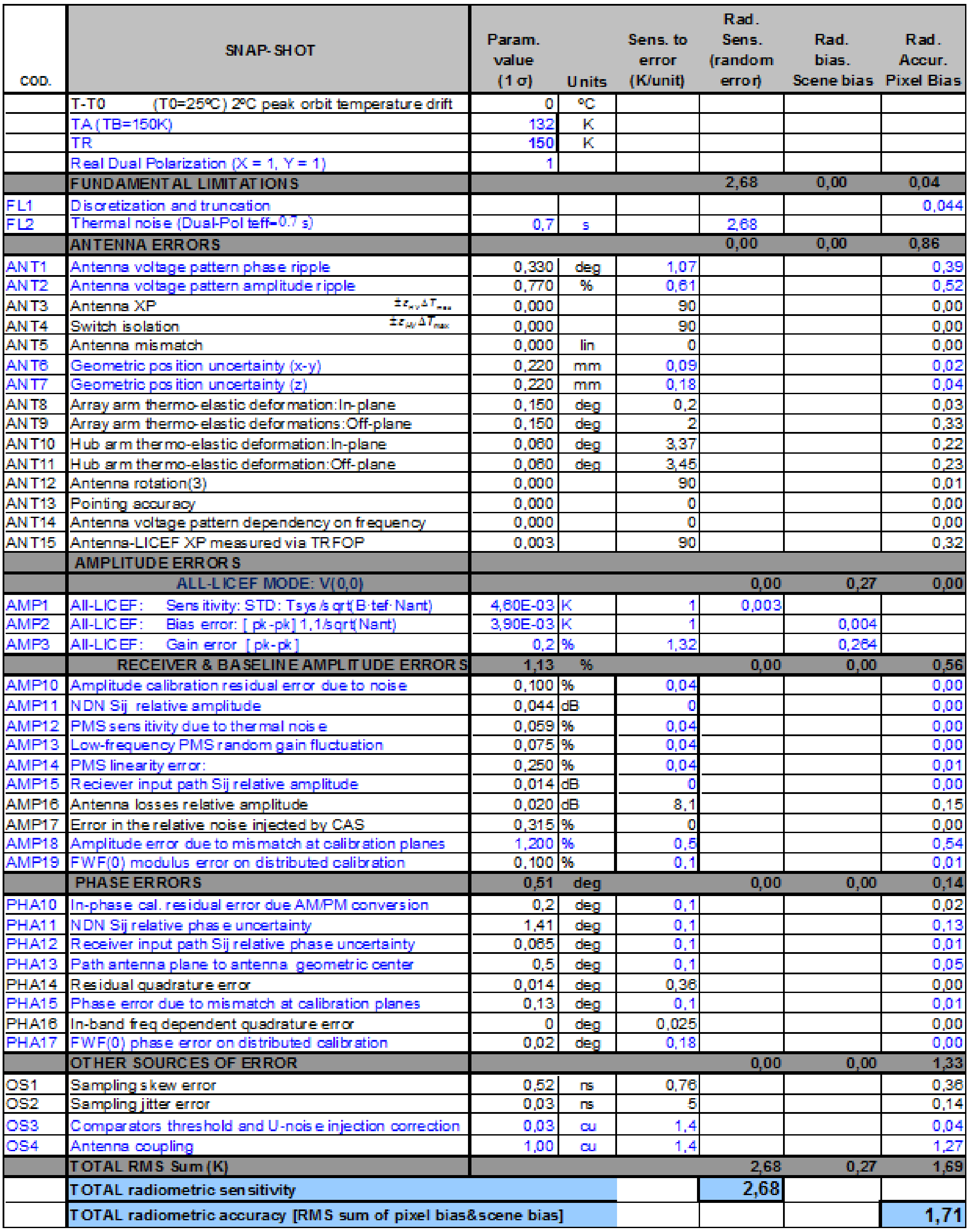

| COD. | SNAP-SHOT | Param. value (1 σ) | Units | Sens. to error (K/unit) | Rad. Sens. (random error) | Rad. bias. Scene bias | Rad. Accur. Pixel Bias |
|---|---|---|---|---|---|---|---|
| | T-T0 (T0=25ºC) 2ºC peak orbit temperature drift | 0 | ºC | | | | |
| | TA (TB=150K) | 132 | K | | | | |
| | TR | 150 | K | | | | |
| | Real Dual Polarization (X = 1, Y = 1) | 1 | | | | | |
| | **FUNDAMENTAL LIMITATIONS** | | | | 2,68 | 0,00 | 0,04 |
| FL1 | Discretization and truncation | | | | | | 0,044 |
| FL2 | Thermal noise (Dual-Pol teff=0.7 s) | 0,7 | s | | 2,68 | | |
| | **ANTENNA ERRORS** | | | | 0,00 | 0,00 | 0,86 |
| ANT1 | Antenna voltage pattern phase ripple | 0,330 | deg | 1,07 | | | 0,39 |
| ANT2 | Antenna voltage pattern amplitude ripple | 0,770 | % | 0,61 | | | 0,52 |
| ANT3 | Antenna XP $\pm\varepsilon_{xy}\Delta T_{max}$ | 0,000 | | 90 | | | 0,00 |
| ANT4 | Switch isolation $\pm\varepsilon_{xy}\Delta T_{max}$ | 0,000 | | 90 | | | 0,00 |
| ANT5 | Antenna mismatch | 0,000 | lin | 0 | | | 0,00 |
| ANT6 | Geometric position uncertainty (x-y) | 0,220 | mm | 0,09 | | | 0,02 |
| ANT7 | Geometric position uncertainty (z) | 0,220 | mm | 0,18 | | | 0,04 |
| ANT8 | Array arm thermo-elastic deformation:In-plane | 0,150 | deg | 0,2 | | | 0,03 |
| ANT9 | Array arm thermo-elastic deformations:Off-plane | 0,150 | deg | 2 | | | 0,33 |
| ANT10 | Hub arm thermo-elastic deformation:In-plane | 0,060 | deg | 3,37 | | | 0,22 |
| ANT11 | Hub arm thermo-elastic deformation:Off-plane | 0,060 | deg | 3,45 | | | 0,23 |
| ANT12 | Antenna rotation(3) | 0,000 | | 90 | | | 0,01 |
| ANT13 | Pointing accuracy | 0,000 | | 0 | | | 0,00 |
| ANT14 | Antenna voltage pattern dependency on frequency | 0,000 | | 0 | | | 0,00 |
| ANT15 | Antenna-LICEF XP measured via TRFOP | 0,003 | | 90 | | | 0,32 |
| | **AMPLITUDE ERRORS** | | | | | | |
| | **ALL-LICEF MODE: V(0,0)** | | | | 0,00 | 0,27 | 0,00 |
| AMP1 | All-LICEF: Sensitivity: STD: Tsys/sqrt(B·tef·Nant) | 4,60E-03 | K | 1 | 0,003 | | |
| AMP2 | All-LICEF: Bias error: [pk-pk] 1,1/sqrt(Nant) | 3,90E-03 | K | 1 | | 0,004 | |
| AMP3 | All-LICEF: Gain error [pk-pk] | 0,2 | % | 1,32 | | 0,264 | |
| | **RECEIVER & BASELINE AMPLITUDE ERRORS** | 1,13 | % | | 0,00 | 0,00 | 0,56 |
| AMP10 | Amplitude calibration residual error due to noise | 0,100 | % | 0,04 | | | 0,00 |
| AMP11 | NDN Sij relative amplitude | 0,044 | dB | 0 | | | 0,00 |
| AMP12 | PMS sensitivity due to thermal noise | 0,059 | % | 0,04 | | | 0,00 |
| AMP13 | Low-frequency PMS random gain fluctuation | 0,075 | % | 0,04 | | | 0,00 |
| AMP14 | PMS linearity error: | 0,250 | % | 0,04 | | | 0,01 |
| AMP15 | Reciever input path Sij relative amplitude | 0,014 | dB | 0 | | | 0,00 |
| AMP16 | Antenna losses relative amplitude | 0,020 | dB | 8,1 | | | 0,15 |
| AMP17 | Error in the relative noise injected by CAS | 0,315 | % | 0 | | | 0,00 |
| AMP18 | Amplitude error due to mismatch at calibration planes | 1,200 | % | 0,5 | | | 0,54 |
| AMP19 | FWF(0) modulus error on distributed calibration | 0,100 | % | 0,1 | | | 0,01 |
| | **PHASE ERRORS** | 0,51 | deg | | 0,00 | 0,00 | 0,14 |
| PHA10 | In-phase cal. residual error due AM/PM conversion | 0,2 | deg | 0,1 | | | 0,02 |
| PHA11 | NDN Sij relative phase uncertainty | 1,41 | deg | 0,1 | | | 0,13 |
| PHA12 | Receiver input path Sij relative phase uncertainty | 0,065 | deg | 0,1 | | | 0,01 |
| PHA13 | Path antenna plane to antenna geometric center | 0,5 | deg | 0,1 | | | 0,05 |
| PHA14 | Residual quadrature error | 0,014 | deg | 0,36 | | | 0,00 |
| PHA15 | Phase error due to mismatch at calibration planes | 0,13 | deg | 0,1 | | | 0,01 |
| PHA16 | In-band freq dependent quadrature error | 0 | deg | 0,025 | | | 0,00 |
| PHA17 | FWF(0) phase error on distributed calibration | 0,02 | deg | 0,18 | | | 0,00 |
| | **OTHER SOURCES OF ERROR** | | | | 0,00 | 0,00 | 1,33 |
| OS1 | Sampling skew error | 0,52 | ns | 0,76 | | | 0,36 |
| OS2 | Sampling jitter error | 0,03 | ns | 5 | | | 0,14 |
| OS3 | Comparators threshold and U-noise injection correction | 0,03 | cu | 1,4 | | | 0,04 |
| OS4 | Antenna coupling | 1,00 | cu | 1,4 | | | 1,27 |
| | **TOTAL RMS Sum (K)** | | | | 2,68 | 0,27 | 1,69 |
| | **TOTAL radiometric sensitivity** | | | | 2,68 | | |
| | **TOTAL radiometric accuracy [RMS sum of pixel bias&scene bias]** | | | | | | 1,71 |

*Figure 8.15 X-MIRAS error budget (EB) based on the SMOS approach. Changes with relation to SMOS are highlighted in blue*

## 8.3 Conclusions

This chapter presents a first approach to the X-MIRAS error budget and calibration scheme. Both are very based on MIRAS/SMOS approaches that have proved to be successful to a large extend [UPC team]. X-MIRAS calibration main novelty is the use of the all-LICEF mode that has been successfully implemented and tested in SMOS within commissioning prospective activities. The bulk of these improvements were already foreseen in the frame of the SMOS ops project [UPC team]. There are also a number of minor improvements both at hardware implementation and calibration sequences that come directly from SMOS experience [UPC team]. The error budget presented in this document has the same structure than in the SMOS case. It has also been computed from the same reference images (TB=150 K within the earth disc at the antenna frame) to easily assess the changes and improvements. The following conclusions developed by the RSLab team are worth to be mentioned:

- In relation to SMOS, X-MIRAS has a larger number of antennas and a larger impact of redundancy. Since these two parameters have a different impact in the radiometric error, X-MIRAS sensitivity to errors can be larger or smaller than in SMOS depending on the structure of the error distribution. In any case, increased redundancy in X-MIRAS has the positive impact that systematic errors present a more random distribution in the FoV for any single instrument.
- The contribution of internal errors (e.g. visibility phase, amplitude and offset errors) to the final radiometric accuracy is very low. SMOS development has demonstrated that both, good hardware implementation and proper calibration schemes can reduce internal errors to have an almost negligible contribution to the final performance.
- The contribution of external errors (antenna errors) in the error budget is also small. However, SMOS experience reveals that antenna errors have been clearly underestimated and require improved modeling and ground characterization. In the same sense, the error budget has been provided for an area of radius r=0.3 in the $(\xi, \eta)$ domain, that is placed in the AF-FoV. This is a best case view since SMOS experience has revealed that the extension of the AF-FoV to the earth contour introduces some problems that require further work and, currently, under investigation in SMOS.
- The reference image used in both, SMOS and X-MIRAS error budget is very simple (Earth disc at TB=150 K at the antenna frame) to allow a simple way to compare the impact of the different errors. However, SMOS experience has shown that more complex reference images are probably required to model properly the impact of antenna errors, errors in the inversion process, Flat Target Transformation, etc.. These images must take into account the effect of errors in the transformation from antenna frame to ground frame and probably be given in the Earth frame for simple images: earth at typical constant ocean, ice and/or soil brightness temperatures.

Simulations have shown that the discrepancies in the antenna patterns, even if they are perfectly known, produce a spatial error:

- If the antenna pattern has a large harmonic content, a non-negligible spatial error can be produced due to truncation, even in the case of having a perfectly known unique antenna pattern. This error is very dependent on the error distribution
- If the antenna discrepancies with relation to a mean antenna pattern are randomly distributed, the spatial error is lower and also randomly distributed. In this case, redundancy further reduces the error and makes a more random distribution
- In the case that the antenna pattern discrepancies present a bias, this produces systematic artifacts in the retrieved images, even in the case that the bias is perfectly known

## 8.4 Open issues

Antenna errors require extensive simulations and are very demanding in terms of memory and computational speed. Therefore, some issues have not been included in the frame of this work and remain open:

- Impact of antenna errors in the Extended AF-FoV.

- Impact of antenna cross-coupling errors.

- Assessment of optimum reference images to give more accurate estimations of system performance:
    - TB modeled from the Ocean.
    - TB modeled from Antarctica.
    - TB at constant temperature at the antenna/ground frame.

- Assessment of advantages/limitations of current SMOS different inversion approaches:
    - Minimum spatial error in the case of antenna pattern differences with relation to a mean antenna pattern.
    - Impact of biased errors in the arms. E.g due to the antenna pattern compression along the arms.
    - Impact of truncation errors due to antenna pattern harmonic content.
    - Impact of redundancy in the averaging of spatial errors. Weight of the shorter baselines antenna pattern discrepancies in the spatial error .

- The Error Budget has shown to be very dependent on the inversion approach, since different types of errors are more or less mitigated in each case. A systematic error analysis regarding the different inversion methods and the expected instrumental errors is mandatory to undertake the design of the X-MIRAS sensor.

# 9 Conclusions

## 9.1 Conclusions and further work

The research undertaken in this PhD has been performed within the framework of RSLAB activities related to the SMOS mission by the European Space Agency, as SMOS Expert Support Laboratory and related projects. Within this context, many of the research tasks developed in this work have been driven by specific troubleshooting activities related to SMOS flight operations and system performance assessments. Although the different activities are scattered along the PhD period, they have been reorganized by subjects in the different chapters (calibration, imaging, system performance,…) to help the reader and give more consistency to the PhD thesis.

Some specific tasks in this work have been addressed in collaboration with other master and PhD students, that are properly credited when appropriate. It is needless to say that all activities have been undertaken under the supervision of my thesis advisors and, frequently, also with the collaboration of other senior research members of the RSLab, mainly professor I. Corbella. Therefore, only those activities that have yielded a co-authored publication have been included in the thesis. Obviously, the depth and amount of details deserved in this thesis to any of those activities are proportional to my specific contribution to the advance of the art.

The main details, procedures and outcomes of each research activity have been systematically and thoroughly reported in Technical Notes (section 9.2.3) in the framework of RSLab projects. The more interesting results have also been regularly presented in the main international conferences in remote sensing as listed in section 9.2.2 (IGARSS, MicroRad, ESA Workshops, etc..). And finally, the key advances in the state of the art have been included in international publications that I have also coauthored (section 9.2.1).

The main outcome of this thesis is related to the so-called “Land-Sea Contamination”, as thoroughly reported in chapter 7. This is an artifact that appears in global error maps that show an anomalous increase in the oceans’ brightness temperature near large land masses. This LSC is related to residual multiplicative errors affecting, in a different way, the visibility at the origin and the other visibility samples. The all-LICEF mode improves the calibration consistency between both kinds, reducing the possible differences to only one single calibration parameter: the correlator efficiency $G_{kj}$. It has been found that a 2% overestimation of this parameter is the dominant contributor to the observed LSC. Using the all-LICEF mode, LSC is insensitive to any antenna temperature error (e.g., due to orbital or seasonal drift) and is corrected only by adjusting the correlator efficiency. This property might consolidate a decision to operate SMOS in all-LICEF mode in a future version of the processor. This results yielded two international publications, one to develop the LSC origin and mitigation strategy [Corbella *et al.,* 2015a] and a second one to validate the procedure by providing improved OS retrievals close to land [González-Gambau *et al.,* 2017].

A second key contribution, developed in the early stages of the research activities in SMOS is related to the so-called "floor error" as addressed in chapter 5 and chapter 6. It is defined as the difference between the reconstructed brightness temperature and the original one after discarding all sources of error due to calibration and limited knowledge of actual antenna patterns [Corbella *et al.,* 2014]. It has two contributions:

- Truncation of the visibility function
- Phase periodicity (aliasing)

In a simplified analysis considering all antenna patterns identical, the first contribution is the Gibbs effect. It can be mitigated by windowing the visibility function before inversion at the expense of reducing the spatial resolution. The second contribution in this case is the aliasing, making unusable the brightness temperature recovered in the alias regions, but keeping the alias free field of view, free of error. In the real case, when all different antenna patterns are considered, both contributions become non-clearly separable and both have impact in the alias-free field of view. To cancel the second contribution, a source with zero brightness temperature outside the principal period (hexagon) should be imaged. This can be achieved approximately by the "Gibbs 2" image reconstruction procedures [Corbella *et al.,* 2014]. It consists of imaging the difference between the measured visibility and that estimated from a model as close as possible to the source brightness temperature, especially in the alias zone.

It has also been found that the floor error has a large impact on SMOS 3rd (A3) and 4th (A4) Stokes parameters, defined at the antenna frame. It has been shown that, once the cross-polar antenna patterns are taken into account by means of the full-pol G-matrix, the dominant source of spatial bias on A3 and A4 is the floor error. This last is dominated by Tx and Ty brightness temperature outside the fundamental hexagon that leak into A3 and A4 AF-FoV through cross-polar antenna patterns and a G-matrix inversion that does not fulfill Fourier alias properties. It has been shown that this floor error can be very much mitigated by a simple Gibbs2 model approach, exclusively defined outside the fundamental hexagon [Durán *et al.,* 2015].

A third contribution worth to be mentioned, is the support to develop SMOS full-pol image reconstruction, as detailed in chapter 4. SMOS full-pol imaging was a key outcome of the PhD thesis by Wu Lin [Wu, 2014], but my contribution to improve SMOS full pol relative phases and the treatment of SMOS cross-polar antenna patterns resulted in a co-authored publication [Wu et al., 2013]. This was a key step forward in the SMOS mission since yielded version v620 (released in May 2015) to be the first L1 Operational Processor to provide high-quality SMOS full-polarimetric data. In particular, the significant improvement in A3 leads to a better correction of ionospheric effects such as Faraday rotation or attenuation [Corbella *et al.*, 2015b] and opens the door to better geophysical parameter retrievals.

Finally, the thesis also includes my contribution to several miscellaneous improvements in SMOS calibration, as summarized in chapter 4. These contributions have been recognized by co-authoring two publications led by ESA-SMOS Calibration and System Performance teams: [Martin-Neira *et al.*, 2015], [Martin-Neira *et al.*, 2016].

Regarding open issues and further work, it must be pointed out that, given the novelty of the SMOS instrument technology, investigations into the calibration, image reconstruction and performance of the instrument are continuously on-going. Although the mission's core objective was to improve our understanding of Earth's water cycle, SMOS has found a multitude of other uses such as tracking hurricanes, measuring thin ice floating in the polar oceans and improving crop-yield forecasts. Thanks to the excellent technical status and the scientific results achieved, the mission (and related funding to SMOS Expert Support Laboratories) has been extended by ESA to 2019 and beyond, pending a successful review of its performance in 2018, to the end of ESA's 5th Earth Observation Envelope Programme.

The following activities can be seen as the two main open issues to further improve SMOS performance:

- **Assessment on the origin of the LSC contamination:** The preliminary analysis performed in section 7.6.2 has revealed that antenna pattern phase errors may have an important role in the LSC artifact. A clear research line consists to model a physical or electromagnetic model that can explain the antenna pattern phase errors in a reasonable way. The main candidate is a displacement of antenna theoretical phase centre due to antenna characterization errors or in-flight array distortion. The tools developed in Chapter 8 to elaborate SuperMIRAS error budget can be adapted to SMOS to assess the impact of both errors.
- **Improved orbital and seasonal stability**. After recent calibration and image reconstruction improvements, SMOS radiometric performance is outstanding since both long term and orbital stability are constrained within a few tenths of a Kelvin. (e.g. see Figure 4.54). However, there still is some margin for further improvement since performance plots reveal a systematic error behavior that can eventually be mitigated after proper assessment and modeling. Moreover, it is clear that, at this point, the errors produced by the instrument are of the same order of magnitude that the uncertainty of the geophysical models used to assess such errors. This activity, devoted to decouple these two different contributions to the error plots, must be addressed in collaboration with the scientific community, mainly the OS teams.

It is needless to say that, since the activity of SMOS ESLs has been extended to 2019 and beyond, the general RSLab activity to support ESA calibration and System Performance teams will carry on.

## 9.2 Thesis outcomes

The original contributions of this work, as summarized in the section before, have resulted in a number of publications in international journals and conference proceedings. Comprehensive assessments of the theoretical developments, simulations and SMOS data processing have also been included in a number of Technical Notes within the frame of the SMOS UPC Level 1 Expert Support Laboratory (L1-ESL):

### 9.2.1 Journal papers

1. González-Gambau, V., Olmedo, E., Martínez, J., Turiel, A., **Durán, I.** (2017). New approach for the improvement of SMOS salinity retrievals in coastal regions. IEEE Trans, no. 99, pp. 1-15

2. Martín-Neira, M., Oliva, R., Corbella, I., Torres, F., Duffo, N., **Durán, I.**, .& Khazaal, A. (2016). SMOS instrument performance and calibration after 6 years in orbit. Remote Sensing of Environment, 180, 19-39.

3. Martin-Neira, M., R.Oliva, Corbella, I., Torres, F., Duffo, N., **Durán, I.**, J.Kainulainen, J.Close, A.Zurita, F.Cabot, A.Khazzaal, J.Barbosa, G.Lopes, J.Tenerelli, R.Díez-García, J.Fauste, F.Martín-Porqueras, V.González, A. Turiel, S.Delwart, R.Caprolicccchio, M. Suess (2015). SMOS instrument performance and calibration after 5 years in orbit.

4. Corbella, I**., Durán**, **I.**, Wu, L., Torres, F., Duffo, N., Khazaal, A., & Martín-Neira, M. (2015). Impact of correlator efficiency errors on SMOS land–sea contamination. IEEE Geoscience and Remote Sensing Letters, 12(9), 1813-1817.

5. Wu, L., Torres, F., Corbella, I., Duffo, N., **Durán, I.**, Vall-llossera, M., & Martín-Neira, M. (2013). Radiometric performance of SMOS full polarimetric imaging. IEEE Geoscience and Remote Sensing Letters, 10(6), 1454-1458.

6. Font, J., Ballabrera-Poy, J., Camps, A., Corbella. I, Duffo, N., **Durán, I.**, Emelianov, M., Enrique, L., Fernández, P., Gabarró, C., González, C., González-Gambau, V., Gourrion, J., Guimbard, S., Hoareau, N., Julià, A., Kalaroni, S., Konstantinidou, A., Aretxabaleta, A. , Martínez, J., Miranda, J., Monerris, A., Montero, S., Mourre, B., Pablos, M., Pérez, F., Piles, M., Portabella, M., Sabia, R., Salvador, J., Talone, M., Torres, F., Turiel, A., Vall-llossera, M. & Villarino, R.(2012). A new space technology for ocean observation: The SMOS mission. Scientia Marina
7. Corbella, I., Torres, F., Duffo, N., González-Gambau, V., Pablos, M., **Duran, I.**, & Martín-Neira, M. (2011). MIRAS calibration and performance: Results from the SMOS in-orbit commissioning phase. IEEE Transactions on Geoscience and Remote Sensing, 49(9), 3147-3155.

## 9.2.2 Conference papers

1. **Durán, I.**, Vizcarro, M., Torres, F., Duffo, N., González-Gambau, V., Corbella, I., Oliva, R. and Martín Neira, M. (2017). The ocean as a calibration target to trim SMOS visibility denormalization errors. IGARSS 2017 (IGARSS).

2. Martín-Neira, M., Oliva, R., Corbella, I., Torres, F., Duffo, N., **Durán, I**., Kainulainen, J., Closa, J., Zurita, A., Cabot, F., Khazaal, A., Anterrieu, E., Barbosa, J., Lopes, G., Tenerelli, J., Díez-García, R., Fauste, J., González-Gambau, V., Turiel, A., Delwart, S., Crapolicchio, R., Suess, M., Mecklenburg & S., Drusch, M. (2017). SMOS instrument performance and calibration after 7 years in orbit. In Geoscience and Remote Sensing Symposium (IGARSS), 2017

3. Corbella, I., González-Gambau, V., Torres, F., Duffo, N., **Durán, I.**, & Martín-Neira, M. (2016). The MIRAS “all-licef” calibration mode. In Geoscience and Remote Sensing Symposium (IGARSS), 2016 IEEE International (pp. 2013-2016). IEEE.

4. **Durán, I.**, Lin, W., Torres, F., Corbella, I., Duffo, N., & Martín-Neira, M. (2016). SMOS simplified iterative full-pol brightness temperature retrieval. In Geoscience and Remote Sensing Symposium (IGARSS), 2016 IEEE International (pp. 842-845). IEEE.

5. Torres, F., **Durán, I.**, Corbella, I., Duffo, N., Closa, J., Oliva, R., & Martín-Neira, M. (2016). Impact of antenna tuning on SMOS correlation loss. In Geoscience and Remote Sensing Symposium (IGARSS), 2016 IEEE International (pp. 2017-2020). IEEE.

6. **Durán, I.**, Torres, F., Corbella, I., Duffo, N., Wu, L., & Martín-Neira, M. (2016). Mitigation of cross-polar antenna pattern errors in SMOS: simplified

approach. In Microwave Radiometry and Remote Sensing of the Environment (MicroRad), 2016 14th Specialist Meeting on (pp. 131-134). IEEE.

7. **Durán, I.**, Lin, W., Corbella, I., Torres, F., Duffo, N., & Martín-Neira, M. (2015). SMOS floor error impact and migation on ocean imaging. In Geoscience and Remote Sensing Symposium (IGARSS), 2015 IEEE International (pp. 1437-1440). IEEE.

8. Corbella, I., **Durán**, **I.**, Lin, W., Torres, F., Duffo, N., Khazâal, A., & Martín-Neira, M. (2015). Mitigation of land-sea contamination in SMOS. In Geoscience and Remote Sensing Symposium (IGARSS), 2015 IEEE International (pp. 1433-1436). IEEE.

9. Martin-Neira, M., R.Oliva, Corbella, I., Torres, F., Duffo, N., **Durán, I.**, J.Kainulainen, J.Close, A.Zurita, F.Cabot, A.Khazzaal, J.Barbosa, G.Lopes, J.Tenerelli, R.Díez-García, J.Fauste, F.Martín-Porqueras, V.González, A. Turiel, S.Delwart, R.Caproliccchio, M. Suess (2015). SMOS instrument performance and calibration after 5 years in orbit. IEEE International Geoscience & Remote Sensing Symposium Program Guide Book: 69 (2015)

10. Corbella, I., Torres, F., Wu, L., Duffo, N., **Durán, I.**, & Martín-Neira, M. (2014). SMOS image reconstruction quality assessment. In Geoscience and Remote Sensing Symposium (IGARSS), 2014 IEEE International (pp. 1914-1916). IEEE.

11. Torres, F., Corbella, I., **Durán, I.**, Lin, W., Duffo, N., & Martín-Neira, M. (2014). Residual calibration error impact on SMOS SLL performance. In Geoscience and Remote Sensing Symposium (IGARSS), 2014 IEEE International (pp. 2542-2545). IEEE.

12. Wu, L., **Durán, I.**, Torres, F., Corbella, I., Duffo, N., Closa, J., Manrique, R., Garcia, Q., Oliva, R. & Martin-Neira.(2014). "Practical issues on SMOS single antenna patterns". 13th Specialist Meeting on Microwave Radiometry and Remote Sensing of the Environment (MicroRad), Pasadena,CA, 2014,pp.197-200.

13. Corbella, I., Torres, F., Wu, L., Duffo, N., **Durán, I.**, & Martín-Neira, M. (2013). Spatial biases analysis and mitigation methods in SMOS images. In Geoscience and Remote Sensing Symposium (IGARSS), 2013 IEEE International (pp. 3415-3418). IEEE.

14. Corbella, I., Torres, F., Duffo, N., **Durán, I.**, Pablos, M., & Martín-Neira, M. (2012). Enhanced SMOS amplitude calibration using external target.

In Geoscience and Remote Sensing Symposium (IGARSS), 2012 IEEE International (pp.2868-2871).IEEE.

15. Corbella, I., Torres, F., Duffo, N., González-Gambau, V., **Durán, I.**, Pablos, M., & Martín-Neira, M. (2010). Some results on SMOS-MIRAS calibration and imaging. In Geoscience and Remote Sensing Symposium (IGARSS), 2010 IEEE International (pp. 3768-3771). IEEE.

16. Corbella, I., Torres, F., Duffo, N., González-Gambau, V., Pablos, M., **Durán, I.**, & Martín-Neira, M. (2010). First results on MIRAS calibration and overall SMOS performance. In Microwave Radiometry and Remote Sensing of the Environment (MicroRad), 2010 11th Specialist Meeting on (pp. 1-4). IEEE.

### 9.2.3 Technical notes

1. **Durán, I.**, Vizcarro, M., Torres, F., Corbella, I., Duffo, N. (2017). Implementation and validation of the PMS offset jumps correction. Ref: SO-TN-UPC-PLM-0173 . Universitat Politècnica de Catalunya

2. **Durán, I.**, Wu, L., Torres, F., Corbella, I., Duffo, N (2015). Gibbs 2 with simplified XPOL terms. Ref: SO-TN-UPC-PLM-0168. Universitat Politècnica de Catalunya

3. **Durán, I.**, Wu, L., Torres, F., Duffo, N., Corbella, I. (2013). IVT Relative phase for Full-Pol mode. Ref: SO-TN-UPC-PLM-0161 v1.0. Universitat Politècnica de Catalunya.

4. **Durán, I.**, Wu, L., Torres, F., Duffo, N., Corbella, I. (2013). Review of IVT relative phases. Ref: SO-TN-UPC-PLM-0159 v1.0. Universitat Politècnica de Catalunya.

5. **Durán, I.**, Wu, L., Torres, F., Corbella, I., Duffo, N. (2013). Impact of visibility errors on SMOS SLL performance. Ref: XMIR-UPC-DD6 v1.0.Universitat Politècnica de Catalunya.

6. Wu, L., F.Torres, Corbella, I., Duffo, N., **Durán, I.** (2012). Multiplicative mask performance assessment. Ref: SO-TN-UPC-PLM-0152 v1.0. Universitat Politècnica de Catalunya.

7. **Durán, I.**, Wu, L.,Torres, F., Duffo, N., Corbella, I. (2012). Simulation of antenna pattern differences impact on SMOS spatial bias. Ref: SO-TN-UPC-PLM-0147 v1.0. Universitat Politècnica de Catalunya.

8. **Durán, I.**, Torres, F.,Corbella, I.,Duffo, N. (2012). XMIR-UPC-DD-5 Super MIRAS Baseline Instrument Calibration Definitionand Error Budget v1_1. Ref: XMIR-UPC-DD-5 v1.0. Universitat Politècnica de Catalunya.

9. Corbella, I., Torres, F., Duffo, N., **Durán, I.**, Pablos, M. (2011). Summary of LICEF antenna models. Ref: SO-TN-UPC-PLM-0139 v1.0. Universitat Politècnica de Catalunya.

10. Pablos, M., **Durán, I.**, Torres, F., Corbella, I., Duffo, N. (2011). LICEF new antenna model: multivariable regression coefficients. Ref: SO-TN-UPC-PLM-0137 v1.0. Universitat Politècnica de Catalunya.

11. Pablos, M., **Durán, I.**, Torres, F., Duffo, N., Corbella, I. (2011). LICEF double slope coefficients. Ref: SO-TN-UPC-PLM-0135 v3.0. Universitat Politècnica de Catalunya.
12. Corbella, I., Torres, F., Duffo, N., **Durán, I.**, Pablos, M. (2011). Definition of a metric for instrument drift analysis. Ref: SO-TN-UPC-PLM-0132 v1.4. Universitat Politècnica de Catalunya.

13. Pablos, M., **Durán, I.**, Torres, F., Duffo, N., Corbella, I. (2011). PMS gain drift 2010. Ref: SO-TN-UPC-PLM-0128 v1.0. Universitat Politècnica de Catalunya.

14. **Durán, I.**, Pablos, M., Torres, F., Duffo, N., Corbella, I. (2011). CAS factors in arm B in nominal configuration. Ref: SO-TN-UPC-PLM-0124 v1.3. Universitat Politècnica de Catalunya.

15. Pablos, M., **Durán, I.**, Torres, F., Duffo, N., Corbella, I. (2011). Review of PMS offset in-flight error. Ref: SO-TN-UPC-PLM-0116 v1.3. Universitat Politècnica de Catalunya.

16. **Durán, I.**, Torres, F., Corbella, I., Duffo, N. (2011). Error budget First Preliminary results. Ref: SO-TN-UPC-PLM-0128 v1.0 Universitat Politècnica de Catalunya.

17. Torres, F., Corbella, I., Duffo, N., **Durán, I.**, Pablos, M. Title: CAS factors independent of antenna efficiency (2011). Ref: SO-TN-UPC-PLM-0140 v1.0. Universitat Politècnica de Catalunya.

18. Torres, F., Corbella, I., Duffo, N., **Durán, I.**, Pablos (2011). Summary of LICEF antenna models. Ref: SO-TN-UPC-PLM-0139 v1.0. Universitat Politècnica de Catalunya.

19. Pablos, M., **Durán, I.**, Torres, F., Duffo, N., Corbella, I (2010). Comprehensive analysis of short terms LICEF front-end. Ref: SO-TN-UPC-PLM-0119 v1.0. Universitat Politècnica de Catalunya.

20. Pablos, M., **Durán, I.**, Torres, F., Duffo, N., Corbella, I. (2010). Impact of temperature drift on antenna patch attenuation L1. Ref: SO-TN-UPC-PLM-0117 v2.2. Universitat Politècnica de Catalunya.

21. Torres, F., Duffo, N., Corbella, I., **Durán, I.**, Pablos, M. (2010). LICEF front-end enhance model. Ref: SO-TN-UPC-PLM-0113 v1.9. Universitat Politècnica de Catalunya.

22. Pablos, M., **Durán, I.**, Torres, F., Corbella, I., Duffo, N. (2010). All-LICEF Performance Assessment. Ref: SO-TN-UPC-PLM-0106 v1.0. Universitat Politècnica de Catalunya.

# 10 List of acronyms

| | |
|---|---|
| A3 | 3rd Stokes brightness temperature at the antenna frame |
| A4 | 4th Stokes brightness temperature at the antenna frame |
| AMIRAS | Airborne MIRAS |
| AP | Antenna Pattern |
| BPF | Band-Pass Filter |
| CA | Circle area |
| CAS | Internal calibration system/ Calibration subsystem |
| CCU | Central Control Unit |
| CDTI | Centro para el Desarrollo Tecnológico Industrial |
| CIP | Calibration Internal Plane |
| CMN | Control and Monitoring Node |
| CNES | Centre National d'Études Spatiales |
| CPG | Co-polar G-matrix |
| DICOS | Digital Correlator System |
| DTFT | Discrete-time Fourier Transform |
| EAF-FoV | Extended Alias-Free Field of View |
| ESA | European Space Agency |
| ESL | Expert Support Laboratory |
| ESAC | European space astronomy centre |
| ETO | External Target Observation |
| FoV | Field of View |
| FPG | Full-pol G-matrix |
| FPI | Formación de Personal Investigador |
| FR | Faraday rotation |

| | |
|---|---|
| FTR | The Flat Target Response |
| FTT | Flat Target Transformation |
| FWF | Fringe-washing function |
| HPBW | Half power beam width |
| IFFT | Inverse Fast Fourier Transform |
| IVT | Image Validation Tests |
| L1-ESL | Level 1 Export Support Laboratory |
| L1 OP | Level 1 Operational Processor |
| LICEF | Lightweight Cost-Effective Front-ends |
| LNA | Low Noise Amplifier |
| LO | Local Oscillator |
| LOCEAN | The Laboratoire d'Océanographie et du Climat Expérimentations et approaches Numériques |
| LSC | Land-Sea Contamination |
| MDB | Miras Data Base |
| M-CPG | Model Co-polar G-matrix |
| M-FPG | Model Full-polarimetric G-matrix approach |
| MIRAS | Microwave Imaging Radiometer with Aperture Synthesis |
| MTS | MIRAS Testing Software |
| NDN | Noise Distribution Network |
| NIC | Noise Injection Circuitry |
| NIR | Noise Injection Radiometer |
| OTT | Ocean Target Transformation |
| PD | Power Divider |
| PMS | Power Measurement System |
| PFC | Proyecto Fin de Carrera |
| PSR | Point Source Response |

| | |
|---|---|
| PSU | Practical Salinity Units |
| RAR | Real Aperture radiometers |
| RFI | Radio Frequency Interference |
| RMS | Root Mean Square |
| RSLab | Remote Sensing Laboratory (UPC) |
| SB | Spatial Bias (usually measured over the pure Ocean) |
| SLL | Side Lobes Level |
| SMOS | Soil Moisture and Ocean Salinity (ESA) |
| SMOS-BEC | SMOS Barcelona Expert Centre on Radiometric Calibration and Ocean Salinity |
| STD | Standard Deviation |
| SOGS | Satellite Operations Ground Segment |
| SSS | Sea Surface Salinity |
| SST | Sea Surface Temperature |
| TPR | Total Power Radiometer |
| TSC | Signal Theory and Communications Department |
| UC | Unity Circle |
| UPC | Universitat Politècnica de Catalunya |
| UTC | Coordinated Universal Time |

# 11 References

Antonov, J.I. et al. (2009). WorldOceanAtlas Volume 2: Salinity, S. Levitus, Ed. Washington, DC, USA: NOAA Atlas NESDIS 69 U.S. Government Printing Office, Mar. 2010, p. 184

Barré, H. M., Duesmann, B., & Kerr, Y. H. (2008). SMOS: The mission and the system. IEEE transactions on geoscience and remote sensing, 46(3), 587-593.

Brown, M. A., Torres, F., Corbella, I., & Colliander, A. (2008). SMOS calibration. IEEE Transactions on Geoscience and Remote Sensing, 46(3), 646-658.

Camps, A. J. (1996). Aplication of Interferometric Radiometry to Earth Observation. Ph.D. thesis. Universitat Politècnica de Catalunya.

Camps, A., Bará, J., Corbella, I., & Torres, F. (1997). The processing of hexagonally sampled signals with standard rectangular techniques: Application to 2-D large aperture synthesis interferometric radiometers. IEEE Transactions on Geoscience and Remote Sensing, 35(1), 183-190.

Camps, A., Corbella, I., Torres, F., Vall-llossera, M., & Duffo, N. (2005). Polarimetric formulation of the visibility function equation including cross-polar antenna patterns. IEEE Geoscience and Remote Sensing Letters, 2(3), 292-295.

Camps, A., Vall-llossera, M., Corbella, I., Duffo, N., & Torres, F. (2008). Improved image reconstruction algorithms for aperture synthesis radiometers. IEEE Transactions on Geoscience and Remote Sensing, 46(1), 146-158.

Colliander, A., Ruokokoski, L., Suomela, J., Veijola, K., Kettunen, J., Kangas, V., Aalto, A., Greus, H., Hallikainen, M., & Lahtinen, J. (2007). Development and calibration of SMOS reference radiometer. IEEE transactions on geoscience and remote sensing, 45(7), 1967-1977.

Corbella, I., Torres, F., Camps, A., Bara, J., Duffo, N., & Vall-Ilossera, M. (2000). L-band aperture synthesis radiometry: Hardware requirements and system performance. In Geoscience and Remote Sensing Symposium, 2000. Proceedings. IGARSS 2000. IEEE 2000 International (Vol. 7, pp. 2975-2977). IEEE.

Corbella, I., Duffo, N., Vall-llossera, M., Camps, A., & Torres, F. (2005a). The visibility function in interferometric aperture synthesis radiometry. IEEE Transactions on Geoscience and Remote Sensing, 42(8), 1677-1682.

Corbella, I., Torres, F., Camps, A., Colliander, A., Martín-Neira, M., Ribó, S. & Vall-llossera, M. (2005b). MIRAS end-to-end calibration: Application to SMOS L1 processor. IEEE Transactions on Geoscience and Remote Sensing, 43(5), 1126-1134.

Corbella, I., Torres, F., Blanch, S., Ribó, S., Beraza, S., Duffo, N., Camps, A., Vall-llossera, M. & Martín-Neira, M. (2006, July). Inter-element phase calibration in interferometric radiometers. In Geoscience and Remote Sensing Symposium, 2006. IGARSS 2006. IEEE International Conference on (pp. 3976-3979). IEEE.

Corbella, I. (2008). ESTEC course. Interferometric Aperture Synthesis Radiometry for Earth observation.

Corbella, I., Torres, F., Duffo, N., Martín-Neira, M., González-Gambau, V., Camps, A., & Vall-llossera, M. (2009a). On-ground characterization of the SMOS payload. IEEE Transactions on Geoscience and Remote Sensing, 47(9), 3123-3133.

Corbella, I., Torres, F., Camps, A., Duffo, N., & Vall-llossera, M. (2009b). Brightness-temperature retrieval methods in synthetic aperture radiometers. IEEE Transactions on Geoscience and Remote Sensing, 47(1), 285-294.

Corbella, I., Torres, F., Duffo, N., González-Gambau, V., Duran, I., Pablos, M., & Martín-Neira, M. (2010a). Some results on SMOS-MIRAS calibration and imaging. In Geoscience and Remote Sensing Symposium (IGARSS), 2010 IEEE International (pp. 3768-3771). IEEE.

Corbella, I., Torres, F., Duffo, N., González-Gambau, V., Pablos, M., Duran, I., & Martín-Neira, M. (2010b). First results on MIRAS calibration and overall SMOS performance. In Microwave Radiometry and Remote Sensing of the Environment (MicroRad), 2010 11th Specialist Meeting on (pp. 1-4). IEEE.

Corbella, I., Torres, F., Duffo, N., González-Gambau, V., Pablos, M., Duran, I., & Martín-Neira, M. (2011). MIRAS calibration and performance: Results from the SMOS in-orbit commissioning phase. IEEE Transactions on Geoscience and Remote Sensing, 49(9), 3147-3155.

Corbella, I., Torres, F., Duffo, N., & Martín-Neira, M. (2012a). Supermiras instrument development, technology and calibration. In Geoscience and Remote Sensing Symposium (IGARSS), 2012 IEEE International (pp. 3427-3430). IEEE.

Corbella, I.. (2012b). PPT XMIRAS MTR: AI-11 (AI-26) from PDR: Synthetic pattern errors for circular window.

Corbella, I., Martin-Neira, M., Oliva, R., Torres, F., & Duffo, N. (2012c). Reduction of secondary lobes in aperture synthesis radiometry. IEEE Geoscience and Remote Sensing Letters, 9(5), 977-979.

Corbella, I., Torres, F., Duffo, N., Durán, I., Pablos, M., & Martín-Neira, M. (2012d). Enhanced SMOS amplitude calibration using external target. In Geoscience and Remote Sensing Symposium (IGARSS), 2012 IEEE International (pp. 2868-2871). IEEE.

Corbella, I., Torres, F., Wu, L., Duffo, N., Duran, I., & Martín-Neira, M. (2013). Spatial biases analysis and mitigation methods in SMOS images. In Geoscience and Remote Sensing Symposium (IGARSS), 2013 IEEE International (pp. 3415-3418). IEEE.

Corbella, I., Torres, F., Wu, L., Duffo, N., Duran, I., & Martín-Neira, M. (2014). SMOS image reconstruction quality assessment. In Geoscience and Remote Sensing Symposium (IGARSS), 2014 IEEE International (pp. 1914-1916). IEEE.

Corbella, I., Durán, I., Wu, L., Torres, F., Duffo, N., Khazaal, A., & Martín-Neira, M. (2015a). Impact of correlator efficiency errors on SMOS land–sea contamination. IEEE Geoscience and Remote Sensing Letters, 12(9), 1813-1817.

Corbella, I., Wu, L., Torres, F., Duffo, N., & Martín-Neira, M. (2015b). Faraday rotation retrieval using SMOS radiometric data. IEEE Geoscience and Remote Sensing Letters, 12(3), 458-461.

Corbella, I., González-Gambau, V., Torres, F., Duffo, N., Durán, I., & Martín-Neira, M. (2016). The MIRAS "all-licef" calibration mode. In Geoscience and Remote Sensing Symposium (IGARSS), 2016 IEEE International (pp. 2013-2016). IEEE.

Durán, I., Torres, F., Corbella, I., Duffo, N. (2012). Baseline instrument calibration definition and Error Budget (XMIR-UPC-DD-5 ver 1.1).

Durán, I., Wu, L., Torres, F., Corbella, I., Duffo, N. (2013). "Review of IVT relative phases (SO-TN-UPC-PLM-0159)".

Duran, I., Lin, W., Corbella, I., Torres, F., Duffo, N., & Martín-Neira, M. (2015). SMOS floor error impact and migation on ocean imaging. In Geoscience and Remote Sensing Symposium (IGARSS), 2015 IEEE International (pp. 1437-1440). IEEE.

Durán, I., Torres, F., Corbella, I., Duffo, N., Wu, L., & Martín-Neira, M. (2016a). Mitigation of cross-polar antenna pattern errors in SMOS: simplified approach. In Microwave Radiometry and Remote Sensing of the Environment (MicroRad), 2016 14th Specialist Meeting on (pp. 131-134). IEEE.

Durán, I., Lin, W., Torres, F., Corbella, I., Duffo, N., & Martín-Neira, M. (2016b). SMOS simplified iterative full-pol brightness temperature retrieval. In Geoscience and Remote Sensing Symposium (IGARSS), 2016 IEEE International (pp. 842-845). IEEE.

Durán, I., M. Vizcarro, Torres, F., Duffo, N., González-Gambau, V., Corbella, I., R. Oliva and M.Martín Neira (2017). The ocean as a calibration target to trim SMOS visibility denormalization errors. IGARSS 2017 (IGARSS).

ESA (2015). Definition of a metric to assess SMOS L1 Data Quality. Ref.: SM-TN-AURO-L1OP-0003.

Font, J., Boutin, J., Reul, N., Spurgeon, P., Ballaberea, J., Chuprin, A., Gabarro, C, Gourion, J., Lavender, S., Martin, N., Martinez, J., McCulloch, M., Meirold-Mautner, I., Petitcolin, F., Portabella, M., Sabia, R., Talone, M., Tenerelli, J., Turiel, A., Vergely, J., Waldteufel, P., Yin, X, Zine, S., & Delwart, S. (2010, December). SMOS: Objectives and approach for ocean salinity observations. In ESA Living Planet Symposium (Vol. 686).

González-Gambau, V., Turiel, A., Olmedo, E., Martínez, J., Corbella, I., & Camps, A. (2015). Nodal sampling: A new image reconstruction algorithm for SMOS. IEEE Transactions on Geoscience and remote Sensing, 54(4), 2314-2328.

González-Gambau, V., Olmedo, E., Turiel, A., Martínez, J., Ballabrera-Poy, J., Portabella, M., & Piles, M. (2016). Enhancing SMOS brightness temperatures over the ocean using the nodal sampling image reconstruction technique. Remote Sensing of Environment, 180, 205-220.

González-Gambau, V., Olmedo, E., Martínez, J., Turiel, A., Durán, I. (2017). New approach for the improvement of SMOS salinity retrievals in coastal regions. IEEE Trans, no. 99, pp. 1-15, April 2017.

Martín-Neira, M., Ribó, S., & Martín-Polegre, A. J. (2002). Polarimetric mode of MIRAS. IEEE Transactions on Geoscience and Remote Sensing, 40(8), 1755-1768.

Martín-Neira, M., Suess, M., Kainulainen, J., & Martin-Porqueras, F. (2008a). The flat target transformation. IEEE Transactions on Geoscience and Remote Sensing, 46(3), 613-620.

Martín-Neira, M., Cabeza, I., Pérez, C., Palacios, M. A., Guijarro, M. A., Ribó, S., Corbella, I., Blanch, S., Torres, F., Duffo, N., González, V., Camps, A., Vall-llossera, M., Tauriainen, S., Pihlflyckt, J., González, J. & Martin-Porqueras, F. (2008b). AMIRAS—An airborne MIRAS demonstrator. IEEE Transactions on Geoscience and Remote Sensing, 46(3), 705-716.

Martin-Neira, M. (2010). In-Orbit Commissioning Phase: High Level Planning.

Martin-Neira, M., Oliva R., Corbella, I., Torres, F., Duffo, N., Durán, I., Kainulainen, J., Closa, J., Zurita, A., Cabot, F., Khazzaal, A., Anterrieu, E., Barbosa, J., Lopes, G., Tenerelli, J., Díez-García, R., Fauste, J., Martín-Porqueras, M., González-Gambau, V., Turiel, A., Delwart, S., Caproliccchio, R, & Suess, M. (2015). SMOS instrument performance after five years in orbit. IEEE International Geoscience & Remote Sensing Symposium Program Guide Book: 69.

Martin-Neira, M., Oliva R., Corbella, I., Torres, F., Duffo, N., Durán, I., Kainulainen, J., Closa, J., Zurita, A., Cabot, F., Khazaal, A., Anterrieu, E., Barbosa, J., Lopes, G., Tenerelli, J., Díez-García, R., Fauste, J., Martín-Porqueras, M., González-Gambau, V., Turiel, A., Delwart, S., Caproliccchio, R, & Suess, M. (2016). SMOS instrument performance and calibration after six years in orbit. Remote Sensing of Environment, 180, 19-39.

McMullan, K. D., Brown, M. A., Martín-Neira, M., Rits, W., Ekholm, S., Marti, J., & Lemanczyk, J. (2008). SMOS: The payload. IEEE Transactions on Geoscience and Remote Sensing, 46(3), 594-605.

Torres, F., Camps, A., Bará, J., Corbella, I., & Ferrero, R. (1996). On-board phase and modulus calibration of large aperture synthesis radiometers: Study applied to MIRAS. IEEE Transactions on Geoscience and Remote Sensing, 34(4), 1000-1009.

Torres, F., Corbella, I., Camps, A., Duffo, N., Vall-llossera, M., Beraza, S., Gutierrez, C. & Martín-Neira, M. (2006). Denormalization of visibilities for in-orbit calibration of interferometric radiometers. IEEE Transactions on Geoscience and Remote Sensing, 44(10), 2679-2686.

Torres, F., González-Gambau, V., González-Haro (2008). One point calibration in interferometric radiometers devoted to Earth observation. , Proc. SPIE 7106, Sensors, Systems, and Next-Generation Satellites XII, 710610 (October 09, 2008); doi:10.1117/12.800078.

Torres, F., Corbella, I., Duran, I., Lin, W., Duffo, N., & Martín-Neira, M. (2014). Residual calibration error impact on SMOS SLL performance. In Geoscience and Remote Sensing Symposium (IGARSS), 2014 IEEE International (pp. 2542-2545). IEEE.

Torres, F., Durán, I., Corbella, I., Duffo, N., Closa, J., Oliva, R., & Martín-Neira, M. (2016). Impact of antenna tuning on SMOS correlation loss. In Geoscience and Remote Sensing Symposium (IGARSS), 2016 IEEE International (pp. 2017-2020). IEEE.

UPC. Study of a high spatial resolution MIRAS (X-MIRAS). ESTEC/ITT: AO/1-6278/09/NL/JD. Statement of work: TRP T106-017ET. Proposal number: UPC-SMI-OF-0001

UPC. Analysis of Instrument Requirements. XMIR-UPC-DD-1B ver 1.0

UPC. SMOS in-orbit calibration plan. Phase C-D. SO-TN-UPC-PLM-0019 v1.1

UPC. KO CCN-1: XMIR-ECE-MIN-0021.
UPC. "In orbit calibration plan. Rev 3.3. 30th of January 2004.SO-TN-UPC-PLM-0001.

UPC. SMOS-Ops Receiver Technology Study: System Level Optimization. ECE-SOP-TN-0001 iss. 2. July 2008.

Pivnenko, S., Nielsen, J.M., Cappellin, C., Lemanczyk, G., Breinbjerg, O. (2007). High-accuracy calibration of the SMOS radiometer antenna patterns at the DTU-ESA spherical near-field antenna test facility. IEEE International Geoscience and Remote Sensing Symposium - IGARSS 2007

Vizcarro, M., Corbella, I. & Torres, F. (2016). Mitigation of PMS jumps (SO-TN-UPC-PLM-0170).

Wu, L., Torres, F., Corbella, I., Duffo, N., Durán, I., Vall-llossera, M., & Martín-Neira, M. (2013). Radiometric performance of SMOS full polarimetric imaging. IEEE Geoscience and Remote Sensing Letters, 10(6), 1454-1458.

Wu, L. PhD Thesis disertation (2014). Contribution to spatial bias mitigation in interferometric radiometers devoted to Earth observation: application to the SMOS mission.

Zine, S., Boutin, J., Font, J., Reul, N., Waldteufel, P., Gabarró, C., Tenerelli, J., Vergely, J., Talone, M., & Delwart, S. (2008). Overview of the SMOS sea surface salinity prototype processor. IEEE Transactions on Geoscience and Remote Sensing, 46(3), 621-645.

# Appendix I: SMOS global error maps

The following SMOS global error maps are computed with the different approaches explained in that chapter (Basic, Gibbs 1 and Gibbs 2) in order to show the comparison between them.

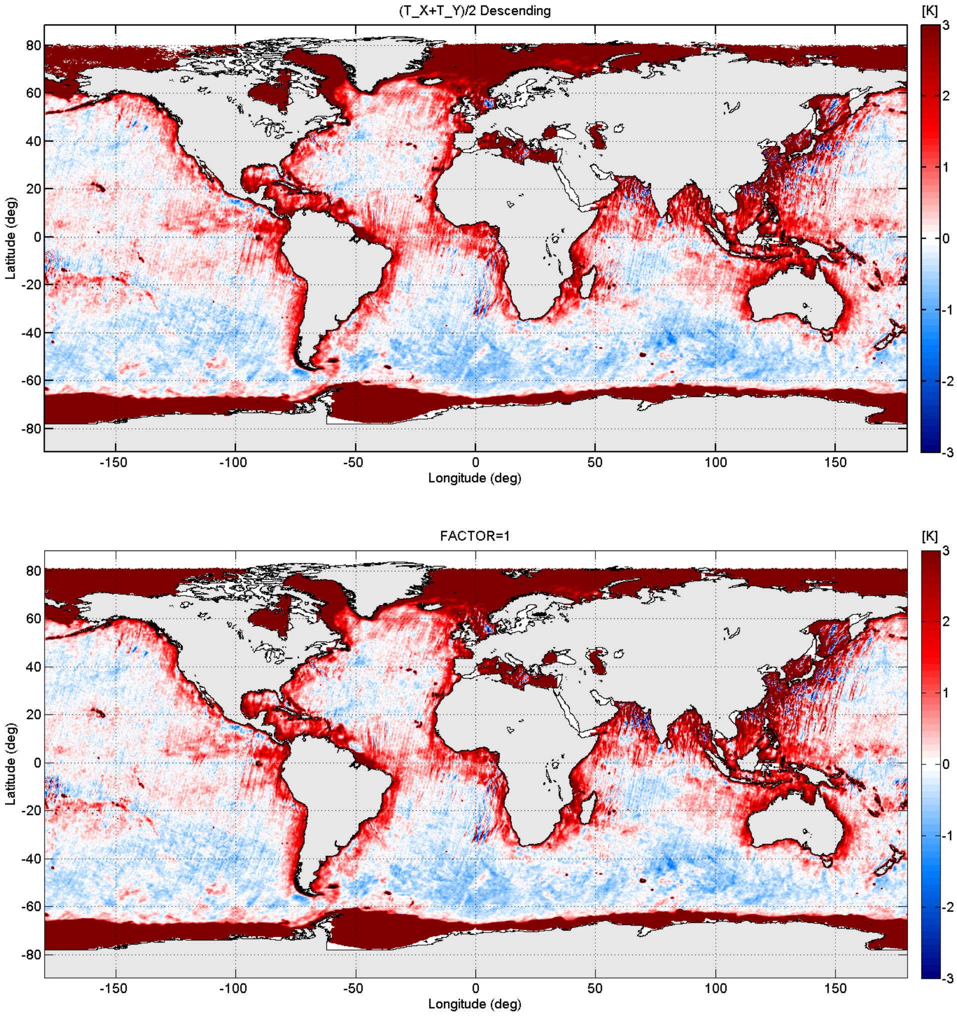

*Figure A-1.1 1st Stokes SMOS global error map (10 days data). Basic approach (top) and Gibbs 1 (bottom).*

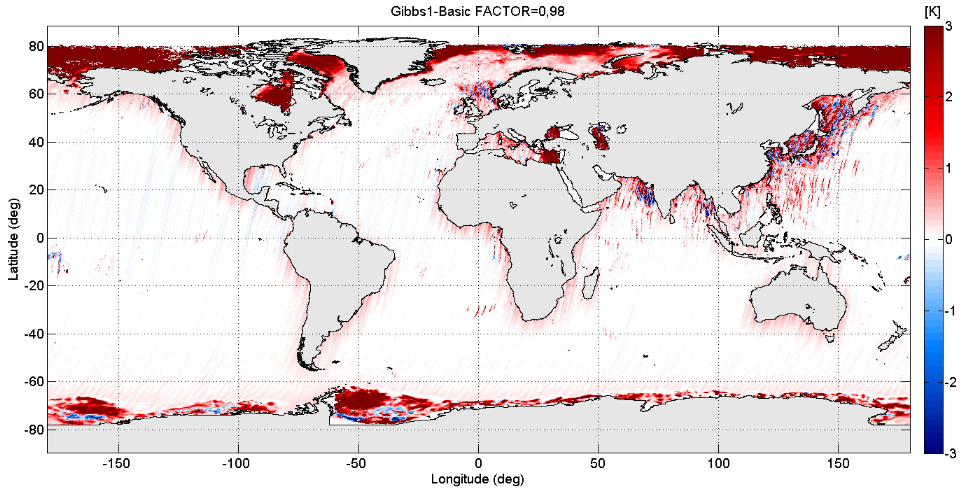
Gibbs1-Basic FACTOR=0,98

*Figure 6.16 1st Stokes SMOS global error map (10 days data). Difference between Gibbs 1 and Basic approach*

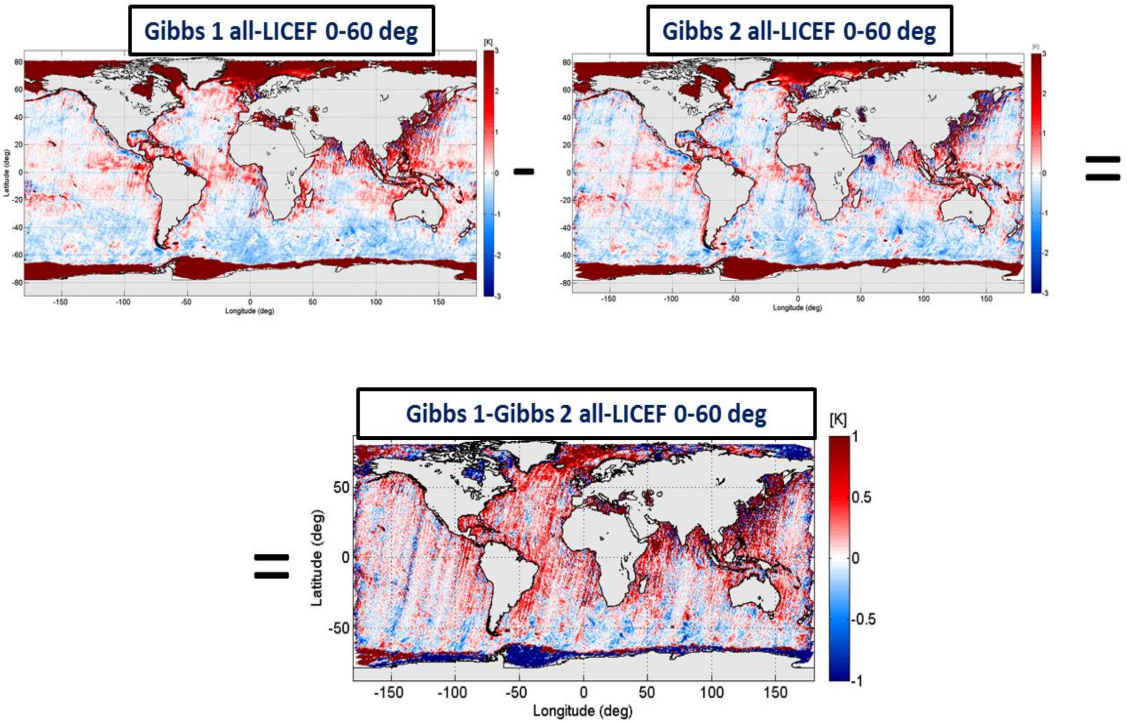
Gibbs 1 all-LICEF 0-60 deg

Gibbs 2 all-LICEF 0-60 deg

Gibbs 1-Gibbs 2 all-LICEF 0-60 deg

*Figure A-1.2 1st Stokes SMOS global error map (10 days data). Difference between Gibbs 1 and Gibbs 2 approach*

# Agradecimientos

Esta tesis se ha llevado a cabo en el marco de la beca FPI BES-2012-053917 del 1 de diciembre de 2012, por el "Secretario de Estado de Investigación del Ministerio de Economía y Competitividad", asociada al proyecto TEC2011-25865 (Universidad Politècnica de Catalunya).

Quiero dar las gracias a todas las personas que han hecho posible la realización de esta tesis.

Muy especialmente, me gustaría agradecer al profesor Ignasi Corbella todo el conocimiento que me ha transmitido durante más de siete años, teniendo siempre la paciencia para explicarme las cosas las veces que hayan sido necesarias, ayudándome a resolver cualquier aspecto técnico del proyecto cuando lo he necesitado, especialmente en la realización y desarrollo de programas. Por último, agradecer a Ignasi su buen trato durante los viajes que hemos hecho facilitando que las reuniones de trabajo fueran siempre tan amenas.

En un lugar relevante, quiero expresar mi sincero agradecimiento a mis tutores por su apoyo durante la realización de esta tesis: Francesc Torres y Núria Duffo.

A Francesc Torres agradecer todo el tiempo que ha empleado en mostrarme qué significa la auténtica investigación, pues ha sido la persona con la que he pasado más horas trabajando en el día a día. Siempre siendo muy competente y agradable en todo momento incluso en los momentos más difíciles cuando no era capaz de avanzar con mi trabajo. De él he aprendido una frase muy importante: "Las cosas cuestan", las cosas cuestan tiempo y esfuerzo pues él me ha hecho valorar el esfuerzo verdadero y la satisfacción del trabajo bien hecho. Creo que no puedo agradecer aquí todo lo que en estos años ha hecho por mí, estoy convencido que si no fuera por su gran apoyo durante todos estos años (especialmente en mis inicios) no hubiera emprendido este camino tan arduo pues él ha conseguido que continuamente yo crea en mis posibilidades dentro del mundo de la investigación. Estaré siempre agradecido por ello.

A Núria Duffo le debo agradecer el participar en la misión SMOS, pues fue ella quien me permitió el acceso mediante la realización de mi proyecto fin de carrera. Durante mis estudios siempre dije que lo que verdaderamente me gustaba de las telecomunicaciones eran los satélites y gracias a que ella me introdujo en este proyecto llevo ya casi ocho años participando activamente en esta increíble misión europea. Al igual que Francesc o Ignasi siempre ha estado apoyándome, supervisándome, enseñándome todo lo que no comprendía con una paciencia infinita siendo así la auténtica maestra que te muestra las cosas desde la sencillez y la humildad.

Gracias Ignasi, Francesc y Núria por estos años tan enriquecedores en los que me habéis mostrado lo que significa trabajar en equipo y ser un gran equipo.

A la profesora Mercè Vall-llossera darle las gracias porque aunque no hemos trabajado en el mismo proyecto, en las pequeñas tareas que hemos tenido en común siempre ha sido una persona amable y agradecida conmigo.

Del mismo modo ocurre con el profesor Adriano Camps, el cual siempre que he acudido a él a realizar una consulta ha tenido tiempo para resolverme cualquier duda con total interés.

Durante estos años he tenido muchos compañeros dentro de mi andadura en el proyecto SMOS, todos han sido unos excelentes compañeros pero quizá con quien más tiempo he pasado trabajando en equipo (y quien más me ha enseñado y ayudado) ha sido Lin Wu. Ahora ya de nuevo en China, gracias por tener siempre la paciencia y el tiempo para enseñarme todo aquello que necesitaba para salir adelante cuando lo he necesitado (谢谢). Muchas gracias a Verónica González, que desde mis principios en SMOS fue como una tutora más y que nunca ha dejado de ayudarme hasta el día de hoy en todo lo que he necesitado, además de ser una gran compañera en todos los congresos o reuniones en los que hemos coincidido. Finalmente cito a todos los otros compañeros con los que he tenido el placer de trabajar en el proyecto SMOS y a los que debo las gracias por su apoyo y buenas palabras hacia mí siempre: Miriam Pablos, Sandra Monerris, Rubén Dávila, Lotta Rehn-Molim, Marc Vizcarro y Roselena Rubino con la que actualmente sigo trabajando.

Durante la realización de la tesis he asistido regularmente a las reuniones de calibración de la ESA, allí he podido aprender y ser guiado por Manuel Martín-Neira, el cual siempre me ha tratado excelentemente y apoyado en todo mi trabajo. En estas reuniones he tenido el placer de conocer a Antonio Turiel (SMOS BEC) al cual quiero agradecer también su gran apoyo. También quiero agradecer a Roger Oliva de ESA su buen trato durante la presentación de resultados en las diferentes reuniones.

Quiero nombrar a todos esos compañeros de laboratorio que han estado ahí y aunque no hemos participado en un mismo proyecto, merecen el mismo agradecimiento pues han aportado muchísima luz durante mi tesis. Primero de todo, a Marc Lort por sus sabios consejos, por escucharme siempre y convertirse en uno de mis mejores amigos, siempre estaré agradecido de todos los grandes momentos que hemos compartido juntos durante este doctorado. Quiero mencionar también a David Chaparro, una gran persona que siempre tiene palabras positivas para el resto de los compañeros y que me ha acompañado en mis desayunos tantas veces. Muchas otras personas han estado ahí y siempre me han echado una mano cuando los he necesitado, seguramente olvidaré algunos de ellos aquí, así que doy las gracias a todo el personal del grupo de investigación, en especial a Aynie Khoe, Alicia Correa y, como no, al apoyo recibido de los servicios informáticos

Durante el 2016 realicé una estancia doctoral en Toulouse (Francia). Debo agradecer al Director de CESBIO Yann Kerr y a todo su equipo de trabajo su maravillosa acogida en los tres meses que allí estuve colaborando con ellos. Me sentí como en casa durante los tres meses que estuve en Francia, quiero agradecer la amistad que me brindaron Philippe Richaume, Ali Mahmoodi, Ali Khaazal, Simone Bircher, François Cabot y Beatriz Molero.

Por último, agradecer a todos aquellos que han estado en mi vida durante estos años fuera del marco académico y que tienen para mí la misma importancia que mis profesores pues son aquellos que fuera del entorno de trabajo han sabido apoyarme y ayudarme para que siga adelante. En primer lugar, agradecer a mi familia, en concreto a mis padres, que han permitido que pueda estudiar una ingeniería y un doctorado, que me han dado total libertad para que haya realizado el camino que quería en la vida. Creo que no hace falta decir que sin ellos ahora mismo no estaría escribiendo este texto, gracias por haberme permitido ser la persona que soy.

Finalmente, agradecer a todos mis amigos su apoyo incondicional estos años, sin todos ellos no habría tenido la energía para llevar a cabo este camino tan largo y lleno de obstáculos. Gracias José Luis, Marc, Roger, Raúl, David, Álex, Verónica, Antonio y tantos otros…